

IVW - Schriftenreihe Band 147

Leibniz-Institut für Verbundwerkstoffe GmbH

Kaiserslautern

Andreas Peter Klingler

**Morphology and Fracture of
Block Copolymer and Core-Shell
Rubber Particle Modified Epoxies
and their Carbon Fibre Reinforced
Composites**

Bibliografische Information Der Deutschen Bibliothek

Die Deutsche Bibliothek verzeichnet diese Publikation in der Deutschen Nationalbibliografie; detaillierte bibliografische Daten sind im Internet über <<http://dnb.dnb.de>> abrufbar.

Bibliographic information published by Die Deutsche Bibliothek

Die Deutsche Bibliothek lists this publication in the Deutsche Nationalbibliografie; detailed bibliographic data is available in the Internet at <<http://dnb.dnb.de>>.

Herausgeber: Leibniz-Institut für Verbundwerkstoffe GmbH
Prof. Dr.-Ing. Ulf Breuer
Erwin-Schrödinger-Straße 58
Technische Universität Kaiserslautern
67663 Kaiserslautern
<http://www.ivw.uni-kl.de>

Verlag: Leibniz-Institut für Verbundwerkstoffe GmbH

Druck: pri-me Printservice & Medienservice
Barbarossastraße 1
67655 Kaiserslautern
D-386

© Leibniz-Institut für Verbundwerkstoffe GmbH, Kaiserslautern 2021

Alle Rechte vorbehalten, auch das des auszugsweisen Nachdrucks, der auszugsweisen oder vollständigen Wiedergabe (Photographie, Mikroskopie), der Speicherung in Datenverarbeitungsanlagen und das der Übersetzung.

Als Manuskript gedruckt. Printed in Germany.

ISSN 1615-021X

ISBN: 978-3-944440-44-6

Morphology and Fracture of Block Copolymer and Core-Shell Rubber Particle Modified Epoxies and their Carbon Fibre Reinforced Composites

Dem Fachbereich Maschinenbau und Verfahrenstechnik
der Technischen Universität Kaiserslautern
zur Erlangung des akademischen Grades

Doktor-Ingenieur (Dr.-Ing.)

genehmigte

Dissertation

von

Herrn

Dipl.-Ing. Andreas Peter Klingler

aus Worms

Tag der mündlichen Prüfung: 26.02.2021

Dekan

Prüfungsvorsitzender

1. Berichterstatter

2. Berichterstatter

Prof. Dr.-Ing. Tilmann Beck

Prof. Dr.-Ing. Eberhard Kerscher

Prof. Dr.-Ing. Ulf Paul Breuer

Prof. Dr.-Ing. Dr. h.c. mult. Klaus Friedrich

Acknowledgements

The present work was completed between September 2015 and November 2020, during my time as a research associate at the Leibniz-Institute for Composite Materials (IVW GmbH) in Kaiserslautern.

First of all, I would like to greatly thank Prof. Ulf Breuer and Prof. Klaus Friedrich for supervising this thesis. It was a great pleasure to work with them during the last five years and I am very grateful for the opportunities they gave me and supported me with, especially with regard to my research stay (DAAD Kurzstipendien fuer Doktoranden, funding no. 57438025) at the Centre for Advanced Materials Technology (Prof. Lin Ye, University of Sydney, Australia) and at the Centre for Advanced Composite Materials (Prof. Simon Bickerton, University of Auckland, New Zealand). I also thank Prof. Eberhard Kerscher for overtaking the chairmanship of the examination committee.

I would like to give special thanks to Dr.-Ing. Bernd Wetzel, for whom everything of the above is true as well, but even more. Thanks, Bernd, for the tirelessly positive view of scientific challenges.

I want to especially thank Prof. Jan Kristian Krüger for bringing me closer to the fundamentals of materials science, his stamina to teach me thermodynamics and his persistent way of pushing me forward. I am really happy we met, Jan!

Furthermore, I want to thank my colleagues and friends at IVW. I cannot name each single one of you, but some of the memories will probably stay forever: Conferences in Bremen, Belgrade (Serbia) and Melbourne (Australia), including an awesome trip along the east coast, a concert at the Völklinger Hütte, Southside festival 2018, organizing the SAMPE conference, uncountable night outs in Kaiserslautern and brain-relaxing gym and running time - it was fun being part of the team!

I also take the chance to thank my parents, Thomas and Petra, for supporting me in all my ideas and especially for giving me the possibility to pursue this pathway into academia. Also thanks to my favourite brothers Stefan, Michael, and Felix.

The work was not funded by any entity, yet some projects accompanied me along my pathway. Therefore, I would especially like to acknowledge the cooperation with Kaneka Belgium N.V.

Kaiserslautern, November 2020

Table of Contents

Table of Contents	I
Kurzfassung	IV
Abstract	V
Glossary	VI
1 Introduction	1
2 State of the Art	4
2.1 Toughness and damage resistance of carbon fibre reinforced epoxies	4
2.1.1 Fibre matrix interphase	8
2.1.2 Interlaminar fracture toughness (Mode I) and resistance to delamination (Mode II)	10
2.2 Thermosets and epoxies	15
2.3 Toughening of epoxy matrices	19
2.3.1 Intrinsic vs. extrinsic toughness	19
2.3.2 Toughness of epoxy matrices induced by second phases	19
2.3.2.1 Core-Shell Rubber Nanoparticles	23
2.3.2.2 Block Copolymers	25
2.3.3 Toughening mechanisms of rubbery type modifiers	29
2.3.4 Geometrical aspects and other considerations	31
3 Motivation and Objectives	34
4 Materials and Experiments	35
4.1 Materials selection	35
4.1.1 Epoxy resin system	35
4.1.2 Block copolymers and core-shell rubber nanoparticles	35
4.1.3 Carbon fibre type and fabrics	36
4.2 Materials processing	39
4.2.1 Systems overview	39
4.2.2 Matrix manufacturing	40
4.2.3 Carbon fibre reinforced epoxy laminate manufacturing	41
4.3 Thermal analyses and basic materials characterization	42
4.3.1 Dynamic Scanning Calorimetry (DSC)	42
4.3.2 Phase separation and volume changes via Temperature Modulated Optical Refractometry (TMOR)	43
4.3.3 Dynamic Mechanical Analyses (DMA)	46

4.4	Mechanical Characterization	48
4.4.1	Tensile properties	48
4.4.2	(Interlaminar) fracture toughness - Mode I	48
4.4.2.1	Matrix	48
4.4.2.2	Carbon fibre reinforced epoxy	51
4.4.3	Interlaminar fracture toughness - Mode II	52
4.5	Damage Resistance	55
4.5.1	Impact performance	55
4.5.2	Post-impact Indentation depth	56
4.5.3	Damage size evaluation via ultrasound	57
4.6	Imaging Techniques	59
4.6.1	Scanning electron microscopy	59
4.6.2	3D X-ray microscopy	59
5	Results and Discussion	61
5.1	Phase separation behaviour of block copolymers in epoxy	61
5.2	Block copolymer modified epoxy	70
5.2.1	Morphologies of block copolymer modified epoxy	70
5.2.2	Thermo-mechanical properties of block copolymer modified epoxy . . .	74
5.2.3	Block copolymers as toughening agents for epoxies	78
5.3	Block copolymer and core-shell rubber particle hybrid modification of epoxy . .	82
5.3.1	Thermal and thermo-mechanical properties of neat DGEBA based epoxy, CAE and block copolymer and core-shell rubber modified CAE .	83
5.3.2	Tensile properties of block copolymer and core shell rubber particle modified epoxy	86
5.3.3	Block copolymer and core shell rubber particles as toughening agents of epoxy	88
5.4	Block copolymers and core-shell rubber nanoparticles in carbon fibre reinforced epoxy	92
5.4.1	Morphology of block copolymer modified carbon fibre reinforced epoxies (Interlaminar Mode I fracture)	92
5.4.2	Interlaminar Mode I fracture toughness (tension) of BCP and CSR nanoparticle toughened carbon fibre reinforced epoxy	97
5.4.3	Interlaminar Mode II fracture toughness (in-plane shear) of BCP and CSR nanoparticle toughened carbon fibre reinforced epoxy	102
5.5	Damage resistance of toughened thermosets	105
5.6	Core-shell rubber nanoparticles as highly efficient toughening agents for passenger car wheels	113

6	Conclusions and Outlook	116
6.1	Conclusions	116
6.2	Outlook	118
	References	120
A	Appendices	143
A.1	Curing reactions of epoxies with anhydrides	143
A.2	Post-curing investigations	145
A.3	Collection of supplemental tables, figures and other data	147
	Publications and Conference Contributions	158
	Supervised Theses	160
	Curriculum Vitae	161

Kurzfassung

Kohlenstofffaserverstärkte Kunststoffe (CFK) sind Hochleistungsverbundwerkstoffe, die sich durch ihre thermischen und gewichtsspezifischen mechanischen Eigenschaften auszeichnen. Eine glasige, hochvernetzte Epoxidharzmatrix verleiht dem Material einen hohen thermischen Widerstand, macht den Verbundwerkstoff jedoch auch spröde und anfällig für Risse und schlagartige Beanspruchungen. Eine Möglichkeit, diese Schlüsseleigenschaft, die Zähigkeit von Epoxidharzmatrixsystemen, zu erhöhen, ist die Modifikation der zugrundeliegenden Morphologie; das Einbringen zusätzlicher Substrukturen erhöht den Widerstand des Materials gegen Rissbildung und -fortschritt. Diese Arbeit liefert einen Beitrag zum Verständnis des Einflusses von Substruktur-bildenden, selbstorganisierenden Block-Copolymeren (BCP) und vorgeformten Kern-Schale-Partikeln (KSP) auf die Zähigkeit und die Schadenstoleranz von dünnen CFK-Strukturen und deren Epoxidharzmatrizes. Mittels einer neuen, thermo-optischen Messmethode wird gezeigt, dass die Bildung von BCP-reichen Substrukturen alleine vom chemischen Umsatz der Vernetzungsreaktion der Epoxidharzmatrix abhängt. Zudem wird die Substrukturbildung im CFK stark durch die Anwesenheit der Kohlenstofffasern beeinflusst. Bereits geringe BCP-Konzentrationen (7 Gew.-%) führen zu einer drastischen Erhöhung (250 %) des interlaminaren Risswiderstands des Faserverbunds (Mode I). Eine Modifikation mittels KSP wiederum steigert den benötigten Energieeintrag zur Initiierung von Delaminationen (160 %, Mode II). Durch eine Hybridisierung beider Modifikatoren ist es so möglich, das Schädigungsvolumen unter Schlagbeanspruchung, wenn beide Lastfälle kombiniert auftreten, um mehr als 67 % zu verringern. Die generierten Materialsysteme und das erarbeitete Verständnis erlauben es, zukünftig noch dünnere CFK-Strukturen herzustellen, ohne deren Strukturintegrität bei Schlagbeanspruchung zu reduzieren.

Abstract

Carbon fibre reinforced epoxies (CFRE) are a class of high performance, light-weight composites that show outstanding, weight-specific (thermo-)mechanical properties. A glassy and highly cross-linked epoxy matrix provides the composite with a high thermal resistance, but makes the CFRE also inherently brittle and susceptible to cracks and impacts. One strategy to overcome this drawback and to improve fracture toughness of epoxy matrices is to modify the underlying morphology with additional substructures (domains in the nano and/or micron size range). This allows increasing the energy that is required to initiate or propagate a crack within the material. The present work contributes to a better understanding of the effect of substructure-forming, self-assembling block copolymers (BCP) and pre-formed core-shell rubber particles (CSR) on the toughness and impact behaviour of thin CFREs and their epoxy matrices. Using a new thermo-optical measurement technique, it is shown that the phase-separation process of BCP-rich domains is solely driven by the degree of cure of the epoxy matrix. Also, it is found that the process of BCP phase-separation, e.g. the BCP-rich domain size, changes strongly in the presence of carbon fibres. Low concentrations of BCPs (7 wt.-%) yield a 2.5-fold enhancement of the resistance to interlaminar fracture of the CFRE (Mode I), already. Using CSR particles, on the other hand, the energy required to initiate delamination (Mode II) within the CFRE increases by 160 %. Subsequently, by a hybridization of BCP and CSR modifiers, after low energy impacts, when both load cases occur in combination, a synergistic damage volume reduction by more than 67 % is achieved. Hence, the generated material systems and the acquired understanding allow future CFRE based structures to be even thinner than current design solutions, without affecting their structural integrity under impact loads.

Glossary

Abbreviation	Description
3PB	<i>Three Point Bending</i>
AR	<i>Auxiliary Reflector</i>
BCP	<i>Block Copolymer</i>
BVID	<i>Barely Visible Impact Damage</i>
BW	<i>Back Wall</i>
CAE	<i>Cycloaliphatic Epoxy</i>
CAI	<i>Compression After Impact</i>
CBR	<i>Carbon Based and Rigid Modifiers</i>
CF	<i>Carbon Fibre</i>
CFRP	<i>Carbon Fibre Reinforced Polymer</i>
CFRE	<i>Carbon Fibre Reinforced Epoxy</i>
CM	<i>Compliant Modifiers</i>
CNT	<i>Carbon Nano Tubes</i>
CPT	<i>Cured Ply Thickness</i>
CSR	<i>Core Shell Rubber</i>
CT	<i>Compact Tension</i>
DCB	<i>Double Cantilever Beam</i>
DGEBA	<i>Diglycidyl Ether of Bisphenol A</i>
DMA	<i>DiMethlyAcrylamid</i>
DMA	<i>Dynamic Mechanical Analyses</i>
DR	<i>Damage Resistance</i>
DSC	<i>Differential Scanning Calorimetry</i>
DT	<i>Damage Tolerance</i>
DTL	<i>Damage Threshold Load</i>
EEW	<i>Epoxy Equivalent Weight</i>
ENF	<i>End Notch Flexure (test)</i>
ELS	<i>End Loaded Split (test)</i>
EPFM	<i>Elastic Plastic Fracture Mechanics</i>
FMT	<i>Fracture Mechanics Theory</i>
FPZ	<i>Fracture Process Zone</i>
FRP	<i>Fibre Reinforced Polymer</i>
FWHM	<i>Full Width Half Maximum</i>
GCM	<i>Group Contribution Method</i>
HVI	<i>High Velocity Impact</i>
IRP	<i>Inorganic and Rigid Particles</i>
LCD	<i>Liquid Crystal Display</i>

LEFM	<i>Linear Elastic Fracture Mechanics</i>
LVI	<i>Low Velocity Impact</i>
MST	<i>Minimum Skin Thickness</i>
NCF	<i>Non Crimp Fabric</i>
NL	<i>Non Linear</i>
PA	<i>Phased Array</i>
PBuA	<i>PolyButylAcrylate</i>
PMMA	<i>PolyMethylMethAcrylate</i>
PRS	<i>Partially Reacted Substructure</i>
PS	<i>Phase Separating Modifiers</i>
PZ	<i>Plastic Zone</i>
SEM	<i>Scanning Electron Microscopy</i>
TMOR	<i>Temperature Modulated Optical Refractometry</i>
US	<i>Ultra Sound</i>
Vis	<i>Visual</i>
XRM	<i>X-ray Microscope/y</i>

Latin Symbols

Symbol	Unit	Description
$A_{n,\omega}$	mm	Frequency dependent amplitude of the refractive index
A_T	K	Temperature amplitude
a	mm	Crack length
B	mm	Length
b	mm	Width
C	mm/N	Compliance
c	m/s	Speed of light
D	μm	Particle/Phase diameter
DTL	N	Damage threshold load
E	MPa	Young's modulus
E_f	MPa	Flexural modulus
E_{Impact}	J	Impact energy
F	N	Force
F_{corr}		Correction factor for large displacements
f	Hz	Frequency
G	J/m^2	Energy release rate
G_{base}	m^2	Area of the base of a cone
G_{Ic}	J/m^2	Critical energy release rate in Mode I
G_{IIc}	J/m^2	Critical energy release rate in Mode II

H	J	Enthalpy
h	mm	Height
i		Imaginary unit
K	$\text{MPa}\sqrt{\text{m}}$	Stress intensity factor
K_{Ic}	$\text{MPa}\sqrt{\text{m}}$	Critical stress intensity factor
l	mm	Length
M_c	g/mol	Average molecular weight between crosslinks
m	kg	Mass
m		Slope
N		Load block correction factor
n		Refractive index
n_c	$1/\text{cm}^3$	Cross-link density
n_u		Number of repeat units
P	N	Load
Q	J	Heat
\dot{Q}	J/s	Heat flow
r	mm	Radius, Distance
r_p	mm	Plastic zone size at crack tip
s	mm	Displacement
t	s	Time
T	K	Temperature
T_g	$^{\circ}\text{C}$	Glass transition temperature
U	J	Energy
U_{acc}	V	Accelerating voltage
U_{surf}	J	Surface energy of a cracked plate
U_{release}	J	Strain energy
x_{fs}	mm	Fibre surface to fibre surface distance
v	m/s	Velocity
v_f		Fibre volume concentration
W	mm	Length
Z		Atomic number
z	mm	Depth

Greek Symbols

Symbol	Unit	Description
α	$^{\circ}$	Angle
α_{US}	$\text{dB}/\text{mHz}\cdot\text{cm}$	Attenuation coefficient of ultrasound in a medium
β	$1/\text{K}$	Thermal volume expansion coefficient

Δ		Crack length correction factor
Δ_{clamp}	mm/F	Compliance of clamping device
δ_f	°	Angle/Phase shift
ε		Mechanical strain
ε_f		Strain to failure
η_{photon}	m^{-1}	Linear attenuation coefficient of X-rays
γ	J/m^2	Specific surface energy
γ_p	J/m^2	Specific energy by plastic deformation
λ	m	Wavelength
ν		Poisson ration
ω	Hz	Angular frequency
Φ	J·K/s	Total heat flow
ϕ	°	Angle/Phase shift
ρ	kg/m^3	Mass density
σ	MPa	Mechanical stress
σ_{res}	MPa	Residual strength
σ_{ys}	MPa	Yield stress
τ	s	Temperature modulation time

Constants

Symbol	Description	Value
q	Front factor	0.725
N	Avogadro constant	$6.0221 \cdot 10^{23} \text{ 1/mol}$
Π		3.1416
R	Universal gas constant	$8.3145 \text{ kg}\cdot\text{m}^2\cdot(\text{s}^2\cdot\text{mol}\cdot\text{K})^{-1}$

1 Introduction

Challenges of carbon fibre reinforced thermosets in modern, high-performance applications

In recent years, the demand for new technologies on the basis of sustainability and recyclability became one of the most important factors for the development of new applications. Regulations and goals set by organizations [1], governments [2, 3] and companies [4] have therefore established a common pathway to drastically reduce world-wide CO₂ emissions, push for recyclability of products and promote resource-efficient handling of materials.

Within the field of materials science, these goals can be translated to material requirements such as (i) a reduction of weight without detrimental effects on performance, (ii) recyclability of components, (iii) multifunctionality and (iv) extension of life-times.

A special class of materials that can uniquely contribute to all of those demands are fibre reinforced polymers (FRP):

- (i) The combination of an anisotropic orientation of high strength fibres within a low mass density polymeric matrix allows a **strong reduction of weight** without reducing a parts' performance compared to metal or non reinforced plastics [5, 6]
- (ii) The selection of an appropriate matrix system allows partial or even full **recyclability** at the end of its life-time [7, 8]
- (iii) Variable manufacturing processes enable **multifunctionality** of FRPs, e.g. by the integration of metal fibres into a polymeric matrix to implement lightning-protection and increase its impact resistance [9, 10]
- (iv) Crack growth can be omitted and **the life-times of polymer composites be strongly extended** by following certain design criteria inherent to FRPs [11].

Such high-performance fibre reinforced polymers must time-limited, or even permanently, withstand extraordinary stress conditions. Therefore, important material properties are high mechanical strength and stiffness, high fracture toughness, damage resistance and damage tolerance, a high cycle fatigue resistance, as well as a high thermal stability and chemical resistance [5, 12]. Within that regard, especially carbon fibre reinforced epoxies (CFRE) are able to satisfy most of those requirements. The epoxy matrix provides thermal stability and chemical resistance, and the carbon fibres provide extraordinary strength and stiffness to a part [13].

Today, CFREs are e.g. used in aircraft structures, in which more than 90% of the primary load carrying composites are made of high-performance CFREs [11] to reduce weight and consequently increase the mass of transportable goods. New developments deal with wheels for new generation high-performance automobiles (cf. Fig. 1.1) and motorcycles [14] to reduce noise and vibrations and enhance steering and handling, and (iii) ultra-fast spinning flywheel applications [15], in which CFREs allow to store energy, based on velocity rather

than mass. However, one of the biggest challenges to another breakthrough in structural mass reduction, especially in transportation systems, is the improvement of lacking toughness of CFREs [16–19].

The inherent brittleness of carbon fibre reinforced epoxies originates from the highly cross-linked molecular network structure of the glassy epoxy matrix that forms during its genesis, i.e. the chemical cross-linking reaction. The densely cross-linked molecular network and the stiffness of chains between the cross-links restrict large-scale plastic deformations during crack growth, i.e. the energy that is introduced into the part by external loads cannot be dissipated by local plastic deformation so that fracture occurs. This is the causal reason for the brittleness of epoxy matrices [17, 20]. Damage tolerant design solutions of epoxy based



Figure 1.1: Commercially available carbon fibre reinforced hybrid wheel with aluminium spokes

CFREs, following "no crack growth" design principles, are state of the art. However, a certain "minimum skin thickness" (MST) is necessary in order to withstand impact loads, due to the relatively brittle failure behaviour [11, 21]. Thus, material dimensions are oversized or high safety factors are applied. All of them reducing the initially weight saving potential of CFREs.

In order to improve the impact tolerance of composite structures and at the same time the light weight design of components, extensive research efforts focus on *intrinsic and extrinsic strategies* to toughen epoxy based carbon fibre reinforced composites. Thereby, a common pathway is the modification of the epoxy matrix by so called *toughening agents* to provide the CFRE with energy dissipating capabilities to omit crack growth.

Toughening agents are materials that are incorporated into the liquid epoxy resin (i.e. before curing) and usually prevail in the matrix after the curing process as nano to micron sized *second phases*. They have either pre-defined shapes and dimensions, e.g. spherical particles, or form respective heterogeneities from an initially homogeneously mixed state with the epoxy resin by thermodynamically driven phase-separation.

Toughening agents are e.g. **rubbery type particles** that are highly efficient to improve fracture toughness of epoxy matrices by *deflecting an approaching crack* and/or *internal cavitation*, which again promotes subsequent *void growth* (plastic deformation of the matrix in the close vicinity of a cavitated particle). On the downside, Young's modulus of such toughened epoxy matrices decreases with increasing rubber concentration [22]. Another type of *classical* toughening agents are phase separating **liquid rubbers**, that form differently shaped and sized second phases, such as particulate domains in the epoxy matrix during the curing process. Similarly to pre-shaped rubber particles, they strongly improve fracture toughness [23]. However, if the phase-separation process is incomplete, i.e. unsegregated macromolecules of the toughening agent remain in the molecular epoxy network, the stiffness of molecular chain segments between cross-links is strongly reduced and the thermal glass transition temperature of the matrix decreases. This can be detrimental to important functional requirements for certain applications.

Today, new materials developments, such as *block copolymers* and *core-shell rubber nano particles* have overcome some of the accompanying, disadvantageous effects of *classical* toughening agents, especially with respect to the thermal glass transition temperature [24, 25].

Pre-shaped core-shell rubber nanoparticles (CSR) for example, usually supplied as powder, suffer from their high specific surface energy and subsequent agglomeration. Nowadays, these modifiers are available in a pre-dispersed state in carrier resins and provide single nanoparticle dispersion in epoxy matrices without the necessity for additional dispersion technologies. Another, even more variable type of toughening modification of an epoxy matrix are block-wise built copolymers (BCP) [26]. Block copolymers are macromolecules of at least two chemically different, covalently bonded types of monomers. Thermodynamically driven, they can self-assemble e.g. into particulate core-shell structures and resemble an advanced type of CSR particles. Thereby, one of the blocks is designed to provide compatibility to the epoxy resin system, the other one is meant to provide toughness in the case of fracture. BCPs have the advantage not to be filtered by the presence of carbon fibres in a resin infusion process, since the phase separation process (i.e. *core-shell structure formation*) occurs first during curing of the already infused system, given the presence of the fibres is not influencing the BCP phase separation process [27, 28]. Also, due to their macromolecular block structure, BCPs do not change the underlying epoxy network, when phase separating, i.e. molecular network chain stiffness and cross-link density as well as the thermal glass transition temperature of the epoxy matrix remain unaltered.

However, the utilization of block copolymers as toughening agents in epoxy matrices is a challenging task. A number of parameters affect and dictate the phase separation process and the resulting morphologies, such as e.g. the BCP block units, the BCPs' molecular weight, the resin-hardener system, and the curing process. Yet, by understanding and controlling

the phase separation process of BCPs, these modifiers do not only allow to tailor fracture resistant morphologies within epoxy matrices but also to adjust interphase properties between a composites matrix and the fibre system, and furthermore to control e.g. the damage resistance of carbon fibre reinforced epoxies.

This dissertation focusses on the damage resistance (DR) and the fracture mechanical properties of carbon fibre reinforced epoxies that have been modified by block copolymer toughening agents as well as blends of BCP and CSR nanoparticles. A special focus is put on understanding (i) the phase-separation process in an epoxy resin, (ii) the fracture mechanical properties of these species in an epoxy matrix and (iii) their effect on the impact behaviour of CFREs. The work wants to contribute to a better understanding of BCP (and CSR) modified (carbon fibre reinforced) epoxy systems, will try to provide answers to afore raised questions and enable the targeted use of BCPs in epoxies and CFREs, i.e. manufacture tough, damage resistant structures by understanding the phase-separation behaviour of such versatile macromolecular species in high-performance resin systems.

2 State of the Art

2.1 Toughness and damage resistance of carbon fibre reinforced epoxies

The impact behaviour of CFREs is characterized by the materials' resistance *to* and *after* sudden loading events. This *robustness* can be grouped into two categories: damage resistance (DR) and damage tolerance (DT). The DR of a carbon fibre reinforced composite is the ability of a pristine material to withstand an impact event and fully maintain its mechanical performance. A damage resistant part can accordingly still fulfil its task to the full extent once impacted, i.e. the full load carrying potential remains, at least up to a pre-defined impact energy threshold.

The DT of materials, on the other hand, is a measure to evaluate the permissive behaviour of a structure to an already existing damage [29]. Both terms are accordingly mutually inclusive.

To evaluate the degree of damage within a material and derive its DR and DT, a variety of non-destructive and destructive test methods can be employed. These can e.g. be (i) ultrasound analyses to determine the extent of a damage after an impact (cf. Sec. 4.5.2) [30], (ii) measuring the remaining dent depth caused by an impact, i.e. the post-impact indentation depth (cf. Sec. 4.5.3), or (iii) assessing the remaining load carrying capability after an impact quantitatively by *compression after impact* (CAI) tests, i.e. the *residual* compression strength of a material σ_{res} after impact [31]. If the material satisfies a certain threshold value ($\sigma_{\text{res}} \geq \sigma_{\text{res,critical}}$), it can be denominated as damage resistant to the

previously applied impact energy.

Within that regard, a distinct hazard to CFRPs are *barely visible impact damages* (BVID), generated by low energy impacts, which may cause severe delamination within the structure [11, 32, 33]. Since the detection of BVIDs is difficult, CFREs need to be *damage tolerant*, until the impact becomes fully visible (visibility threshold). Therefore, it is of special interest to understand the relationship between different material design parameters, such as e.g. fracture toughness or the resistance to interlaminar crack propagation and the impact behaviour of FRPs, to manufacture thin, DR and DT CFREs, as done within this work.

Figure 2.2 illustrates exemplarily a 30 J instrumented impact event on a 4 mm thick, quasi-isotropic $[0/45/90/-45/0/45/90/-45]_S$ CFRE by a hemispherical indenter. The force-time

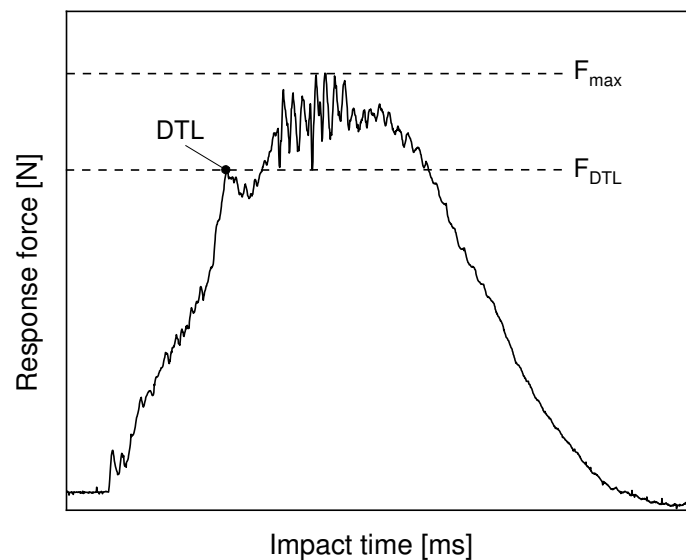


Figure 2.2: Force-time history of a lab-scaled impact test using a hemispherical indenter, DTL denominates the *damage threshold load*, when delamination is initiated.

history is characterized by small oscillations that are caused by elastic vibrations of the specimen [34], simultaneously the slope increases without creating any damage within the material. At a certain load, a sudden drop of the same occurs, which can be assigned to the initiation of delamination between plies, i.e. the damage threshold load (DTL) has been reached. Subsequently, the force further increases up to a maximum force F_{max} showing significant oscillations. The DTL is usually seen as the starting point of failure during an impact. Davis et al. [35] developed a very simplified model that is often applied to predict *damage initiation by impacts* based on the interlaminar fracture toughness in shear mode (cf. Sec. 2.1.2 and Sec. 4.4.3).

Impact events can furthermore be categorized according the impact velocity of the impactor into low velocity impacts (LVI) and high velocity impacts (HVI) [36]. LVIs are rather to be expected from events like tool drops during maintenance tasks, whereas HVIs describe impact

events that are caused by high speed projectiles, such as bullets, in-flight hail or runway debris. The transition from an LVI to an HVI event is thereby in the range of 20 m/s.

The relationship between impact velocity and impact energy is given in Eq. 2.1. In general, the higher the impact energy, the more severe the damage to a body, i.e. the residual strength decreases with increasing impact energy [36].

$$E_{\text{impact}} = \frac{1}{2}mv^2 \quad (2.1)$$

where m is the mass of the body and v the velocity of the impactor at impact.

During LVIs, the composite material behaves more elastic, since the response time to the impact is longer, i.e. slow impact velocities allow energy dissipation via large scale matrix deformation [37]. However, the geometry, such as the free length and the width of the part, also influence macroscopically the stiffness and deformation behaviour of the composite [36]. HVIs, on the other hand, are impact events that promote a very localised materials' response with less influence on the damage pattern by the geometry of the impacted structures. Hence, HVIs rather cause severe damage and eventually the penetration of a structure [36, 38]. Robinson et al. [39] examined the influence of the impact velocity on the failure behaviour of CFREs by changing the impactor mass to keep the total impact energy constant. They did not find any differences in the extent of the damage, no matter which impact velocities were employed. However, the impact velocity of the test was limited to speeds as high as 6 m/s, which is well in the LVI regime. Other researchers, such as Breen et al. [40] analysed the influence of the impact velocity on *thick* CFREs ($t=8$ mm), again without changing the impact energy. They compared a *quasi-static impact* (pushing the impactor into the specimen rather than impacting it) to an LVI at 9.2 m/s and found notable differences of the damage pattern as well as of the residual tensile strength, which was about 20 % larger for the quasi-static impacted specimen than the dynamically impacted one. These results were supported by Cantwell et al. [36] and Aryal et al. [38]. Hence, the damage patterns caused by LVIs depend not only on the total impact energy but also on the velocity (or mass) of the impactor. Higher mass at similar impact energies induces more severe damage patterns including matrix and fibre cracking, as well as delamination. If geometrical aspects (fibre orientation etc.) are neglected, differences of the impact behaviour at different impact velocities are most likely related to the visco-elastic nature (i.e. time-dependent material behaviour) of the polymeric matrix. However, differences only become measurable if the impact velocity notably changes, e.g. from an LVI to a HVI event, and vice-versa.

The type and extent of impact failure depends furthermore on other **non-matrix related properties**, such as e.g. (i) the projectile itself, (ii) the laminate thickness, (iii) the ply thickness as well as (iv) the stacking sequence of the plies. **Matrix related properties**, on the other hand are mainly governed by (I) the matrix strain to failure ε_f , (II) the matrix fracture toughness $G_{Ic,m}$ and (III) the composites interlaminar fracture toughness to shear loads $G_{IIc,c}$ [29, 41].

With regard to the **impacting body**, a quite recent study by Lie et al. [42] investigated the influence of projectile hardness on the impact behaviour (HVI) of a carbon fibre reinforced composite. The study showed that soft gelatine projectiles rather cause a bending of the material without actually damaging it, whereas hard projectiles severely damaged the composite, due to the high contact pressure between the projectile and the laminate. The impacted body was in this case a CF/Poly(etheretherketone) composite. Examining the influence of the **laminate thickness** on the occurring failure pattern, Fig. 2.3 illustrates the behaviour of a *thick* and a *thin* laminate. Usually, literature distinguishes between thick and thin laminates at a thickness of around 2 mm [29]. The thick structure fails in a *pine-tree*

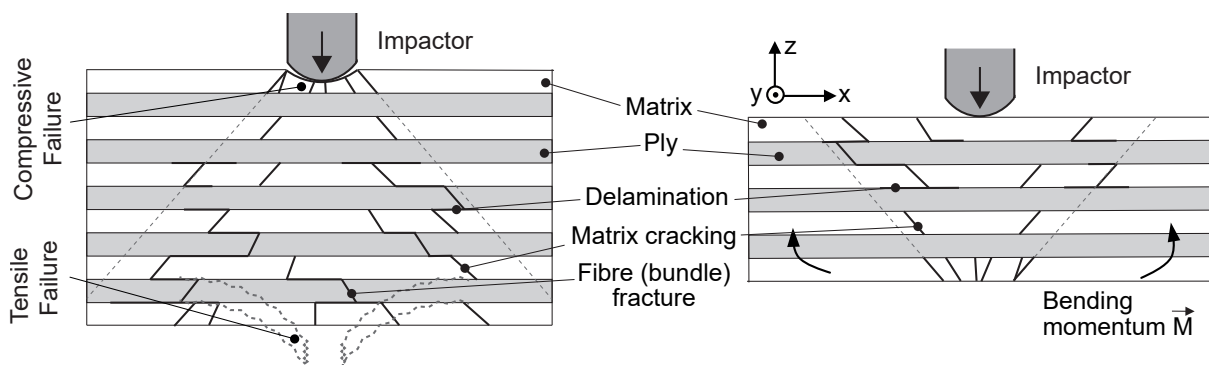


Figure 2.3: Empirical damage phenomena after low velocity impact of a thick and a thin laminate (same ply thickness), showing a pine-tree (left) and a reversed-pine tree damage pattern (right) [11, 43].

manner, i.e. the matrix fractures brittle under highly localized contact stresses when the load is introduced into the specimen by the indenter. Matrix cracks within the plies form that subsequently initiate large scale delaminations, especially in between differently oriented plies [43, 44]. At the bottom side of the specimen tensile failure occurs. A thin laminate on the other hand shows a *reversed pine-tree type of failure*. The lower bending stiffness of the specimens promote failure initiation on the bottom side of the sample, propagating to the top, where the actual indent occurred [29, 43]. The failure pattern of thin laminates shows a more severe through-thickness damage than thick specimens, when being impacted with the same impact energy and being built with the same number of plies [44]. This is because less impact energy is absorbed by delamination than in thick structures.

By using **thin plies** to built a CFRE, intralaminar stresses between plies are reduced, enabling a smoother stress transfer from one ply to another [37]. Thus, the chance to initiate delamination decreases. However, more plies are required to obtain a certain laminate thickness. Hence, from a design point of view, CFREs need to be sufficiently thin (weight-saving potential), to be built with thin plies to allow a smooth stress transfer between the plies, but also need to be thick enough to be damage tolerant. This design dilemma is also the reason for a *minimum skin thickness* (MST) requirement of CFREs for certain applications.

Currently, the MST for an aircraft fuselage is around 1.6 mm [11, 45].

With regard to laminate manufacturing and ply orientation, Fuoss et al. [46] stated that ply grouping, i.e. **stacking sequences** having plies oriented in the same directions, should be omitted, since larger delamination (x-y area) is created, rather than through thickness failure (z-direction). Caminero et al. [44] adds that quasi-isotropic layups show a larger damage pattern than e.g. cross-ply laminates, in which the through thickness damage was more severe. Ghelli et al. [47] examined low velocity impact damages of ~ 2.75 mm thin laminates, having been impacted at different energy levels (6, 12 and 18 J). They found that the damage patterns were related to the flexural stiffness of specimens, influenced by different stacking sequences. The stiffer samples showed much more severe fibre fracture than the more elastic systems.

Focussing on *matrix system related*-pathways to increase DR and DT of CFREs, an essential strategy is to adapt the resin system to an expected impact load case. Thereby, energy dissipation via matrix deformation should be enabled as well as interactions between the fibre and matrix be enhanced, to dissipate externally induced mechanical energy locally by delamination. Thereby, the matrix' strain to failure ε_f is especially important when considering damage initiation [29]. As long as the matrix is in a pristine, undamaged state (no crack exists), and ε_f is high enough, crack growth does not need to be hindered; the CFRE can simply absorb the impact energy until ε_f is reached. Then, the development of a defect (crack) can be avoided in the first place. Yet note, impacts are highly dynamic events, i.e. strain-rate effects might affect the matrix systems' mechanical performance. However, when a damage event creates cracks, the matrix needs to withstand further crack propagation. That is when energy dissipating capabilities of the matrix are activated, i.e. a high fracture toughness is required. Both properties originate from the molecular network structure of the epoxy matrix. Delamination damages strongly depend on the interaction between the matrix and the fibre, i.e. the fibre matrix interphase. They mainly occur at interfaces of plies that have different orientations to each other and strongly reduce the residual strength of a composite [43].

In order to provide a material with a high damage resistance during a low velocity impact all of those properties have to be considered.

2.1.1 Fibre matrix interphase

The vital role of an interphase, which is probably the most crucial subparameter to control the resistance to impact damages of CFREs [48], is to establish a connection between carbon fibres and the epoxy matrix in order to allow for a load transfer from the matrix to the fibres. To form an interphase functional carboxylate groups, such as e.g. COO- and COOH- bonds on the carbon fibre surface (also denominated as *sizing*, cf. Fig. 4.18) chemically react or bond with the epoxy matrix and/or provide physical compatibility to the epoxy system [49,

50]. Usually a gradual transition from one property to another, e.g. fibre to matrix, can be observed, cf. Fig. 2.4.

Note, *interphase* usually refers to the region between fibre and matrix and its individual components, i.e. the interphase is an object of interest. *Interface*, on the other hand, rather refers simply to the connection between two constituents, no matter how it is designed.

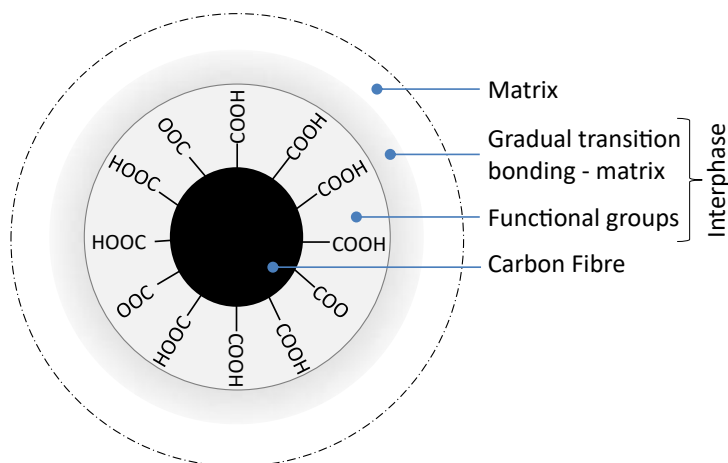


Figure 2.4: Schematic (not to scale), showing the interphase between a carbon fibre and an epoxy matrix. Reactive carboxylate groups react with the epoxy matrix and form a gradual transition zone of e.g. the Young's modulus from the carbon fibre to the matrix system. The sizing, as well as the gradual transition zone are denominated as the *interphase*, adapted from [50]

Depending on the *quality* of the interphase, i.e. stiffness, strength and dimension, macroscopic properties can be tailored. A *weak* interface will promote slippage between the fibre and the matrix, when impacted. Energy is then consumed by large delaminations and the DR is low, since the load transfer from fibre to matrix is restricted. A *strong* interface, on the other hand, will allow delaminations only locally to occur, when impacted. The impact will cause more likely a brittle type of failure of the matrix itself and a through-thickness damage of the carbon fibres themselves, i.e. the DT is strongly reduced. Atkins [51] showed that an intermittent bonding between matrix and fibre seems to be a successful strategy to toughen brittle CFRPs, i.e. to toughen regions between fibre and matrix that have a strong interfacial bonding to transfer stresses along the fibre, but also having regions of a weak fibre-matrix bonding to potentially blunt cracks.

Other phenomena, such as the selective adsorption of resin or hardener onto carbon fibres, can influence the interphase formation by affecting the cross-link density of an epoxy matrix, since some of the functional groups are no longer available for participation in the cross-linking reaction [52]. If such *secondary* reactions at the fibre interface are not considered, they can lead to differences in the performance of CFREs during impact.

However, not only resin and hardener can influence the interphase formation. Also phase separating toughening agents, such as block copolymers can alter the interphase structure

[53]. Kishi et al. [54] investigated the influence of different functional monomers that were copolymerized with an poly(methylmetacrylate) (PMMA) on the fibre-matrix interaction of a CFRP. They found that modifying the PMMA with a hydroxyethyl acrylamide copolymer was able to double the flexural strength of the composites. They observed a change of the fracture mode from a delamination dominated failure on the compression side to a fibre breakage failure mode on the tension side of the specimens. I.e. the interphase interaction between fibre and matrix increased, due to the copolymer modification. This is especially interesting since block-copolymer toughening agents can also make use of PMMA as block constituent within their molecular structure to enhance the the compatibility to epoxy resins.

2.1.2 Interlaminar fracture toughness (Mode I) and resistance to delamination (Mode II)

Another strategy to especially tackle the problem of delaminations during impacts is *interleaving* [55–57]. Interleaving means the targeted modification of ply interfaces by placing thermoplastic or rubbery layers (veils) in between single plies to specifically increase the interlaminar fracture toughness in tension and shear mode. During curing, the epoxy system physically or chemically bonds to the veils. Quan et al. examined the difference of such meltable (Polyamide-12) and non-meltable (Polyethyleneterephthalate and Polyphenylened-sulfide) veils on the interlaminar fracture toughness of unidirectional CFREs in Mode I [56] and Mode II [57]. In the case of Mode I, they showed that non-meltable veils strongly adhered to the carbon fibres and caused severe *veil*-bridging, when crack propagation occurred. The meltable Polyamide-12, on the other hand, cohesively failed and did not promote other fibre induced toughening mechanisms. The non-meltable veils tripled the energy required for crack propagation compared to the respective control system. However, applying the Polyamide-12 meltable veils to a $[90/0]_{4s}$ layup large scale carbon fibre bundle delamination occurred and enhanced the interlaminar fracture toughness far beyond the non-meltable veil systems. This study illustrates the complexity when interleaving of CFREs is applied, as well as the influence of other extrinsic parameters on the mechanical performance of CFREs, such as the fibre orientation. So far it is e.g. not understood, how meltable veils dissolve into the epoxy resin, or how they interact with the carbon fibres themselves. Hence, in one case a cohesive type of failure prevails and a quite low improvement of a property is achieved, and in the other case, the same property is drastically improved, if the stress distribution is changed. In the case of Mode II crack propagation [57], the fracture toughness again depended on the layup, yet a quite similar enhancement was found for the meltable and non-meltable veil modification.

Since the late 1960s' numerous efforts have been made to increase the resistance to delamination of CFRPs by inherently toughen the epoxy matrix of the composite. Thereby, the goal is not necessarily to alter interphase properties between fibre an matrix, the goal is rather to provide the matrix with energy dissipating capabilities. This can be achieved

by making use of different types of matrix modifications, employing e.g. rigid or compliant modifiers that dissolve into the epoxy matrix. In this work, the focus is put on such *initially phase separated* and *during the curing process phase-separating* (dissolving and *second phase forming*) species, specifically addressed in depth in Sec. 2.3.

However, toughening the epoxy matrix is usually only the first step to improve the interlaminar fracture toughness of a fibre reinforced composite. The gained toughness has to be transferred from the matrix to the CFRE.

In order to transfer fracture toughness properties from a polymeric matrix to the fibre composite a pre-requirement is a proper bonding between the constituents, i.e. some kind of interphase interactions between fibre and matrix need to prevail. Figure 2.5 is an important graph to illustrate this transfer of properties from the matrix to the fibre composite. It presents the relationship between the Mode I (tension) energy release rate, i.e. fracture toughness of the matrix, $G_{Ic,m}$, without carbon fibre reinforcement, and the fracture toughness of the respective CF reinforced matrix, $G_{Ic,c}$. The graph shows an accumulation of data gathered from literature being comprised of neat, i.e. untoughened epoxy matrices and a variety of differently modified epoxy matrices and CFREs: *rigid* refers to modifiers that are stiffer than the matrix, *carbon based* refers to CNTs and graphene modified matrices, *compliant* means modifiers being more elastic than the surrounding matrix, such as CSR particles and BCPs. An extended description of the different types of modifiers is given in Sec. 2.3.2.

Analysing the data, the investigated systems show a higher or at least equal energy release rate in the composite as in the matrix system (slope: $m=1$), up to an energy release rate of about $G_{Ic,m}=500 \text{ J/m}^2$. Up to this value, the full potential of energy dissipation provided by the matrix can be utilized and transferred to the fibre composite. Even more, the energy release rate of the CFREs is in average about ~ 2.3 times larger than the respective energy release rate of the matrix systems. The reason for this behaviour are additional, CF induced energy dissipating mechanisms. Even if the main purpose of CFs is to provide strength and stiffness to a CFRE, they also act as extrinsic tougheners. Provided the carbon fibres adhere well to the epoxy matrix, interactions between CF and the matrix can dissipate energy, and contribute to the toughness of the composite by bridging a crack or being pulled out of a matrix (G_b), by debonding from the matrix G_{deb} or even by fracturing G_f . Whereas carbon fibre fracture ($\approx 20-60 \text{ kJ/m}^2$) requires about 4 to 10 times more energy than debonding of a fibre from a matrix, due to the covalent bond orientation of the CF along the fibre axis [69]. The same mechanism can be utilized e.g. with crack bridging carbon nanotubes [70, 71]. The CF induced toughening mechanisms are schematically depicted in Figure 2.15, along other, intrinsic toughening mechanisms of epoxy based CFRPs.

However, therefore a CF reinforced composite's fracture toughness $G_{Ic,c}$ is not only dominated by the matrix fracture toughness $G_{Ic,m}$, but rather the sum of several fracture resistance

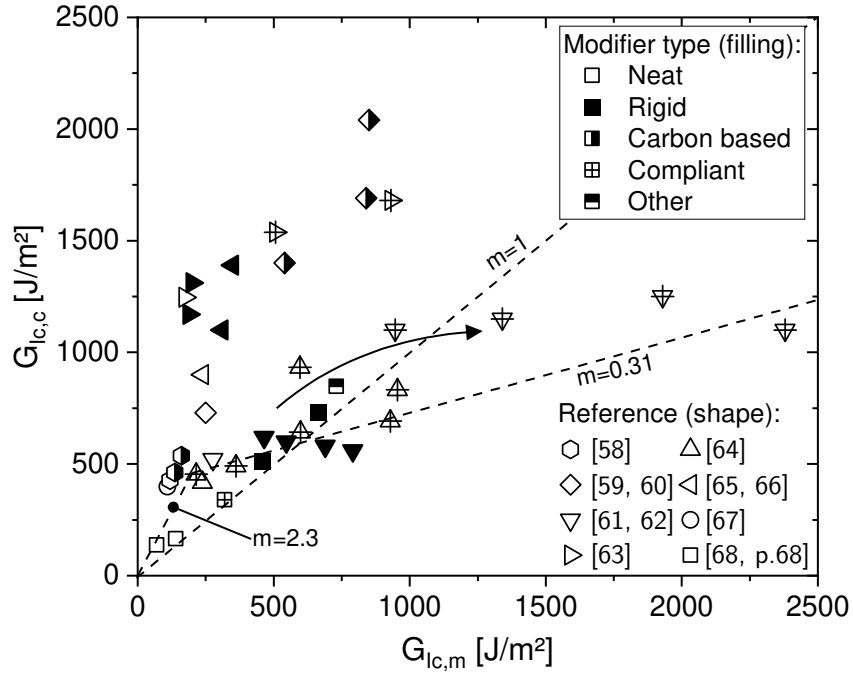


Figure 2.5: Relationship between the critical energy release rate of CFREs (interlaminar fracture toughness, $G_{Ic,c}$) and the energy release rate of the respective matrix (fracture toughness, $G_{Ic,m}$). The filling of the symbols indicates the type of toughening agent used (neat, rigid, carbon based, compliant and other), the symbol shape provides the respective reference.

enhancing parameters [29]:

$$G_{Ic,c} = G_{Ic,m} + G_f + G_{deb} + G_b \quad (2.2)$$

Beyond the threshold value of $G_{Ic,m}=500 \text{ J/m}^2$, the data do not necessarily follow the initial, strongly increasing trend. The lower boarder threshold slope drops off to a value of about $m=0.31$. Interesting to see is that the data points that show the strongly increasing trend at small energy release rates of the matrix are mostly neat, unmodified epoxy systems. When toughening agents are involved, no matter which type, the data are much more scattered and drop below the $m=1$ -slope. Yet, especially systems that have been modified using compliant types of second phases and have the biggest potential to enhance fracture mechanical properties of epoxies (cf. Sec. 2.3.2) cannot transfer their full toughening performance to the CFRE. Hunston [72] and others [63] explain this trend based on the plastic zone (PZ) size of the matrix, i.e. the capability of the matrix to dissipate energy by elastic-plastic deformation. When a load is applied to a crack a PZ develops in front of the crack tip. At a certain degree of fibre volume fraction in the CFRE, the PZ becomes restricted. With regard to Eq. 2.2, $G_{Ic,c}$ is at least also a function of the fibre volume concentration v_f .

However, if one considers a carbon fibre diameter of $7 \mu\text{m}$ and a fibre volume concentration of $v_f=55 \text{ vol.}\%$, the interfibre distance x_{fs} [73] (Eq. 2.3), i.e. the matrix region available to plastically deform, is only as small as $2 \mu\text{m}$, which is below the size of the plastic zone r_p that

even brittle epoxy systems can exhibit ($r_p \approx 10 \mu\text{m}$, cf. Eq. 4.24 and [25]).

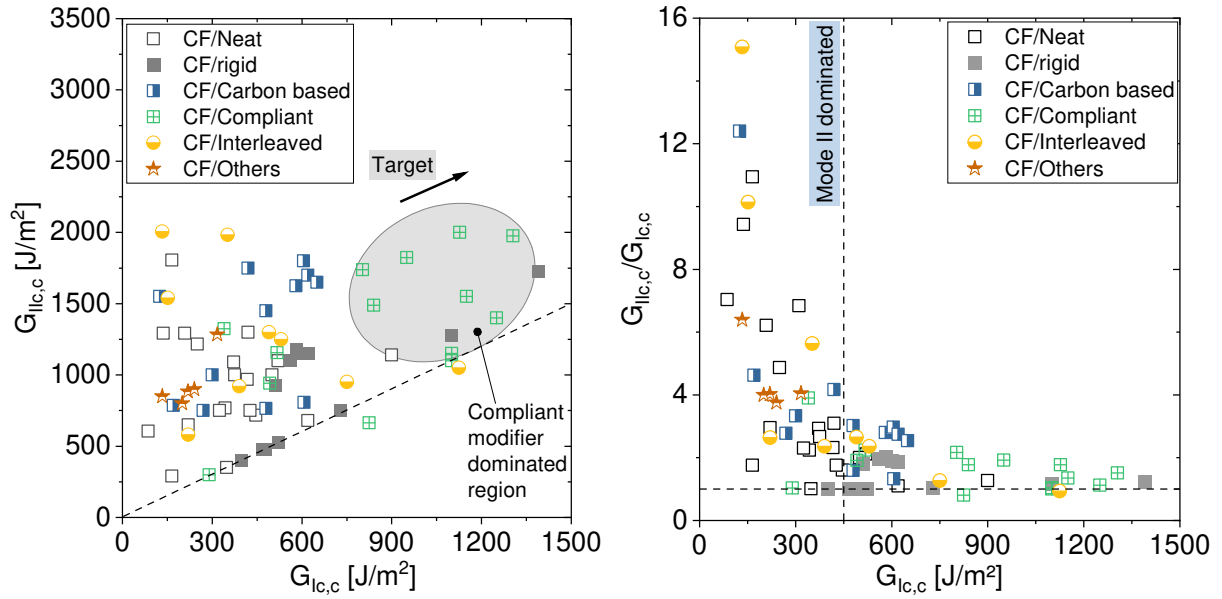
$$x_{fs} = 2r \left(\sqrt{\frac{\pi}{2v_f\sqrt{3}}} - 1 \right) \quad (2.3)$$

In conclusion further factors, such as interphase interactions between matrix and fibres, need to be considered in extension to Eq. 2.2. If a weak interphase prevails in a CFRE, fracture toughness enhancing mechanisms, such as fracture toughness of the matrix, fibre bridging or fibre matrix debonding cannot be utilized at all.

With regard to matrices that have been toughened by rubbery and thermoplastic modifiers, van Velthem et al. [74] investigated the Mode I interlaminar toughness and the interlaminar shear strength of four different toughening agents, amongst others a polymethylmetacrylate-b-polybutylacrylate-b-polymethylmetacrylate BCP at a modifier concentration of 10 wt.-%. The BCPs phase separated into macro domains in a Diaminodiphenylsulfone cured Tetraglycidydiaminodiphenylmethane based epoxy resin and slightly increased the Mode I fracture toughness. However, the interlaminar shear strength dropped by about 30 %, due to reduced interface interactions. The results were reflected in the damage area obtained by ultrasound C-scans after impacting: the damage area of the BCP modified system had doubled. Indicating that the important interlaminar shear properties have a severe effect on the damage resistance of such toughened samples. Kamar et al. [75], on the other hand, found that polystyrene-b-polybutadiene-b-polymethylmetacrylate BCPs formed nanostructures within a DGEBA based epoxy resin that had been cured by a phenylenediamine. Thereby no effect on the thermal glass transition occurred and the Mode I fracture toughness had increased by a four-fold. Similar results were obtained by [76], yet even though the BCPs had nano phase separated; again, the shear strength dropped slightly. These examples indicate the influence of different parameters (i) on the phase separation process of block copolymers and (ii) the resulting fracture mechanical properties of fibre reinforced composites thereof. Based on literature results, BCPs seem to be able to strongly enhance Mode I fracture toughness, yet are rather detrimental to the interlaminar shear properties. Investigations on core-shell rubber toughened CFREs have shown similar trends with regard to Mode I interlaminar fracture toughness, i.e. the addition of 10 wt.-% of nanosized core-shell rubber particles enhanced the Mode I interlaminar fracture toughness of the CFRE by about 200% [77]. The interlaminar fracture toughness in shear mode (Mode II) [61] increased as well, but much less than the Mode I fracture toughness.

To gain an idea of the relationship between Mode II and Mode I interlaminar fracture toughness, Figure 2.6a shows Mode II data as a function of Mode I for a variety of untoughened, i.e. neat epoxy systems as well as differently modified epoxy matrices.

The data are quite scattered and no correlation can be established between both modes [93]. However, Mode II fracture toughness is always equal or higher than the Mode I value of the



(a) Mode II interlaminar fracture toughness as a function of the respective Mode I data
 (b) Ratio between Mode II and Mode I interlaminar fracture toughness as a function of the respective Mode I data

Figure 2.6: Relationship between Mode I and Mode II interlaminar fracture toughness of differently toughened CFREs. The data were collected from [61, 62, 65, 67, 68, 78–92], reference to each data point is given in Table A.9.

respective composite. This can be explained by the additionally occurring friction between the fractured surfaces, under the assumption that the same toughening mechanisms have been activated, even though different stress states prevail in the composite. Figure 2.6b) illustrates that especially CFREs that show a low Mode I interlaminar fracture toughness can, relatively speaking, bare very high interlaminar shear stresses (Mode II), relative to the Mode I value. The higher the Mode I interlaminar fracture toughness gets, the more the Mode II/Mode I value levels asymptotically towards 1, i.e. the tougher the system, the more $G_{IIc,c}$ becomes the same as $G_{Ic,c}$.

Amaral et al. and Danesjoo et al. [87, 94] focussed their research on specifically this problem and tried to tackle the issue from a physics point of view, yet within the boundary conditions of a linear elastic (brittle) and isotropic material. They hypothesized that once the stored energy in an externally loaded structure, independent of the energy source, i.e. shear stresses, normal stresses or combinations thereof, reach a critical value, fracture occurs. Based on this assumption they showed that during pure Mode II loading failure initiation actually occurs at the same strain energy as Mode I failure. Hence, it can be deduced that the actual onset of delamination during impacts occurs at far lower energy release rates (in the range of Mode I) than usually expected (Mode II) [41].

2.2 Thermosets and epoxies

Thermosets (old greek: *thermós* = warm, hot, middle english: *sett* = fixed, rigid) are a special class of polymers that are characterized by their irreversibly, highly cross-linked, three dimensional, carbon-based network structure [95]. Within the vast field of thermosets such as e.g. unsaturated polyesters, vinylesters, polyurethanes or polybenzoxazines, the class of epoxy resins is one of the most common ones [96]. In the cross-linked state, epoxies are of special interest as matrix materials in high-performance carbon fibre reinforced composites, due to their high thermal stability, high strength and stiffness as well as the variety of processing advantages.

Epoxy resins, i.e. epoxy oligomers can be characterized by the presence of at least two *Oxirane ring structures* or *epoxide groups* (-COC), cf. Fig. 2.7; one at each end of the molecule. These groups are highly reactive and are the "to be activated reaction sites" of an epoxy resin, in order to allow cross-linking with the curing agent. The reactivity of epoxide groups depends strongly on the location within the molecule. Terminal epoxide groups are e.g. more reactive than groups that are situated within the molecular structure [97]. Furthermore, the overall reactivity can be influenced by the presence of other reactive groups, such as hydroxyls [98–100]. Typical molecular weights of such epoxy oligomers are in the range of 90-600 g/mol. However, special thermosetting resins, so called *Phenoxies* can have molecular weights of up to several 10000 g/mol [98]. To transfer epoxy oligomers to a

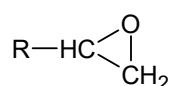


Figure 2.7: Epoxide group

cross-linked material a reaction between the oligomers and a curing agent needs to take place, usually under controlled thermal conditions. To form an ideal molecular network between both species, the constituents are *stoichiometrically* mixed; meaning every reactive group of the resin can theoretically covalently bond to a reactive site of the curing agent. However, this is in practice not necessarily the case, since a proceeding network formation causes the viscosity of the reactive system to increase and hinders active species to react with each other, i.e. inhibits the cross-linking reaction. The stoichiometric ratio is thereby based on the *epoxy equivalent weight* (EEW) - the weight of the resin containing one epoxide group (e.g. a difunctional epoxy molecule has an EEW of half of its molecular weight). Depending on the curing agent, potential catalysts and the performance requirements of the application the mixing ratio is adjusted, also to control curing kinetics (e.g. time and degree of exothermy). The subsequent curing process is then following a temperature profile to, again, control the cross-linking reaction with regard to the curing kinetics and the goal to enable the formation of a macroscopically homogenous and molecularly flawless network between epoxy and curing agent moieties. Note, most thermosets are also able to cure at room temperature in the

presence of a curing agent, prevailing enough time is given. Other pathways make use of a controlled homopolymerization process that allows cross-linking of the epoxy monomers with themselves, yet requires either a catalyst or high temperatures to initiate a reaction [101].

The final properties of a glassy epoxy depend on the conformation of the monomers, i.e. distance between epoxide groups in a molecule, presence of aromaticities, aliphatic structures or ether-links as well as the functionality of the liquid epoxy resins and the hardener. On the other hand, the properties are defined by the final molecular network structure during curing, such as the molecular weight of chains between cross-links M_c or the number of cross-links in a certain volume, i.e. the cross-link density [98, 101].

The cross-link density n_c is thereby a function of the functionality of the molecules, the number of possible reactions per epoxide group, the distance between those groups, the molecular weight of the molecule as well as the side-groups of the molecule. Increasing the cross-link density of the glassy epoxy will result in a solvent resistance and higher thermal stability of the cured material, since the free volume between chains is reduced and motions are restricted [102]. Aromaticities hinder segmental motions and restrict flexibility of molecules [98]. Ether links (R-O-R) provide more flexibility to chain movements and reduce the glass transition temperature [102].

Diglycidyl ether of bisphenol A and cycloaliphatic epoxy resins: pre-cured and cured state

Diglycidyl ether of bisphenol A (DGEBA) and cycloaliphatic epoxies (CAE) are the two representatives of epoxy resins that are of special interest within this dissertation. The DGEBA based resin is the resin the BCPs will be introduced into, the CAE based resin is the carrier resin of the CSR nanoparticles and the BCP/CSR hybrid system. Details with regard to the manufacturing process of the different systems are provided in Sec. 4.1.

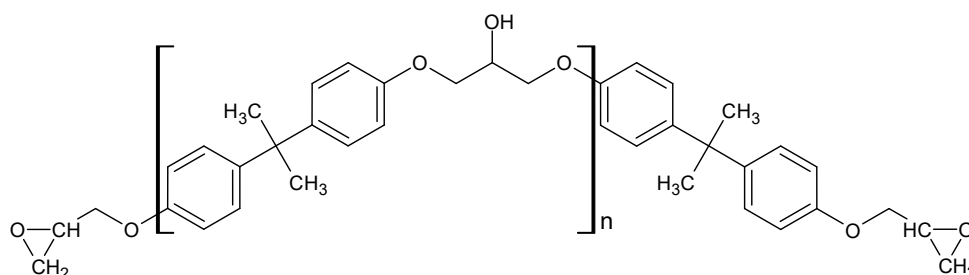
Both resin systems offer in the reactive yet liquid state advantageous processing properties, low viscosities and, depending on the selection of the curing parameters, very long pot lives. In the cured state, they show a high mechanical strength, due to strong covalent bonds between molecules, as well as a high thermal stability [103]. However, both materials are different in their molecular structure and form networks with different cross-link densities that affect (fracture) mechanical properties. Table 2.3 summarizes some of the basic resin properties, Fig. 2.8 shows the molecular structures of interest.

The differences between DGEBA and CAE on a molecular level are the aromatic vs. cycloaliphatic backbone structure, as well as the presence of alkyl end groups (e.g. $-\text{CH}_3$) in DGEBA based resins, cf. Fig. 2.8. This increases the flexibility of the DGEBA molecule [102]. However, the monomer molecular weight of CAE is about 29 % lower compared to DGEBA, yet both molecules have an epoxy functionality of 2 (Note: at elevated temperatures other

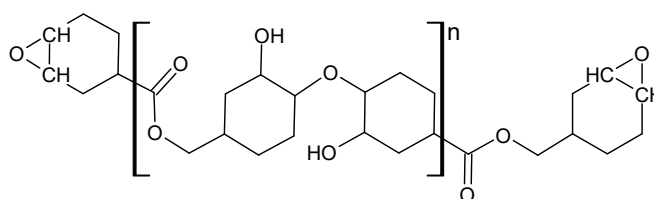
Table 2.3: Overview of uncured resin properties at 25°C

Constituent	DGEBA	CAE
Molecular weight* [g/mol]	~380 [101]	~272 (based on EEW)
EEW [g/eq]	174-200 [104]	133-140 [98]
density [g/cm ³]	~1.16 (data sheet)	~1.17 (data sheet)
functionality	2 [101]	2 [104]
T_g [°C]	~-29 (stat.) [105]	~-37 (data sheet)
Viscosity [mPa·s]	~12000 [101]	~350 [98]
Refractive index	1.571	1.498

*molecular weight of the monomer unit



(a) Diglycidyl ether of Bisphenol A (DGEBA)



(b) Cycloaliphatic epoxy (CAE) - 3,4-Epoxy cyclohexylmethyl 3,4-epoxycyclohexanecarboxylate

Figure 2.8: Molecular structures of two basic epoxy resins, n is the number of repeat units, usually $n=0$ (monomer) in technical epoxy resins, the higher the "purity" of the resin the smaller the distribution of molecular weights within the epoxy, i.e. the less oligomer structures ($n>0$) are present.

functional groups of the epoxy resin might be activated).

In the cured state CAE resins are much more brittle than DGEBA based epoxies. This is because of the direct link of the epoxide groups to the backbone of the main molecule. Hence, CAE resins inherently possess a more dense and rigid molecular structure [104]. Furthermore, the distance between the epoxide groups is shorter [98], yielding to higher cross-link densities than DGEBA based epoxies. CAE resins react quite slowly in the presence of a curing agent at room temperature, i.e. the pot life is very long and makes them ideally suited e.g. for filament winding. Furthermore, they are perfectly transparent and show a high resistance against UV radiation. This enables them e.g. for applications in liquid crystal displays (LCD) [106].

DGEBA resins on the other hand are mass products and offer compared to CAE a good balance between costs and performance. They are able to react with a variety of curing agents even at room temperature, and are e.g. widely used as adhesives. However, the aromatic ring structure in DGEBA (Fig. 2.8a) causes very high viscosities, especially compared to cycloaliphatic resins [98]. Therefore both resins are often blended with each other to adjust viscosities for processing and still satisfy cost requirements [107]. Such epoxy blends were characterized in more detail by Kwak et al. [108]. Tab. 2.4 summarizes some of the basic mechanical properties of anhydride cured DGEBA and CAE systems. However, especially with regard to the fracture toughness, it should be noted that those values are just indicative. Depending on the curing-agent the values can vary in a wide range [109].

Table 2.4: Overview of cured resin properties (tensile) at 25°C using an anhydride curing agent

Property	EP/DGEBA	EP/CAE
E [MPa]	2950-3200 [13, 110]	3050-3100 [13, 111]
σ [MPa]	80-90 [13]	48-65 [13]
ε [%]	5-7 [13]	1.8-2.5 [13]
K_{Ic} [MPa \sqrt{m}]	0.55-0.65	0.46-0.5 (data sheet)
T_g [°C]	145-153 [13, 110]	188-193 [13]

Anhydride cured epoxies, as used within this study, possess a high thermal resistance, are transparent due to the amorph molecular arrangement, and show exceptional electrical insulation properties [98]. Compared to epoxy resins cured by amines, anhydride cured epoxies show superior glass transition temperatures and a lower exothermic reactions, which specifically enable them for the production of large scale applications [99, 106]. The cured molecular structure is usually formed by a *catalyzed* curing reaction between the epoxy resin and an anhydride curing agent. However, these processes are complex and not fully understood yet [97, 99, 100, 106, 112–114]. A short description of an widely accepted cross-linking reaction is given in App. A.1.

2.3 Toughening of epoxy matrices

Toughening of epoxy matrices and composites thereof is a decades-long, still ongoing topic within the field of materials science. Yet also emphasizes the unsolved issues regarding fracture mechanical properties of epoxy based materials as well as the importance to further explore possibilities to improve the fracture toughness of those types of materials; not only from a scientific point of view but also from an application point of view.

2.3.1 Intrinsic vs. extrinsic toughness

Increasing the toughness of a brittle epoxy matrix can be achieved in essentially two ways: (i) either by enabling the material to withstand higher stresses at the crack tip i.e. increasing the plastic zone size r_p by modifying the epoxy matrix molecularly and/or on a morphological level or (ii) by reducing the stresses that act at the crack tip and hinder them to reach a critical value, e.g. by restricting the opening of the crack faces. The first approach is denominated as *intrinsic toughening*, the latter one as *extrinsic toughening* [20].

The *intrinsic toughness* of an epoxy matrix is defined by its molecular network conformation, e.g. the cross-link density, the backbone structure of resin, hardener and accelerator as well as dangling side-chains [20]. All of them restrict energy dissipation in the plastic zone (PZ) behind the crack tip.

Accordingly, selecting appropriate epoxy resin systems that e.g. do not contain aromaticities in the backbone structure to provide the matrix with more flexibility, or using non-stoichiometric resin-hardener ratios to reduce the cross-link density are pathways to adjust the intrinsic fracture toughness of epoxy matrices [115, 116] (cf. Tab. 2.4 for a comparison of the mechanical properties of different epoxy matrices).

Extrinsic toughening, on the other hand, is rather active in the wake of the crack, i.e. in front of the crack tip and *shields* the crack tip from eventually excessively applied loads and reduces the stress intensity e.g. by deviating the crack front from its original path. Fig. 2.15 gives an idea of the intrinsic and extrinsic working principles and summarizes the toughening mechanisms that will be discussed in more detail below.

2.3.2 Toughness of epoxy matrices induced by second phases

To *toughen* an epoxy system, i.e. to increase the level of energy required for fracture, without detrimentally changing other properties, the epoxy matrix can be modified with *second phase fillers* [117–119]. These nano to micro size ranged materials are incorporated into the liquid epoxy resin and prevail in the matrix after the curing process. Thereby, such second phases can either have pre-defined shapes, e.g. as spherical particles, or form particulate phases from an initially macromolecularly mixed state with the epoxy resin, i.e. thermodynamically driven phase-separation. Such toughening agents can *intrinsically and extrinsically* improve

fracture mechanical properties, yet are most efficient behind the crack tip. Throughout this thesis, the different terms (i) toughening agent, (ii) modifier and (iii) second phase (fillers) are interchangeable. Thereby, a *toughening agent* is a goal-oriented description of such a constituent, e.g. to increase an epoxy matrix' toughness, a *modifier* alters the epoxy matrix morphologically, yet not necessarily its cross-linked network structure, and a *second phase (filler)* prevails aside the first phase (the matrix), but has no pre-defined geometrical shape, e.g. spherical.

Second phases can e.g. be grouped as follows:

1. Inorganic and rigid modifiers (IRP), i.e. toughening agents that are stiffer than the surrounding matrix, such as e.g. Al_2O_3 or TiO_2 [120], SiO_2 [121, 122] or WS_2 [123],
2. Compliant or rubbery modifiers (CM), i.e. toughening agents more elastic than the surrounding matrix (depending on the relaxation temperature of the second phase with regard to the application temperature) such as e.g. liquid rubbers (e.g. Carboxyl-terminated butadiene (CTBN) [23]) or thermoplastics (e.g. Polyethersulfone (PES) [124] or Polymethylmetacrylate (PMMA) [125]), as well as core-shell rubber particles [24, 25, 126]. Other studies focus e.g. on cross-linked rubber particles [127].
3. Phase-separating modifiers (PS), such as e.g. inter-penetrating networks (IPN) [128], partially reacted substructures (PRS) [129, 130] or block-copolymers [25, 74, 131–134]
4. Carbon based and rigid modifiers (CBR), such as e.g. carbon nanotubes (CNT) [70, 135] or graphene [136]. Note: CBR are a special group of toughening agents and will only be addressed where necessary. CBRs offer a different pathway to fracture toughness than CMs or IRPs. Also, due to their carbon crystal structure, they offer access to further properties of epoxy based composites, such as the electrical conductivity or to permeability properties (e.g. hydrogen-proof).

Inorganic and rigid particles (IRP) are mainly applied as nanoparticles to improve fracture mechanical properties and make use of mechanisms originating e.g. from the debonding of such phases from the surrounding matrix (see the *plastic void growth mechanism* in Sec. 2.3.3). Also, these kind of modifiers increase the stiffness of a matrix system, if a bonding between the phases is properly established. Yet, this is a pre-requirement for all type of modifier applications to make use of their energy dissipating capabilities. Otherwise, the particles create voids that can still promote a certain kind of energy dissipation, yet not to the full potential of the initially thought modification.

Another type of modifier, i.e. rubbery modifiers (CM), more specifically liquid rubbers were one of the first modifiers used for toughening of epoxy [137] by making use of a phase-separating process during the curing process within the epoxy matrix into micron sized domains. However, the disadvantage of liquid rubbers is that they tend to phase separate incompletely, i.e. some of the rubber molecules remain as single moieties in the epoxy network. This detrimentally affects the cross-linking reaction and accordingly reduces

important mechanical properties, such as e.g. strength and especially the thermal glass transition temperature [138].

Figure 2.9 summarizes the effect of different modifiers on the thermal glass transition temperature, such as liquid rubbers, BCPs, as well as initially *phase-separated* modifiers, such as CSR particles and IRPs. Liquid rubbers rather decrease the thermal glass transition

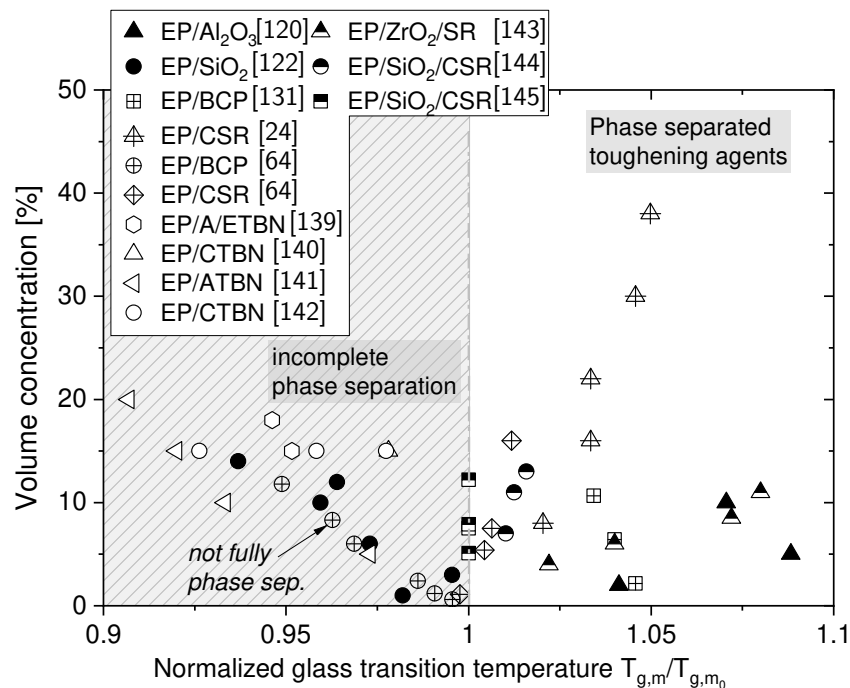


Figure 2.9: Effect of phase-separating modifiers, i.e. liquid rubbers (A/C/ETBN: Amine-, Carboxyl- and Epoxy terminated butadiene acrylonitrile, respectively) and BCPs, and initially phase-separated modifiers, i.e. CSR particles, silicone rubber (SR) and IRPs and their influence on the thermal glass transition temperature $T_{g,m}$. $T_{g,m0}$ denominates the respective untoughened matrix

temperature, as discussed above, whereas CSR particles, IRPs and BCPs, if fully phase-separated tend to not affect or even increase T_g , cf. the data from Quan et al. [24]. This latter effect might be related to a hindered chain mobility due to the modifiers, or, if the shell structures allow a chemical bonding to the epoxy resin, the modifiers might work as additional cross-linking nodes. The data set from Zhang et al. [122] used a colloidal epoxy masterbatch of silica nanoparticles. If the epoxy resin encapsulates the particles, and the curing agent does not interact with a portion of the epoxy resin, since the resin is physically bonded to the nanoparticles, the degree of cure is accordingly reduced (excess of unreacted hardener) and the thermal glass transition temperature decreases compared to the respective neat system.

Within the field of *epoxy matrix toughening agents*, core-shell rubber particles and block copolymers represent a further development of liquid rubbers, and can also be grouped as a compliant type of epoxy matrix modification (additionally to PS). Block copolymers and

core-shell rubber particles are discussed in more detail below (Sec. 2.3.2.1 and 2.3.2.2).

To get a general idea of the energy dissipating capabilities of rubber type modifiers and inorganic and rigid particles, their effect on the fracture toughness and Young's modulus of bulk epoxy matrices is summarized in Fig. 2.10. The data set is based on available literature given in the Figure. As shown, IRPs do not only enhance the energy to fracture but also

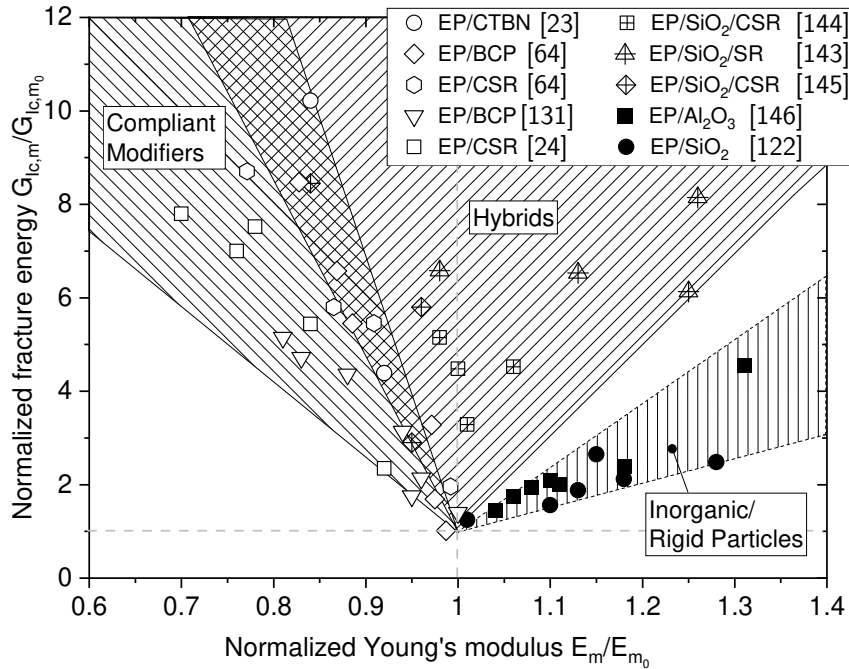


Figure 2.10: Influence of compliant (rubber-based and thermoplastic), inorganic and rigid, as well as hybridized (compliant and rigid) toughening agents on the energy release rate $G_{Ic,m}$ and Young's modulus E_m of an epoxy matrix. The data sets are normalized to the neat, i.e. unmodified epoxy matrix, $G_{Ic,m0}$ and E_{m0} , respectively.

Young's modulus. Compliant modifiers, on the other hand, are twice as efficient in improving fracture mechanical properties than IRPs; a ten-fold enhancement can be achieved, compared to the neat epoxy matrix. The reason is the activation of additional energy dissipating mechanisms, being discussed in depth in Sec. 2.3.3. Disadvantageously, Young's modulus of compliantly toughened epoxy matrices drops.

The elastic modulus of a homogenous, isotropic solid is proportional to the bonding energies of its atoms or molecules. If bonds are missing (vacancies) or the volume is comprised of different bonds, the elastic modulus will be a sum of the individual bonds per volume. In the case of a rubber toughened epoxy matrix, assuming ideal bonding between a toughening phase and its matrix, E will be comprised of both phases with regard to the respective volume they occupy, following a rule of mixtures. I.e. $E_{rubber} \sim 100 \text{ MPa} \leq E_{EP} \sim 3000 \text{ MPa}$, E_{total} will be in between the two values, depending on the composition.

Besides simply modifying epoxy resin systems with one of the above mentioned toughening

agents, some researchers focus on hybridization concepts to benefit from synergies between the constituents, hence, to e.g. balance a loss of stiffness introduced by compliant types of modifiers by an additional modification of rigid fillers [10, 118, 147], cf. Fig. 2.10. Other examples with regard to an additional enhancement of fracture toughness are the combination of e.g. silicon oxide and core shell rubber particles [144, 148], CTBN-rubber and CNTs [149], BCP and Al_2O_3 [150] or silicone rubber and ZrO_2 [143]. However, synergies do not always appear as demonstrated in the case of BCP-CNT hybrids [151, 152].

Applications that are based on bulk epoxy materials without fibre reinforcement might indeed suffer from a loss of stiffness (depending on the application). Nevertheless, CFRE based applications do not necessarily require a stiff matrix, since strength and stiffness originate from the fibre reinforcement. In fact, a reduced stiffness can be beneficial for CFRE based applications if the yield stress is not affected, since the material is more elastic, i.e. tougher.

2.3.2.1 Core-Shell Rubber Nanoparticles

The first evolutionary step in the development of CMs after liquid rubbers, was the synthesis of core-shell rubber particles (CSR). Core-shell rubber particles are preformed spheres, comprised of a rubbery core (usually polybutadiene [153, 154] or polybutylacrylate [22]) and a resin compatible shell material, i.e. incomplete phase separation is omitted, due to the pre-formed structure, cf. Fig. 2.11. Core-shell particles are manufactured using an emulsion polymerisation process that is comprised of a polymer dispersion (e.g. rubber latex) in water and a subsequent polymerization process of a *thin*, glassy shell around the particles [155]. The particles are subsequently dried and can be applied as toughening agents in epoxy resins. Specifically the tailored shell material has the advantage to provide a high compatibility to

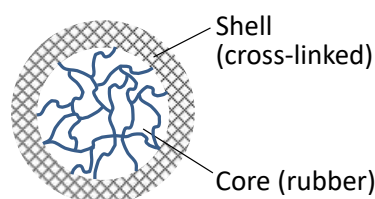


Figure 2.11: Schematic of a core-shell particle, having a rubbery core and a cross-linked shell structure

the selected resin system [156], either via physical interactions or chemical cross-linking, even being able to influence the curing reaction, if the reactivity of the other constituents is not respected. Thereby, the particle size and the core-shell composition can be precisely controlled to e.g. adjust the cavitation resistance of the particles and the compatibility to the resin system [22]. CSR particles can be synthesised within a broad range of dimensions down to the nano scale. Yet, depending on the size of the particles, the relative amount (thickness) of the shell layer increases, since the surface to volume ratio strongly increases [157]. Changing the relative shell layer thickness might again influence the cavitation

resistance of the particles and detrimentally affect fracture mechanical properties. However, reducing the particle size into the nano size ($\varnothing \leq 100$ nm) the surface-to-volume ratio of the particles strongly increases. This enables enhanced interfacial interactions of particles with the surrounding matrix. Also, decreasing the surface-to-surface distance between particles, at constant volumetric concentrations is highly beneficial for improving the fracture toughness of brittle glasses using CSR nanoparticles (cf. Sec. 2.3.4 and the influence of geometrical aspects of toughening agents on the mechanical properties of epoxy matrices). However, core-shell rubber particles tend to agglomerate in their initial nano-powdery form and require extensive dispersion efforts to be distributed as individual nanoparticles homogeneously in the resin. Agglomerates are rather detrimental to fracture toughness [158, 159]. To avoid such agglomeration, the newest generation of CSR toughening agents is transferred from a liquid solvent after the emulsion polymerisation process into an epoxy resin. This allows a very even particle dispersion throughout the carrier resin and later in the matrix system. Such systems are nowadays commercially available as *masterbatches* (modified resin systems that are meant to be diluted to a target concentration). Such a system is also part of the current study. The details are presented in Sec. 4.1. Applying this procedure, extensive dispersion processes can be avoided [160, 161] and the benefits of nanoparticulate core-shell structures can be utilized to toughen epoxy matrices.

However, CSR particles are highly efficient toughening agents. Quan et al. [24] investigated the influence of a 200 nm sized CSR on a dicyandiamide cured DGEBA based epoxy matrix. They found that the energy release rate required for crack propagation increased from about 343 J/m^2 (which is a relatively high fracture toughness for an epoxy system) to 2671 J/m^2 . The strongly increased fracture toughness was ascribed to extensive plastic void growth and shear band yielding (again cf. Sec. 2.3.3). However, the enhancement was achieved at the expense of Young's modulus, which strongly dropped from 3.29 GPa to 2.31 GPa. The thermal glass transition temperature was found to have even slightly increased, ascribed to surface functionalities in the shell structures that might have interacted with the resin and/or hardener.

Following the hybridization approach, Quan et al. [144] also examined synergistic toughening effects of CSR particles (200 nm) and nano-sized silicon oxide (20 nm) on a lightly crosslinked epoxy resin using a secondary amine curing agent (Piperidine). Hybridization with 4 vol.-% of silica and 7 vol.-% CSR increased G_{Ic} by more than 400 % while only marginally affecting the Young's modulus. The incline was ascribed to mechanisms such as cavitation, plastic void growth and shear yielding between the rubbery CSR particles and the silica particles which occupied space between CSR particles. Accordingly, the interparticle distance played a significant role in toughening. Similar findings were reported by Carolan et al. [148] on the toughness of an anhydride cured DGEBA based epoxy matrix, which has usually a higher cross-link density than the above employed resin system. The toughness improvement achieved was about

7-times the fracture toughness of the neat epoxy matrix. However, the absolute toughness was only half the values reported in Quan et al.'s study, yet also a lower particle concentration was employed (20 wt.-%). Interestingly, the toughenability of the epoxy matrix strongly increased once a reactive diluant was introduced into the system (hexanediol diglycidylether). The capability of the matrix system to undergo shear yielding and plastic void growth, was improved by the presence of the diluant, i.e. a lower cross-link density prevailed. Thus, combining rigid and soft fillers in an epoxy system appears to be an interesting route for toughening of epoxy matrices without reducing the stiffness of the material. CSR particles, on the other hand, are quite efficient for toughening purposes but detrimental to the modulus. IRPs increase the stiffness of the systems but have much less effect on the energy release rate.

2.3.2.2 Block Copolymers

The most advanced type of compliant toughening agents for brittle epoxy systems are block copolymers (BCP) [26]. They represent a new class of synthetic materials that enable unexpected pathways within the field of polymer science and application, such as tailoring and designing (fracture resistant) morphologies and respective bulk material properties [162].

BCPs are macromolecules comprised of at least two chemically different, covalently bonded monomer units [163]. The units of monomers are denominated as blocks and can be either randomly (copolymers) or block-wise arranged (block copolymers). Usually, one of the blocks is epoxy miscible, i.e. compatible to the epoxy resin, the other block is epoxy immiscible. The combination of both shall allow the thermodynamically driven formation of nanophase structured core (epoxy immiscible)-shell (epoxy miscible) morphologies to provide the epoxy matrix with a high fracture toughness.

The possibility to create block copolymers was established in the mid 1950s', when Szwarc et al. [164, 165] discovered the *living polymerization*. This method allows the growth of polymer chains without termination of the reactive chain side or chain transfer, i.e. the polymerization process does not stop as long as monomer units are available for chain growth. Once all monomer units are consumed, the end chains of the formed macromolecules stay active for continuing the polymerization process until more, unreacted monomers are added. If a different set of monomers is added, copolymers form [165]. The reactivity of the chain ends needs to be actively terminated by respective chemical species. The advantage of the method over other, e.g. non-living polymerization processes, is the stable and uniform polymer chain growth, enabling small molecular weight distributions with distinct block structures.

Common conformations are e.g. diblock (AB), triblock (ABA, ABC), multiblock, alternating or even tapered copolymers [163]. Figure 2.14 summarizes some of the possible linear

conformations of BCPs.

However, the structure does not necessarily need to be linear. Other designs are possible such as cyclic or branched conformations. Furthermore, the BCP architecture can be controlled, i.e. the combination of different types of blocks (e.g. A, B, C and D), block length (m_w of the different blocks), block sequence (e.g. ABC vs. ACB) etc.

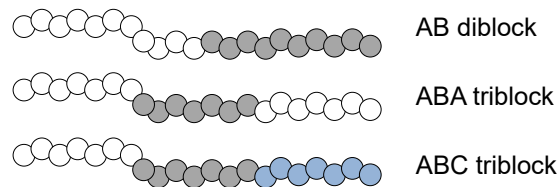


Figure 2.12: Schematic representation of a selection of different block copolymer conformations that are used as toughening agents of epoxy matrices and CFREs, the size and the structure are arbitrarily.

The benefit of BCPs over other toughening agents, as well as the huge challenge from a materials science point of view, is the self organization. Thermodynamically driven, the BCPs self-assemble in the epoxy resin, ideally into core-shell structured nano-phases, having a rubbery core and a self-driven even dispersion, without the need for any kind of additional dispersion processes. Thereby, the assembling process often yields so-called (*spherical*) *micelles*, which represent a kind of core-shell structure. Such structures were found to specifically form when ABA type-triblock copolymers were applied [166, 167]; similarly architected BCPs as within this work. *Vesicles* can form as well, and are structures that encapsulate epoxy resin during the self-assembling process, i.e. their size does not scale with the initially added BCP concentration within the epoxy resin [168]. Micelles and vesicles form in a broad range of diameters from the nano scale up to the micron size, cf. Fig. 2.13.

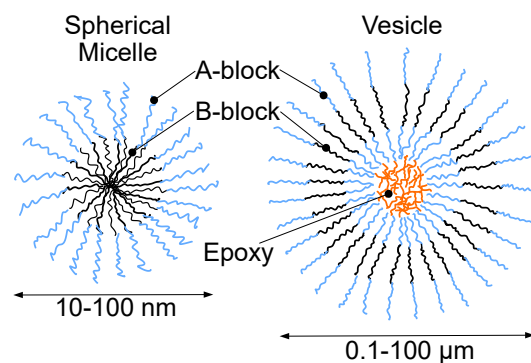


Figure 2.13: Schematic of BCP based spherical micelles and vesicles. A-blocks: epoxy miscible, B-blocks: epoxy immiscible. In the case of vesicular conformations, the BCPs can encapsulate epoxy resin and largely extend their size (depending on the time of assembling and the chemical potentials, the epoxy denominates in that case either the neat epoxy resin or the reactive system with hardener).

Besides those two morphological structures, other, (dis-)continuous morphologies can potentially be assembled [163, 169, 170], such as e.g. large scale macroscopic phase inverted structures; when the dominating phase is not represented by the epoxy matrix anymore, but rather by the block copolymers.

In conclusion, the morphological versatility of BCP toughened epoxies is close to limitless, due to the possibility to tailor the molecular architecture of the BCPs [26, 171]. BCP induced morphologies depend e.g. on:

- block copolymer concentration [168]
- block copolymer size [132, 172], i.e. molecular weight [27]
- block conformation [173], e.g. AB [170, 174], ABA [131], ABC [175]
- block symmetry [170], e.g. to control vesicle structures
- individual block length [170], e.g. short epoxy miscible blocks to obtain vesicles
- block reactivity: improving adhesion to matrix [168]
- resin and hardener [167, 174, 176–179]
- the BCP-resin preparation process [175, 180].

The phase separation process itself is induced by energetic potentials between the assembled BCP structure (e.g. A and B blocks) and the interaction with the epoxy resin system. The self-assembling process can either occur prior to curing [27, 172], during the curing process, due to a reaction induced phase separation mechanism (RIPS) [28, 181, 182], or in combinations thereof [183–185]. Note, it would exceed the scope of the current work to discuss the topic of phase separation from a thermodynamics point of view. However, the interested reader is referred to [162, 186, 187], which discuss the thermodynamic concepts of phase separation phenomena.

With regard to fracture toughness, Dean et al. [168] were one of the first who systematically investigated the toughening effect of diblock copolymers on a Bisphenol A based epoxy resin cured by a tetrafunctional aromatic amine. They obtained nano-sized spherical BCP micelles and vesicles as dominating second phases. These drastically increased the fracture toughness already at low BCP concentrations.

Fig. 2.14 summarizes the effects of vesicles and micelles on the fracture toughness of an epoxy matrix, induced by diblock copolymers [168]. It becomes obvious that very small concentrations of block copolymers can enhance the fracture toughness drastically, e.g. blending 3 wt.-% of this diblock copolymer resulted in a 3-4-fold increase of $G_{Ic,m}$. Its important to emphasize that fracture toughness does not scale with the BCP concentration in the epoxy matrix, due to the variable formation of phase separated morphologies. I.e. this example nicely illustrates the relation between the morphology and the fracture mechanical performance of an epoxy matrix.

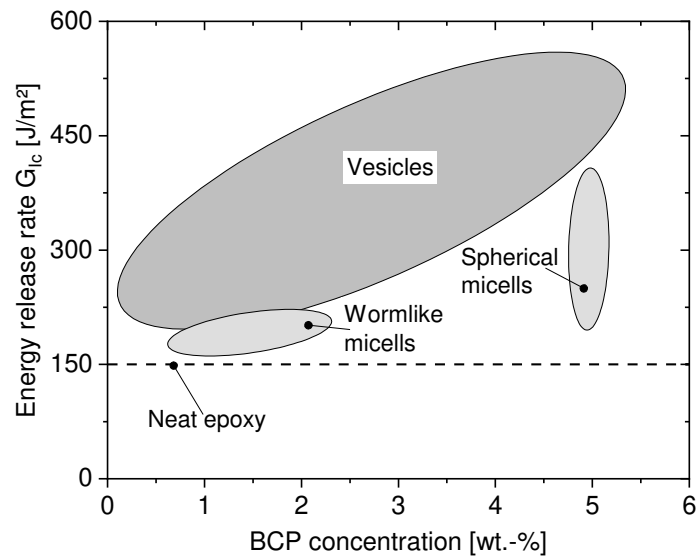


Figure 2.14: Influence of micellar and vesicular BCP structures, based on different diblock copolymers, on the energy release rate $G_{Ic,m}$ of the epoxy matrix, adapted from [168]. The formation of vesicular structures can occur over a broad range of concentrations and lead to different degrees of fracture toughness improvement.

In the same paper, Dean et al. also showed that the strain energy release rate of these composites was strongly related to the distance between nanoparticles (matrix ligament). Similar results were found by Wetzel [120] for epoxy/alumina nanocomposites and by Zhang et al. [122] for nano-sized silica. On the contrary, totally different structures of triblock copolymer (ABA) toughened epoxy (Bisphenol A based and cured by Phenol Novolac) in the nano-range were obtained by Kishi et al. [188], who examined the morphology and respective fracture mechanical properties. Spherical micelles, cylindrical micelles and curved lamellae were generated, and the highest fracture toughness was obtained by cylindrical structures.

Other studies introduced BCPs into anhydride cured, epoxy based CFRPs [74, 189]. The CFRPs were toughened by a poly(styrene)-block-poly(butadiene)-block-poly(methylmethacrylate) (SBM) copolymer, which phase separated and homogeneously dispersed throughout the composite. The energy release rate of the composite was increased by about 42% at low filler concentrations (2.5 wt.-%). In this case, the type of fibre-matrix failure changed from an adhesion dominated (debonding) to a cohesion dominated failure mechanism.

Preliminary studies on the matrix level by Bajpai et al. [174] found that the hybridization of diblock copolymers and core-shell rubber particles did not affect Young's modulus, yet drastically increased the fracture toughness of a high strength epoxy system (mixture of a di- and tri-functional epoxy and cured by an anhydride system). Shear yielding and plastic void growth were ascribed as the main toughening mechanisms. The CSR nano particles were evenly distributed within sub-micron sized block copolymer-rich precipitates and did, visually judging, not affect the phase precipitation behaviour of the block copolymers.

2.3.3 Toughening mechanisms of rubbery type modifiers

All of the aforementioned modifiers provide in their own way toughness to a brittle epoxy matrix. However, the micromechanical toughening mechanisms of epoxy matrices basically originate from the bulk moduli, the Poisson ratios and the shear moduli of the epoxy matrix and the modifier. Furthermore, their ratio to each other and the bonding to the surrounding matrix. In the following section the most relevant *rubbery* induced toughening mechanisms of epoxy matrices will be discussed, owing to the fact that BCP and CSR modifiers have a rubbery character and accordingly induce rubber-type mechanisms.

One of the most relevant micro-mechanical, extrinsic toughening mechanisms is **crack deflection** [20]. Energy is dissipated by a tilting process of the crack front, i.e. it deviates the crack front from its original path (changing fracture mode) [190, 191]. Efficient toughening agents in that regard are usually IRPs or second phases that have a higher stiffness than the surrounding matrix. When this mechanism becomes activated the actual fracture surface area increases. This is accompanied by a corresponding increase of the surface roughness [146, 192]. Crack deflection is rather independent of the particle size, yet strongly depends on the aspect ratio of the obstacle and the volumetric loading [190]. This makes e.g. high aspect ratio graphene platelets so interesting for toughening applications of epoxy matrices [136].

Figure 2.15 shows the intrinsic and extrinsic processes taking place at the crack tip, i.e. toughening mechanisms that can be activated during crack propagation.

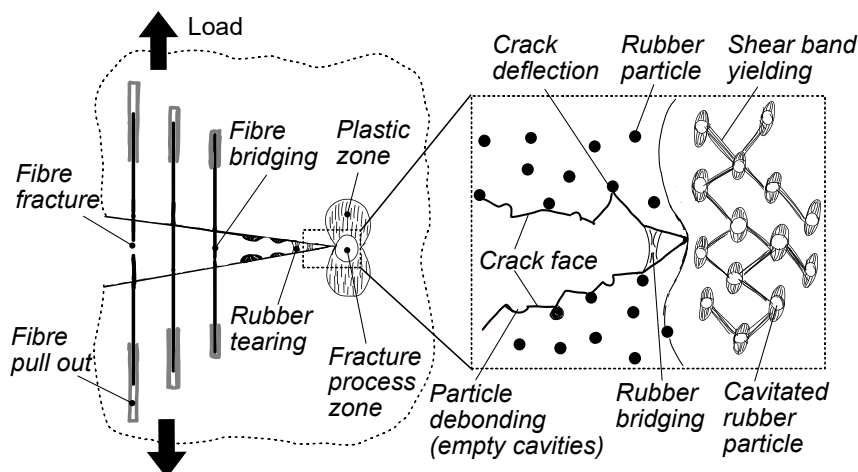


Figure 2.15: Schematic of different fracture mechanisms that act in the wake of the crack tip (extrinsic toughening) as well as behind the crack tip, within the fracture process zone (intrinsic toughening). Inspired by [17, 20].

Note: Some researchers further divide the PZ into a *dissipation zone* and a *fracture process zone* (FPZ) [193–195]. The FPZ is a region in the immediate vicinity of the crack surfaces in which fracture related processes take place, such as non-proportional loadings or large strains [196]. Quan et al. [193] used transmission optical microscopy to relate the fracture process

zone to the region in which most of the second phase-modification induced toughening mechanisms are activated. The *dissipation zone* is rather composed of extended structural processes, indicating that other toughening mechanisms are activated [195] or limited plastic deformation of the epoxy matrix occurs.

Within the plastic zone, three main mechanisms can usually be utilized to improve toughness of epoxy matrices [197, 198]: (i) shear band yielding, (ii) cavitation and plastic void growth and (iii) rubber particle bridging.

Shear (band) yielding is an energy dissipative phenomenon of plastic deformation. It occurs in cross-linked polymers when an axial stress is applied and chain molecules shift along each other. It is one of the main sources of energy absorption within epoxy matrices [16]. Because of the cross-linked state of epoxy matrices the extent of shear yielding is restricted and occurs at nearly 45° to the applied load, where the highest shear stresses occur. Shear band yielding is a very localized process and restricted to the plastic zone, where the yield stress of the epoxy matrix is exceeded. To promote shear yielding in a glassy epoxy and to increase its energy absorption capabilities, the matrix can be modified with particulate toughening agents. When a load is applied to an isotropic and elastic bulk material that contains well bonded dispersed spherical rubber particles, a triaxial stress state forms around each of those spheres (Note, the bulk modulus K of the rubber is in the same range as the bulk modulus of the epoxy matrix, prevailing a hydrostatic stress within the rubber, when a load is applied). First, small stress concentrations at the equator of the rubbery particles initiate weak shear band yielding of the matrix between adjacent particles, secondly the rubbery particles start cavitating. Thereby, the prevailing hydrostatic stress in the rubber particles is relieved, since the macromolecular structure fails. Voids form in the rubber and the particle internally cavitates. Thereby, the hydrostatic stresses at the particles equator are relieved and the stress is redistributed to a plane stress condition, allowing plastic deformation of the matrix ligaments between particles, i.e. severe shear band yielding occurs [16, p.427][22, 198–200], cf. Fig. 2.15.

Accordingly, the more particles are present in the crack tip vicinity (particle size and volumetric particle loading depended) the more shear yielding can be initiated, hence the higher is the energy dissipation.

The process of shear band yielding also applies to rigid particle modifications, yet the stress concentrations occur at the poles of the particles [198] and initiated by debonding of the particles. However, the benefit of rubber particles is their capability to cavitate due to the dilatation process within the plastic zone at the crack tip, i.e. the formation of voids within the rubber particle and cause *post-yield toughening effects* [16], such as rubber bridging. Hence, rubbery toughening agents are usually more efficient in terms of improving fracture toughness of epoxy matrices.

The activation of shear yielding requires sufficiently small particle sizes with regard to the plastic zone size. Large particles, with respect to the plastic zone, can, from a geometrical point of view, simply not cavitate and will rather tend to bridge or deflect a propagating crack [201]. However, this mechanism also depends on the **cavitation resistance** of the rubbery particle [201, 202]. A high cavitation resistance, e.g. caused by a thick shell-layer of a CSR particle, could hinder internal cavitation of the rubbery core, especially if the adhesion to the surrounding matrix is weak, i.e. K_{Ic} is low, since the particles do not cavitate and do not promote shear yielding of the matrix. A low cavitation resistance on the other hand will cause easy cavitation of the particles, yet the stresses that can be borne are low, i.e. K_{Ic} is low. Accordingly, the cavitation resistance of the rubber particle needs to be balanced to bare a maximum of stresses but still being able to cavitate. However, the role of the cavitation resistance is debatable. Bagheri et al. [203] examined the role of rubber particles and hollow plastic spheres, i.e. no cavitation resistance, and did not observe any difference between the applied toughening agents.

The shear yielding phenomenon, preceded by internal cavitation of a rubbery particle is one of the main mechanisms to enhance fracture toughness of brittle epoxy matrices.

Another mechanism that can be triggered by cavitation events, or even debonding of fillers within a matrix is **plastic void growth** [197, 203, 204], i.e. the plastic dilation of the matrix around a cavitated particle. This dilation causes the void to grow, similar as in the shear yielding mechanism. This localized plastic deformation is a second mechanism associated with an improved fracture toughness. Thereby, the stress concentrations that act at the equator of a cavitated particle are the same that act at a void, as shown by Huang et al. [197] based on the van-Mises stress criterion, i.e. also voids can create such a toughening effect and questions the relation to the cavitation resistance of rubbery modifiers that is not conclusively solved. Other mechanisms, such as **rubber particle bridging** or **crack pinning** are rather weak toughening mechanisms and do not particularly contribute to fracture toughness of modified epoxy matrices [201].

2.3.4 Geometrical aspects and other considerations

The activation of the discussed mechanisms is not only depending on the type of toughening agent applied within the epoxy matrix, but also a set of other, e.g. geometrical parameters, such as (i) the particle size [195, 201, 205, 206], (ii) the cross-link density of the epoxy matrix [138, 201], (iii) the volume fraction of a rubbery phase [139, 207], the (iv) particle distribution [159] as well as (v) the inter-particle distance [25, 122, 200, 208].

Considering the **cross-link density** on the toughenability of epoxies by rubber particles, Pearson et al. [138] showed that the fracture toughness of an untoughened epoxy matrix can only

be marginally improved when the cross-link density n_c is reduced. However, n_c has a large effect on fracture toughness if the materials are modified with rubber particles. The higher the mobility of molecular chains, the better is the epoxy matrix' toughenability. As discussed before, to initiate shear band yielding the matrix needs to be able to yield at the crack tip. This process is inherently restricted by the cross-linked network, yet is totally suppressed if the matrix cannot yield. I.e. to toughen an epoxy matrix, it needs to be *ductile* up to a certain degree. Similar results were obtained by Kim et al. [202]. They quite excessively examined the influence of different parameters of the core-shell structure (particle size, volume concentration in the epoxy matrix and core and shell composition) on the fracture toughness performance on two differently cross-linked epoxy matrices. The core-shell composition was based on a Polybutadiene core and a Methamethylacrylate shell. Thereby, toughening of a highly cross-linked epoxy matrix by CSR particles did not yield a significant improvement of fracture toughness. But very high **particle volume concentrations** in an highly cross-linked epoxy matrix can still lead at least to some improvement of fracture toughness. The authors concluded that CSR particle cavitation is still activated as an energy dissipating mechanism, but did not initiate the important shear band yielding mechanism of the epoxy matrix. From a more general point of view, increasing the rubber volume concentration in such systems will lead to an increased fracture toughness, but only up to a certain threshold concentration, according to Michler [198]. When the particle concentration in a toughenable epoxy matrix is increased (with the same particle diameter) the number of cavitation events and respectively the amount of shear band yielding increases [202]. Such volumetric particle changes decrease the **inter-particle distance**, i.e. the surface-to-surface distance between particles, according:

$$r = \left(\sqrt[3]{\frac{\pi}{6v_f}} - 1 \right) \cdot D \quad (2.4)$$

where r is the average distance between particles, v_f the particle volume fraction and D the particle diameter.

Within that regard, Wu [208] observed a transition from a brittle to a ductile behaviour of a rubber toughened Polyamide-6,6, independent of the particle size, when a certain ligament thickness, i.e. the interparticle, distance decreased below a certain value. This was reasoned by the transition from a plane strain to a plane stress state of the matrix ligaments between adjacent particles. However, Bagheri et al. [200] applied a variety of different **particle sizes** to an epoxy resin with varying concentrations and did not observe such a size-independent transition from a brittle to ductile state. The transition rather occurred at larger interparticle distances, when the particle size increased. They explained this behaviour with the number of cavitation events and the subsequent shear yielding, i.e. when the number of cavitation events increased, due to an increasing number of CSR particles (yet not the concentration), shear band yielding increased as well [202].

Michler [198, p.310] performed stress analyses on the stress concentrations between particles with regard to the effect of the influence of the inter-particle distance r . He was able to

show the existence of a threshold value r_{\max} , below which the material behaviour changes from more brittle to rather ductile. However, at a certain interparticle-distance r_{\min} , when a maximum fracture toughness value had been reached, K_{Ic} dropped again. Below this critical value stress concentrations could not be built up properly and the material did not shear band yield anymore. Thus, an optimum interparticle distance exists in which the triaxial stress concentrations the matrix can bare are the highest. Michler related these findings to the movements of segments within macromolecules and stated that the minimum interparticle distance should be in a range from ten to hundreds of nanometers. Furthermore, the average ratio between the interparticle distance to the particle diameter (r/D) should thereby be smaller than 1 to allow stress fields to overlap.

Bucknall et al. [209] showed that the smaller the diameter of a rubbery particle became the harder it got to initiate cavitation, which is again well in agreement with the findings from Michler as well as the considerations about the importance of the cavitation resistance of rubber particles. This goes along with the findings reported by Kim et al. [157]. Below a threshold diameter of about $0.2\ \mu\text{m}$ of CSR particles cavitation was omitted. Also, when a rigid PMMA based particle type ($\varnothing=0.35\ \mu\text{m}$) was used, fracture toughness was on the level of the neat epoxy resin. The reason was that the particles did not cavitate and were not able to initiate shear yielding. The particles rather debonded, since the **cavitation resistance** of the CSR particles, as mentioned in Sec. 2.3.3, was too high.

Due to the visco-elastic nature and the time-temperature equivalence of thermosetting polymers [210, p.402] fracture toughness is not only related to the test temperature but also to environmental conditions, e.g. **loading rates**. When the loading rate increases fracture toughness of the material drops [16, p.295], since the material artificially embrittles. This effect was particularly illustrated by Raghavan et al. [211], who showed that the type of fracture of a CTBN toughened brittle DGEBA based-epoxy matrix can even result in a ductile type of failure, if the loading rate is sufficiently low.

In conclusion, there is not a simple relation between a rubber particle and the fracture toughness enhancement of a cross-linked polymer, it is rather a function of the underlying molecular network-structure of the epoxy resin, i.e. the *toughenability* as well as the particle volume concentration, the particle size and its cavitation resistance. It can be stated:

- (i) the matrix needs to be strong to be tough, i.e. it must be able to bare high stress concentrations that cause cavitation and shear band formation. Thereby the cavitation resistance needs to be not too high, so that the particles are still able to cavitate, yet also not too low, so that the stress concentrations can built up and cause the subsequent shear bands.
- (ii) the particles should have a *small* interparticle distance, i.e. a high volumetric particle concentration to allow a high degree of shear band formation.

- (iii) the particle size should not be smaller than about 0.1 μm to allow cavitation of rubbery particles.
- (iv) the selection of the aforementioned parameters depends on the cross-link density of the matrix. The higher the cross-link density, the more difficult it is to induce shear yielding.

3 Motivation and Objectives

As has been shown in the first part of this work, the demand for damage resistant and damage tolerant carbon fibre reinforced composites has not been satisfied yet, especially due to the still persisting drawback of an insufficient toughness originating from highly cross-linked epoxy matrix systems. A variety of pathways have been developed in the last 60 years and some success has been achieved in toughening of epoxy matrices and to transfer this property from the matrix to a carbon fibre reinforced composite. Block copolymer toughening agents provide the opportunity not only to adjust fracture mechanical properties of the matrix system, but also to tailor interphases between carbon fibres and epoxy matrices. This combination allows the enhancement of DR and DT of CFREs during LVIs, without the necessity for additional manufacturing efforts, such as extensive dispersion of second phase modifiers into the epoxy resin or the application of interleaving veils. At the same time the benefits of epoxy resin systems can be utilized, such as e.g. a low viscosity during processing and a high strength to fracture in the solid state. However, the utilization of block copolymers as toughening agents in epoxy matrices and CFREs is still a challenging task. A number of parameters, such as the BCP block units or the resin-hardener system can affect and dictate the phase separation process, i.e. the second phase morphology, and in this way the fracture mechanical properties. Therefore, this dissertation focusses on gaining a better understanding of (i) the phase-separation phenomena of an ABA-type triblock copolymer in a commercially available epoxy resin, (ii) its effects as second phase modifier on the fracture mechanical properties, and (iii) the damage resistance (DR) of a carbon fibre reinforced composite. Moreover, (iv) the BCPs were additionally blended with a core-shell rubber nanoparticle masterbatch system (cycloaliphatic resin) to further increase the total modifier concentration within the epoxy matrix. This allows examining the influence of a third constituent on the fracture mechanical performance of the composite matrix and the CFRE (the epoxy matrix and the BCPs being the first and second one). Thereby, the work wants to contribute to a better understanding of BCP modified (carbon fibre reinforced) epoxy systems, so as to allow the controlled application of BCPs in epoxy matrices and CFREs. The final target is to tailor tough, damage resistant composites.

4 Materials and Experiments

4.1 Materials selection

4.1.1 Epoxy resin system

In the present work the main resin system is comprised of a diglycidyl ether of bisphenol A (DGEBA) based epoxy (*Biresin CR144* from *Sika Deutschland GmbH*, epoxy equivalent weight: 182-192 g/eq), which is cured by a cycloaliphatic anhydride mixture (*Aradur CY917* from *Huntsman Corp.*, molecular weight: 166 g/mol [212]). The curing-agent contains primarily a *tetrahydro-4-methylphthalic anhydride*, but can also contain small portions of other phthalic anhydride derivatives, such as *1,2,3,6-tetrahydro-3-methylphthalic anhydride* [213]. To initiate and accelerate the chemical reaction between the epoxy resin and the curing agent serves 1-methylimidazole (*DY070* from *Huntsman Corp.*). An accepted chemical reaction sequence is presented in App. A.1.

As a second prepolymer a *3,4-epoxycyclohexylmethyl 3,4-epoxycyclohexanecarboxylate* cycloaliphatic epoxy resin (CAE, *Celloxide P2021* from *Daicel Corp.*) was used. Celloxide P2021 is the neat polymeric carrier resin of the applied core-shell rubber particles (cf. Sec. 4.1.2). It has an EEW of 130 g/eq and a viscosity of 240 mPa·s at room temperature [214].

4.1.2 Block copolymers and core-shell rubber nanoparticles

Block Copolymers

The block copolymer type used in this work is an ABA-type triblock copolymer: *Nanostrength M52N* from *Arkema S.A.* The material is supplied as powder and has a poly(methylmethacrylate-block-butylacrylate-block-methylmethacrylate) structure (PMMA-PBuA-PMMA). Thereby, the outer epoxy-miscible PMMA block, or segment, surrounds a epoxy-immiscible block of PBuA. The latter is at least in a bulk shape incompatible to DGEBA based epoxy resins [215]. The ductile PBuA block content of this modifier is about 50 vol.-% [216]. The density of the BCP was measured as $\rho_{BCP} = 1.116 \text{ g/cm}^3$ at ambient temperature. Due to its transparency in the bulk state it is assumed that the BCPs have an amorphous character from a macroscopic point of view. In the outer PMMA-blocks additional functional dimethylacrylamid groups (DMA) are included to increase the compatibility to the epoxy resin [27]. Fig. 4.16 shows a schematic arrangement of the different constituents within *M52N* [216].

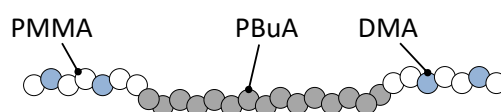


Figure 4.16: Schematic block copolymer structure of M52N

The complete molecular structure of M52N is not certain, yet the pristine molecular struc-

tures of each constituent are given in Fig. 4.17. During the copolymerization process (cf. Sec. 2.3.2.2) the molecules are connected via the repeat units.

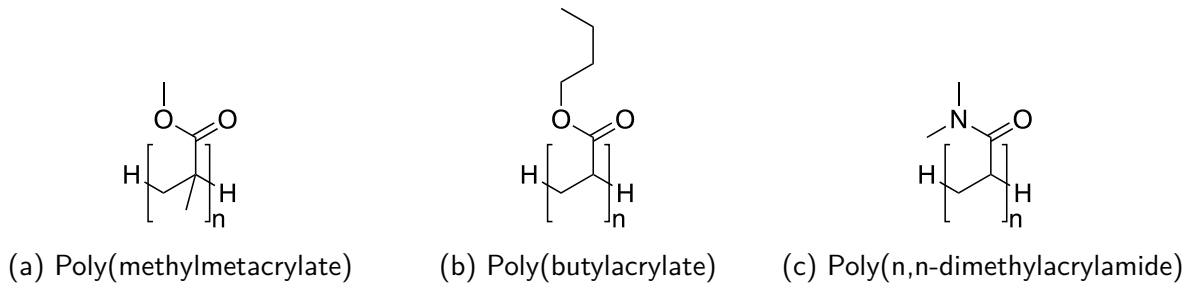


Figure 4.17: Oligomeric structures of the individual constituents of the M52N triblock copolymer, n is the number of repeat units, $n=0$: monomer

Core-Shell Rubber Particles

The core-shell rubber (CSR) particle system (*KaneAce MX553*) was supplied as a **masterbatch** by *Kaneka Belgium N.V.*, meaning the CSR particles are predispersed in a carrier resin (*Celloxide P2021* from *Daicel*) at a concentration of 30 ± 1 wt.-% and have an average diameter of $\varnothing \approx 100$ nm, given by the manufacturer. The particle core is made of Polybutadiene (PBd). However, no information is available on the molecular weight of the core. For orientation, depending on the isomeric typical glass transition temperatures of PBd are in the range of -107 to -95 °C [217]. Also, no certain information is available on the shell structure, however it is most-likely that the shell is comprised of at least one derivate of a methylmethacrylate (MMA) and the shell-to-core composition is in between 15-30 parts by weight of the shell to 100 parts by weight of the core [218]. Accordingly, based on an average diameter of 100 nm, the shell layer should have a thickness of at most 4.5 nm. Neglecting the thin molecular shell layer, the density at ambient temperature of the particles was taken as $\rho_{\text{CSR}}=0.94$ g/cm³.

The epoxy equivalent weight of the masterbatch was given as 192 g/eq and considers the CSR particles as an **unreactive** species within the resin. I.e. correcting the given EEW of the masterbatch by the amount of unreactive CSR particles (Eq. 4.5), yields a typical EEW of a cycloaliphatic epoxy resin (cf. Sec. 2.2).

$$192 \frac{\text{g}}{\text{eq}} \cdot (100\% - 30\%) = 134.4 \frac{\text{g}}{\text{eq}} \quad (4.5)$$

4.1.3 Carbon fibre type and fabrics

The carbon fibre reinforcement within this work is based on *HTA40 E13 (5131)* high tenacity carbon fibres from *Toho Tenax*. A single carbon fibre has a cross sectional diameter of 7 μm and is coated with ca. 1.3% of an epoxy surface sizing [219]. Assuming this number as relative weight percentage, the fibre sizing has a thickness of about 30 nm [50], which is less than 1% of the diameter of the CF. Some of the basic carbon fibre properties are summarized in Table 4.5.

Table 4.5: Properties of a Toho Tenax HTA40 E13 carbon fibre along fibre direction [6, 219].

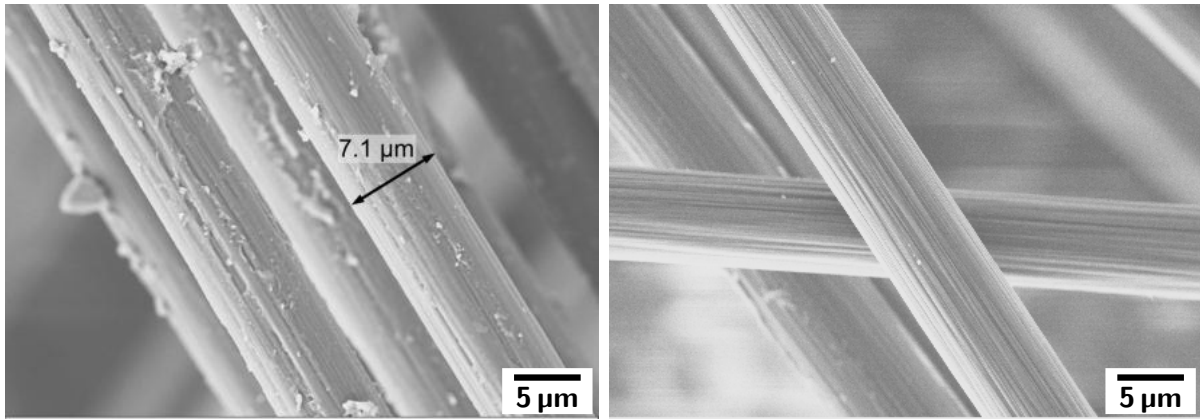
Filament diameter	[μm]	7
Mass density	[g/m^3]	1.76
Tensile strength	[MPa]	3950
Young's modulus	[GPa]	238
Strain at failure	[%]	1.7
Spec. heat capacity	[$\text{J}/\text{kg}\cdot\text{K}$]	710
Thermal conductivity	[$\text{W}/\text{m}\cdot\text{K}$]	10
Coef. thermal exp.	[$10^{-6}/\text{K}$]	-0.1
Spec. electr. resistance	[$\Omega\cdot\text{cm}$]	$1.6 \cdot 10^{-3}$

To get a better understanding of the selected type of carbon fibre, Fig. 4.18 shows a sized and an unsized *HTA40* CF. The sizing of the latter one was removed via an organic solvent following the *Soxhlet procedure*, as described in *EN ISO 10548, procedure A*. Compared to the unsized CF, the sized fibres show small features that probably represent sizing material that is applied during an immersion process. So, instead of an ideal shell layer around the carbon fibre, the sizing is only partially covering the CF.

Generally, the importance of the sizing comes from handling and manufacturing requirements of the CF, e.g. into woven semi-finished parts [103]. Secondly, the sizing provides chemical and physical bonding sites to the epoxy matrix, even though bare, i.e. unsized carbon fibres can also physically and chemically interact with a surrounding matrix via unsaturated valences of carbon atoms [11].

At this point, it should be noted that interphase engineering, i.e. tailoring the interfacial interaction between carbon fibres and the matrix is of crucial importance for the performance of the part since it is a pre-requirement for enabling a load transfer from the matrix into the carbon fibres. The interested reader is referred to Sec. 2.1.1 as well as [50, 53, 220] for further information. However, within this work, the interphase is not subject of quantitative investigations, even though potential interactions with such versatile materials as block copolymers are acknowledged. The influence of the interphase is qualitatively assessed and potential implications on test results are discussed.

Based on *HTA40 E13 (5131)* carbon fibres, two different non-crimp fabrics (NCF) were chosen. The first NCF is a quasi-unidirectional material *HexForce G1157 D1300 HS06K* from *Hexcel Corp.* (cf. Fig. 4.19a) and has a fibre areal weight of $277 \text{ g}/\text{m}^2$ (97 wt.-% carbon fibre, 6k roving). The construction is stabilized with 3 wt.-% of glass fibres (EC9 34 Z40 1383) [221] and has a cured ply thickness (CPT) of $256 \mu\text{m}$ at 60 vol.-%. This material is used for the basic laminate characterization, i.e. Mode I and Mode II tests (cf. Sec 4.4). The material was selected since it satisfies the physical and chemical requirements according

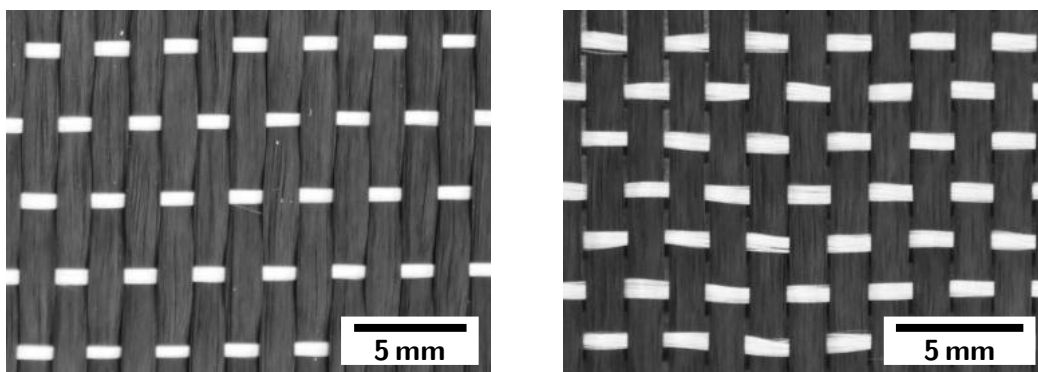


(a) Epoxy sized carbon fibres (E13) - as received (b) Unsized carbon fibres via *Soxhlet procedure*

Figure 4.18: SEM images of Toho Tenax HTA40 CF

Airbus Material Specification AIMS 05-01-001-C, Grade B for aerospace applications.

The second material (*Carbon Fabric Style 763* from *C. Cramer, Weberei, GmbH & Co. KG, Division ECC*) has a fibre areal weight of 140 g/m^2 (88 wt.-% carbon fibre, 3k roving) and is stabilized using 12 wt.-% of glass fibres, due to its delicate structure, cf. Fig.4.19b. The 3k rovings enable manufacturing laminates having a pre-defined aircraft skin structure layup at a total thickness of only 1.65 mm (Sec. 4.2.3). This thickness currently represents the *minimum skin thickness* in commercial aircraft applications. The performance of such laminates is therefore of special interest, especially with regard to impact damages. The cured ply thickness (CPT) of this fabric is $129.6 \mu\text{m}$ at a fibre content of 60 vol.-%.



(a) Hexcel HexForce
G1157 D1300 HS06K, 277 g/m^2

(b) ECC Carbon fabric Style 763,
 140 g/m^2

Figure 4.19: Non-crimp fabrics (dry) based on Toho Tenax HTA40 CF with epoxy sizing (E13). a) HexForce G1157 with 6k fibre bundles, being densely packed, b) ECC style 763 with 3k fibre bundles and a reduced areal weight of 140 g/m^2 , the fibre bundles are more loosely packed.

4.2 Materials processing

4.2.1 Systems overview

The following series of (modified) resin systems were manufactured, based on the above presented raw materials. The manufacturing process itself is described in detail in Sec. 4.2.2:

- (1) seven BCP modified systems (incl. the neat reference) with varying concentrations between 0.5 and 10 wt.-%, based on the diglycidyl ether of Bisphenol A (DGEBA) epoxy resin, i.e. *Sika Biresin CR144*.
- (2) two CSR nanoparticle modified systems (incl. the neat reference), having a CSR nanoparticle concentration of 16 wt.-%, based on the cycloaliphatic epoxy (CAE) carrier resin, i.e. *Daicel Celloxide P2021*. The CSR nanoparticle modified epoxy resin masterbatch is *Kaneka KaneAce MX553*.
- (3) one CSR and BCP modified hybrid epoxy system: the CSR particle modified epoxy resin *Kaneka KaneAce MX553* was therefore blended with 11.6 wt.-% of BCPs, yielding a final CSR/BCP concentration in the cured system of 27.6 wt.-%.

Fig. A.97 in the appendix gives an overview of the optical appearances of the resin systems and their BCP and CSR modified versions in the pristine state. Table 4.6 summarizes the different systems, including volumetric concentrations of the modifiers, based on the densities given in Sec. 4.1.2. A density of $\rho_{EP}=1.2\text{ g/cm}^3$ at ambient temperature was assumed for both epoxy systems in the cured state.

Table 4.6: Composition and nomenclature of the cured matrix systems (EP) and respective CF reinforced composites (CFRE)

System EP/ or CFRE/	Modifier [wt.-%]	Modifier [vol.-%]	total [vol.-%]	CFRP	
				3 mm	1.65 mm
DGEBA	0	0	0	x	x
BCP-0.5 %	0.5	0.5	0		
BCP-1 %	1	1.1	1.1		
BCP-2 %	2	2.1	2.1	x	x
BCP-5 %	5	5.4	5.4	x	
BCP-7 %	7	7.5	7.5	x	x
BCP-10 %	10	10.7	10.7	x	
CAE	0	0	0	x	
CSR-16 %	16	19.5	19.5	x	x
CSR/BCP-16/12	16 + 11.6	19.5 + 12.5	32.0	x	x

All further discussions in this work in terms of percentage concentrations refer to weight concentrations of the used modifiers, if not specified otherwise. The nomenclature applied

(e.g. EP/BCP-x, CFRP/BCP-x or EP/CSR/BCP-x/x) refers to a bulk matrix system (EP) or a laminate (CFRE), followed by the respective toughener (BCP or CSR or CSR **and** BCP) in wt.-%. If required, the nomenclature further distinguishes between DGEBA based epoxy systems, i.e. EP/DGEBA or CFRE/DGEBA, and CAE systems, i.e. EP/CAE or CFRE/CAE.

4.2.2 Matrix manufacturing

Prior to manufacturing the EP/BCP-systems, a BCP-masterbatch was manufactured having a concentration of 25 wt.-%. The respective amount of modifier was added to the DGEBA resin, heated up to 100 °C and mixed with a dissolver aggregate (*Dispermat*, *VMA Getzmann GmbH*) until an optically homogenous and transparent mixture was obtained. The masterbatch-step was followed by the actual matrix and CFRE manufacturing: the BCP-masterbatch was diluted with neat DGEBA epoxy resin at 50 °C to the targeted concentration, then a stoichiometric amount of curing agent (Huntsman CY917) was added, based on the EEWs given in Sec. 4.1.1. After stirring the solution for 20 min, 1.8 wt.-% of the accelerator (Hunstman DY070, with respect to the neat epoxy resin) was added and the mixture was stirred for another 10 min. Finally, the reactive system was cast into glass molds (300 × 200 × 3.8 mm³), which were coated with a release agent (*PAT-607/FB* from *E. und P. Würtz GmbH & Co KG, Germany*). The molds were coated at least two hours before sample manufacturing to allow evaporation of the water component of the release agent at about 120 °C in an oven. The neat epoxy reference systems were processed in the same way. A schematic showing the mixing process is given in Fig. 4.20.

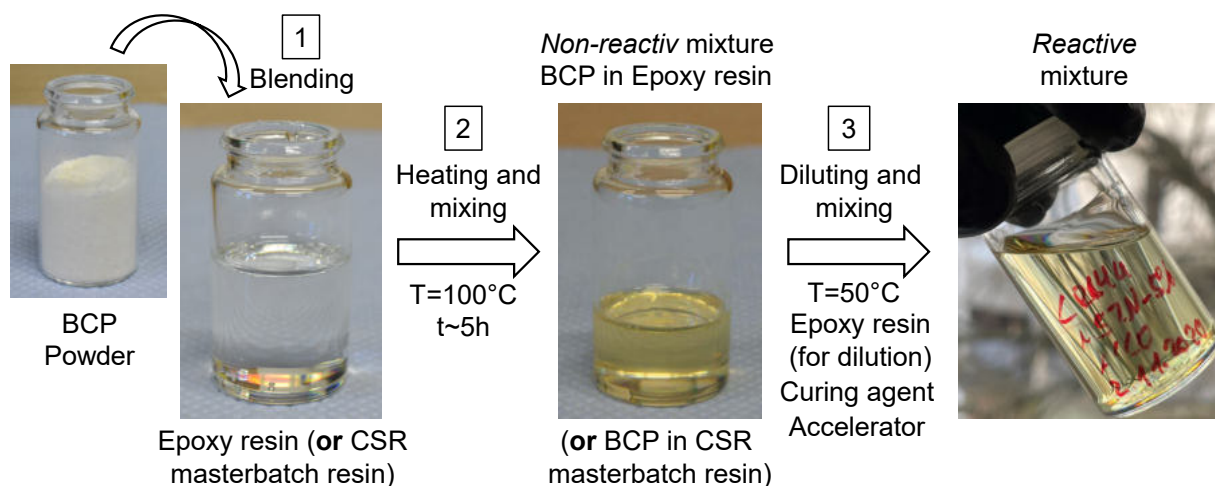


Figure 4.20: Manufacturing process of reactive EP/BCP and EP/CSR/BCP resin systems: 1) Blending powdery BCPs with the DGEBA based epoxy resin, 2) Homogenizing and mixing at 100 °C and 3) Eventually diluting (to obtain varying BCP concentrations) and mixing with curing agent and accelerator

The preparation of the CSR modified epoxy system followed a similar procedure as for the BCP systems: *Kaneka KaneAce MX553* was heated up to 40 °C and mixed with a

stoichiometric amount of the curing-agent. After 20 minutes 1.8 wt.-% of the accelerator was added and the mixture was stirred for another 10 minutes, and cast into glass molds.

For preparing the BCP/CSR hybrid epoxy system, the CSR-masterbatch (*Kaneka KaneAce MX553*) and 11.6 wt.-% of BCPs (with respect to the final system: resin, hardener, CSR and accelerator) were mixed with the dissolver aggregate and heated up to 100 °C until an optically homogenous and transparent mixture had been obtained. After cooling the BCP/CSR hybrid epoxy resin system to 50 °C a stoichiometric amount of curing agent was added, stirred for 15 minutes, then the accelerator was added and stirred again for 10 minutes and finally cast into glass molds.

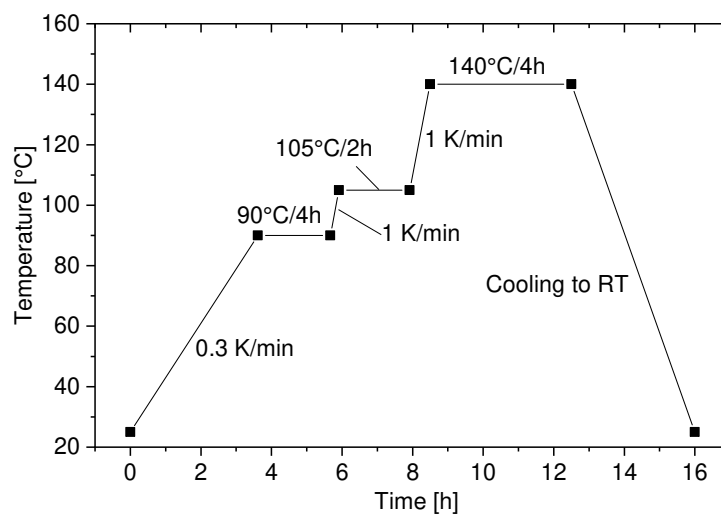


Figure 4.21: Three step curing cycle, used for matrix and CFRP samples

The samples were cured using a three step curing cycle (cf. Fig. 4.21): (1) 90 °C for 4 h, (2) 2 h at 105 °C, and (3) 140 °C for 4 h.

To obtain a pristine BCP sample for dynamic mechanical thermal analysis the BCP powder was pressed by a plate-press (*P300M, Dr. Collin GmbH, Ebersberg, Germany*) at 180 °C for five minutes under ambient pressure and then for 1 min at 100 bar.

4.2.3 Carbon fibre reinforced epoxy laminate manufacturing

Carbon fibre reinforced samples were manufactured based on selected resin systems (cf. Tab. 4.6) in two categories:

- (1) as plates with a unidirectional fibre layup (UD) and a thickness of 3 mm based on *Hexcel HexForce G1157 D1300 HS06K* for characterizing basic material properties, such as the interlaminar fracture toughness Mode I and Mode II
- (2) as *thin* plates with a multidirectional fibre layup of about 1.65 mm thickness to satisfy

the minimum skin thickness requirement and to investigate the effect of a CSR and BCP modification on the impact resistance, based on *Carbon fabric Style 763 from ECC*.

For manufacturing both laminate thicknesses a hand-layup process was chosen. This allows a flexible handling and variation of the resin system. Thereby a fibre volume content of 60 vol.-% was anticipated, based on the areal weight of the respective material, neglecting the glass fibre portions. This approach reduced the effective carbon fibre volume content to 58.2 vol.-% and 52.8 vol.-% for the 3 mm thick and 1.65 mm samples, respectively.

To manufacture the 3 mm thick laminates (300 mm × 500 mm × 3 mm) all the plies were stacked having a CF orientation in the same direction (0°). During the lay-up, in between each ply a portion of resin was applied, using an ink roller. In between ply no. 6 and 7 a 12 µm thick polytetrafluorethylen (PTFE) film insert was placed on one end of the laminate to gain an artificial pre-crack. This allows subsequently to extract double cantilever beam specimens (DCB) to determine the interlaminar fracture toughness. Following the lay-up procedure the laminates were vacuum bagged and cured in an autoclave. The curing cycle was the same as for the matrix systems, under 24 bar of pressure, to ensure a proper impregnation of the fibres (Fig. 4.21). The reactive resin systems were prepared just before the hand-layup process according the procedure described in Sec. 4.2.2. It took about 60 minutes from extracting the resin systems from the dissolver aggregate to starting the autoclaving process. No information is available on potential evaporation events of the liquid and reactive resin system at the beginning of the curing cycle by applying the vacuum.

To manufacture the thin laminates (500 mm × 580 mm × 1.65 mm) the stacking sequence followed an aircraft skin structure layup (15 % 0° / 23 % 90° / 62 % ±45°) and was (45/-45/45/-45/90/0/90)_s [21, 30]. The hand-layup process and the subsequent curing procedure were the same as for the 3 mm thick laminates.

4.3 Thermal analyses and basic materials characterization

Thermal analyses of polymers allow the investigation e.g. of the curing behaviour of polymers or their viscoelastic behaviour, i.e. the time, temperature and frequency dependency of properties. Various analytical techniques were used within this work to investigate these properties, such as *Differential Scanning Calorimetry (DSC)*, *Dynamic Mechanical Analyses (DMA)* or a quite newly developed method *Thermo Modulated Optical Refractometry (TMOR)*.

4.3.1 Dynamic Scanning Calorimetry (DSC)

DSC is used to measure the *total heat flow* Φ_{total} during the chemical reaction of the different resin systems, i.e. the heat that is needed to transfer the liquid and reactive resin systems to a cured state, cf. Eq. 4.6. The experiments were performed under non-isothermal conditions,

using a Mettler-Toledo DSC3 STAR® system.

$$\Phi_{\text{total}} = \int_{T_{\text{start}}}^{T_{\text{end}}} \dot{Q}_{\text{total}} dT = \int_{T_{\text{start}}}^{T_{\text{end}}} (H_{\text{morph}} + H_{\chi} + H_{\text{heat}}) \frac{dT}{dt} \quad (4.6)$$

where T_{start} and T_{end} are the starting and end temperatures in between the reaction occurs, \dot{Q} is the heat flow and H the enthalpy. Under isobaric conditions ($p = \text{const.}$) $Q = \Delta H$. Thereby, Φ_{total} contains enthalpy contributions from morphological changes H_{morph} , the chemical reaction H_{χ} and the heating rate H_{heat} .

The liquid and reactive resin samples were heated from $T=0^{\circ}\text{C}$ to 200 or 250°C , depending on the base resin, with a heating rate of 5 K/min. Then the samples were cooled to $T=0^{\circ}\text{C}$ again (cooling rate 5 K/min). The procedure was repeated to ensure complete curing of the system.

The same experiments were performed using the oven-cured matrix specimens (cf. Sec. 4.2.2). To determine the *degree of cure* of the matrix specimens, the residual reaction enthalpy ΔH_{rest} was then related to the total reaction enthalpy ΔH_{total} :

$$\eta = \frac{\Delta H_{\text{rest}}}{\Delta H_{\text{total}}} \quad (4.7)$$

Relaxation phenomena are strongly frequency and heating/cooling rate dependent, i.e. the obtained data are always to be considered along with the selected parameters.

4.3.2 Phase separation and volume changes via Temperature Modulated Optical Refractometry (TMOR)

TMOR is an experimental technique that combines *Abbe* refractometry with a superimposed temperature modulation. This unique setup allows not only to e.g. determine the *refractive index* n of a material over time and temperature, but also to simultaneously measure other properties such as the *complex thermal volume expansion coefficient* β^* . This enables gaining valuable information on phase transitions of polymers [222–224], or, e.g. derive temperature induced shrinkage phenomena [223]. Thereby, the thermal volume expansion coefficient is to a certain extent the counterpart to the *specific heat*, obtained via DSC measurements [225].

Within this work, TMOR is used to get deeper insights into the phase-separation process of block copolymer-epoxy resin mixtures. The goal is to access and investigate temperature and curing driven phase-separation phenomena of complex multicomponent BCP-epoxy resin mixtures.

Since the technique is rather new, a more detailed description of its working principle is given below.

The refractive index n is a material property of a liquid or a solid that depends on its mass density ρ and its specific refractivity r [226, 227]. It is furthermore defined by the degree of

refraction of light at an interface, when passing from a known medium (n_1) to an unknown medium n_2 (e.g. polymer sample), cf. *Snell's law*, Eq. 4.8

$$n_1 \cdot \sin(\alpha_1) = n_2 \cdot \sin(\alpha_2) \quad (4.8)$$

where n_1 and n_2 are the refractive indices of the materials and α_1 and α_2 are the angles of incident and refracted beams of light, as illustrated in Fig. 4.22.

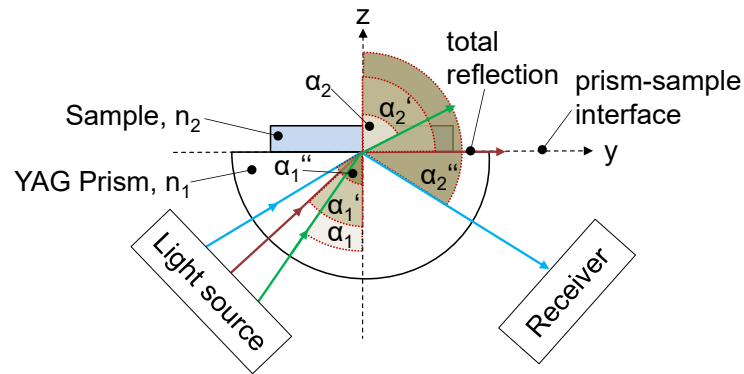


Figure 4.22: Schematic to illustrate the phenomenon of total reflection.

A divergent light beam illuminates a sample through a YAG-prism under different angles α_1 , α_1' , α_1'' , with respect to the prism-sample interface. These incident beams of light interact with the sample via reflection and transmission (absorption is neglected in the present work). According to Eq. 4.8, when a beam of light hits an optically less dense material ($n_2 < n_1$), the beam of light is refracted away from its optical axis. When increasing the incident angle α_1 , the angle α_2 of the refracted light beam increases as well up to 90° , the critical angle of total reflection.

A more thoroughly perspective on total reflection is given by the Fresnel equations, illustrated for s-polarization in Fig. 4.23, left. The measured quantity is the intensity of the reflection, determined as a function of the angle α_1 of the incident light beam. When the critical angle $\alpha_{1,crit}$ is reached, and total reflection appears, n_2 is determined.

A relationship between n and the mass density ρ of the penetrated sample can be described by the Lorentz-Lorenz equation

$$\frac{n^2 - 1}{n^2 + 2} = r \cdot \rho \quad (4.9)$$

where r is the specific refractivity of the material; a quantity that is usually almost independent of temperature changes. However, if chemical reactions change the electric polarisation of a material, the specific refractivity r might be affected [228]. Hence, mass density ρ can be determined via Eq. 4.9 as a function of external parameters, such as e.g. temperature, pressure, or kinetic influences such as chemical reactions, provided $r = \text{const.}$ is known. Hence, the chemical reaction induced shrinkage of a material, which is of utmost importance when designing epoxy matrices, can be assessed.

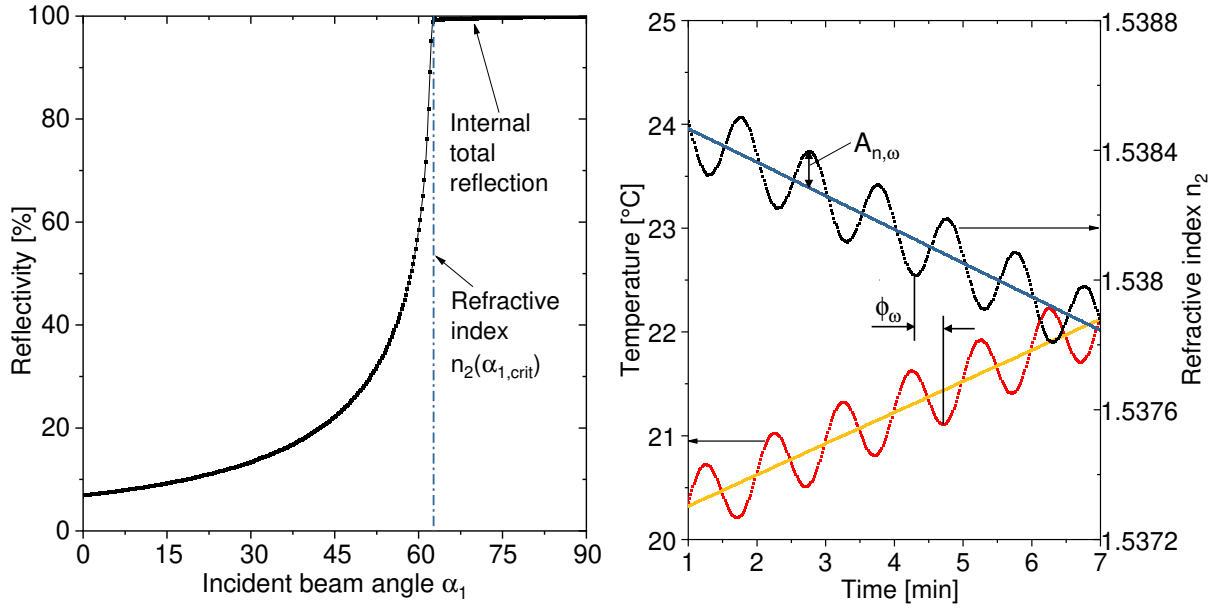


Figure 4.23: left: Exemplarily Fresnel curve at $T=25^\circ\text{C}$ of an epoxy resin, showing the transition from a low degree of reflection to total reflection, s-polarization is experimentally realized. When total reflection occurs, i.e. the position of the kink, n_2 can be determined, right: Thermo-modulation ($A_T=0.3\text{K}$) superimposed to a heating rate of 0.3K/min and the refractive index response, modulation time $\tau=60\text{s}$

A further important quantity that can be derived when refractive index or volume changes occur, is the *static* thermal volume expansion coefficient β_{stat} . Eq. 4.10 is derived from Eq. 4.9 under the condition that the temperature dependence of r is neglectable. If reaction induced effects are omitted β_{stat} can be measured via a sufficiently low heating rate at every increment of temperature change. It should be pointed out that already classical Abbe refractometry allows determining the static thermal volume expansion coefficient of transparent samples.

$$\beta_{\text{stat}} = \frac{-1}{\rho_0} \cdot \frac{d\rho}{dT} = \frac{-6n_0}{(n_0^2 + 2)(n_0^2 - 1)} \frac{dn_0}{dT} \quad (4.10)$$

Compared to Abbe refractometry, *TMOR* makes use of a superimposed sinusoidal temperature perturbation $T(t) = T_{\text{mean}} + A_T \cdot \sin(\omega t)$ of the sample (Fig. 4.23, right, yellow and red curves).

At every time (or temperature) the complex refractive index $|n_\omega^*|$ can be measured

$$|n_\omega^*| = n_0 + A_{n,\omega} \cdot \sin(\omega t - \phi_\omega) \quad (4.11)$$

where n_0 is the mean refractive index, $A_{n,\omega}$ the amplitude at a certain frequency f ($\omega = 2\pi f = 2\pi/\tau$, τ is the temperature modulation time) and ϕ_ω a phase shift between sinusoidal temperature excitation and refractive index response.

The temperature modulation allows accessing the complex thermal volume expansion coefficient β_ω^* (Eq. 4.12) even during isothermal measurements. Hence, this technique enables

time-dependent investigations e.g. of thermal relaxation phenomena of polymers. In contrast to classical DSC, structural changes on a molecular level can be examined without superimposed heating rate effects. Using sufficiently small temperature amplitudes of $\lesssim 0.3$ K, non-linear thermal excitations of the material are omitted.

$$|\beta_{\omega}^*| = \sqrt{\beta_{\omega}'^2 + \beta_{\omega}''^2} = \frac{-6n_0}{(n_0^2 + 2)(n_0^2 - 1)} \left| \frac{dn_{\omega}^*}{dT} \right| \quad (4.12)$$

The real part of Eq. 4.12 shows the *dynamic* thermal volume expansion coefficient:

$$\beta_{\omega}' = |\beta_{\omega}^*| \cdot \cos(\phi_{\omega}) \quad (4.13)$$

Dissipative thermal relaxation processes are represented by the imaginary part and reflect the degree of entropy production.

$$\beta_{\omega}'' = |\beta_{\omega}^*| \cdot \sin(\phi_{\omega}) \quad (4.14)$$

TMOR has been implemented in an Abbe refractometer (*TORC 5000*) from *Anton Paar OptoTec GmbH, Seelze, Germany*. The refractometer is equipped with a LED having a wavelength of $\lambda(n_D)=589$ nm. The information depth that can be collected from the sample is accordingly limited to about 300 nm. A photo diode array detects the reflected light and provides a relative accuracy of the refractive index of $2 \cdot 10^{-6}$. The temperature can be varied in a range from -20 to $+130^{\circ}\text{C}$ with an accuracy of ± 0.03 K.

To investigate the curing behaviour of the BCP modified epoxy, i.e. via simultaneous changes of the dynamic thermal volume expansion coefficient β_{ω}^* , three systems were selected for investigation, the neat reference DGEBA, the 5 wt.-% and 10 wt.-% system. The materials were prepared as described in Sec. 4.2.2. Immediately after the mixing procedure the samples were transferred to the refractometer. The measurements were conducted at a constant heating rate of 0.3 K/min from 20 to 128°C , adapting the conditions of the curing cycle for materials processing. The thermo-modulation took place with an amplitude of $A_T=0.3$ K at a frequency of $f=16.7$ mHz ($\tau=60$ s). The modulation time τ was chosen in such a way that no conflict appears with the heating rate.

Noteworthy, applying a heating rate during the measurement will not necessarily lead to a static refractive index, if the temperature perturbation is too high. However, the heating rate selected should not distort assumed static property, due to kinetic influences.

4.3.3 Dynamic Mechanical Analyses (DMA)

The principle of DMA is based on a frequency depended excitation (e.g. a displacement s or strain ε) of a specimen, which leads to a time and/or frequency f related complex response, i.e. a phase (δ_f) shifted force F or stress σ_f^* . Vice versa, a stress can be applied and a strain response can be measured. Additionally, the measurement can be superimposed by a kinetic component, i.e. a heating rate. Furthermore, a variety of experimental setups can be used anticipating e.g. the stiffness of the material. Accordingly, the sample geometry and the

response function vary, i.e. $\sigma^* = f(\varepsilon, f, \text{geometry})$ or $\varepsilon^* = f(\sigma, f, \text{geometry})$.

DMA is a versatile method to assess e.g. (i) time or temperature induced mechanical relaxation phenomena, (ii) the dynamic glass transition temperature T_g or (iii) material compositions by analysing the aforementioned properties.

In DMA measurements, the storage modulus E' and the loss modulus E'' , real and imaginary part of the complex dynamic response (Eq. 4.15), respectively, are usually evaluated, Eq. 4.16 and 4.17.

$$|E_f^*| = \frac{|\sigma_f^*|}{\varepsilon} \quad (4.15)$$

$$E'_f = |E_f^*| \cdot \cos \delta_f \quad (4.16)$$

$$E''_f = |E_f^*| \cdot \sin \delta_f \quad (4.17)$$

E' represents the materials' capabilities to store energy, whereas E'' is a measure of the dissipated energy, caused by molecular motions and friction [229]. Based on the ratio of both, the mechanical damping $\tan \delta$ can be assessed:

$$\tan \delta = \frac{E''}{E'} \quad (4.18)$$

Measuring elastic properties and relaxation processes via dynamic and kinetic methods is a challenging task, since the mechanical behaviour of polymers can be drastically different depending on the experimental conditions. The measurements are valid in the linear elastic region of a material, i.e. non-linear excitations need to be omitted by selecting sufficiently small excitation parameters.

The DMA tests within this study were conducted using a *TA Instruments Q800* as well as a *TA Instruments 850* after following the sample preparation procedure as described in Sec. 4.2.2. The measurements were performed in a single cantilever beam setup using a heating rate of 2 K/min, in a deformation controlled manner ($\varepsilon_0=0.041\%$). To perform measurements over the full temperature range from -100°C up to 300°C (depending on the matrix or CFRP system), a test frequency of $f=10$ Hz was selected. The specimen dimensions were 35 mm in length, 10 mm in width and 3.8 mm in thickness. The dynamic glass transition temperature was determined at the peak value of the mechanical damping $\tan \delta$.

The crosslink density n_c was calculated according Eq. 4.19 [115], where ρ is the mass density of the polymer (calculated, based on given densities at ambient temperature in Sec. 4.1.1), N is the Avogadro constant, and M_c the average molecular weight, given by Eq. 4.20.

$$n_c = \frac{\rho \cdot N}{1.5 \cdot M_c} \quad (4.19)$$

$$M_c = \frac{q\rho RT}{E'_{T_g+50K}} \quad (4.20)$$

The average molecular weight is based on the theory of rubber elasticity [230–233], where $E'_{T_g+50K} = E_{\text{stat}}$ is the storage modulus measured by dynamic mechanical analysis at 50 K above T_g in the rubbery plateau. As described above, the temperature increasingly surpasses the frequency domination of the measurement when the temperature is increased far above the α -relaxation. Accordingly, E'_{T_g+50K} represents a material value that is rather temperature dependent than frequency dependent in the frequency range used. R is the universal gas constant, T the absolute temperature and q the front factor ($q=0.725$ [138]), a dimensionless factor that accounts for changes of the chain length during the cross-linking process [234]. Due to a variety of assumptions, e.g. applying the model to a heterogeneous system even though it is only meant for homogenous materials, or applying the model based on material properties obtained from non-equilibrium measurements (e.g. influence of the heating rate and frequency), the results, i.e. cross-link densities obtained from BCP and CSR particle modified epoxies are only of indicative character.

4.4 Mechanical Characterization

4.4.1 Tensile properties

Quasi-static tensile properties of the **matrix systems** were performed on a *Zwick 1474 universal testing machine*, following *ISO DIN EN 527* to determine Young's modulus E , the materials' strength σ_{max} and the respective strain value ε_{max} , as well as the strength and strain at fracture, $\sigma_{\text{t=total}}$ and ε_{t} , respectively. Tensile testes were conducted to obtain Young's modulus and to be able to apply some of the relationships provided by LEFM (cf. Sec. 4.4.2.1).

For testing, a 10 kN load cell was used. The selected specimen geometry was the *preferred* specimen geometry given in the standard *1B*, having a total length of 150 mm. A pre-load of 1 N was applied and the deformation in the linear-elastic region during the test was measured using a clip-on extensometer, having a gauge length of 50 mm. The testing speed was 1 mm/min.

4.4.2 (Interlaminar) fracture toughness - Mode I

4.4.2.1 Matrix

The stress intensity factor in Mode I K_{Ic} was determined for the various matrix systems following linear elastic fracture mechanics, as described in ISO 13586 using a *Zwick 1474 universal testing machine*. This factor uniquely describes the **intensity** of a stress field around a crack tip, when tensile forces are applied to initiate crack growth in a material [16]. Mode I fracture represents the most critical fracture mode, since it is e.g. not affected by frictional events, such as in the case of Mode II (in-plane shear) or Mode III (anti-plane shear) fracture, and therefore of special interest. A more detailed description of fracture mechanics theory

and the differences between linear-elastic, non-linear elastic and inelastic fracture the reader can also be found in [16, 235, 236].

The basic equation that relates the experimentally measured data to the stress intensity factor is:

$$K_{Ic} = \frac{F_{\max}}{B\sqrt{W}} f(\alpha) \quad (4.21)$$

$$f(\alpha) = \frac{2 + \alpha}{(1 - \alpha)^{3/2}} (0.866 + 4.64\alpha - 13.32\alpha^2 + 14.72\alpha^3 - 5.6\alpha^4)$$

where F_{\max} is the maximum force during the compact tension test that causes crack growth, B the sample thickness, W the effective, load carrying length and $f(\alpha = a_0/W)$ a geometry function [237].

Machined compact tension (CT) specimens (cf. Fig 4.24) of previously casted plates (cf. Sec. 4.2.2) were used for testing, having an *effective length* of $W=31.2$ mm and a thickness of $B=3.8$ mm (plate thickness). The selected specimen dimensions ensure a state

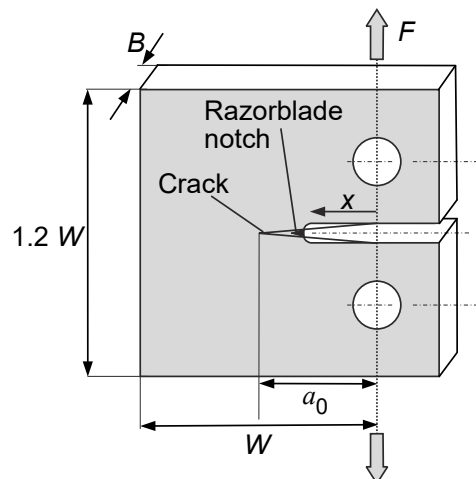


Figure 4.24: Schematic of a compact tension specimen for measuring the fracture toughness in the pre-cracked, yet untested state (adopted from [146])

of plane strain at the crack tip, at least up to a certain degree, since usually small scale yielding events can occur in the close vicinity of the crack tip during loading. However, as long as the material of interest shows a linear elastic stress-strain behaviour and infinitesimal strains, linear elastic fracture mechanics theory (LEFM) can be applied [16, 235].

The test was performed at a deformation rate of 1 mm/min and a preliminary force of 1 N. The displacement was measured by the movement of the machine cross-head. For statistical evaluation, at least five samples of each system were examined. Prior to testing, a sharp notch, i.e. the initial crack length a_0 , was introduced into the samples by razor blade tapping [238]. *Post-mortem* analyses of a fractured CT-specimen clearly show the initial crack length a_0 after the test is performed, cf. Fig. 4.25. Therefore a_0 was determined on the fracture surface by an electronic caliper after the experiment was conducted. Preliminary tests did not show

a difference of fracture toughness by evaluating the crack length via an electronic caliper or using additionally a light microscope. However, to be a valid data set the crack length had to satisfy the requirement $0.45 \leq a_0/W \leq 0.55$ (cf. ISO 13586).

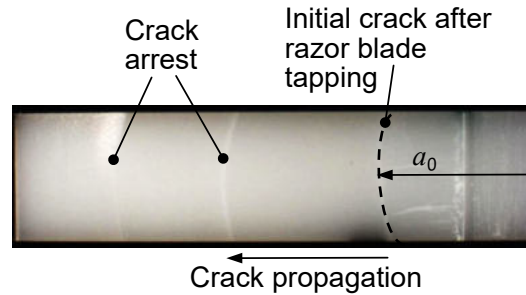


Figure 4.25: Fracture surface of a CT specimen, thickness $B=3.8$ mm, the notch was introduced into the specimen by razor blade tapping

Another measure to describe the initial fracture process is an energy based approach that considers the energy change in the system ΔU due to crack growth ΔA (newly generated fracture surface) [239], the **strain energy release rate** G_{Ic} . G can respectively be experimentally obtained from the force displacement curves of the CT tests [240, 241]. However, in LEFM G is also related to the stress intensity factor via Eq. 4.22.

$$G_{Ic, \text{matrix}} = \frac{dU}{dA} = \frac{K_{Ic}^2}{E^0} \quad (4.22)$$

where $E^0 = E$ (plane stress) or $E^0 = E/(1 - \nu^2)$ (plane strain).

In the present work G_{Ic} was determined based on the given relationship to K_{Ic} , considering ν as 0.34, i.e. the Poisson ratio of the neat DGEBA matrix for all matrix systems. The conversion from the stress intensity factor K_{Ic} to the energy release rate G_{Ic} allows the comparison of fracture mechanical properties of matrices and laminated composites. The stress intensity factor approach (Eq. 4.21) is not valid in heterogeneous systems such as fibre reinforced polymers.

As described above, LEFM is an applicable method, in the case of small scale yielding events, as long as the bulk material behaviour is plane strain dominated [16]. If the yield stress σ_{ys} , i.e. the stress that induces plastic deformational events is exceeded, a dog-bone shaped region in front of the crack tip develops that is referred to as the **plastic zone** (cf. *Irwin* model [242]). The yield stress, the intensity of the stress field K and the corresponding extent of the plastic zone size, i.e. its radius r , are related to each other via Eq. 4.23

$$\sigma_{ys} = \frac{K}{\sqrt{2\pi r}} \quad (4.23)$$

The equation yields an estimate of the size of the plastic zone in front of the crack tip prior to failure (Eq. 4.24). It is another parameter to access the fracture toughness of a material, within the limits of LEFM under plane strain conditions.

$$r_p = \frac{1}{6\pi} \frac{K_{Ic}^2}{\sigma_{ys,ps}^2} \quad (4.24)$$

where K_{Ic} represents the stress intensity factor and $\sigma_{ys,ps}$ is the yield stress under plane strain conditions. Note, in the case of plane strain conditions the stress field is further constraint, i.e. $\sigma_{ys} = \sqrt{3} \cdot \sigma_{ys,ps}$ [16].

4.4.2.2 Carbon fibre reinforced epoxy

To investigate the effects of a BCP and CSR nanoparticle matrix modification in the presence of carbon fibre reinforcements it is necessary to be able to compare the resistance to crack growth of the CFRE to that of the neat matrix (without CF, yet modified). This allows investigating the interaction between carbon fibres and the (modified) matrices as well as potential influences of the phase separation behaviour of the BCPs or the degree of dispersion of the CSR modifiers, due to different surface energies, on the CFREs. Therefore, the interlaminar fracture toughness of the fibre composites, i.e. the strain energy release rate (Mode I, G_{Ic}), which should be from a physics point of view the same value as for the matrix without fibre reinforcement (Sec. 4.4.2.1), is determined. Within this study, the procedure according the

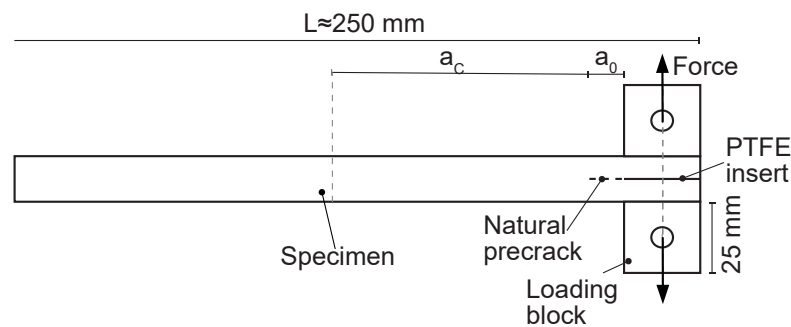


Figure 4.26: Schematic of the double cantilever beam test setup for determining the Mode I interlaminar fracture toughness prior to testing

European standard EN 6033 as well as ISO 15025 was followed. Double cantilever beam (DCB) specimens (cf. Fig. 4.26 and 4.27) were cut from the unidirectional laminates (cf. Sec. 4.2.3) with dimensions of 250 (0° fibre orientation) \times 25 \times 3 mm³. Loading blocks (25 \times 25 \times 25 mm³) were subsequently bonded to the specimens using a two-component epoxy adhesive to open the artificial pre-crack that was introduced in the laminate by a PTFE insert during the manufacturing. By pre-loading the sample, before the actual experiment, the artificial pre-crack is propagated by about 10-15 mm, to generate a *natural* pre-crack a_0 . The test velocity was set to 10 mm/min and the load was measured by a 10 kN load cell. Load displacement curves were recorded and a travelling microscope was used to observe the crack propagation until a crack length a_c of ≥ 100 mm was reached. This allows the correlation between crack length, force and displacement. The steady-state interlaminar energy release rate $G_{Ic,composite=c}$ was then calculated according Eq. 4.25, based on EN 6033, which is an integral method and gives an overall energy release rate.

$$G_{Ic,init,composite} = \frac{U}{a_c \cdot b} \quad (4.25)$$

where U corresponds to the total energy consumed during crack propagation (loading and unloading), a_c is the crack length and b the specimen's width.

However, following ISO 15014, the energy release rate can also be calculated for each crack propagation step based on the *corrected beam theory* approach (Eq. 4.26). This approach allows obtaining information about the development of G over an increasing crack length, i.e. the examination of so called resistance curves (R-curve) or the determination of an energy release rate at crack initiation $G_{Ic,init}$. This value is ideally not affected by the presence of any fibres in the CFRE and can therefore be correlated to G_{Ic} of the matrix systems. The crack initiation toughness $G_{Ic,init}$ was measured based on the onset of non-linearity of the load-displacement curve and were determined from the pre-crack. The distance between the load line and the tip of the pre-crack was taken as the crack length a_0 .

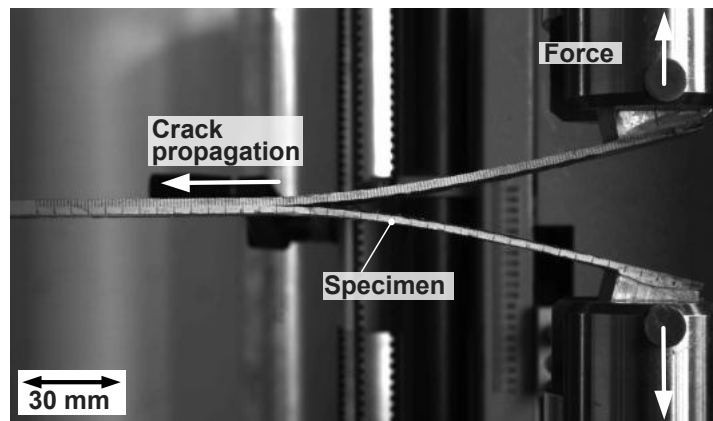


Figure 4.27: Double cantilever beam test setup at the end of the experiment. The crack has already interlaminarly propagated through the sample

$$G_{Ic,init,composite} = \frac{3P\delta}{2b(a_c + |\Delta|)} \cdot \frac{F_{corr}}{N} \quad (4.26)$$

where P is the load, δ is the displacement along the load line, b the specimens' width, a_c is the crack length, Δ is a crack length correction factor based on specimen compliance, F is a correction factor in the case of large displacements, N is a correction factor if load blocks are used, as it is in this work. The correction formulas can be found in ISO 15014.

4.4.3 Interlaminar fracture toughness - Mode II

The Mode II critical energy release rate G_{IIc} is a measure to describe the resistance to crack growth in a shear loading mode. This loading mode usually yields higher G values than Mode I, since additional energy consuming effects, such as frictional events hinder crack growth. However, from an application point of view Mode I loading is usually not the dominating load case. The Mode II energy release rate is of great interest, since it reflects a *delamination*

induced failure behaviour of carbon fibre composites. Delamination events are one of the major impact induced damage modes of fibre composites. Delaminations within fibre reinforced structures can e.g. be a tool drop during an assembling process or in a more severe case a gun projectile that penetrates a CF reinforced structure. Furthermore, empirical models show a direct correlation between G_{IIc} and the response of a material to impact events, i.e. improving the resistance to shear induced crack growth can be used as an indicator to an improved damage resistance (cf. Sec. 2.1).

To investigate the effects of BCP and CSR nanoparticle modifications in CFRP on this loading mode, ISO 15114 was followed. The standard makes use of a special test setup, the so called *end-loaded split test*, as schematically shown in Fig. 4.28.

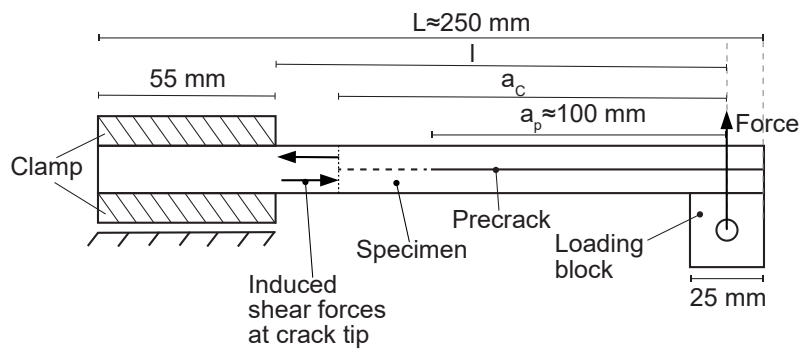


Figure 4.28: Schematic of the interlaminar fracture toughness in shear mode test setup with a specimen

Thereby double cantilever beam specimens from Mode I tests were used (Sec. 4.4.2.2) and clamped at one end. The clamping can horizontally move and reduce bending stresses in the laminate due to the loading at the other end of the specimen. This allows the crack a_c to propagate mostly in a shear mode.

Using DCB specimens from the Mode I test ensures the presence of a natural pre-crack and satisfies the test requirement that the ratio between the length of the natural precrack a_p and the free length l is bigger than $a_p/l \geq 0.55$. The top loading block ($25 \times 25 \text{ mm}^2$) was removed from the Mode I test specimen and the fixture clamped the specimen over a length of 55 mm, allowing the free length l to be around 182.5 mm. The mode I initiated precrack was at least 100 mm for every specimen in this study. The test velocity was set to 5 mm/min and the load was measured by a 10 kN load cell. Load displacement curves were recorded. The crack propagation was calculated based on the corrected beam theory using the *effective* crack length approach (cf. Eq. 4.27 as well as [243]), i.e. the crack length a_e was measured based on the reduction of stiffness of the DCB specimen, due to crack propagation (cf. Eq. 4.28, not to be confused with a_c).

$$G_{IIc, \text{init, composite}} = \frac{9P^2 \cdot a_e^2}{4b^2h^3E_f} \cdot \frac{F_{\text{corr}}}{N} \quad (4.27)$$

where P is the applied load, b is the specimen width, h the specimen thickness and E_f the flexural modulus of the systems, determined during the clamp correction procedure (cf. ISO 15114), a_e is given in Eq. 4.28. N is a correction factor if load blocks are used, as it is in this work. The correction formulas can be found in the respective standard.

$$a_e = \left(\frac{1}{3} (2bCh^3 E_f - (l + \Delta_{\text{clamp}})^3) \right)^{\frac{1}{3}} \quad (4.28)$$

where b is the specimen width, C the compliance $C = \delta/P$, h the specimen thickness, E_f the flexural modulus and l the free length. Δ_{clamp} accounts for the compliance of the clamping device.

According to the standard, the flexural modulus of the systems can be obtained from a clamp correction procedure. However, this procedure should be applied to an additional specimen from each test set using high loads. Since the specimen thickness varied in a certain range over a full test set, E_f was measured according DIN EN ISO 14525 for all systems. Then a relationship between the thickness of the specimens and the corresponding flexural modulus of the composite was established (neglecting the differences in the flexural modulus of the matrix due to the different modifications). Based on a *best-fit*, the flexural modulus for the Mode II measurements were calculated (cf. Fig. A.102):

$$E_f = 75345.05 + 1462483.46 \cdot 0.320^t \quad (4.29)$$

where t is the specimens' thickness.

The test enables determining the steady-state critical energy release rate $G_{\text{IIc,propagation}}$ as well as the shear induced crack initiation $G_{\text{IIc,initiation}}$. A picture of the test setup is given in Fig. 4.29. Crack initiation was (1) visually observed $G_{\text{IIc,init,vis}}$ using a travelling light microscope and (2) determined according the maximum force F_{max} from the force-displacement curve $G_{\text{IIc,init,Fmax}}$.

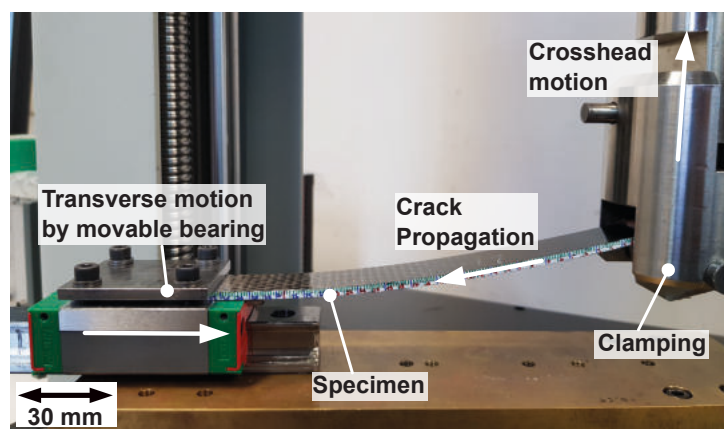


Figure 4.29: Endloaded split clamping fixture with specimen for investigating the interlaminar fracture toughness in shear mode

4.5 Damage Resistance

4.5.1 Impact performance

To analyse the damage resistance of matrix modified carbon fibre reinforced laminates that meet the current MST requirement, impact tests were carried out using a drop tower with varying drop heights ($m_{\text{impactor}}=2.065 \text{ kg}$), Fig. 4.30. The energy levels varied from 1 J, 3 J, 7 J, 9 J to 13 J, corresponding to impact velocities of 1 m/s, 1.7 m/s, 2.6 m/s, 3 m/s and 3.6 m/s, respectively. The goal was to select a load range that induces on one end only *barely visible impact damages* (1 J) and on the other severe damage to the laminates, but no penetration (13 J). The impact tests were performed following Airbus standard AITM1-0010

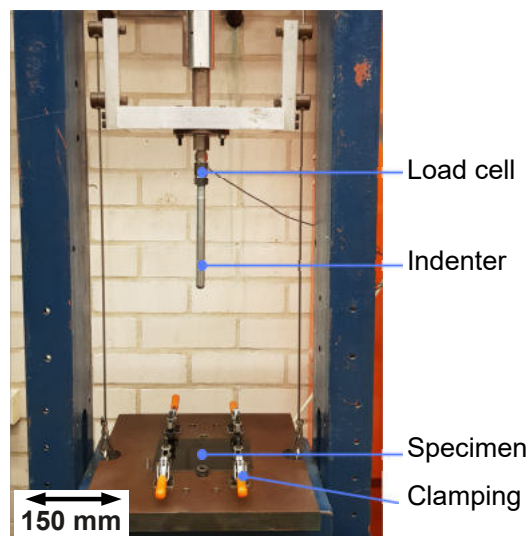


Figure 4.30: Drop tower setup

(cf. Fig. 4.31). Accordingly, sample dimensions were 150 mm in length (0° fibre orientation) and 100 mm in width. The drop tower was equipped with a 4.5 kN load cell, the force-time data were recorded using an oscilloscope (*DPO4034B Digital Phosphor Oscilloscope* from *Tektronix inc., USA*) and subsequently filtered with a low pass filter (SAE J211 standard, Channel Frequency Class 4) using a Matlab script. The acquisition time was 10 ms, capturing

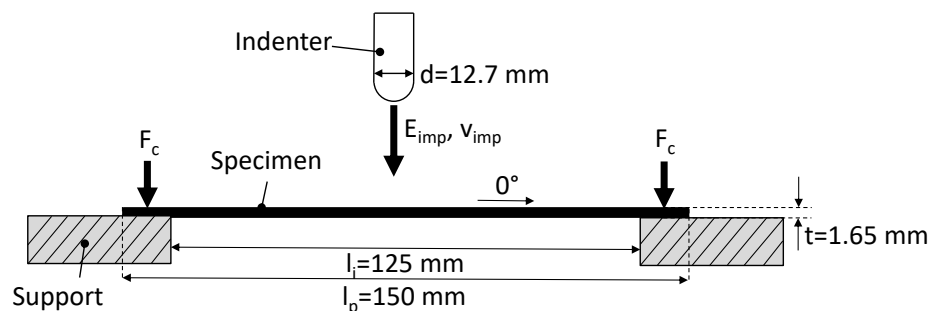


Figure 4.31: Schematic of the impact test setup: F_c is the clamping force, E_{imp} the impact energy, v_{imp} the impact velocity just before impacting the specimen, CF orientation 0° from left to right

1 million data points. The diameter of the indenter tip was 12.7 mm. For all energy levels one specimen was tested. This procedure does not necessarily provide quantitatively substantiated results but is able to compare the influence of the different modifiers (and concentrations) on the damage resistance. During the impact tests it was ensured that the impactor hit the specimen only once. In the case of the 9 J impact level, a second set of specimens was impacted twice (each time 9 J), to get an impression of the damage tolerance to the previous impact event.

The analyses of the differently modified laminates was done by (1) analyses of the force response during an impact event, (2) evaluation of the indentation depth after impact (Sec. 4.5.2), (3) visual damage assessment, (4) ultrasound analyses (Sec. 4.5.3), (5) light microscopy and (6) 3D X-ray microscopy (Sec. 4.6.2).

4.5.2 Post-impact Indentation depth

Impacting a structure is a three dimensional event, i.e. damage occurs in the x-y plane perpendicular to the main impact direction and in the z-plane in the direction of the impact. Depending on the impact energy, a permanent deformation remains in the structure.

To examine the permanent deformation in y-z-direction after the impact, i.e. the indentation depth through the crosssection of the impact, an in-house built chromatic confocal sensor stage was used based on a *Chromatic Confocal Sensor CHR 150* from *Stil*, Fig. 4.32. The sensor has a in depth resolution of 300 nm and a scanning range of 300 μm . The working

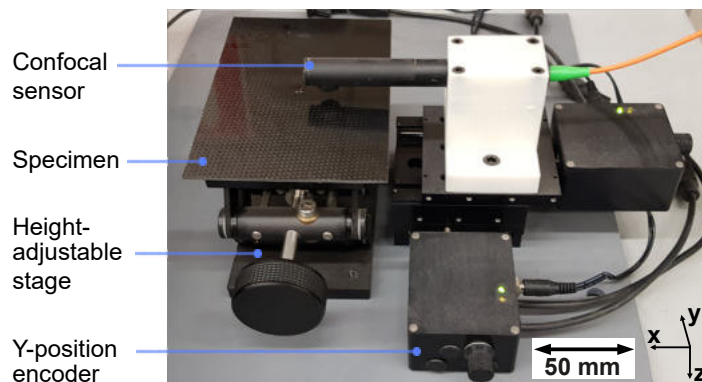


Figure 4.32: Chromatic confocal sensor with semi-automated scanning stage

principal of a confocal sensor is based on the variation of the intensity of light. If a sample is in perfect focus of the emitted light beam, the reflected light intensity is high, defocussing the beam leads to a loss of intensity. A respective electronics device calculates the profile value. For further background on chromatic confocal sensors and respective techniques, the reader is referred to [244].

The impacted specimens were set on supports (not visible in Fig. 4.32) to avoid an uneven profile scan due to the indent and were scanned in y-direction. An example is shown in Fig. 4.33.

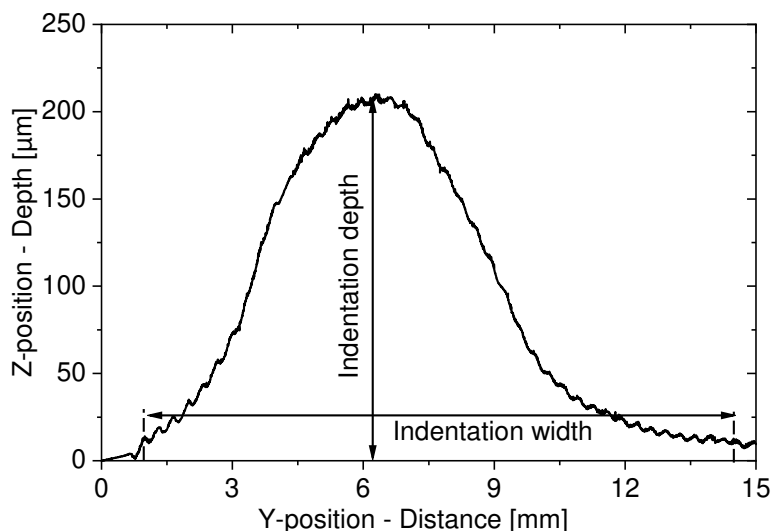


Figure 4.33: Profile scan of a CF laminate after impact showing permanent deformation

In a first step, a pre-scan was used to determine the deepest position caused by the impact with respect to the undamaged surface of the laminate. Subsequently the profile scan was performed through this position ensuring covering the maximum deviation from the undamaged surface structure. Afterwards the data set was graphically evaluated. In the case the indentation depth exceeded $300\ \mu\text{m}$ (confocal sensor limitation), the indentation depth was incrementally scanned, i.e. after a first scan, the distance between probe and sample was reduced by $250\ \mu\text{m}$ and the scan was repeated. However, this technique suffers from the restriction to obtain only two dimensional information (y-z). To obtain additional information on the extent of the damage in the x-y-plane, ultrasound analyses were performed, cf. Sec. 4.5.3.

4.5.3 Damage size evaluation via ultrasound

After the different material systems are impacted (cf. Sec. 4.5.1), the extent of the damage and an eventual reduction of the damage size by the BCP and CSR modification of the CFREs are evaluated. To obtain such information ultrasound analysis (US) were performed. Ultrasound analysis is a non-destructive type of acoustic microscopy technique that allows visualizing features, such as defects within a material. It was originally developed for the maintenance and quality control of parts and makes use of the interaction of sound waves with interfaces, defects or inhomogeneities. Sound waves can, similarly to light waves, be reflected, transmitted or absorbed. Post-mortem ultrasound analysis, usually in a *pulse-echo* setup, allows the detection and analyses of such altered sound signals [11, 245].

A variety of setups and modifications of ultrasound techniques exist to investigate material properties and eventual anomalies in CFREs.

Within this thesis, the *phased array ultrasound technique* (Olympus Omniscan MX2 phased array (PA) test instrument) in a pulse-echo setup was used. The setup is shown in

Fig. 4.34 and 4.35. Thereby a measuring probe (*Olympus 5L64A12*, 5 MHz probe, resolution: 0.6 signals/mm, 64 piezo elements, measuring width: 38.4 mm) equipped with a 0° wedge (*Olympus SA12-0L*), induced mechanical vibrations into the CFRP panel, in the shape of a focused ultrasound beam [246]. To capture the data in y-direction, an encoder wheel (*Olympus ENC1-2.5LM*, resolution 0.5 signals/mm) was attached to the side of the wedge. US analysis at air-specimen interfaces lead to a very high degree of reflections, i.e. do not allow for depth analyses of material defects, because of the large difference between the acoustic impedances of air and a solid. Since the acoustic impedances are much more similar between water and a solid, the experimental setup was additionally immersed in a water bath. This allows transmitting most of the ultrasound signal (energy) into the specimen (about 74%). Yet, a high degree of reflections at air-specimen interfaces enables the detection of pores and defects in a material that is immersed in water by US. Note, in this case no transversal sound waves can be transmitted and the detected signals are only of longitudinal character.

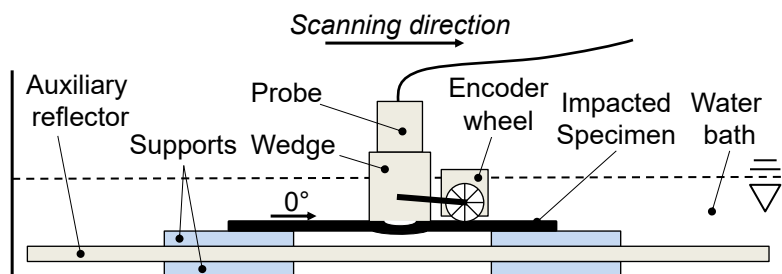


Figure 4.34: Schematic of the ultrasound setup with an impacted CFRP specimen, 0° fibre orientation from left to right

Generally, if the sound wave hits an inhomogeneity, e.g. a fibre-matrix delamination, the reflected or scattered sound signal changes. However, this also depends on the size of the defect. Then, amplitude, frequency and duration of the received signal are evaluated against the emitted one. In the case of *pulse-echo US* the sender is also the receiver of the reflected sound waves.

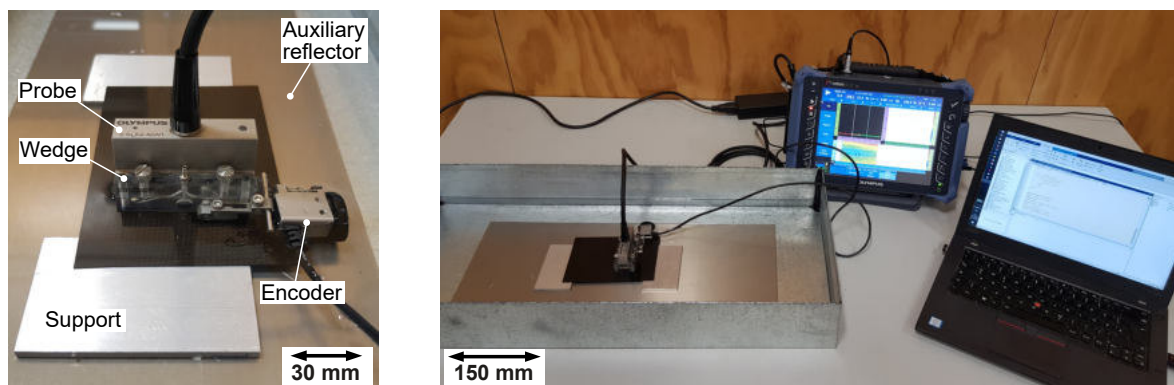


Figure 4.35: left: Ultrasound probe, wedge and encoder wheel on CFRP specimen, right: Phased array ultra sound setup: waterbath, PA and computer for data acquisition and post processing

In the used setup, the CFRE plate was set onto two supports above an auxiliary reflector (AR), which was as well mounted onto two supports. The stacked setup was chosen to clearly identify and differentiate the different amplitude echos during the measurement, i.e. (1) the interface between the wedge and the CFRE panel, (2) the back wall of the CFRE panel (BW), (3) the upper side of the AR as well as (4) the bottom side of the AR. For analyses of the extent of damages of the differently toughened systems, caused by the different impact energies the AR echo technique was chosen. Especially for thin panels it is difficult to determine delaminations accurately by measuring the classical BW echo. The signals, indicating materials failure, might then be superimposed by rapidly after occurring signals of the back wall [245], i.e. the damage zone through the thickness of the panel cannot be fully or even at all captured. By using an AR the signal travels through the specimen (and the defect) twice, first when it is released from the probe as well when it is reflected from the AR. This attenuates the reflections of the defect, but it will be less superimposed by other signals of the panel and can be clearly detected. For visualization and quantitative analyses the amplitude C-scans were examined. Damage within the samples was defined if the captured signal was damped by 70 %, i.e. a damage threshold level of 10 dB.

4.6 Imaging Techniques

4.6.1 Scanning electron microscopy

Scanning electron microscopy (SEM) is a well-established imaging technique that overcomes the classical limitation of visible light, being restricted to only image features in the range of the half of its wavelength ($d_{\text{feature}} \geq \lambda \approx 200 \text{ nm}$, based on the *Abbe* equation $d = 0.5\lambda / (n \sin \alpha)$, where λ is the wavelength of light, n is the refractive index) by employing a high energy electron beam. This allows imaging surface topographies down to spatial resolutions in the sub-nano meter range [247].

To perform SEM (fracture) surface analyses within this study, a *Zeiss Supra 40VP* was used. The accelerating voltage was in most cases set to $U_{\text{acc}}=5 \text{ kV}$. The fracture surfaces were sputtered with a gold-palladium layer at $I=40 \text{ mA}$ for 70 seconds (Balzers Sputter Coater SCD050) to allow a thin sputter coating to *de-charge* the specimen when hit by the electron beam. In the case of fracture surfaces, all images were taken ahead of the initial crack tip. For analysing the dimensions of fracture surface features, e.g. particle size, the image analysis software *ImageJ* was used.

4.6.2 3D X-ray microscopy

3D X-ray microscopy (or computer tomography) is a non-destructive technique to in-situ analyse structures and defects, such as delaminations and/or fibre fracture in carbon fibre reinforced polymers at high resolutions. State of the art XRM overcome the limitations of classical X-ray microscopes, which rely solely on the absorption of X-rays and the incident

photon energy to generate contrast from the presence of a material [248]. Thereby, the degree of X-ray absorption of a material can be described via η_{photon} and is denominated as the *linear attenuation coefficient* [249, 250]:

$$\eta_{\text{photon}} \propto \frac{Z^4}{U^3} \quad (4.30)$$

where Z is the atomic number and U is the energy of the incident photon. The higher the atomic number, the more electrons are available for excitation by incident photons, the lower the photon energy the higher its wavelength.

More general, the larger the linear attenuation coefficient, the more photons become absorbed from the material, i.e. have excited electrons, the lower η_{photon} the more transparent is the material to an incident X-ray photon. Hence, to obtain useful X-ray micrographs the materials should have large linear attenuation coefficients and the linear attenuation coefficients should differ from each other.

Therefore, performing X-ray analyses especially of polymers and carbon fibres is a challenging task using such classical devices. Both material classes are mainly based on carbon atoms, which have a low atomic number and nearly no difference between their attenuation coefficients (neglecting other atoms in the polymer structure), i.e. they suffer from a low *phase contrast* between each other.

State of the art XRM makes use of a so called *in-line phase contrast* technique that is based on the difference of the phase shift of X-rays caused by refraction of two adjacent materials and enables high contrast images of materials that are difficult to image using classical X-ray microscopes [248, 250, 251]. The technique is even capable of imaging interface regions between materials that barely absorb X-rays or have very similar electron densities to the surrounding constituents, such as e.g. a single carbon fibre and a thermosetting matrix [252]. Furthermore, the combination of classical X-ray analyses, based on a geometrical magnification and optical magnification enables state-of-the-art computer tomography not only to perform X-ray scans but also to magnify the same, allowing spatial resolutions in the nanometer region down to ≤ 70 nm per Voxel.

A more detailed description of the relation between attenuation (i.e. damping), diffraction and the complex index of refraction can be found elsewhere [249].

To examine post-mortem potential in-situ damages within this work, i.e. BVIDs, delaminations and fibre fracture, and supplement the information gained from ultrasound analysis and the indentation depth measurements of the impacted CFREs (cf. Sec. 4.5.1) a *Zeiss Versa 520* X-ray microscope (XRM) was used to non-invasively extract volume information of the carbon fibre laminates from the region of immediate impact. The scanning parameters were set to an accelerating voltage of $U_{\text{acc}}=70$ kV at a power of $P=6$ W. A resolution of $9 \mu\text{m}/\text{Voxel}$ was reached. Voxel clustering (binning) was omitted (2000×2000 px).

5 Results and Discussion

5.1 Phase separation behaviour of block copolymers in epoxy

This chapter investigates the phase separation process of a triblock copolymer in an anhydride cured epoxy resin. The main interest is to better understand the molecular BCP phase separation process in order to tailor macroscopical properties of a CFRE, such as the interlaminar fracture toughness and damage resistance. The parameters to investigate the phase separation processes via TMOR and DSC (cf. Sec. 4.3) were adapted to the conditions of the curing process at ambient pressure used for matrix and CFRE manufacturing (Sec. 4.2.2). This is the first time, TMOR is used to investigate phase separation phenomena of reactive BCP-epoxy systems. Therefore a more detailed description of the processes follows.

The macromolecular BCPs in this study are comprised of two different molecular segments: polybutylacrylate (PBuA) and polymethylmetacrylate (PMMA) (cf. Sec. 4.1), arranged in an ABA triblock structure, having molecular weights in the dimensions of several 10000 g/mol. Hence, their molecular weight is about 100 times higher than the molecular weights of the epoxy resin and the curing-agent moieties. However, in the liquid state the BCPs interact with the constituents of the resin system, i.e. can be optically and homogeneously mixed.

To investigate the underlying polymerization and phase separation processes via TMOR, the liquid and reactive, yet unmodified resin system was applied onto the prism of the refractometer at room temperature. The sample was then heated to 128 °C, using a heating rate of 0.3 K/min. The time and temperature induced development of the refractive index, the underlying Fresnel curves as well as the dynamic thermal volume expansion coefficient were monitored during the curing reaction. Fig. 5.36 shows n and β' as a function of the average temperature for the polymerization process of the reference system. The polymerization process can be divided into three regions based on the temperature dependent development of the refractive index: a temperature dominated region I, which is characterized by the expected quite linearly dropping refractive index, caused by the temperature induced decreasing mass density, and a constant dynamic thermal expansion coefficient β' . No effects of the polymerization process itself are visible at this stage. Then, at around 67.8 °C an inflection point of n_0 indicates that the chemical polymerization process becomes the dominating factor (region II) and the refractive index strongly increases up to a another inflection point at 99.2 °C. Afterwards, the reaction process becomes inferior to the temperature driven change of n_0 again (region III).

The course of β' strongly drops in region II, when the material passes the transition from the liquid phase to a glass. The chemically induced dynamic glass transition occurs at 97.7 °C (based on the inflection point of β'' and influenced by the frequency $f=17$ mHz). This region is superimposed by temperature induced relaxation processes as well as curing induced

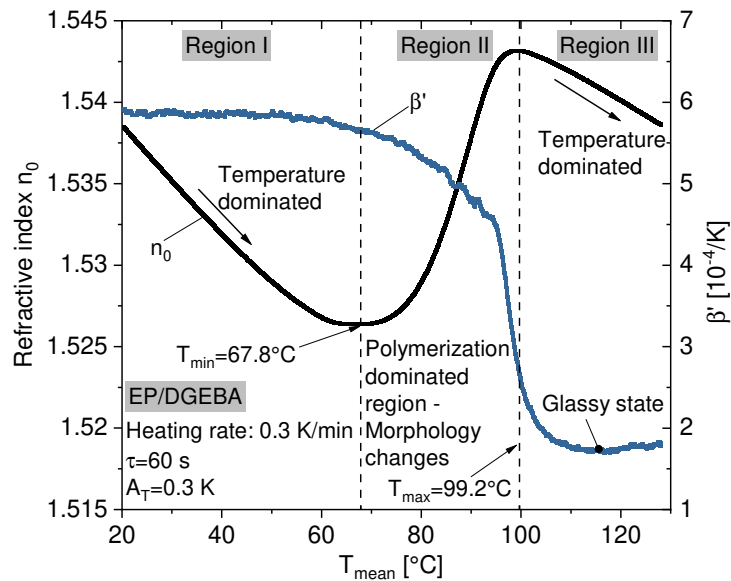


Figure 5.36: Temperature and curing driven change of the refractive index n_0 and the thermal expansion coefficient β' of the unmodified reference system (DGEBA cured by anhydride)

morphological changes. When the temperature is further increased, the polymerization process comes to an halt (self-hindrance of further cross-linking by the molecular network formation) and β' becomes constant again. β' has reached a typical value of the thermal expansion of a glassy epoxy material, $\beta' \approx 1.8 \cdot 10^{-4} / \text{K}$ [223].

Fig. 5.37 summarizes besides β' also the behaviour of the damping component β'' of the visco-elastic system. When β' reaches an inflection point, β'' shows a peak value, indicating the systems' polymerization induced transition into a glassy state. The temperature dependent *shift* of n_0 , i.e. the shift of the underlying Fresnel curves, is shown in Fig. 5.38. Supplementary data from region II and III can be found in the appendix, in Fig. A.98.

The same experiment was conducted with 5 wt.-% and 10 wt.-% BCP modified epoxy systems, as shown in Fig. 5.39. Examining and comparing the refractive index development of the different systems, one can see that the fundamental behaviour of all systems is very similar and follows the above mentioned transitions from region I to III. The higher the concentration of the modifier is, the lower is the refractive index, which makes sense considering the much lower refractive index of the co-polymeric component (neat EP/DGEBA $n_{0,CR144}^{25^\circ\text{C}} = 1.5369$ and neat BCP $n_{0,BCP}^{25^\circ\text{C}} = 1.4834$). Such a behaviour can be modelled applying a *group-contribution method* (GCM) [228]. Group contribution methods are used to predict properties of substances or materials based on their basic building blocks, such as e.g. dominant macromolecular structures or certain repetitive end groups, such as e.g. alkyl groups. They work in that sense similar to a macroscopic rule-of-mixtures for e.g. fibre composites, but on a molecular level. A well-known GCM is e.g. the *UNIFAC*-method, which is a semi-empirical model and uses the functional groups of different molecules to predict their interaction behaviour.

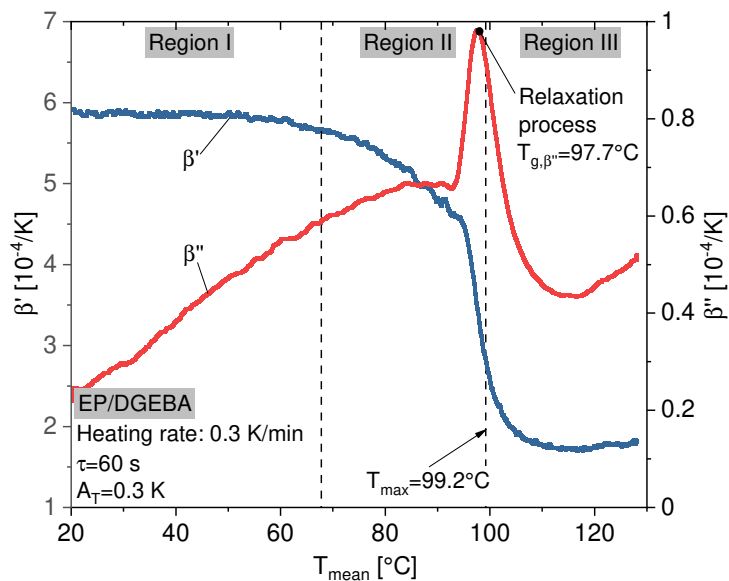


Figure 5.37: Thermal expansion and damping over temperature induced curing of the unmodified reference system (DGEBA cured by anhydride)

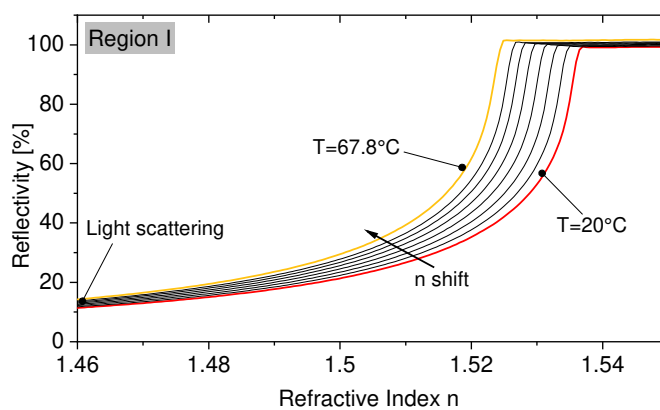


Figure 5.38: Selected Fresnel curves from region I showing the successive shift of the Fresnel curves to lower refractive indices of the reactive, yet liquid epoxy system (mass density decreases). The Fresnel curves are smooth and homogenous, indicating a homogeneously mixed sample composition, red: starting temperature, yellow: end temperature

However, here the most basic type of GCM was applied, considering the volumetric concentrations and the temperature dependent refractive indices of the EP/DGEBA system and the neat BCP:

$$n_{0,\text{Model}}(T) = n_{0,\text{EP/DGEBA}}(T) \cdot (1 - v_f) + n_{0,\text{BCP}}(T)v_f \quad (5.31)$$

where v_f is the volumetric concentration of the BCP in the resin system.

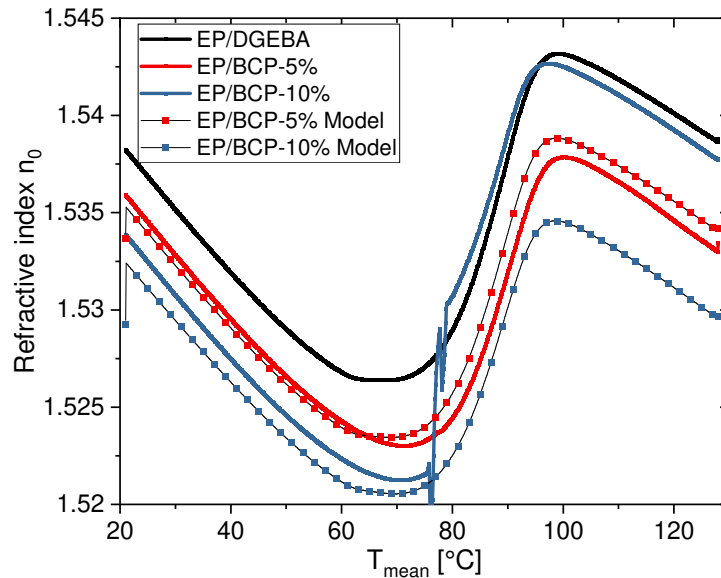


Figure 5.39: Comparison of the refractive index development of the polymerization process of the reference EP system and the influence of a 5 wt.-% and 10 wt.-% BCP modification (bold lines), heating rate: 0.3 K/min. The data sets show a temperature dominated region I, when the refractive index drops, a region II that is dominated by the polymerization process and n_0 increases, once the polymerization process comes to an end, the refractive index drops again. The dashed lines show the development of the refractive index according to the group contribution method.

This model was expected to show at least reasonable data for the initially homogenous, liquid, yet reactive systems (EP/BCP-5% and EP/BCP-10%), when the reaction process does not dominate the development of the refractive index yet. As can be seen, this is true within a certain range for the EP/BCP-5% system up to about 70°C, i.e. the model is able to reflect the refractive index development of a modified epoxy resin using a 5 wt.-% concentration of BCP and suggests that the BCPs are mixed with the reactive resin on a molecular scale. Above $T=70^\circ\text{C}$ the model over-predicts the experimental data for this system and the deviations become larger. Also, the deviations between the model and the experimental data increase when the modifier concentration is raised to 10 wt.-%. This might suggest that the BCPs do indeed phase-separate in a certain way *before* the curing reaction takes place, being reflected by the differences between the experimental and the modelled data. However, such a demixing process was not detected when the DGEBA/BCP masterbatch system was examined. I.e. the system might behave different in the reactive

state. Interestingly, at 75.7°C the refractive index of EP/BCP-10% shows a sharp rise close to the value of the unmodified EP/DGEBA system and remains there. Even though the model cannot quantitatively describe the course behaviour at this temperature stage, it indicates that such a *jump* is quite unexpected.

To further elucidate this peculiarity the simultaneous development of the Fresnel curves EP/BCP-5% and EP/BCP-10% in region II were examined, Fig. 5.40.

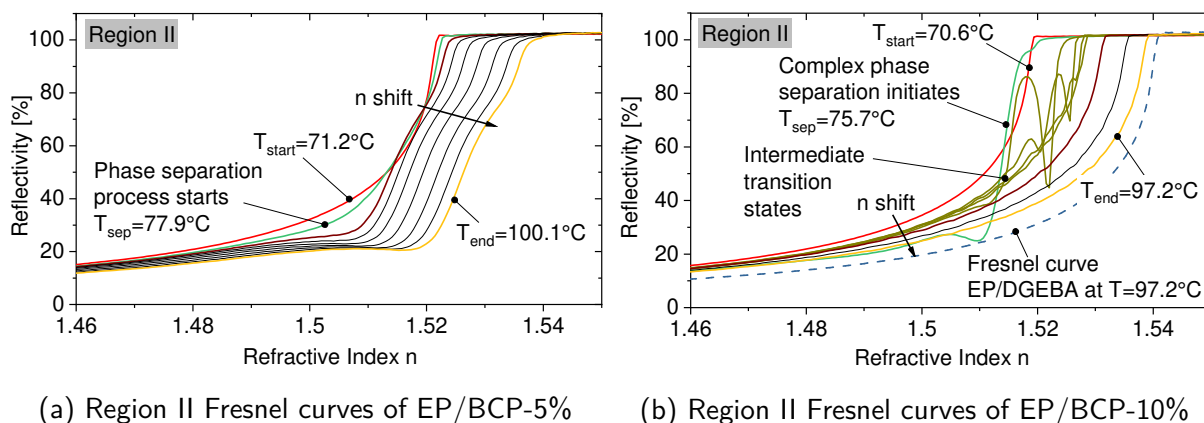


Figure 5.40: Selected Fresnel curves of the modified systems showing the phase-separation behaviour during the heating experiment

Note, the Fresnel curves of the modified systems, especially in region II are only of qualitative character. Since the material is changing its inherent molecular structure (polymerization) and at the same time morphological changes occur, the gathered data are strongly influenced by overlapping events. The same is true for the derived values of β' and β'' .

The polymerisation dominated region, based on the first turning point of the refractive index (Fig. 5.39), starts at 71.2°C (red curve) for EP/BCP-5%, cf. Fig. 5.40a. Suddenly, at 77.9°C the shape of the Fresnel curve changes, which is not only a temperature induced shift of the curve to higher refractive indices, as seen before in the reference EP system (Fig. 5.38), but rather a change of the shape itself (green curve). Further increasing the temperature (equivalent to time in the case of applying a heating rate) the Fresnel curve solidifies (brown curve), having a *two step* appearance, which does not change in shape anymore in the subsequent polymerization process. At 100.1°C the polymerization dominated process-shift to higher refractive indices is completed. Such a behaviour has not been observed for the neat, unmodified system. Hence, the changing shape of the Fresnel curve can at this stage be associated with the phase separation process of the block copolymers in the reactive epoxy system. The *two step* Fresnel curve indicates the formation of morphological inhomogeneities throughout the polymerization process that prevail afterwards.

The development of the Fresnel curves in region II of the highly modified EP/BCP-10% system is shown in Fig. 5.40b. The phase separation process starts at 75.7°C, i.e. in a similar

temperature range than the phase separation in the EP/BCP-5% system. However, the process is much more complex. In about 13 minutes ($\Delta T=4$ K) the Fresnel curves show highly varying shapes (dark yellow), which indicate the formation of complex morphological transition states in the immediate vicinity to the prism surface of the refractometer. Thereby, the system undergoes a demixing process alike EP/BCP-5%, indicated by similar Fresnel curves, cf. the double-step curves in Fig. 5.40a (yellow) and 5.40b (green). These complex processes cannot take place in a homogenous material and show the formation of heterogeneities that have different refractive indices. At the end of the process the Fresnel curve becomes unexpectedly inconspicuous, as known from the reference EP system, and the shape is retained in the glassy state.

Comparing the EP/DGEBA Fresnel curve (blue dashed) to the EP/BCP-10% system at the same temperature, the curves do not overlap, i.e. the mass density of the modified system is lower at the same temperature. Hence, the refraction processes at the sample-prism interface have to be different (cf. also reflectivity values at $n=1.46$). Both features indicate that the phase separation process of EP/BCP-10% has affected the morphology of the formed glass compared to EP/DGEBA.

Examining the real part of the dynamic thermal volume expansion coefficient and the damping behaviour of the three materials, Fig. 5.41, with respect to the observations made so far, it becomes obvious that the phase separation process occurs far below the dynamic glass transition in all systems ($T_{g,\beta''max}^{EP}=97.7^\circ\text{C}$ vs. $T_{\text{Start,phase-sep}}^{EP/BCP-5\%}=77.9^\circ\text{C}$ and $T_{\text{Start,phase-sep}}^{EP/BCP-10\%}=75.7^\circ\text{C}$). Also, the phase separation behaviour of EP/BCP-10% can be found back in β' and β'' ,

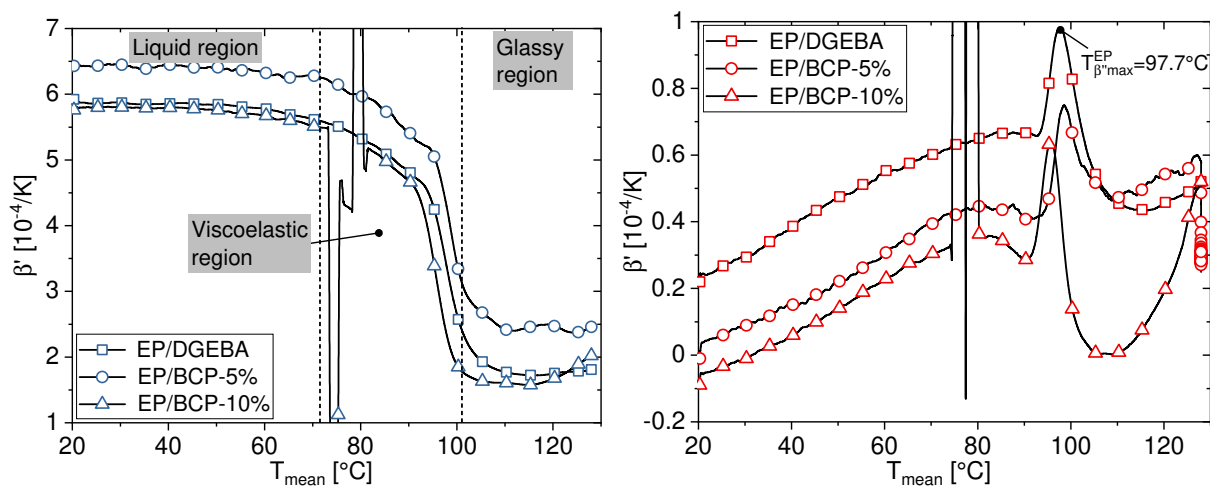


Figure 5.41: Comparison of the dynamic thermal volume coefficient (left) and the damping behaviour (right) of EP/DGEBA and EP/BCP-5% and -10%

when the values suddenly jump. As already observed, when analysing the Fresnel curves, β' of EP/BCP-10% tends generally to be very similar to EP/DGEBA (except for the phase transition behaviour), whereas EP/BCP-5% can be clearly distinguished and lies above the values of EP/DGEBA and EP/BCP-10%. The thermal volume expansion coefficient is usually

quite similar for different epoxy systems in the glassy state. However, the deviation of the EP/BCP-5% system might be related to the distortion of the Fresnel curves. On the other hand, the damping behaviour β'' of all three systems is quite different, especially after passing the glass transition, i.e. the underlying molecular dynamics are quite different of the three systems.

To get a better idea of the processes taking place in the volume of the material, the samples were extracted from the refractometer after the experiments and cryo-fractured. The respective fracture surfaces are shown in Fig. 5.42 and 5.43.

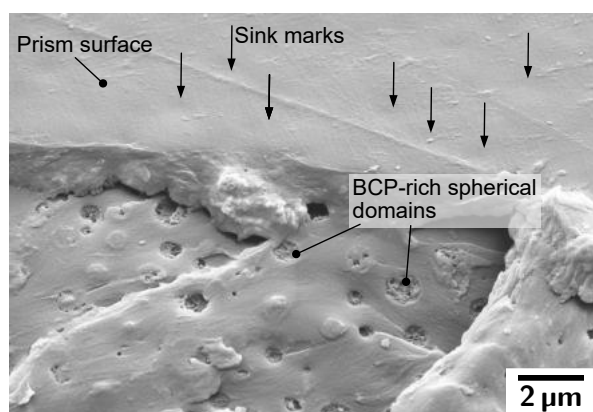
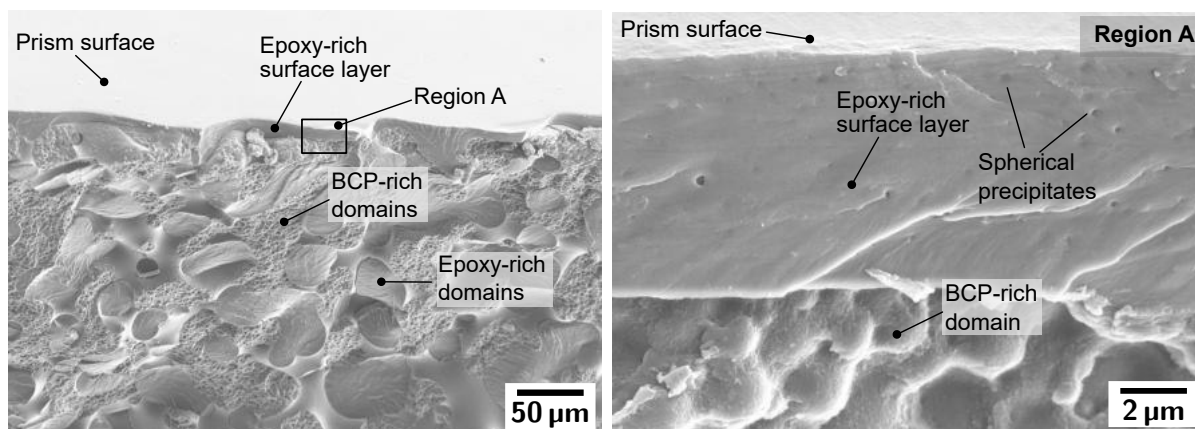


Figure 5.42: Particulate phase domain separation of EP/BCP-5%

In the case of EP/BCP-5% spherical phase segregations are visible, having a size $\leq 1 \mu\text{m}$, which can also be distinguished as sink marks on the sample surface (arrows), i.e. in close proximity to the measuring prism and within the detection depth of the refractometer ($\sim 300 \text{ nm}$). Accordingly, the *distortion* of the Fresnel curves, as seen in Fig 5.40a, is caused by the formation of the segregated phases and is not only a surface but also a volume effect. A totally different



(a) Macroscopic phase domain separation

(b) Sub-microscopic phase domain separation

Figure 5.43: Fracture surfaces of EP/BCP-10% system after polymerization in the refractometer using a constant heating rate of 0.3 K/min

microstructure is present on the fracture surface of the EP/BCP-10% system, Fig. 5.43a and 5.43b. It is comprised of large regions of BCP-rich (BCP dominated, yet interspersed by epoxy network) and EP-rich (single BCP molecules might prevail, yet do not form defined areas) domains. It becomes obvious that the phase separation process is strongly depending on the modifier concentration, even if other parameters, such as mixing viscosity, changed intermolecular polarities etc. might additionally affect the process. Close to the prism surface an epoxy-rich layer has formed that contains sub-micron sized particulate segregations in the range of $\varnothing=260 \pm 63$ nm. At this point it is worth mentioning that obviously extreme demixing processes take place during the curing reaction of the system to create such morphologies from a previously visually homogeneous mixed system of epoxy and block copolymers.

Fig. 5.43b shows the epoxy-rich layer, which is still modified with sub-micron sized precipitates. Considering the Fresnel curves, and the noticeable similarity to the neat system (Fig. 5.40b), the micrographs suggest that the demixing process of EP/BCP-10-% caused a dual structural morphology in the volume, but created an epoxy-rich domain in the close proximity to the measuring prism. With regard to the temperature dependent development of n of the EP/BCP-10% system (Fig. 5.39), it becomes less surprising that the measured refractive indices nearly overlap with EP/DGEBA after the phase separation process has taken place, i.e. after the *jump*. The formation of an epoxy-rich layer in the close-vicinity to the prism changes the refractive index of the EP/BCP-10% system to the value of the neat EP/DGEBA. However, *EP-rich* also means that single or more BCP macromolecules remained in the domain close to the prism and distorted the respective Fresnel-curve compared to EP/DGEBA. The separated phases are in the range of ≤ 200 nm, hence below the actual detection range of TMOR. Nevertheless, such precipitates cause additional reflections within the material. The effects can be seen in the increased degree of light scattering at lower refractive indices of the Fresnel curve plot, cf. Fig. 5.40b, EP/DGEBA and EP/BCP-10% at $T=97.2^\circ\text{C}$, $n=1.46$.

This shows that the refractive index is, even though indirectly, sensitive to volume changes of the whole governing sample caused by species having dimensions below the actual detection range of the measuring device.

One more result of the phase separation process investigations is shown in Fig. 5.44. It illustrates the development of the refractive index of EP/BCP-5% (when the phase separation process was initiated, based on the first distortion of the Fresnel curves) as a function of the polymerisation temperature. The measurements were in this case performed isothermally. As shown, the refractive index is linearly related to the polymerization temperature (black dots). However, if the data are normalized, in this case to the refractive index at 40°C , to eliminate temperature effects on n , the slope becomes zero. This shows that the phase separation process is actually independent of the curing temperature. Phase separation is always initiated at the same refractive index, which is only a function of the *degree of cure* of the reactive system, since heating rate effects do not apply. The respective BCP

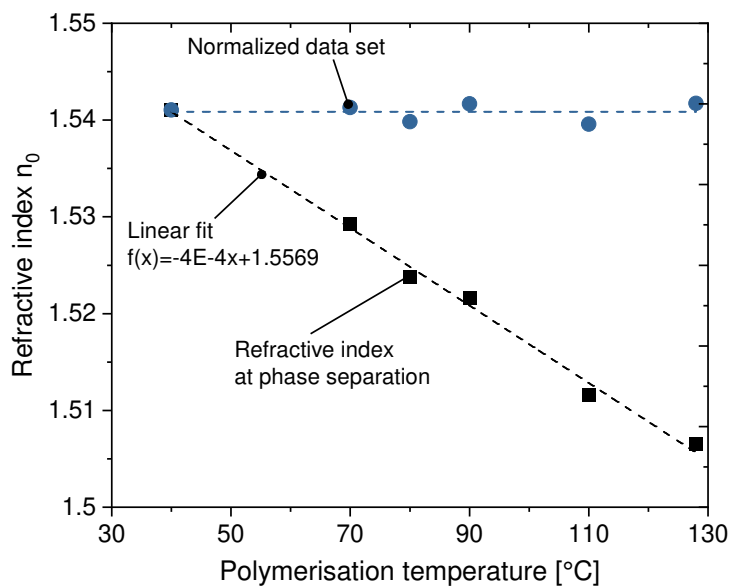


Figure 5.44: Development of the refractive index n_0 of EP/BCP-5%, when phase-separation is initiated (based on Fresnel curve distortion) as a function of the polymerisation temperature (black dots). The data were normalized to $n(T=40^\circ\text{C})$, to exclude temperature induced changes of the mass density (blue dots).

morphologies strongly varied in their size from the nano to the macro range (not shown). This technique and the understanding of such phase separation phenomena provide a trigger for future works to tailor BCP/EP morphologies and respective fracture mechanical properties.

In conclusion, by using *TMOR* it was possible to detect and examine the phase separation process of a BCP modified epoxy system during curing. First attempts to better understand a phase separation process by investigating the underlying Fresnel curves were made and allow a better interpretation of the processes. Thereby, the distortion of the curves (two steps-course) is based on the superposition of different morphologies. It is accordingly affected by different molecular structures in the measuring volume during the phase separation process. Dynamic thermal expansion coefficient β' and damping β'' clearly show the materials' transition from the liquid to the glassy state. The reaction process seems not to be affected by the presence of the block copolymers, since n_0 indicates that the beginning and the end of region II are passed simultaneously by EP/DGEBA and the modified EP systems (Fig. 5.39). Also, β'' reaches its peak value roughly at the same temperature (Fig. 5.41), i.e. at a similar degree of cure. The observations are in accordance with DSC measurements (Fig. 5.45). The specific reaction enthalpy from the freshly mixed state to the fully cured state is nearly the same for both systems ($\Delta H/m \sim 30 \text{ J/g}$). Hence, the BCPs do not or only very little affect the polymerization process.

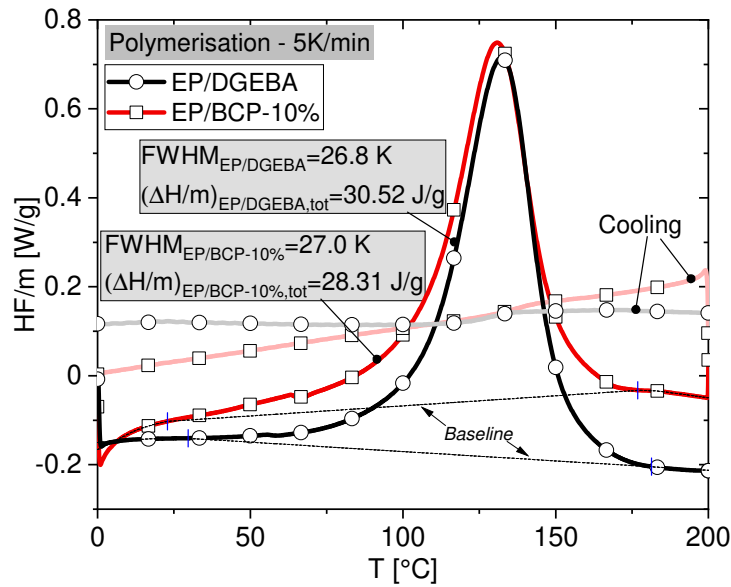


Figure 5.45: Comparison of the specific heat flow during polymerization of EP/DGEBA and EP/BCP-10%

5.2 Block copolymer modified epoxy

5.2.1 Morphologies of block copolymer modified epoxy

Mechanical properties of materials, especially the fracture mechanics performance of epoxies, are, besides the prevailing network structure, dominated by their morphology. Cracks need to overcome detailed features of the morphology by fracture, deformation or by-passing, which requires an increased energy input. In other words the crack is hindered to propagate (cf. Sec. 2.3). As has been shown in the previous section, block copolymers are able to phase-separate in a variety of structures, depending, amongst others, on the curing temperature, the time, and the volumetric concentration (Sec. 5.1).

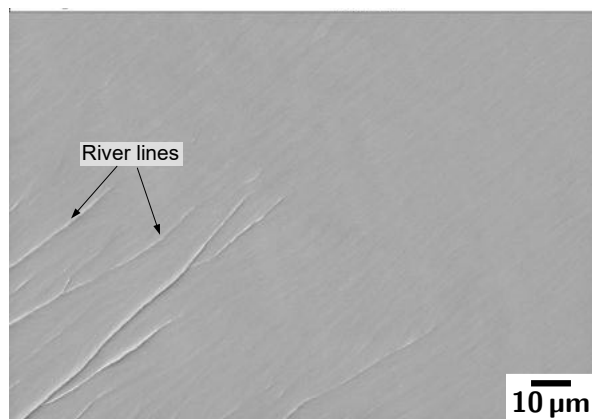


Figure 5.46: Fracture surface of the unmodified EP/DGEBA showing river lines

With respect to the selected manufacturing process, Fig. 5.46 to 5.49 show fracture surfaces of differently BCP modified epoxy systems obtained from compact tension specimens. As a

reference, Fig. 5.46 depicts a fracture surface of the neat, unmodified EP/DGEBA system; only river lines, caused by fracturing of the specimen on slightly different height levels are visible.

Introducing 0.5 wt.-% BCPs into the epoxy system causes the formation of submicron sized precipitates (Fig. 5.47a) that continuously increase in size and number when the modifier concentration is raised to 5 wt.-%, Fig. 5.47b and Table 5.7.

Assuming a previously homogeneously mixed EP/BCP system, it is interesting to see that the molecular structures obviously diffuse throughout the system by several microns and form quite large precipitates, only driven by thermodynamic forces. Once the modifier concentration exceeds 5 wt.-%, the previously particulate segregations form BCP-dominated, interconnected regions, Fig. 5.48 and 5.49.

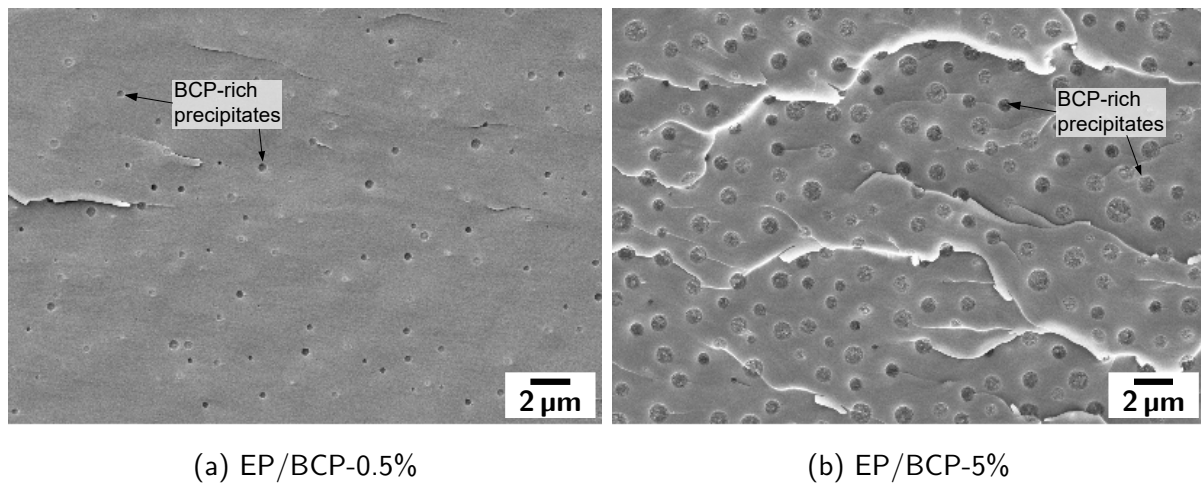


Figure 5.47: Fracture surfaces of EP/BCP-0.5% and 5%, showing the varying morphology depending on the block copolymer concentration, EP/BCP-1% and -2% have been omitted.

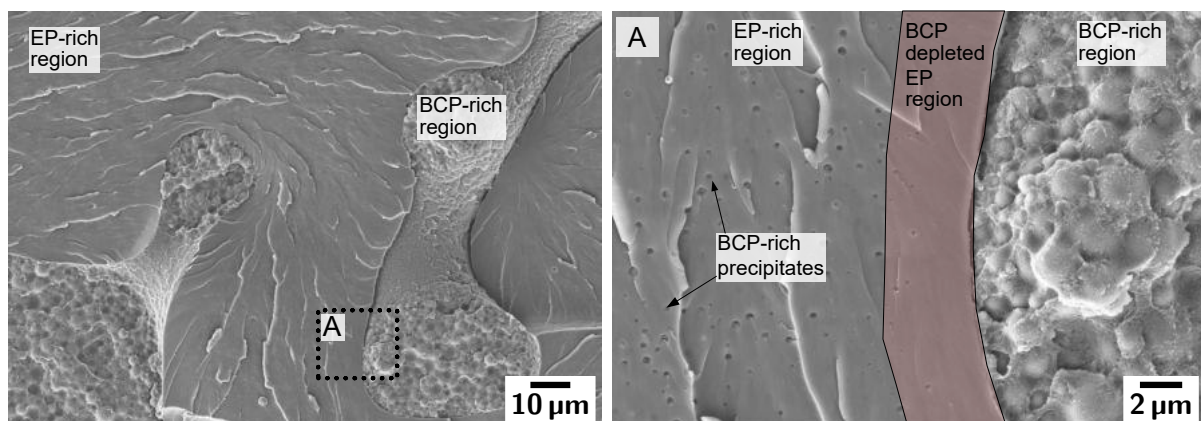


Figure 5.48: Fracture surfaces of EP/BCP-7%, dominated by an EP-rich structure

Thereby epoxy-rich domains prevail in EP/BCP-7%. At 10 wt.-%, it seems as if a phase-

inversion occurred, i.e. visually a BCP-rich phase structure has formed. However, this is not the case as will be shown by dynamic mechanical analyses, Sec. 5.2.2. The morphologies of EP/BCP-5% and -10% coincide well with the morphologies formed during the TMOR measurements (Fig. 5.42 and 5.43). Furthermore, high-resolution micrographs show that the EP-rich regions in EP/BCP-7% and -10% contain submicron sized spherical precipitates in the range of 270 nm and 180 nm, respectively. In the close vicinity to the BCP-domains a reduction or depletion of phase segregations is visible, cf. Fig. 5.48, right. Presumably the macromolecular structures diffuse either into the BCP-rich domains or assemble in submicron size precipitates further in the EP-rich domains.

Chen et al. [132] investigated the same block copolymer in an anhydrid cured DGEBA system. A 7 wt.-% modification yielded particle-like precipitates in the epoxy matrix, i.e. totally different structures than in the present work. This illustrates the effect of other extrinsic parameters on phase separation process of the BCPs, such as the curing cycle. Block copolymer

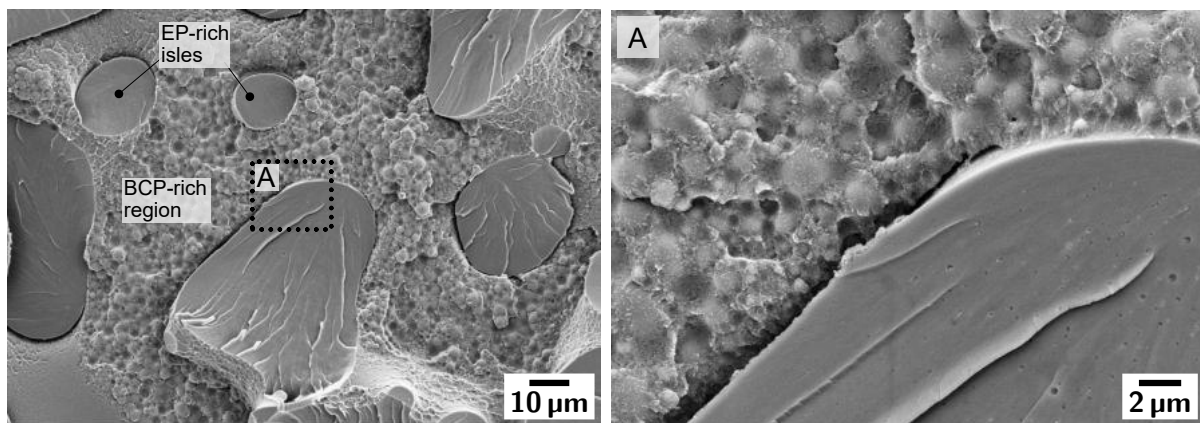
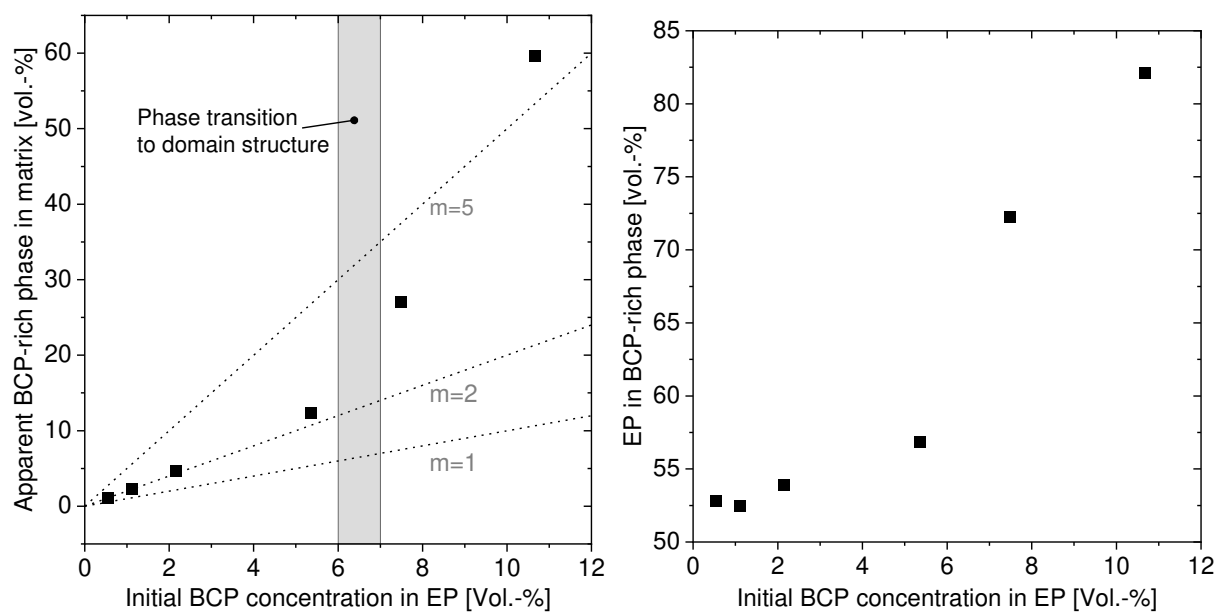


Figure 5.49: Fracture surfaces of EP/BCP-10%, showing a BCP-rich dominated phase morphology, encapsulating epoxy isle-like structures

macromolecules tend to phase separate e.g. in micellar, vesicular or network-like structures in epoxy matrices (cf. Sec. 2.3.2.2). However, it becomes obvious, when the volumetric phase fractions of the different EP/BCP systems are analysed, that the precipitated phases cannot only be made of BCP macromolecules themselves. The initial concentrations are simply too low to justify second phase dimensions in the submicron to micron size range.

To determine the actually occupied volume of the second phase domains, the size of the particulate precipitates (0.5 to 5%) and the dual domain structures (7 and 10 wt.-%) based on SEM micrographs were measured using *imageJ* image analyses software. Fig. 5.50a and Table 5.7 show that the BCP phase in the matrix is double the initial volume concentration of the BCP modification of the epoxy matrix, as long as the precipitates are spherical (up to EP/BCP-5 wt.-%). The fraction of the BCP-dominated morphology increases drastically up to nearly 60 vol.-% at an initial BCP concentration of 10.7 vol.-%. In that regard, Fig. 5.50b shows that about 82 vol.-% of the BCP-rich, interpenetrating network domain has to be comprised of epoxy phase.



(a) Resulting volumetric phase dimensions caused by the initial BCP modification (b) Epoxy volume fraction in BCP-rich domains

Figure 5.50: Effect of initial BCP modification of epoxy and resulting volumetric phase structures (assuming a stochastically uniform distribution throughout the volume)

Table 5.7: Overview of the effects of BCP modification on the shapes of resulting phase separated domain structures

System	Modifier [wt.-%]	Modifier [vol.-%]	BCP-rich phase in matrix [%]	EP fraction in BCP-rich phase [%]	Diameter of 2. phases [μm]	Number of spherical phases per $10 \mu\text{m}^2$
BCP-0.5	0.5	0.5	1.1	52.8	0.25 ± 0.10	2.0
BCP-1	1	1.1	2.3	52.5	0.35 ± 0.12	2.2
BCP-2	2	2.1	4.7	53.9	0.49 ± 0.14	2.3
BCP-5	5	5.4	12.4	56.9	0.68 ± 0.19	3.1
BCP-7	7	7.5	27.0**	72.3**	$*0.27 \pm 0.11$	*4.4
BCP-10	10	10.7	59.6**	82.1**	$*0.18 \pm 0.08$	*6.0

*determined in EP-rich regions

**does not consider the BCP precipitates in the EP domains

Two conclusions can be drawn from these observations: a) the precipitated phases are in no case purely assembled structures of neat block copolymers and the BCP-rich domains become less BCP-rich, the higher the initial BCP concentration, and b) a simple modification of epoxies by a *rubbery phase* is not possible, since complex morphological structures are formed, that represent mixtures of epoxy and block copolymers.

From a morphological-property-relationship point of view, some more questions can be raised (not extensive):

- i) How are the thermal properties, especially the thermal glass transition temperature, affected if a rubbery, second phase structure presumably dominates the morphology (EP/BCP-10%)? Also, BCP monomers might still be dispersed in the epoxy matrix, if the segregation process was not completed before the gelling point of the system was reached. What is the consequence?
- ii) What is the effect of such structures on the (fracture) mechanical performances?
- iii) How do those structures look like in fibre reinforced systems, when carbon fibres, that have similar dimensions, are present in the microstructure?

Answers to question (i) will be given below, question (ii) and (iii) will be addressed in Sec. 5.2.3 and Sec. 5.4.1, respectively.

5.2.2 Thermo-mechanical properties of block copolymer modified epoxy

To examine the viscoelastic behaviour of the different EP/BCP systems, dynamic-mechanical analysis (DMA) was performed. Figure 5.51 and 5.53 summarize the degree of mechanical damping $\tan \delta$ and the storage and loss moduli E' and E'' , respectively (graphical representations of EP/BCP-0.5% and -1% have been omitted). Also, a summary of the data is given in Table A.10.

Generally, the damping behaviour of the EP/BCP systems shows a similar behaviour with two relaxation peaks, Fig. 5.51; a broad one at around $T_{\beta} \sim -70^{\circ}\text{C}$ and a more distinct one at $T_{\alpha} \sim 154^{\circ}\text{C}$. Both peaks are characteristic for a cured epoxy resin and indicate the β -relaxation (weak polymer chain motions) and the α -transition (major chain mobility) of the matrix system, respectively [102].

The neat thermoplastic BCP sample shows as well two distinct $\tan \delta$ -peaks, i.e. relaxation processes take place at $T_{\text{BCP},1} = -24.45^{\circ}\text{C}$ and $T_{\text{BCP},2} = 95.39^{\circ}\text{C}$. The relaxation phenomena occur at very similar temperatures to the characteristic thermal glass transition temperatures of *bulk* PBuA and PMMA ($T_{\text{g,PBuA}} \approx -46^{\circ}\text{C}$ [253] and $T_{\text{g,PMMA}} \approx 105\text{-}160^{\circ}\text{C}$). This behaviour is not necessarily to be expected from a *segmentally* built macromolecule comprised of both types of polymers, i.e. the BCP. The relaxation behaviour of an PMMA-PBuA covalently bonded macromolecule might be strongly influenced by its (different) nearest neighbour

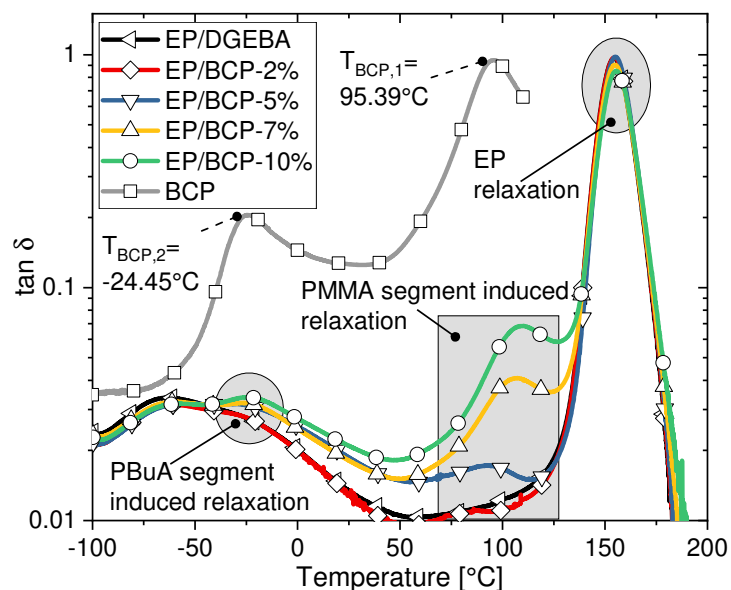


Figure 5.51: Mechanical damping $\tan \delta$ of different BCP modified systems and the neat components: EP/DGEBA and BCP

monomer (PMMA vs. PBuA), as well as its molecular structure in the bulk BCP. However, it seems like as if the bulk BCP is in a partially glassy state at room temperature.

When the EP/DGEBA system is modified with BCPs, respective relaxation peaks appear in the data set and increase in size with increasing concentration. The α -relaxation peak of the epoxy network is not altered by the BCP modification in the investigated range of BCP concentrations. Hence, the block copolymers do not affect the inherent epoxy network structure (i.e. the cross-link density) and, with respect to the measuring accuracy of the applied method, do not affect the dynamic glass transition temperature of the material. Secondly, the peak maxima of the presumably PMMA-segment relaxations shift to higher temperatures with increasing BCP concentrations, away from the peak location of the neat BCP samples. This trend could indicate that the BCPs become interspersed by the epoxy network when the BCP concentration increases. If the epoxy network would have been penetrated by the BCPs, the epoxy- α -relaxation peak should shift towards the BCP-induced PMMA peak, i.e. a reduction of the (matrix governing) dynamic glass transition temperature could be expected. The ability of the BCPs to phase separate as neat species apparently decreases with increasing BCP concentration (cf. Sec. 5.2.1 and Fig. 5.50). On the other hand, the PBuA-segment related relaxation peak becomes more pronounced when more BCPs are dispersed in the system. Additionally, the degree of PBuA assembled-blocks (eventually in the shape of micellar substructures) might increase, since single molecules do not have a glass transition and would accordingly not show such a phenomenon.

In conclusion, the higher the initial BCP concentration in the epoxy is, the higher is the tendency to form *BCP-rich agglomerates* that are increasingly intermingled by the cross-linked

epoxy network. Both features can be seen in Fig. 5.50b, showing the strongly increasing amount of epoxy in the segregated phases and in Fig. 5.49, having a bicontinuous morphology of an EP-rich and a BCP-rich domain structure.

The gathered data so far shows (i) a clear phase-separation between BCPs and EP (SEM), (ii) intermingled yet BCP- and epoxy-rich separated domains, (iii) no effect on the dynamic glass transition temperatures of the epoxy matrices due to the BCP modification (DMA measurements), (iv) no indication of BCP-epoxy phase separation in the uncured state (TMOR and DSC). This allows an interpretation of the assembling process of the BCP domains within the epoxy matrix, as shown in Fig. 5.52.

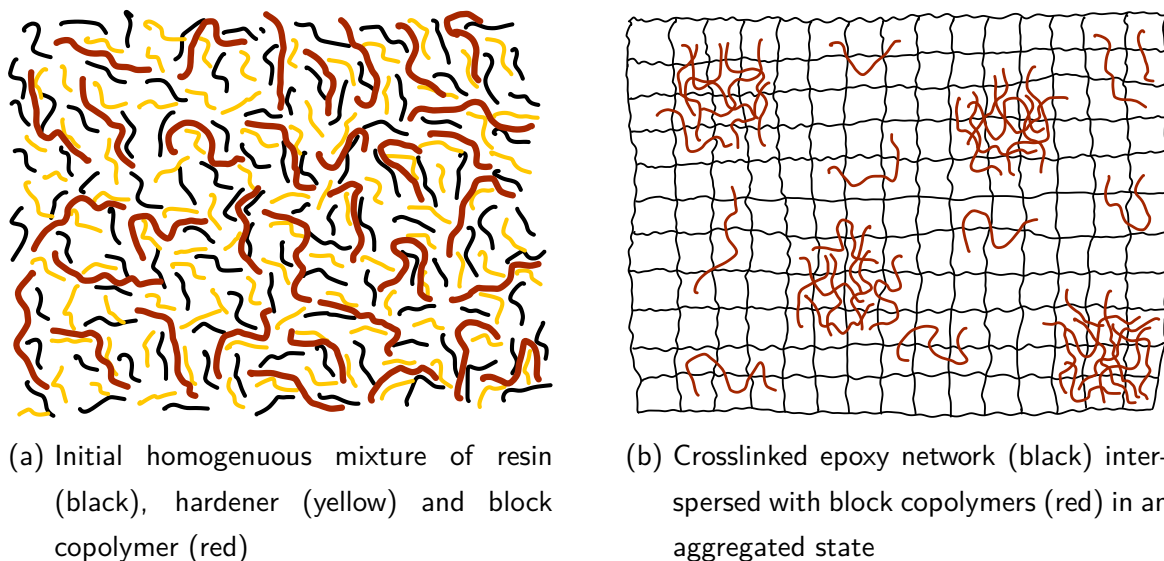


Figure 5.52: a) Homogenous mixture of all constituents (based on the available experimental lengths scales and susceptibilities), b) The polymerization process promotes the accumulation of BCP macromolecules that form in lower concentrated epoxy resin systems types of particulate precipitates, whereas in higher concentrated epoxy resin systems domain structures form (the orientation of the BCP macromolecules to each other and PBuA-segment to PMMA-segment orientation is not clear.)

Analysing the elastic behaviour E' (Fig. 5.53a), the neat BCP sample shows a two-step softening of the block copolymers at around -25°C and 90°C . Above 90°C , the bulk BCP material strongly softens. On the other hand, E' of the EP/BCP modified systems remain at around 20-30 MPa, even at 200°C . This illustrates that even at high BCP concentrations of 10 wt.-% no phase inversion (i.e. the formation of a BCP matrix) occurred and the epoxy phase is still the governing one in all the matrix systems investigated.

Questions that might be raised are a) how an EP/BCP systems' morphology looks like at temperatures above such BCP induced secondary and tertiary relaxation temperatures, b) how it influences interfacial interactions between BCP precipitates and epoxy, and c) which implications it might have on the fracture mechanical performance.

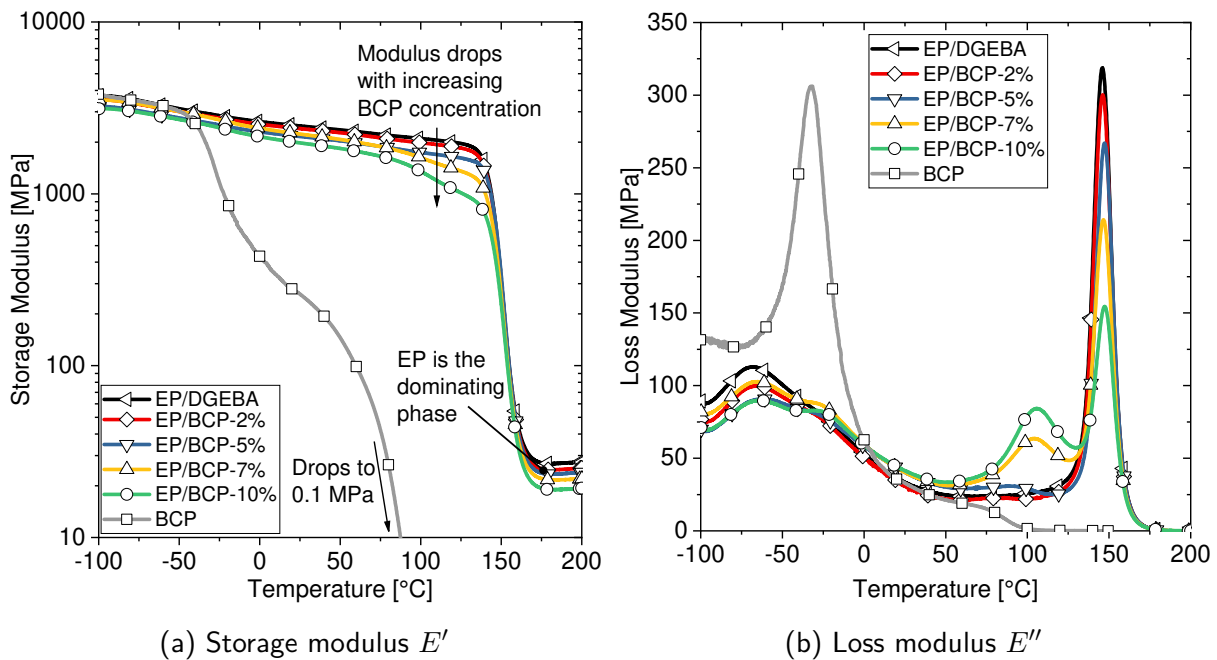


Figure 5.53: Thermo-mechanical analyses of different BCP modified systems

It is noteworthy that the higher the BCP concentration in the epoxy matrix is, the stronger is the reduction of E' . When, the BCP-rich domains are formed, i.e. at 7 and 10 wt.-%, E' is strongly reduced from $E_{EP/DGEBA}^{T=120^{\circ}\text{C}}=1999\text{ MPa}$ to $E_{EP/BCP-10\%}^{T=120^{\circ}\text{C}}=1068\text{ MPa}$. The relaxation of the PMMA-segments becomes obviously more important with regard to the structural integrity of the whole specimen. This is also reflected in the damping behaviour of the materials, Fig. 5.53b. At 10 wt.-%, the loss modulus of the epoxy network is drastically reduced, whereas the PMMA-segments related peak has risen strongly. As has been discussed before, the matrix, including the BCP-rich domains is most likely interdispersed with epoxy network, yet the question remains what effect another increase of the BCP concentration would have on the formed morphology.

Based on the approach presented in Sec. 4.3.3, the cross-link density of the copolymer modified matrices was evaluated in the rubbery region of the storage modulus (E'_{stat}) at 50 K above the dynamic glass transition temperature of the epoxy matrix, Fig. 5.54. Thereby, the average molecular weight between the cross-links M_c of the neat epoxy system coincides well with the data gained by Karger and Friedrich [231]. Furthermore, M_c seems to be a function of the BCP concentration in the epoxy matrix. Considering that the epoxy network structure has obviously not changed in the matrix when modified with BCPs (cf. the DMA measurements in Fig. 5.51), the apparent relationship between M_c and BCP concentration only holds when the volume of the epoxy network is considered along with the volume of the un-linked BCP fractions. I.e. Fig. 5.51 does not reveal a direct correlation to the molecular weight between crosslinks in the EP phase but is rather a function of the stiffness of the toughened systems, which is a value depending on the amount of soft phase in the modified matrices.

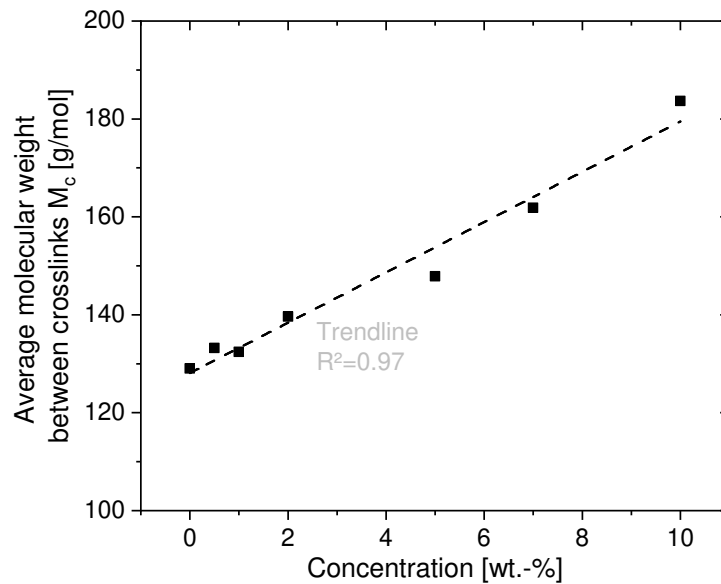


Figure 5.54: Average molecular weight between crosslinks based on the theory of rubber elasticity as a function of BCP concentration in the epoxy matrix

5.2.3 Block copolymers as toughening agents for epoxies

One of the main objectives of the present work is to gain a better understanding of the fracture mechanical performance of BCP modified epoxy and the transferability of this important property to carbon fibre reinforced laminates. Within this section the fracture mechanical properties of different EP/BCP systems are discussed and the underlying mechanisms are assessed and evaluated.

Using compliant modifiers, i.e. materials that have a lower stiffness than the surrounding matrix and that are capable of plastic deformation to modify epoxy based matrices aims at improving the resistance against crack propagation by activating mechanisms that not only make use of being an obstacle to a propagating crack such as rigid modifiers do [146]. Compliant modifiers dissipate energy *by themselves*, via tearing and/or cavitation. Subsequently, they initiate void growth or promote shear yielding of the matrix [17, 254]. Fig. 5.55 illustrates the relationship between the fracture toughness K_{Ic} as well as the energy release rate G_{Ic} to the BCP concentration in the epoxy matrix. Table A.12 summarizes the data for completion.

The neat reference system EP/DGEBA shows a fracture toughness and an energy release rate that are typical of a brittle epoxy system; $K_{Ic}=0.58 \text{ MPa}\sqrt{\text{m}}$ and $G_{Ic}=98.5 \text{ J/m}^2$, respectively. The low fracture toughness is thus caused by the strongly restricted plastic deformation capabilities of the highly cross-linked network structure (cf. the brittle fracture surface of the EP/DGEBA sample in Fig. 5.46).

By modifying the epoxy system with increasing concentrations of block copolymers up to 2 wt.-%, when spherical precipitates still prevail, fracture toughness increases up to $K_{Ic,BCP-2\%}=0.85 \text{ MPa}\sqrt{\text{m}}$, which is nearly a 50% improvement over EP/DGEBA. This il-

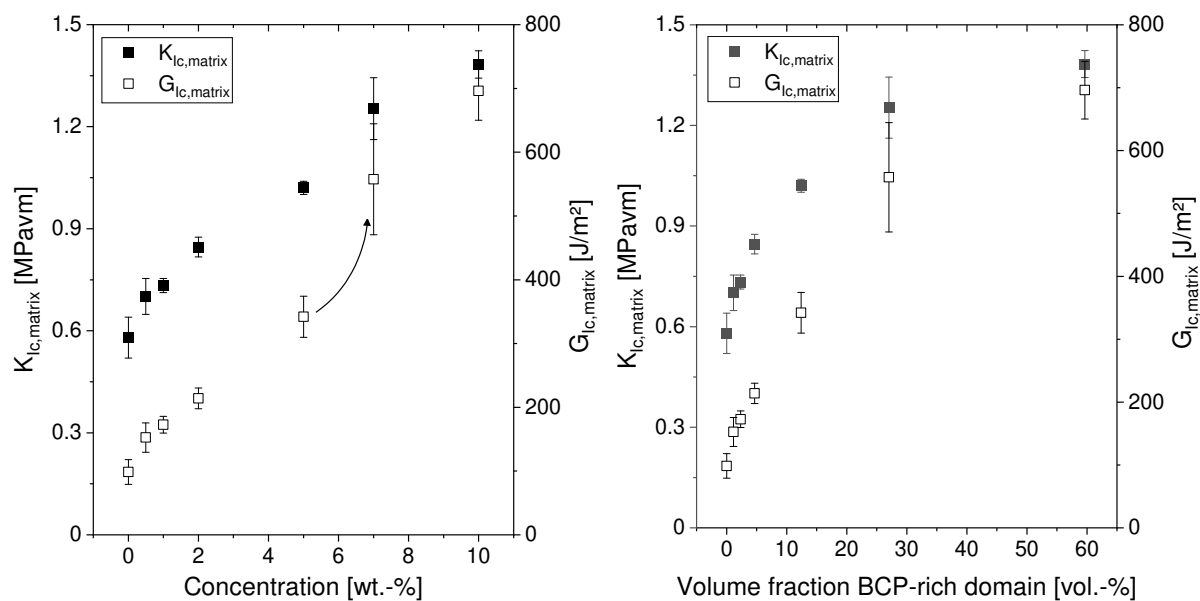


Figure 5.55: Fracture toughness K_{Ic} and energy release rate G_{Ic} of the differently modified EP/BCP systems as a function of (left) the initial BCP concentration in the epoxy matrix and (right) the actual volume fraction of the phase-separated BCP-rich domains, for the determination of the volume fractions cf. Fig. 5.50

illustrates the efficiency of *extrinsic toughening* of epoxies to improve such an important property. By further increasing the modifier concentration to 5 wt.-% K_{Ic} nearly doubles ($K_{Ic,BCP-5\%}=1.02 \text{ MPa}\sqrt{\text{m}}$).

As seen in Sec. 5.2.1 and Table 5.7, the diameter of the precipitated phases increases with increasing modifier concentration, yet the composition of the precipitated phases is not really altered and is constantly a mixture of about 50 % BCP and 50 % epoxy, at least up to the EP/BCP-5% system. The increasing fracture toughness can in this case most likely be ascribed to the increasing total amount of ductile phase within the system, whereas an increasing phase size tends to have a more negative effect on fracture toughness, since the phase dimensions allow less efficient energy dispersive mechanisms to be activated, such as crack deflection or particle bridging.

Fig. 5.56 shows an already discussed even distribution of sub-micron sized spherical inclusions within the EP/BCP-5% system, which, qualitatively judged, well adhere to the surrounding matrix. The figure also illustrates an uneven crack plane, at least on the micro-scale, which is a sign of a certain degree of crack deflection, i.e. energy dissipation due to local mixed mode stresses and crack deviations from the original crack path. Furthermore, the precipitated spheres have plastically deformed, indicating rubber tearing by trans-particle fracture. Sink marks remain after a respective deformation.

Once the BCP-rich domain structure forms, i.e. at 7 and 10 wt.-% an even higher fracture toughness can be obtained ($K_{Ic,BCP-10\%}=1.38 \text{ MPa}\sqrt{\text{m}}$). Interesting to see is the eventually disproportional increase of G_{Ic} in the phase transition zone (Fig. 5.55, left, arrow), i.e. the

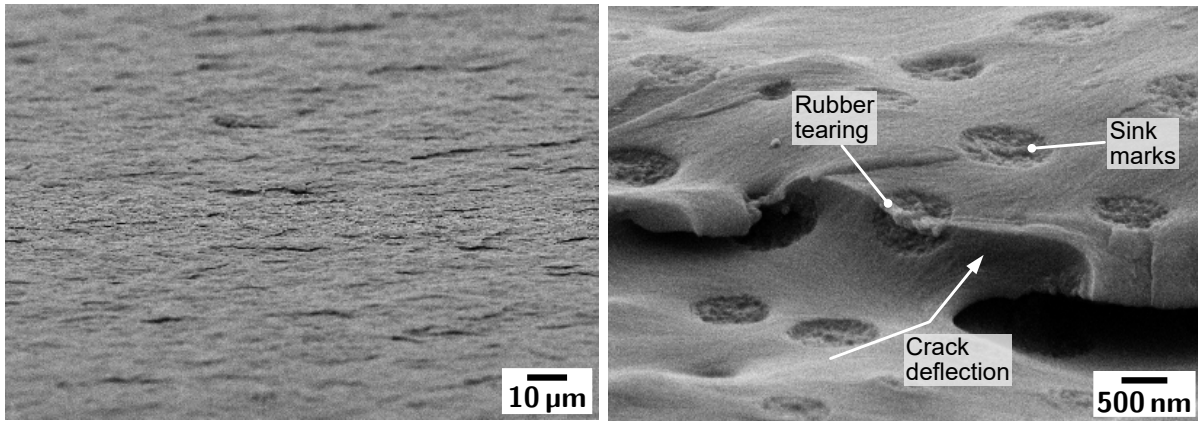


Figure 5.56: 20° perspective of a fracture surface of 5 wt.-% modified BCP/EP system showing precipitated, BCP-rich spheres within an epoxy rich matrix (Macroscopically, crack propagation occurred from left to right)

bi-continuous morphology is quite beneficial in terms of toughening. This becomes clearer when analysing Fig. 5.57 (left). The low magnification image reveals a strongly increased crack deflection mechanism, compared to EP/BCP-5%, Fig. 5.56. The excellent toughness originating from this type of morphology is believed to be a result of the combination of the macroscopical, alternating EP-BCP phase structure and the BCP-rich precipitates of nano- and submicron size in the EP-rich domains (Fig. 5.57, right). The latter dissipate energy by crack pinning and cavitation and eventually subsequent void growth.

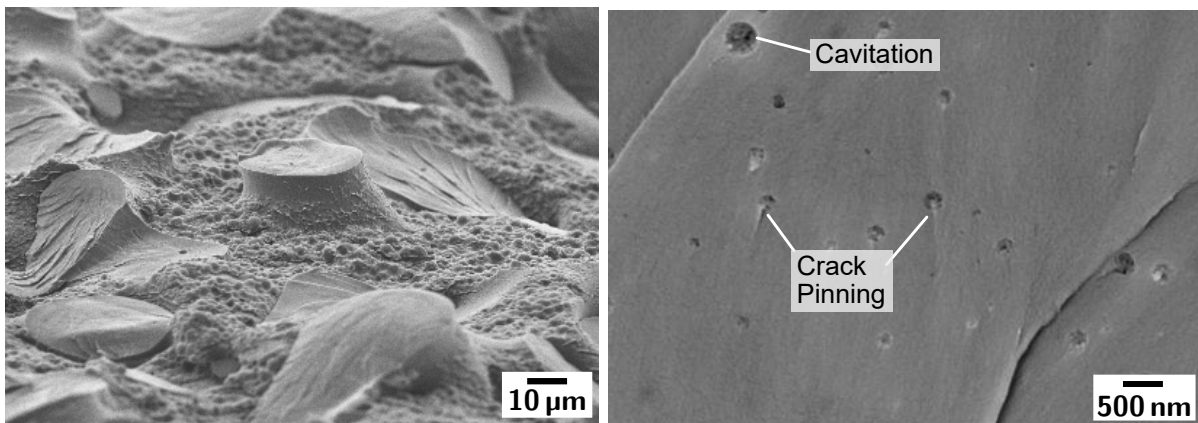


Figure 5.57: Fracture surfaces of EP/BCP-10%, left: 20° perspective, showing an interpenetration of epoxy-rich and BCP-rich phase (Macroscopically, crack propagation occurred from left to right), right: EP-rich region within bicontinuous structure

To further illustrate the role of the domain sizes on the fracture toughness, K_{Ic} and G_{Ic} are plotted as a function of the volume fraction the BCP-domains actually occupy, Fig. 5.55, right. Based on this visual representation, the transition of K_{Ic} and G_{Ic} , when the precipitates undergo a transition from spherical phases to domain structures, is much smoother. It strengthens the assumption that the fracture mechanical parameters are much more related to the volume fractions of the BCP-rich domains. It is unclear how this seemingly asymptotic

behaviour of K_{Ic} and G_{Ic} in the present case continues at higher BCP concentrations. If the BCP-rich domain size simply further increases without affecting the underlying epoxy network, the asymptotic fracture behaviour could prevail, since the maximum toughenability of the epoxy matrix has been reached [138, 200]. Yet, if the BCP modification yields a phase-inversion, i.e. the BCP domain structure becomes the dominating matrix, fracture toughness could e.g. jump to the value of the BCP.

Inherent to the critical fracture toughness K_{Ic} is the size of the plastic zone (Eq. 4.24), i.e. a region in which very locally plastic deformation events can occur. Hence, via the correlation between the K- and G-approach (Eq. 4.22), one can establish a relation of the plastic zone size r_p to:

$$G_{Ic} = 6\pi\sigma_{ys}^2 \cdot \frac{r_p}{E} = m \cdot r_p \quad (5.32)$$

where r_p is the plastic zone size, σ_{ys} is the yield stress of the material and E is Young's modulus of the matrix system. Accordingly, a critical energy release rate is a product of stiffness, yield stress and an intrinsic length.

Fig. 5.58 illustrates the relationship between r_p to K_{Ic} and G_{Ic} ; the plastic zone size increases with increasing filler concentration. With more and more BCP added, the precipitates lead to a

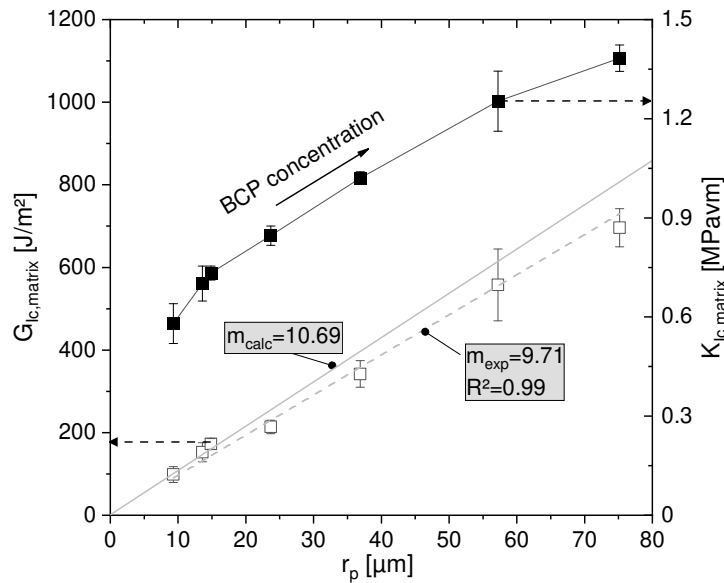


Figure 5.58: Fracture toughness and energy release rate as function of the plastic zone size r_p

larger number of deformation events allowing higher stress intensities in the stressed volume at the crack tip. Such energy dissipative events are the previously discussed mechanisms. Furthermore, the slope m that is calculated based on the relationship given in Eq. 5.32 shows a very good agreement to the experimentally obtained data ($m_{exp}=9.7$ vs. $m_{calc}=10.7$, uncertainties in the total data chain of $> 10\text{-}20\%$ might occur due to deviations of the K_{Ic} measurement, which was used to derive r_p). It also emphasizes that the origin of toughening comes from the intrinsic length associated with the plastic zone size, and related fracture mechanisms.

5.3 Block copolymer and core-shell rubber particle hybrid modification of epoxy

A second toughening approach within this study focussed on a block copolymer and core-shell rubber hybrid modification of an anhydride cured epoxy resin (EP/BCP/CSR). The original aim was to supplement the investigations on the EP/BCP systems, since stiffness of BCP modified matrices is strongly reduced, as will be shown in (Sec. 5.3.2. Preliminary studies on the modification of an anhydride cured, high strength epoxy system with BCP/CSR hybrids indicated a quite successful pathway of toughening epoxy with only minor reductions of the stiffnesses of the matrix systems [174].

However, within this study the selected CSR nano particles were predispersed in a cycloaliphatic masterbatch, which required an adaption of the resin system from a DGEBA based epoxy to a CAE based epoxy system (cf. Sec. 4.1). Investigations of respective DGEBA/CAE mixtures were performed as well, since it is a common pathway in industry to dilute the highly-viscous DGEBA resin by low-viscous CAE [107], yet neglecting the fact that the cross-linking reaction will change. These examinations were not part of the present work to avoid further influencing parameters on the phase separation phenomenon of BCPs [25]. This means, the systems considered within this chapter were based only on a cycloaliphatic epoxy resin that has a higher cross-link density than the DGEBA based epoxy (cf. Tab. 2.3). But the higher the cross-link density is, the more difficult it is to improve fracture toughness properties, as shown by [138].

The aim of the following chapter is:

- i) to investigate the interaction of block copolymers and core-shell rubber nano particles with respect to the (thermo-)mechanical properties and the fracture mechanical performance of the epoxy matrix as well as the underlying morphology.
- ii) to obtain a highly modified epoxy system (~ 28 wt.-%) to investigate the effects of very high *particle* concentrations on the fracture performance of the epoxy matrix and the respective CFRE.
- iii) to examine potential synergistic interactions of molecular species (BCP) and nano moieties (CSR) in modified epoxies and CFREs thereof.

Thereby, three systems will be in focus, i.e. the neat CAE based epoxy system EP/CAE, EP/CSR-16%, containing 16 wt.-% of core-shell rubber nano particles (the maximum amount that was able to realize considering the unaltered hardener, the accelerator and the stoichiometric mixing ratio) and EP/CSR/BCP-16/12, containing a total modifier concentration of nearly 28 wt.-%. Cf. Sec. 4.1 for more detailed information on the chemical background and the mixing ratios.

5.3.1 Thermal and thermo-mechanical properties of neat DGEBA based epoxy, CAE and block copolymer and core-shell rubber modified CAE

In a first analytical step, the thermal and thermo-mechanical properties of the EP/CAE systems were investigated. Fig. 5.59 shows a non-isothermal DSC scan of the polymerization processes, i.e. the transition from the liquid to the glassy state of the anhydride cured CAE in comparison to the DGEBA based epoxy. In the anhydride cured cycloaliphatic resin a double peak phenomenon can be observed (green); a first peak at around 140 °C and a second peak at around 210 °C. The first peak can be assigned to the reaction initiated by the catalyst $\Delta H/m_{EP/CAE-1}=32.4 \text{ J/g}$, the second peak is caused by the uncatalyzed reaction between the anhydride moieties and the CAE monomers ($\Delta H/m_{EP/CAE-2}=2.0 \text{ J/g}$) [112]. The polymerization process of the DGEBA system does not show such a second peak, since

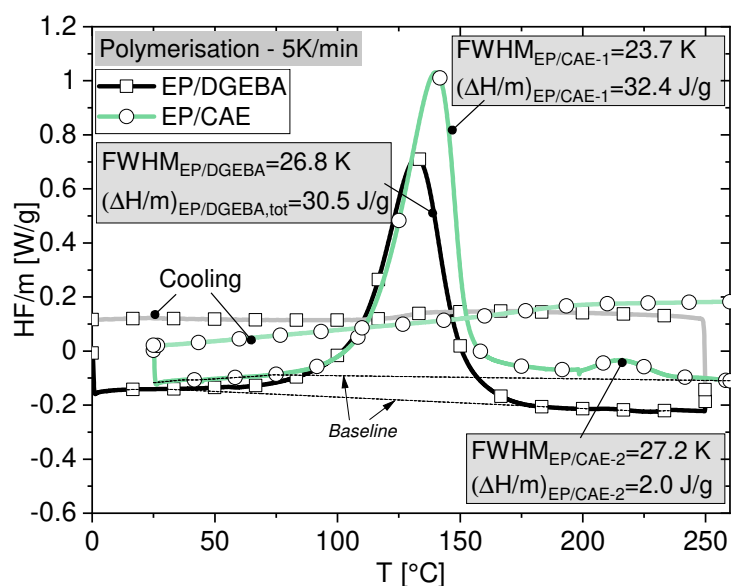


Figure 5.59: Comparison of the specific heat flow during polymerization of EP/DGEBA and EP/CAE

the reaction between the anhydride hardener and the DGEBA molecules takes completely place at lower temperatures. Comparing the total specific reaction enthalpy of the two systems ($\Delta H/m_{EP/CAE-1+EP/CAE-2}=34.4 \text{ J/g}$ and $\Delta H/m_{EP/DGEBA,tot}=30.5 \text{ J/g}$), one can see that more energy is required to cure the EP/CAE system, i.e. more cross-linking reactions occur. This is caused by the lower molecular weight of the CAE and a stoichiometrically adapted amount of anhydride curing agent. Hence, the absolute number of reactive species is higher (more linking reaction sites).

Analysing the peak reactivity as well as full width at half maximum (FWHM) of the main reaction peaks, it becomes obvious that the cross-linking reaction of EP/CAE is more exothermic (higher peak value) and the main reaction occurs in a smaller temperature range ($\text{FWHM}_{EP/CAE-1}=23.7 \text{ K}$ and $\text{FWHM}_{EP/DGEBA}=26.8 \text{ K}$). Since the reactive species have less time to arrange themselves and to reach a state of equilibrium, residual stresses are usually

higher in such highly exothermic epoxy systems (Note: cross-linking reactions can never reach a full state of equilibrium).

However, the selected mixing ratio of resin, hardener and accelerator of the EP/CAE system causes the small exothermic peak at around 210 °C (peak: EP/CAE-2). In the present case, an adaptation of the accelerator concentration would have been beneficial, to allow a catalyzed curing of all resin and hardener moieties at lower temperatures.

The thermo-mechanical behaviour of the cured EP/CAE based matrices, i.e. the degree of mechanical damping $\tan \delta$, and the storage and loss moduli, E' and E'' , respectively, were assessed via DMA, Figure 5.60 and 5.61. A summary of the data is given in Table A.10. Firstly,

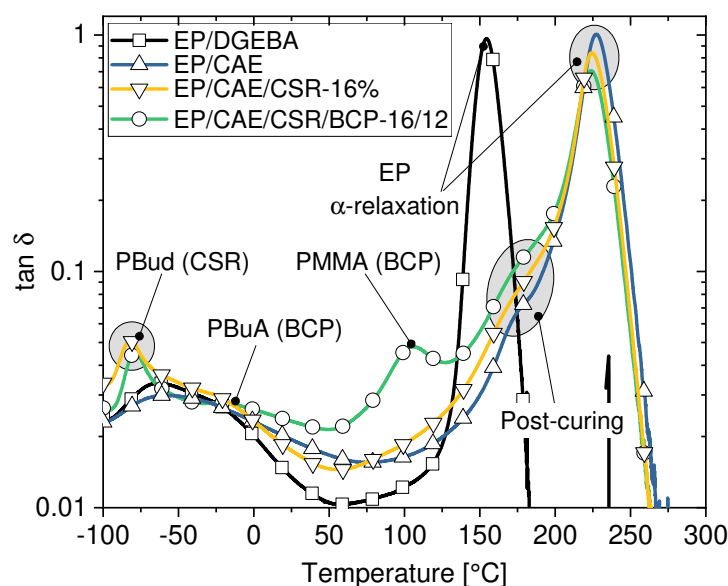


Figure 5.60: Mechanical damping behaviour $\tan \delta$ of the reference matrix systems and the CSR and CSR/BCP modified CAE, measured via DMA. The test frequency was 10 Hz and the heating rate 2 K/min.

comparing the mechanical damping behaviour $\tan \delta$ of EP/CAE and EP/DGEBA to each other, the α -relaxation phenomenon has shifted from $T_{g,EP/DGEBA}=154.5^\circ\text{C}$ to $T_{g,EP/CAE}=227.5^\circ\text{C}$, which is a result of the changed, underlying chemical reactions and subsequent higher cross-link density of EP/CAE.

Based on the rubber theory approach, i.e. deriving the cross-link density from the stiffness of a matrix in the visco-elastic region (cf. Sec. 4.3.3), n_c of EP/CAE is about $n_c=2.94 \cdot 10^{21}/\text{cm}^3$. Modifying the CAE matrix with BCP and CSR the cross-link density becomes seemingly reduced ($n_{c,EP/CAE/CSR/BCP-16/12}=1.74 \cdot 10^{21}/\text{cm}^3$, cf. Table A.10). The phenomenon is a similar one as seen from the EP/BCP system and is an effect of the respective modifier concentration. It is not an effect of the cross-link density of the epoxy matrix.

The course of $\tan \delta$ shows a quite distinct shoulder in the range from 150 to 200 °C, which is most-likely a post-curing effect of previously not reacted resin and hardener species, as discussed above. Especially E'' illustrates the reaction induced losses in this temperature

range (cf. Fig. 5.61b). The phenomenon is present in all CAE based systems and needs to be kept in mind when fracture mechanical properties of those systems are assessed. The post-curing phenomenon and some of its effects are discussed in more detail in the Appendix A.2.

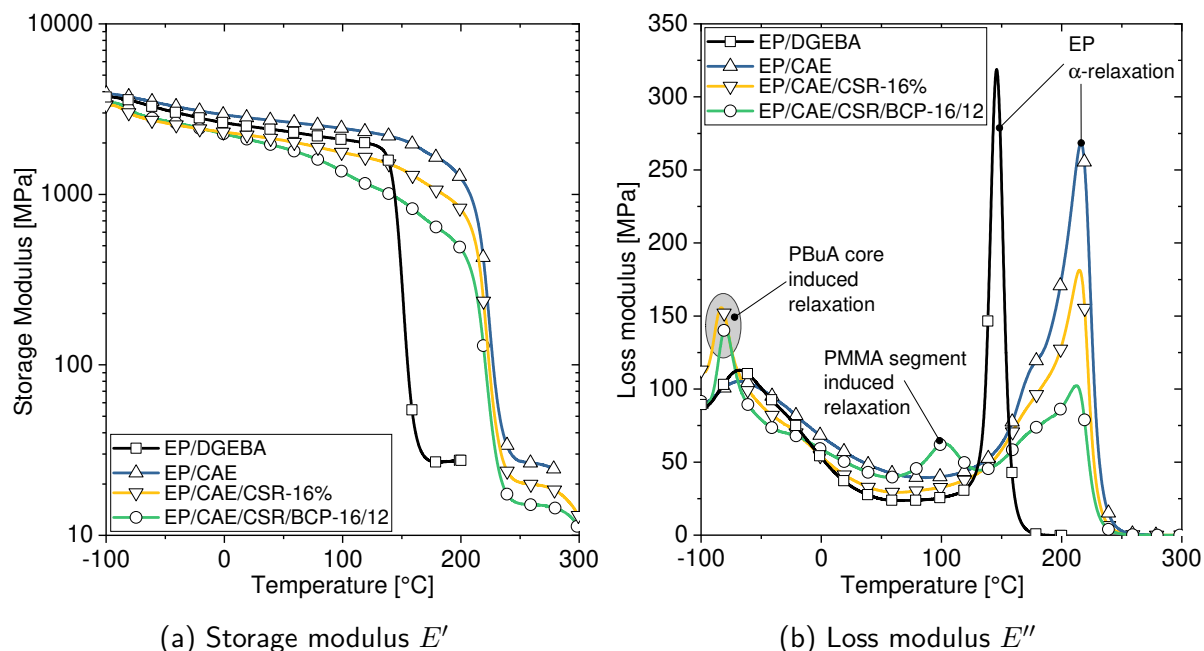


Figure 5.61: Dynamic-mechanical analyses of the reference matrix systems and the CSR and CSR/BCP modified CAE over a temperature range from -100°C to 300°C ; the EP/DGEBA system reaches its thermal glass transition at about 150°C (based on E'), whereas the denser cross-linked EP/CAE transits from a glassy to a rubbery state at around 210°C . The CSR and BCP/CSR modifications do not affect the glass transition temperature of the epoxy matrix, yet show different relaxation phenomena caused by the modifiers.

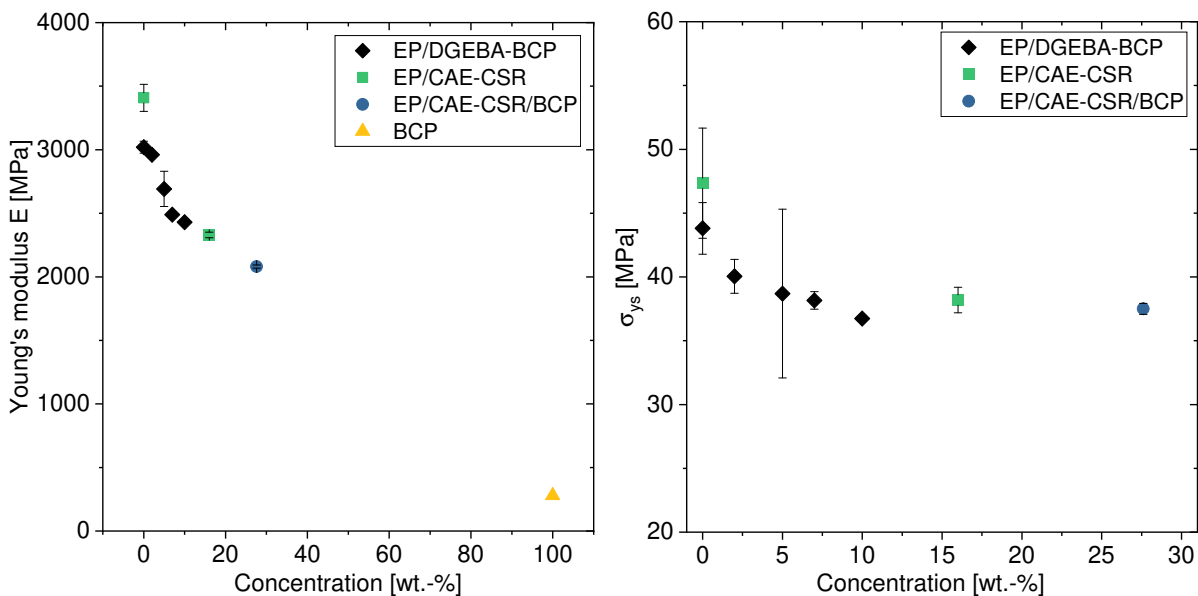
Furthermore, the α -relaxation of EP/CAE/CSR-16% shows a representative relaxation peak of the Polybutadiene-core-component at around -82°C , which also appears in the EP/CAE/CSR/BCP-16/12 system, where it has slightly shifted to higher temperatures. This system also shows a quite prominent peak at 106.1°C that can be assigned to PMMA segment relaxations of the BCPs in the matrix. The acrylate based shell-structure ($T_g \sim 100^{\circ}\text{C}$) of the CSR modifier is not apparent in the data set. Presumably, the shell concentration is either too low, or has, as a molecularly thin layer (only several nm thickness), not the possibility to cause large scale relaxations.

As discussed in Sec. 5.2.2, the shift of the PMMA segment related peak of the EP/BCP systems to higher temperatures with increasing block copolymer concentration indicates that the BCP phase separation process was increasingly suppressed. The BCPs became rather penetrated by EP species. Transferring those findings to EP/CAE/BCP/CSR-16/12, having the PMMA- α -relaxation peak shifted to *lower* temperatures (compared to $T_{g,\text{PMMA}}=110.12^{\circ}\text{C}$ of

EP/BCP-10% in Fig.5.51), one could assume that the compatibility of the BCPs to the epoxy resin decreased in the case of the hybrid modification, i.e. the BCPs are less interspersed with epoxy network. However, the morphology of EP/CAE/CSR/BCP-16/12 will be discussed in more detail in Sec. 5.3.3.

5.3.2 Tensile properties of block copolymer and core shell rubber particle modified epoxy

The tensile properties of EP/DGEBA and EP/CAE were examined to establish a correlation between the fracture mechanical K- and G-approaches via Young's modulus (cf. Eq. 4.22). Figure 5.62a shows Young's modulus of the BCP modified matrices (EP/BCP) and the CSR and BCP/CSR modified EP/CAE systems as well as of the neat BCP sample. The latter one was obtained from DMA measurements (E').



(a) Young's modulus as a function of initial modifier concentration, the higher the absolute modifier concentration the lower Young's modulus
 (b) Yield stress as a function of initial modifier concentration; yield stress decreases with increasing modifier concentration up to 10 wt.-%, then the yield strength levels off

Figure 5.62: Tensile properties of modified EP/DGEBA and EP/CAE systems

Due to the denser molecular arrangement of the neat EP/CAE system, i.e. the higher cross-link density than the EP/DGEBA system, Young's modulus at room temperature of EP/CAE ($E_{EP/CAE} = 3409$ MPa) is higher than E of the unmodified EP/DGEBA matrix ($E_{EP/DGEBA} = 3020$ MPa). However, with increasing modifier concentration Young's modulus drops (cf. also Tab. A.11). Thereby, the development of E seems again to be a function of the modifier concentration rather than the cross-link density of the epoxy matrices. Unknown is the effect of even higher BCP concentrations on Young's modulus. A variety of researchers have reported the formation of phase inverted structures at BCP concentrations $>10\%$,

i.e. the initial epoxy matrix is not the governing constituent anymore and a BCP-rich, eventually interpenetrated morphology prevails, which then strongly reduces Young's modulus. Such a morphology has not been formed in the matrices in the present work.

The stiffness of the neat BCP sample (the morphology of this sample is unknown), obtained from DMA measurements ($f=10$ Hz, heating rate= 2 K/min, $T=21^\circ$), fits well in a projected drop of Young's modulus and sets the lower threshold of Young's modulus to $E_{\text{BCP}}=278$ MPa. The decreasing trend of Young's modulus of a toughened epoxy matrix is well-known and a variety of empirical relationships exist to reflect the effects of pores and/or dense second phases on brittle matrix systems [255]. All these approaches are based on a *best-fit strategy*, therefore an application is omitted, in this case.

However, to understand this behaviour one must be aware of the origin of elastic moduli. It is dictated by bonding energies of cross-linked species. If non-covalently bonded species, or at least weakly bonded species, e.g via Van-der Waals forces, are introduced into a liquid system, the cross-link density of the forming, glassy epoxy is macroscopically reduced (as seen in the average molecular weight obtained by dynamic-mechanical analyses in the frequency-independent region of E_{stat} , cf. Fig. 5.54). Thus, Young's modulus decreases. Vice versa, one can derive from the reduction of E that the block copolymers do either not covalently bond to the remaining matrix or, due to their large molecular weights and potentially kneaded-state, they do at least not provide any additional strength to it. Based on the considerations taken so far, with respect to the assembled BCP structures (cf. Fig. 5.52), a non-covalently bonded presence of the BCPs is most likely. Also, E is obviously not dominated by the morphological structure of the EP/BCP systems, since there is no anomaly when the BCPs phase separate into domain structures at a modifier concentration between 5 to 7 wt.-%. It is rather a function of the absolute modifier concentration. A similar behaviour was observed for an amine cured epoxy, although a different block copolymer was used [131]. Hence, the stiffness of the EP/BCP systems is dominated by the BCP concentration in the system, but less sensitive to the developed morphology. On the other hand, when a bicontinuous BCP-epoxy morphology has formed, i.e. epoxy-rich and BCP-rich domains are intermingled, strength and strain are strongly reduced, most likely caused by a weak interphase strength.

Another parameter, the yield stress σ_{ys} , i.e. the stress at which the tensile behaviour of a material leaves a linear-elastic course, drops sharply in a BCP modifier range from 0 to 5 wt.-% (Fig. 5.62b), yet remains on a similar level at higher modifier concentrations, neglecting again the type of modification. Indeed, it seems as long as the epoxy matrix is the domination phase the macroscopic tensile behaviour is dominated by the amount of soft modifier concentration. However, the yield strength is directly related to the stress intensity factor K_{Ic} via Irwin's plastic zone size equation (cf. Eq. 4.24).

$$K_{\text{Ic}} \propto \sqrt{r_p} \sigma_{\text{ys}} \quad (5.33)$$

Accordingly, one could expect to decrease the resistance to crack propagation of the epoxy matrix, if σ_{ys} decreases. Considering the 7-fold enhancement of the plastic zone size r_p of EP/BCP-10% over EP/DGEBA (cf. Fig. 5.58), a reduction of the yield stress from $\sigma_{ys,EP/DGEBA}=43.8\text{ MPa}$ to $\sigma_{ys,EP/BCP-10\%}=36.7\text{ MPa}$ does not significantly affect the fracture mechanical performance of the toughened systems. However, the reduction of σ_{ys} is an undesirable side effect of the modification of an epoxy matrix by a soft, second phase.

5.3.3 Block copolymer and core shell rubber particles as toughening agents of epoxy

Having seen the effect of block copolymers on the fracture mechanical performance of a DGEBA-based matrix in Section 5.2.3, the purpose of the present chapter is to discuss and compare the fracture toughness enhancement of the CSR and CSR/BCP toughened CAE matrix.

Figure 5.63 shows a plot of the stress intensity factor K_{Ic} and the energy release rate G_{Ic} , based on the calculation via Young's modulus (cf. Sec. 5.3.2). The numerical data are summarized in Tab. A.12. The fracture toughness of the neat EP/CAE system is found

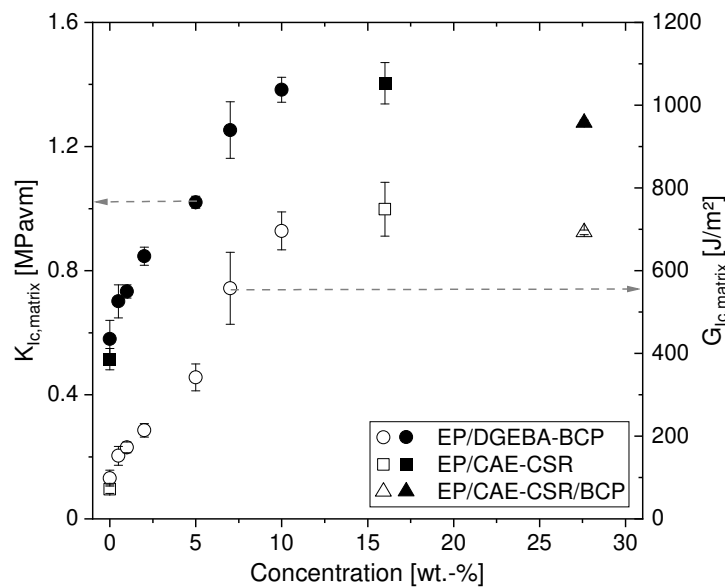


Figure 5.63: Stress intensity factor K_{Ic} and the energy release rate G_{Ic} of the CSR and BCP/CSR toughened EP/CAE system in comparison to the BCP toughened EP/DGEBA system.

to be about 12% below the value of EP/DGEBA ($K_{Ic}=0.58\text{ MPa}\sqrt{\text{m}}$), illustrating the embrittlement caused by the higher cross-link density of EP/CAE. Fig. 5.64 shows the nearly featureless fracture surface of the respective neat matrix. Introducing CSR nanoparticles into the epoxy system, K_{Ic} strongly increases up to $1.4\text{ MPa}\sqrt{\text{m}}$. It is interesting to see the enhancement of the CSR particles in comparison to the BCP toughened DGEBA system. A similar fracture toughness has been obtained at a BCP concentration of 10 wt.-%, but

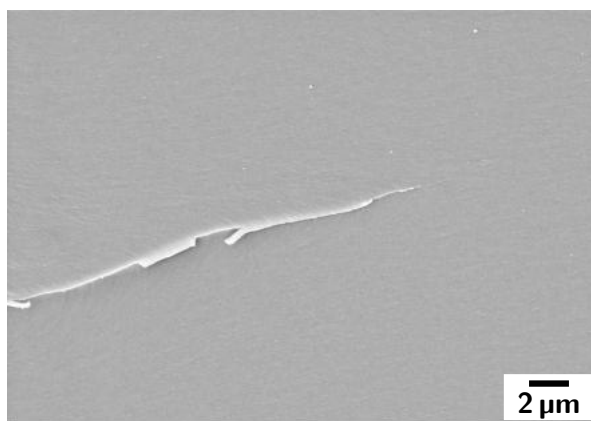


Figure 5.64: Neat EP/CAE system: the fracture surface is nearly featureless, yet shows a *river line*, an artefact from the fracture process, usually observed in the close vicinity to the crack initiation site, yet as single feature not strongly contributing to fracture toughness

the activated fracture mechanisms are different. EP/BCP-10% is characterized by a rugged morphology that has experienced large scale crack deflection. The fracture toughness improvement of the EP/CSR-16% system originates from CSR particle cavitation and void growth (cf. Fig. 5.65). Cavitation and void growth can only prevail if particle agglomeration is omitted, i.e. if particles have been evenly dispersed and the triaxial stress state within the plastic zone surrounds the particles, cf. Fig. 5.65, right. Even though the modifier concentration of EP/CSR-16% is 1.6 times higher than in the EP/BCP-10% system, the same fracture toughness has been reached. When further increasing the modifier concentration to nearly 30 wt.-% (EP/CSR/BCP-16/12) fracture toughness even tends to decrease. As discussed before, fracture toughness is a product of the stiffness, the yield stress σ_{ys} and an intrinsic length r_p (Eq. 5.32). Accordingly, in the case of CSR and BCP/CSR hybrid toughening of EP/CAE, the activation of fracture mechanisms has reached a maximum value, restricted by the toughnability of the epoxy matrix [138, 200]. Hence the cross-linked network omits further plastic void growth and/or shear yielding, at least in the CAE based system.

The analyses of the fracture surface morphology of EP/CSR/BCP-16/12, Fig. 5.66, reveals, similar to the BCP toughened system, a very high degree of crack deflection, i.e. the crack propagated through the specimen and was deviated from its path, resulting in hills and valleys. Furthermore, the morphology is assumed to be comprised of separate BCP-, CSR- and epoxy-rich regions. Recalling the morphology of the EP/BCP-10% system (Fig. 5.49), the phase-separated structure is totally different, even though the BCPs were initially homogeneously mixed with the CSR toughened CAE resin. The morphology has changed from distinct BCP-rich and epoxy-rich separated domains with single nano-sized BCP-rich particulate phases to a morphology that is comprised of epoxy-rich domains, voids created by CSR particle cavitation and presumably BCP rich regions. The BCPs have not formed large, separate domains any-

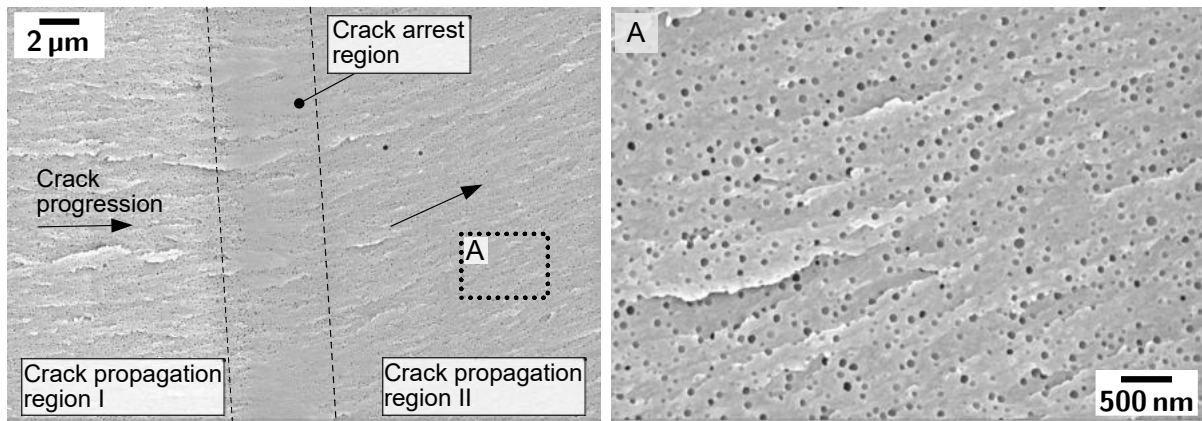


Figure 5.65: Fracture surfaces of EP/CSR-16% at different magnifications; left: crack arrest and crack propagation regions are visible. The crack arrest region is characterized by minor CSR particle cavitation (blunt appearance). The crack propagation region shows a strong degree of particle cavitation events. Also note the change of crack progression direction; right: crack propagation region, very even dispersion of nano-sized holes, being remnants of large scale core-shell particle cavitation and subsequent void growth. The holes are most likely filled with fractured CSR particles (not visible via SEM, yet shown for rubber particles in [199]).

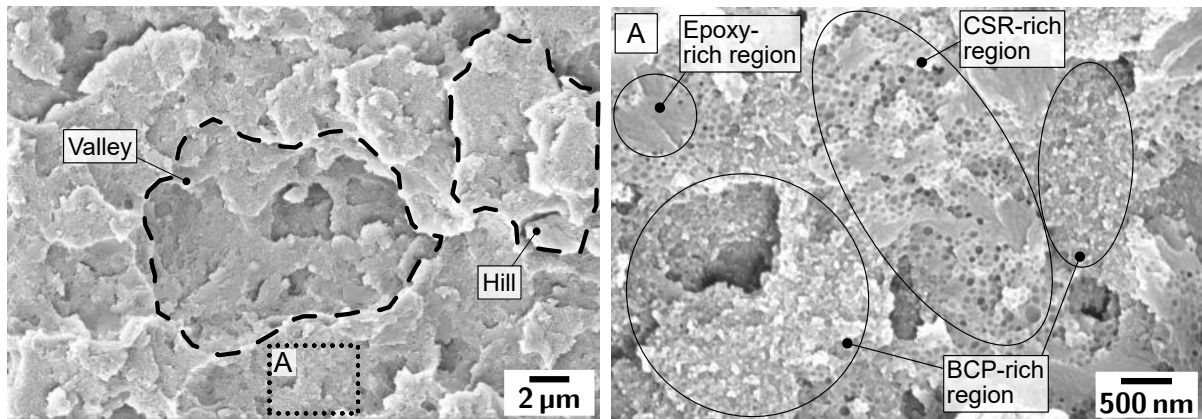


Figure 5.66: Fracture surfaces of EP/CSR/BCP-16/12 at different magnifications; left: severe crack deflection has occurred and created a rugged morphology comprised of valleys and hills; right: the morphology is comprised of features that can be assigned to voids caused by the CSR particles (CSR-rich region), and regions showing a lot of tail-like features, which might arise from the deformation of the soft phase of assembled BCPs. Some regions show no tail features nor CSR particle voids (epoxy-rich region).

more. It is unclear what these BCP-rich domains are comprised of, i.e. compositions of neat block copolymers or mixtures of BCPs and epoxy matrix. Based on the dynamic mechanical analyses, which showed a strong PMMA-block-related relaxation peak and a nearly unaltered α -relaxation of the epoxy matrix, the BCPs seem not to have affected the underlying epoxy network structure of this highly complex system. The presence of the nanosized CSR particles, or even the cycloaliphatic molecule structure of the epoxy resin, might have affected the phase separation process.

However, fracture toughness of the DGEBA and CAE based systems increased strongly by the addition of BCP, CSR nanoparticles and hybrids thereof, yet levelled at concentrations above 10 wt.-%. Having in mind the impact performance of those systems, and the damage initiation, which is governed by the strain to failure, as stated by Gilliot [29], Fig. 5.67 shows a plot of the already discussed energy release rate of the matrix systems G_{Ic} and the respective strain to failure ε_f behaviour. The relationship between both properties with regard to a BCP

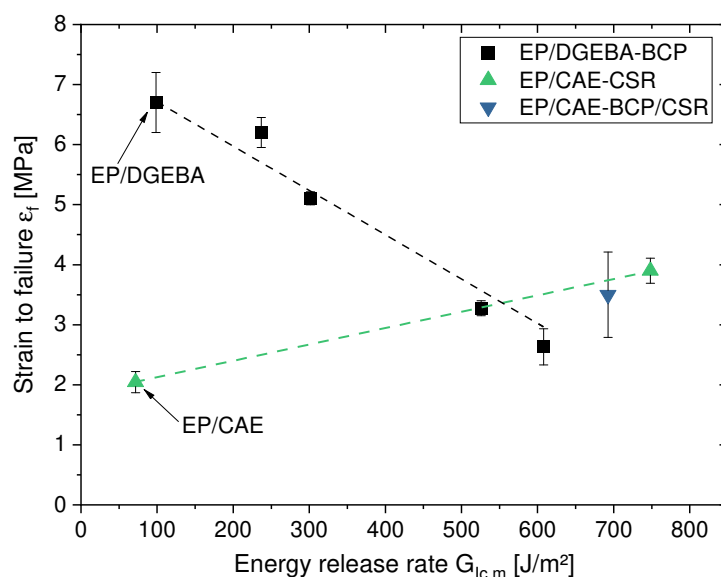


Figure 5.67: Relationship between strain to failure ε_f and the energy release rate $G_{Ic,m}$ of the modified matrix systems. ε_f is reduced with increasing $G_{Ic,m}$ (i.e. modifier concentration) for EP/DGEBA-BCP. A contrary behaviour prevails for the EP/CAE based systems.

modification is quite antagonistic: the higher $G_{Ic,m}$ is, the lower is the respective strain to failure ε_f value. On the other hand, ε_f of EP/CAE/CSR-16% doubles compared to EP/CAE. The CSR nanoparticles obviously better bond to the surrounding epoxy matrix. Based on this data plot it will be interesting to see what degree of damage resistance differently tough but similarly ductile matrices (e.g. EP/DGEBA-BCP-7% and EP/CAE-CSR-16%) will show.

5.4 Block copolymers and core-shell rubber nanoparticles in carbon fibre reinforced epoxy

To investigate the resistance to interlaminar fracture in Mode I and II unidirectional CFREs were manufactured as described in Sec. 4.1.3. They had an average fibre volume content of 55.9 ± 3.1 vol.-% and a thickness of 3.1 mm, i.e. a cured ply-thickness of $258.3 \mu\text{m}$ was reached, cf. Fig. 5.68.

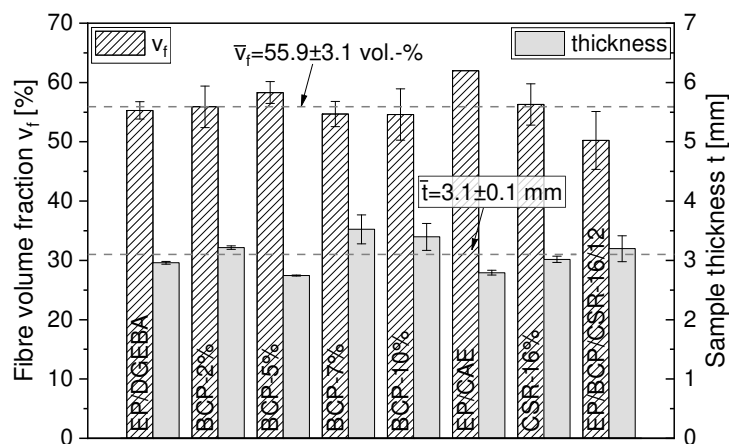


Figure 5.68: Fibre volume fraction and sample thickness of the unidirectional sample plates of different CFRE systems. The fibre volume concentration was determined based on computer aided grey-scale analyses of cross-sectional images of the various materials. The samples were polished with a $1 \mu\text{m}$ polish. Note, the value of the EP/CAE system is based on the total CF fabric weight and the total sample plate weight after curing, i.e. $v_{f,EP/CAE} = w_{CF-fabric}/w_{laminare}$

The laminates were well impregnated by the resin during the manufacturing process and did not show pores or other inhomogeneities during microscopy analyses (Fig. A.101). However, the fibre volume concentration varied slightly, mainly caused by the different viscosities of the systems.

Based on the findings and morphological variety the BCPs introduced into the epoxy matrix systems, it was especially important to investigate the phase separation behaviour of BCPs in a material that is comprised of additional partially reactive obstacles, i.e. the carbon fibres. The reactive epoxy sizing might alter the phase separation behaviour. However, respective analyses are limited to a qualitative assessment of the fracture morphology (interlaminar, Mode I).

5.4.1 Morphology of block copolymer modified carbon fibre reinforced epoxies (Interlaminar Mode I fracture)

Based on fracture surfaces from Mode I interlaminar fracture toughness tests obtained via SEM imaging, the prevailing (fracture) morphology of the various BCP toughened CFREs was analysed. Fig. 5.69 depicts a fracture surface of the neat, unmodified CFRE/DGEBA

system. The matrix partially adheres to the carbon fibres (matrix residues), but also large

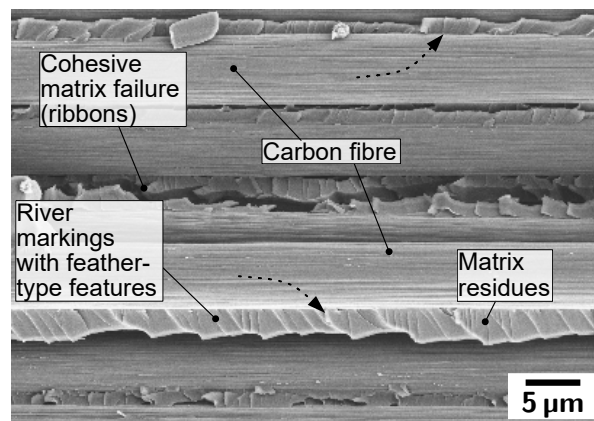


Figure 5.69: Fracture surface of CFRE/DGEBA, several carbon fibres are visible with partially adhering matrix residues, the macroscopic crack propagation occurred from left to right, a variety of fracture features are present

areas of the bare carbon fibres are visible, especially in the direction of the acting stresses (paper plane). This type of post-damage fibre feature indicates rather an adhesive failure between fibre and matrix. Furthermore, cohesive matrix fracture is present, indicated e.g. by *ribbons* (crack propagation on different heights within the matrix) as well as the prevalence of matrix residues. These features are characterized by *river markings*, which are indicative for a Mode I tensile type of fracture. The river markings themselves show in high resolution images a *feather type* appearance and can serve as additional features to identify the local direction of crack propagation. On the present fracture surface, based on the identified fracture morphology, it seems as if the crack travelled along the fibre into the matrix system (dotted arrows). This supports the idea of a weak fibre matrix adhesion as a starting point for fracture within this CFRE. For a collection and detailed description of CFRE fracture morphologies the reader is referred to [256].

Modifying the DGEBA system with 2 wt.-% of BCP did not affect the main matrix morphology as shown in Fig. 5.70, left. Similar fracture type features prevail as in the unmodified reference system (Fig. 5.69). However, higher magnifications (Fig. 5.70, right) reveal nano-sized precipitates or voids within the epoxy matrix, evenly dispersed throughout the whole matrix. These features originate from the BCP modification of the epoxy matrix. The number, but not the feature size increases when the modifier concentration is increased to 7 wt.-% (cf. the highly magnified SEM fracture surface of CFRE/BCP-7% in Fig. 5.71). Image analyses via *imageJ* showed that the feature size was in a very similar range of about 30 nm for both material systems. Comparing the morphologies of the 2 wt.-% and 7 wt.-% CFRE systems to their counterparts without fibres (cf. Fig. 5.47 and Fig. 5.48), it becomes obvious that the BCP phase precipitation morphology has dramatically changed. The size of the features embedded in the matrix has changed from micron sized particles (EP/BCP-2%)

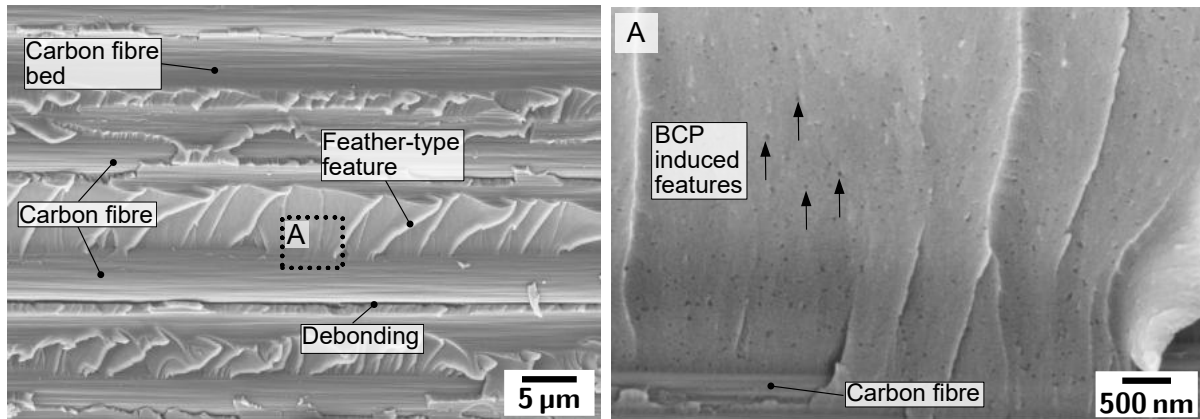


Figure 5.70: left: CFRE/BCP-2% system showing a rather unaltered main morphology compared to the CFRE/DGEBA system, right: nanosized precipitates or voids induced by the BCP modification in the range of 20 to 40 nm are visible in the epoxy matrix residues (indicated by arrows)

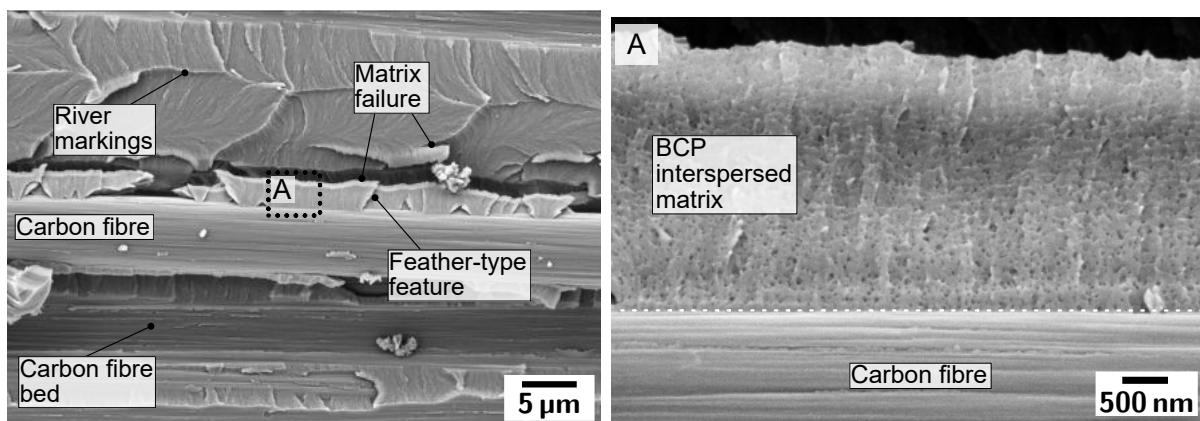
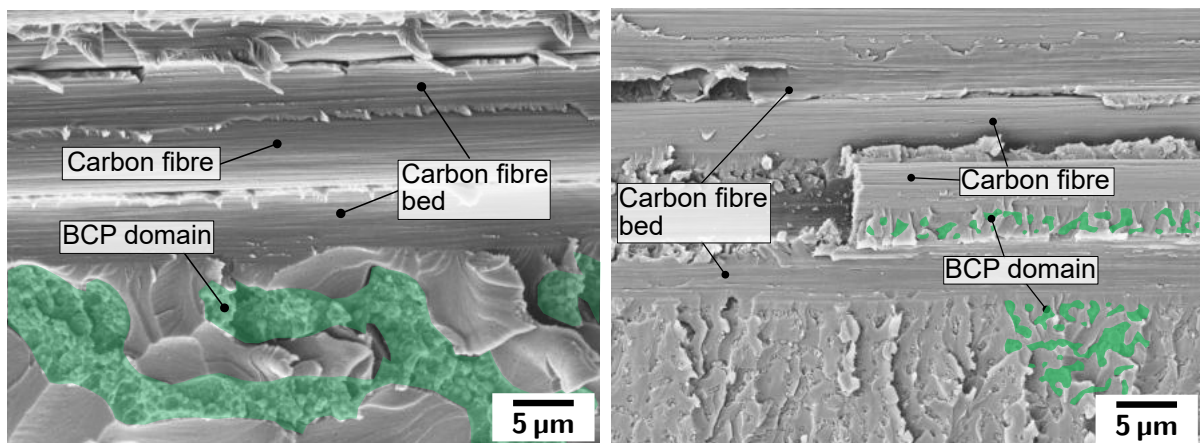


Figure 5.71: CFRE/BCP-7% system: the fracture surface morphology (left) has slightly changed and appears *smoother*, being rather unaltered compared to the CFRE/DGEBA system. Nanosized precipitates or voids induced by the BCP modification in the range of 20 to 40 nm are visible in the epoxy matrix residues (right).

and BCP-rich domains (EP/BCP-7%) to very much evenly dispersed nano-sized precipitates (CFRE/BCP-2% and -7%). This type of BCP precipitation should be, from a fracture mechanics point of view, highly preferential and increase the fracture toughness of the CFRE via large scale particle cavitation and subsequent plastic void growth of the precipitates (depending in the end on the cavitation resistance of the formed precipitates).

The questions that might be raised at this point are: (1) What is the parameter that hinders the large-scale domain formation of the BCPs within the CFRE, compared to the EP? (2) Is it e.g. the presence of the fibres or the did the processing pressure influence the phase-precipitation process (autoclaving was done under $p=24$ bar to consolidate the CFREs, cf. also [257])?

Two experiments were performed, first the EP/BCP-5% matrix system (without CF) was cured in the autoclave at $p=24$ bar and the fracture surface compared to a sample cured under ambient pressure with the same curing cycle. No differences between both morphologies were found. EP/BCP-5% showed the same micron-sized, BCP-rich precipitates as the one cured under ambient pressure (cf. Fig. A.100). The second experiment was to check the influence of the fibre concentration on the precipitation process. Two CFREs with varying fibre volume concentrations (33 vol.-% and 47 vol.-%) were manufactured based on the EP/BCP-7% system. The fracture surface morphologies are shown in Fig. 5.72.



(a) Fibre volume concentration 32.8 ± 4.2 vol.-% (b) Fibre volume concentration 47.2 ± 4.5 vol.-%

Figure 5.72: Influence of fibre volume concentration on the phase dimension of BCP-rich domains in the CFRE/BCP-7% system. A higher fibre volume concentration yields smaller but also more precipitated BCP-rich domains.

As can be seen, the lower the fibre volume fraction the larger the precipitated BCP-rich domains (highlighted in green). Hence, the presence of the fibres strongly influences the phase-separation process of the BCPs. So far, it is unclear if this effect is caused by the presence of the fibres itself, acting simply as obstacles to the phase-separation process or if surface energies (chemical and/or physical potentials between the resin system (resin,

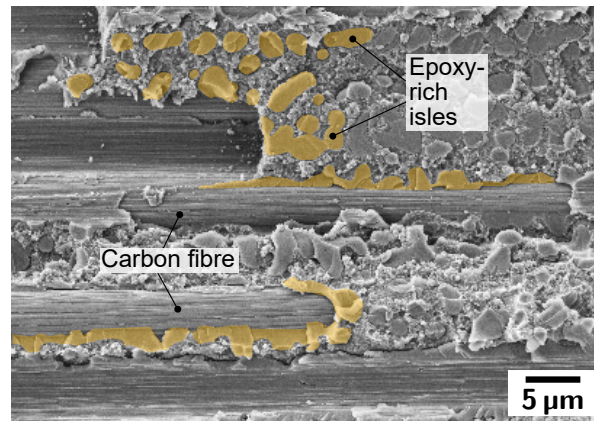


Figure 5.73: CFRE/BCP-10% system, fibre volume concentration 54.6 ± 4.3 vol.-%

hardener, BCPs) and the carbon fibres) hinder the evolution of large domains. What contradicts the first hypothesis is the formation of the very same domain-structures as found in the CFRE/BCP-7% (33 vol.-%) system in matrix-rich regions (not shown). It remains an open question for now if and how CF affect the long-range order of the BCP phase-separation process.

To eventually increase the number of nano-sized BCP precipitates even more, the epoxy matrix was blended with 10 wt.-% of BCPs. The resulting fracture surface is shown in Fig. 5.73. The morphology has changed again to an EP-rich domain structure (isles, indicated in orange). The BCP-rich domains govern the morphology, as already seen in EP/BCP-10% (Fig. 5.49). However, it seems as if the EP-rich domains have preferentially formed in the vicinity to the carbon fibres. This observation is highly interesting since SEM analyses of EP/BCP-10% after TMOR measurements revealed the formation of an epoxy-rich layer close to the prism surface (cf. Fig. 5.43a). Hence, it seems, once the BCP-concentration reaches a certain threshold in the epoxy resin and the phase-separation process starts, certain areas, preferentially close to interfaces, become BCP depleted. Furthermore, as shown in Fig. 5.74, the formed morphology in CFRE/BCP-10% is self-similar to EP/BCP-10% yet on a totally different length scale. The epoxy-rich isles are 10 times smaller than in the CFRE than in the EP. Considering the observations made for CFRE/BCP-2% and -7% with regard to the respective epoxy matrices, the phase-separation process yields similar precipitates in the CFRE, but on different length scales.

Even though the phase separation process has changed significantly, especially with regard to the length scale, no effect on the thermo-mechanical behaviour was found (Fig. A.99). The underlying epoxy network structure has not changed in the BCP modified CFREs at all concentrations, as already seen for the matrix systems (cf. Fig. 5.51). Based on the gathered data the phase separation process seems to generally follow the same pathway as sketched in Fig. 5.52. However, obviously another parameter, related to the presence of the carbon fibres, alters the phase-separation process not only in the close vicinity of the CF. Thus, the CF sizing

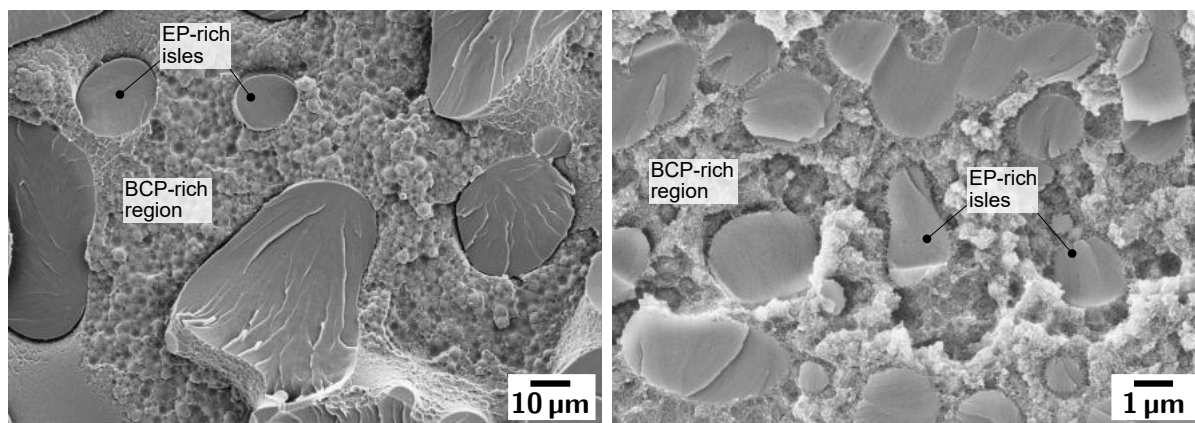


Figure 5.74: Fracture surfaces of EP/BCP-10% (left) and CFRE/BCP-10% (right), showing a BCP-rich dominated phase morphology, encapsulating epoxy isle-like structures, yet on different lengths scales

might play a crucial role in the phase-separation process of BCP-EP mixtures in CFREs.

5.4.2 Interlaminar Mode I fracture toughness (tension) of BCP and CSR nanoparticle toughened carbon fibre reinforced epoxy

The Mode I interlaminar fracture toughness $G_{Ic,c}$ (tension) is the most crucial property in terms of fracture mechanical properties of a composite. In Mode II and III, in-plane and off-plane shear, respectively, frictional effects between the cracked faces increase, at least apparently, the materials' resistance to delamination.

Figure 5.75 presents the results obtained from Mode I fracture tests as the energy release rate from the different CFREs over the respective toughening agent concentration in the matrix system (numerical data are provided in Table A.13). Generally, each type of modification yields an improved energy release rate over the neat CFRE. $G_{Ic,c}$ increases quite linearly for the BCP toughened systems at low concentrations and levels out at higher concentrations, as seen for the CSR and CSR/BCP toughened system. The BCP modification increases the energy release rate step-wise from 310 J/m² (unmodified CFRE/DGEBA) up to 795 J/m² for CFRE/DGEBA-BCP-7%. This strong increase originates from the well distributed and nano-sized BCP precipitates observed on the fracture surfaces (Fig. 5.71), which hinder crack growth within the epoxy matrix. As soon as the morphology changes to a BCP-rich domain structure, as in the case of CFRE/DGEBA-BCP-10%, G_{Ic} drops. As shown in Fig. 5.73, the CF-matrix interface region of this system is BCP depleted. Hence, the close vicinity to the CFs is most likely only in contact with neat epoxy matrix. Since $G_{Ic,c}$ is comprised of several energy dissipating contributions that require a proper bonding between CF and matrix, one can assume in this case that at least the toughening contribution of the matrix system cannot be properly activated. However, a restriction of the PZ would at least yield the same energy release rate as the CFRE/DGEBA-BCP-7% system. Therefore, it is more likely that the load

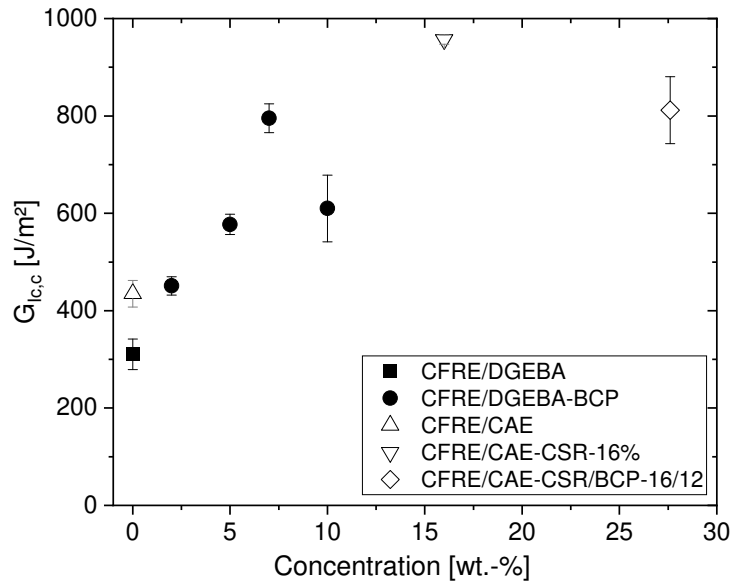
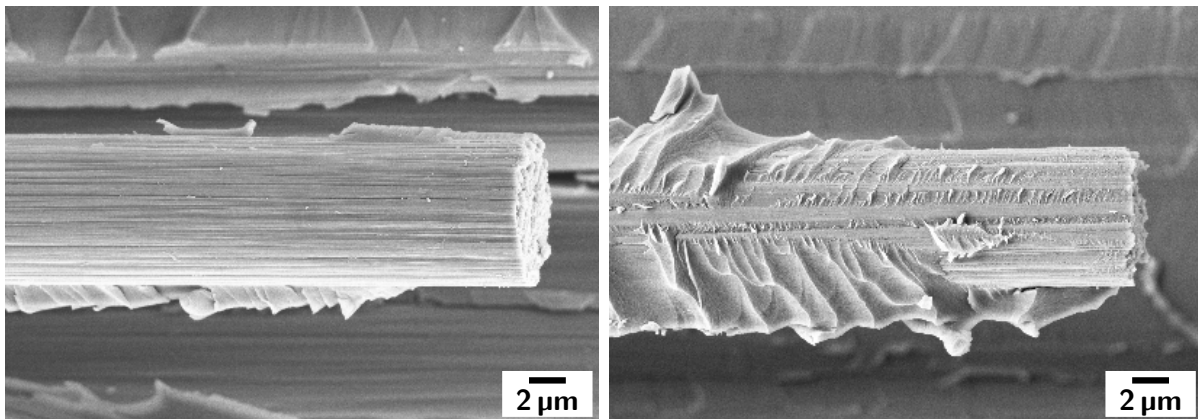


Figure 5.75: Interlaminar fracture toughness Mode I (tensile) of DGEBA and CAE based CFREs toughened with BCP and CSR nanoparticles.

transfer from the matrix to the CF is hindered, in the case of CFRE/DGEBA-BCP-10%, due to a reduction of the interface strength, i.e. G_{Ic} drops. Based on this statement, one can furthermore argue that the high interlaminar toughness of CFRE/DGEBA-BCP-7%, compared to the neat system, is not only an effect of the toughness of the matrix. The improved toughness has to be related to an enhanced bonding between CF and matrix, caused by the BCPs.



(a) CFRE/DGEBA

(b) CFRE/CAE

Figure 5.76: Influence of the epoxy resin system on the fibre-matrix adhesion. The figure shows a nearly bare fibre of the CFRE/DGEBA system and a well matrix-covered CF from the CFRE/CAE system.

The energy release rate of the CFRE/CAE system is remarkably higher (about 100 J/m^2) than the one from CFRE/DGEBA, even though the DGEBA system showed a much higher fracture toughness as neat matrix system, 98.5 J/m^2 and 71.7 J/m^2 , respectively (cf. Fig. 5.55).

The (fracture) morphology of the cycloaliphatic epoxy system appears quite different compared to the DGEBA based CFRE morphology, cf. Fig 5.76. Much more matrix residues can be found on the fibre surface and the number of formed ribbons has drastically increased. The carbon fibre is almost completely covered with epoxy matrix. The CAE based epoxy seems to better adhere to the carbon fibres, which were the same for all the systems.

The CSR nanoparticle modified CFRE/CAE system (Fig. 5.77, left) shows similarly a very high degree of fibre matrix adhesion. The fracture surface is comprised of *river markings* and

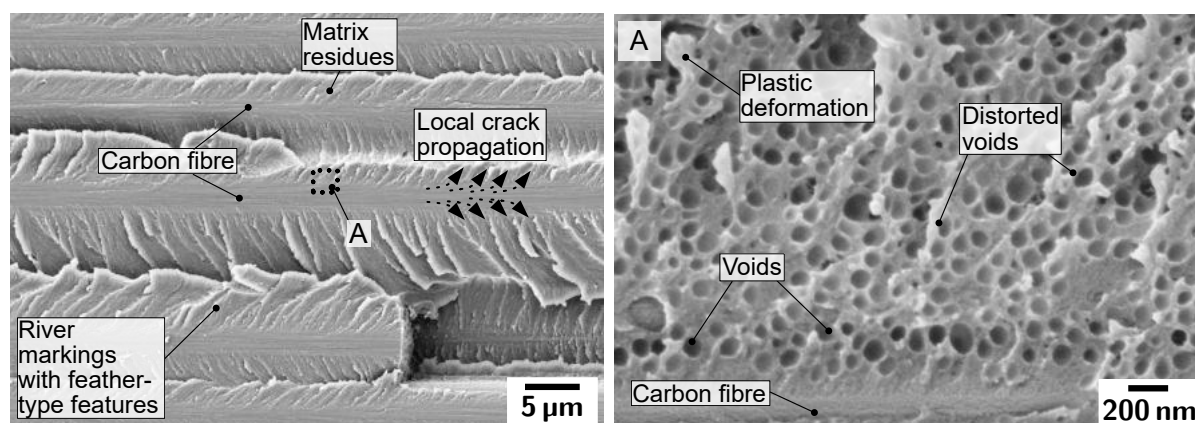


Figure 5.77: Fracture surfaces of CFRE/CAE-CSR-16%. The high CSR nanoparticle concentration yielded an evenly CSR interspersed matrix. Based on the CAE resin, the fibre matrix adhesion has not changed and crack propagation, as indicated by the arrows, propagated stringently along the CF into the epoxy matrix (left). The CSR nanoparticles cavitated and caused subsequent plastic void growth of the surrounding epoxy matrix.

feathery type of features. Assuming crack propagation originates, as in the CFRE/DGEBA system from the fibre matrix region, the bonding has to be much stronger, since the distance between the ribbons is much smaller. Fig. 5.77, right, illustrates the even distribution of CSR nanoparticles (voids, and CSR remnants appear on the fracture surface). The features on the fracture surface suggest a very high degree of particle cavitation and subsequent localized deformation of the matrix by shear yielding and void growth.

The toughness enhancement originates from a well suited particle size range for the activation of respective toughening mechanisms (cavitation size of 100 nm). Furthermore, the high degree of adhesion between the fibre and the matrix of the CAE system allows energy dissipation via large scale crack propagation *in* the epoxy matrix, rather than at the fibre matrix interface, cf. Fig. 5.76b. The CSR toughened system showed the highest measured Mode I energy release within this study (956.7 J/m²). Once the CSR toughened CFRE is additionally modified with block copolymers, CFRE/CAE-CSR/BCP-16/12, as shown in Fig. 5.78, the morphology becomes chaotic and does not allow assigning certain toughening mechanisms to the underlying morphology. The fracture surface indicates a highly adhesive bonding between the fibres and the matrix system. Fig. 5.78, right, shows a carbon fibre, which is completely covered with

matrix residues comprised of block copolymer-domains, CSR nanoparticles and epoxy-rich regions. However, G_{Ic} does not increase above the value of CFRE/CSR-16%. One reason, besides morphological implications, might be the restriction of the plastic zone size at high modifier concentrations, as discussed in Sec. 2.1.2. Once the plastic zone size of the toughened system exceeds the space that is provided by the composite in between fibres the toughness improvement is restricted and levels off.

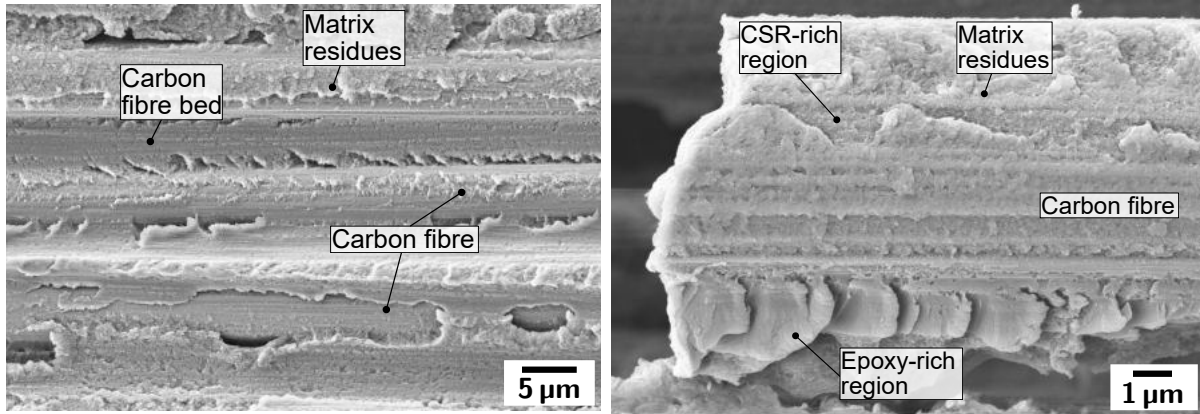


Figure 5.78: Fracture surfaces of CFRE/CAE-CSR/BCP-16/12. The high concentration of BCP and CSR modifiers yields a complex morphology that originates from interactions between resin constituents, block copolymers, core-shell rubber nanoparticles and carbon fibres. The fracture morphology suggests a high degree of fibre matrix interaction, probably originating from the cycloaliphatic base resin. No distinct BCP-rich region was found. However, CSR-rich regions were identified based on fracture features assumedly originating from CSR nanoparticles.

This trend is well illustrated in Figure 5.79, showing the relationship between the interlaminar fracture toughness Mode I for the CFRE as a function of G_{Ic} of the respective matrix. Note, this comparison is only valid when neglecting the morphology of the systems and idealizing the fracture induced properties based on the modifier concentration. This is because the BCP phase separation yielded totally different morphologies in the matrix and the fibre composite, but the concentrations were the same.

The energy release rate of the composite is far higher than the values obtained from the matrix systems, originating from additional fibre induced effects, as argued in Sec. 2.1.2. For the neat CFREs (CFRE/DGEBA and CFRE/CAE), those fibre contributions lead to a 3- to 4-fold increase over the energy release rate obtained from the neat matrices. Then, G_{Ic} of the CFRE/DGEBA-BCP systems drop to a ~ 2 -fold enhancement. Once $G_{Ic,m}$ reaches a value of about 500 J/m^2 , $G_{Ic,c}$ starts leveling off. Especially the toughening performance of CFRE/DGEBA-BCP-10% is reduced, as already discussed with regard to Fig. 5.75. A similar behaviour is observed for the highly modified hybrid system CFRE/CAE-CSR/BCP-16/12. However, the graph illustrates for all the systems that at least the respective matrix toughness, was successfully transferred to the composite ($m=1$ slope). It also shows the importance to

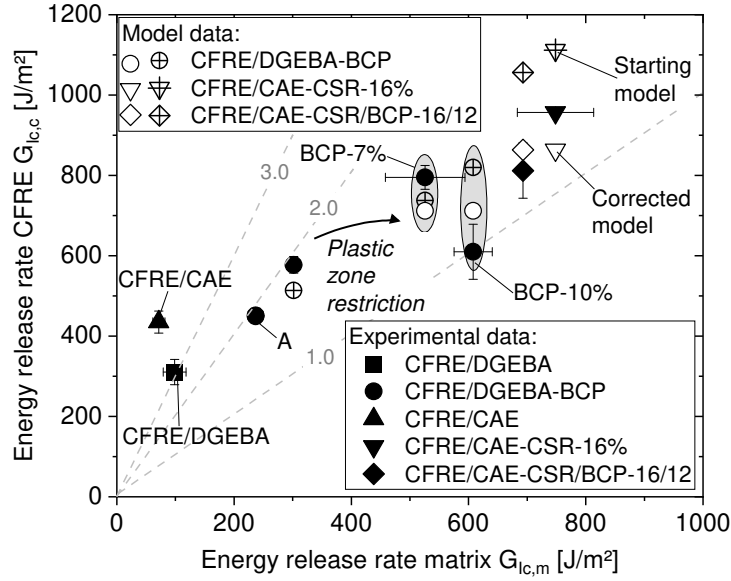


Figure 5.79: Relationship between the energy release rate (propagation values) of the CFRE and the matrix, modelled data are given as unfilled and crossed symbols and discussed below, A: modelled and experimental data overlap

understand the different interaction parameters prevailing in such complex structures as BCP toughened carbon fibre reinforced composites.

To predict the Mode I interlaminar fracture toughness of a toughened composite, $G_{Ic,c,mod}$ can be approximated based on the sum of a variety of energy dissipating parameters, such as (i) the critical energy release rate of the toughened matrix $G_{Ic,m,mod}$, (ii) fibre fracture G_f , (iii) fibre-matrix debonding G_{deb} (which accounts for energy release rate contributions from the interphase) and (iv) fibre bridging or pull out G_b [29]:

$$G_{Ic,c,mod} = G_{Ic,m,mod} + G_f + G_{deb} + G_b \quad (5.34)$$

To avoid assessing each single contribution of Eq. 5.34 experimentally, a simplified pathway was chosen, based on the already obtained data sets. The energy release rate of each matrix system (unmodified and modified) $G_{Ic,m,unmod/mod}$ has been experimentally determined within this work and is known. Furthermore, the energy release rate contributions from G_{deb} , G_f and G_b are collectively present in $G_{Ic,c,unmod}$, which has been determined as well. It applies according Eq. 5.34, in the unmodified case: $G_f + G_{deb} + G_b = G_{Ic,c,unmod} - G_{Ic,m,unmod}$. This yields to:

$$G_{Ic,c,mod} = G_{Ic,m,mod} + G_{Ic,c,unmod} - G_{Ic,m,unmod} \quad (5.35)$$

To not account for the toughness contribution of the unmodified matrix twice (included in $G_{Ic,c,unmod}$ and $G_{Ic,m,mod}$, which is again a sum of the fracture toughness of the neat matrix and the activation of different toughening mechanisms) the equation needs to be corrected by $G_{Ic,m,unmod}$. Also, it is assumed that within one set of epoxy resin based laminates, i.e. within all CFRE/DGEBA systems or within all CFRE/CAE systems, these energy release rate contributions are constant and do not change.

The modelled data set (crossed symbols) in Fig. 5.79 show a quite good agreement for the CFRE/DGEBA-BCP systems up to 7 wt.-%. At higher concentrations, the deviations between modelled data and experimental data become large (cf. CFRE/DGEBA/BCP-10%). Obviously, different parameters that have been neglected in the model dominate the experimental data, such as e.g. the plastic zone size restriction. Especially in the case of CFRE/DGEBA/BCP-10%, the heterogeneous morphology might additionally alter the interaction between matrix and fibres highly BCP-CF depleted interface regions (cf. Fig. 5.73). However, a boundary condition for Eq. 5.35 can be formulated. As stated before, the experimental findings show that the plastic zone size of the matrix becomes restricted in the CFRP at around 500 J/m^2 [63, 72], similar to this study, hence the energy dissipating capability of the matrix diminishes in the composite. Based on this, the contribution of $G_{Ic,m}$ in Eq. 5.35 is limited to $G_{Ic,m} \leq 500 \text{ J/m}^2$, i.e. $G_{Ic,m}$ of each matrix system that has an experimental energy release rate larger than 500 J/m^2 is set to $G_{Ic,m} = 500 \text{ J/m}^2$ within the model.

The results of the corrected model are given in the plot as unfilled symbols. The modelled data agrees much better with the experimental data sets, and shows smaller deviations from the experimental data than the starting model. This simple model provides a good starting point for further examinations. Supporting data about energy dissipation e.g. via debonding might further improve the prediction quality.

5.4.3 Interlaminar Mode II fracture toughness (in-plane shear) of BCP and CSR nanoparticle toughened carbon fibre reinforced epoxy

The Mode II interlaminar fracture toughness (in-plane shear) is a crucial parameter and indicator for the resistance to delamination (caused by impact events). The different CFRE systems were tested via the *ELS*-test as described in Sec. 4.4.3. The numerical data are gathered in the Appendix in Table A.13.

The *ELS*-test allows determining so-called *resistance curves* (R-curves) that relate the energy release rate G_{II} to the crack propagation at every increment of crack growth Δa . Fig. 5.80 summarizes respective representative R-curves of the different CFREs tested in Mode II. The R-curve behaviour of all CFREs is quite similar: at a certain energy release rate, which corresponds to a load, the crack is initiated, and starts propagating. This initiation was either determined, when crack propagation occurred visually (using a microscope, dotted, short lines) and/or when the maximum load (F_{max}) was reached (red dots). The R-curve rises in the first part, since fibre induced effects, e.g. fibre bridging, start acting at the crack tip, similarly as discussed for the Mode I case. Then, the R-curve flattens and reaches a plateau; the activation of mechanisms and crack growth are in a state of equilibrium. In the case of the hybrid system it was observed that the R-curve reached a peak and continuously decreased afterwards. This behaviour might indicate that the crack path changed (introduced from the Mode I fracture test, cf. the test setup in Sec. 4.4.3) to a less energy requiring path. However, such a deviation

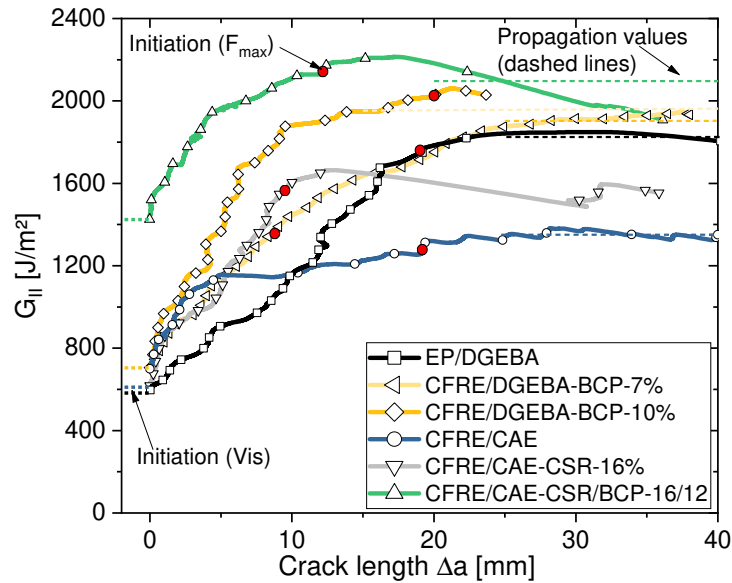


Figure 5.80: Resistance curves (selection), based on the ELS-interlaminar fracture toughness Mode II (shear) tests of DGEBA and CAE based CFREs, toughened with BCP and CSR nanoparticles.

was microscopically not observed. The average propagation values, based on at least 10 mm of the steady-state crack propagation, are indicated as dashed lines in the graph.

Fig. 5.81 shows the fracture surface of the neat CFRE/DGEBA system. The weak fibre-matrix interaction becomes obvious, but also shear introduced *hackle structures* appear on the fracture surface. These features are characteristic for shear failure of brittle epoxy systems [256].

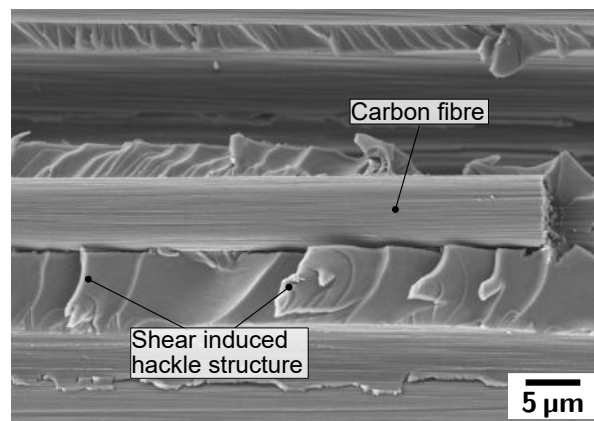


Figure 5.81: In-plane shear load (Mode II) generated fracture surface of CFRE/DGEBA showing the formation of hackle features

Based on the R-curve, the average steady-state energy release rate during crack propagation was derived and is summarized together with the visual and F_{max} -related crack initiation values in Fig. 5.82. It appears that the average propagation values for the toughened CFRE/DGEBA-BCP systems do not vary much, especially with respect to the neat CFRE/DGEBA system.

The neat CFRE/DGEBA shows an average energy release rate of $G_{IIc}=1857 \text{ J/m}^2$, which is slightly higher than expected from an epoxy based CFRE (cf. Fig. 2.6a). However, the DGEBA matrix has a quite high ductility ($\varepsilon_f=6.7\%$, cf. Tab. A.11). As stated before, this might be one of the reasons leading to an enhanced resistance to delamination. These observations are in accordance with the high crack initiation value at F_{max} , which step-wise decreases with increasing BCP concentration, besides for the CFRE/DGEBA-BCP-10% system. This changing trend might be caused by the underlying morphology that has severely changed from 7 to 10 wt.-%, again (cf. Fig. 5.71 and 5.73).

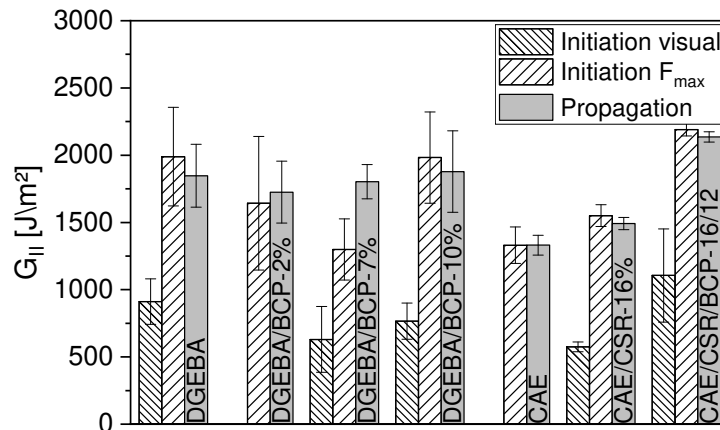


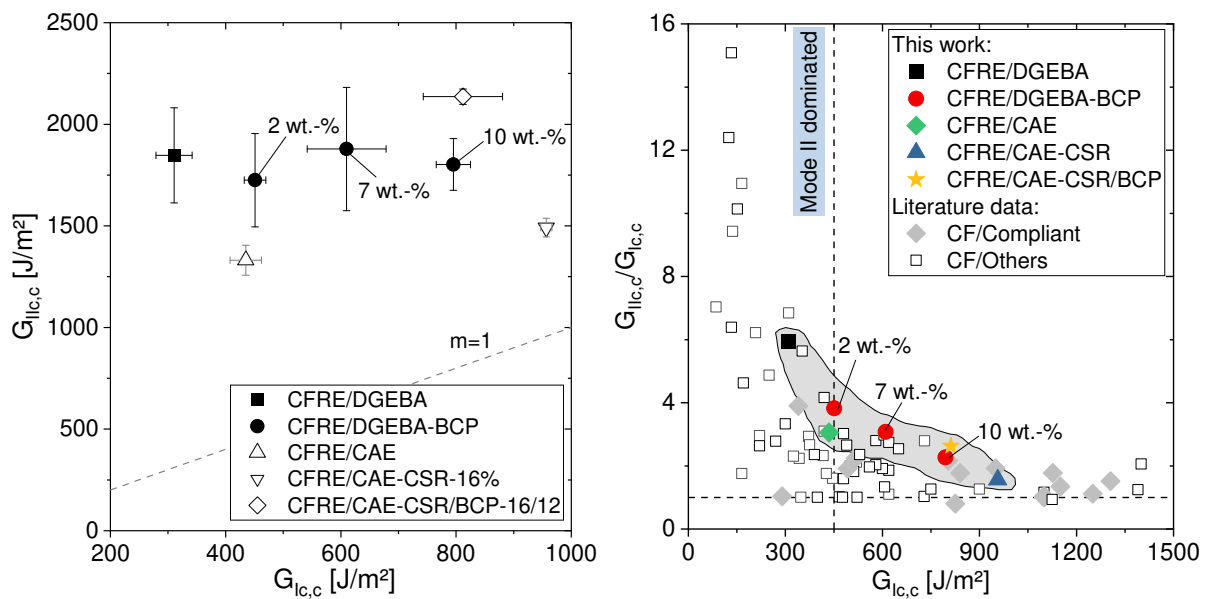
Figure 5.82: Interlaminar fracture toughness Mode II (in-plane shear) of DGEBA and CAE based CFREs toughened with BCP and CSR nanoparticles. Given are the visually determined crack initiation values, crack initiation based on F_{max} and the average crack propagation on G_{II} , which was measured at least over a crack length of 10 mm. No visual initiation values are available for CFRE/DGEBA/BCP-2% and CFRE/CAE

The situation appears different in the high-temperature resistant CAE systems. The propagation value indicates a markedly lower resistance to shear mode fracture than CFRE/DGEBA. The lower cross-link density and thus the higher fracture toughness and the much higher strain to failure (assumedly the Mode II strain to failure correlates to the Mode I tensile strain to failure) of the CFRE/DGEBA system are superior to CFRE/CAE. The energy release rate for initiation and propagation increase with increasing modifier concentration. Considering the enhanced bonding between the fibres and the matrix for the CAE based systems, the crack less likely changes its propagation path, i.e. G_{IIc} rather increases with the modifier concentration since toughness and strain to failure both increase for CFRE/CAE-CSR-16% and CFRE/CAE-CSR/BCP-16/12.

In conclusion, crack propagation in Mode II loading was not found to improve by BCP and/or CSR matrix modifications, with respect to the CFRE/DGEBA system. On the contrary, as discussed in Sec. 5.4.2, the interlaminar fracture toughness in Mode I, i.e. tension introduced failure, is strongly enhanced by the matrix modifications. The relationship is shown in Fig. 5.83.

It appears that the energy release rate in Mode II is not related to Mode I: Hence, different energy dissipating mechanisms underlie the two modes. Mode I is rather a matrix dominated parameter in which the interphase for sure contributes its stake, however, Mode II seems to be more related to the fibre-matrix interphase.

Normalizing the energy release rate in Mode II to the energy release rate in Mode I, G_{IIc}/G_{Ic} , yields respectively a relationship between the resistance to crack propagation dominated by the interface to one dominated by the matrix, Fig. 5.83b. The measured data were plotted together with the obtained data from literature. The investigated systems within this work provide a very good balance between Mode I (matrix toughness) and Mode II (interphase strength) interlaminar fracture toughness (grey region).



(a) Mode II interlaminar energy release rate (shear) as a function of the Mode I interlaminar energy release rate (tension) (b) Normalized Mode II interlaminar energy release rate as a function of Mode I interlaminar energy release rate

Figure 5.83: Relationship between Mode II interlaminar fracture toughness and Mode I interlaminar fracture toughness; CF/Compliant refers to data sets based on compliant types of modifiers in an epoxy matrix, CF/Others refers to other types of modifications, references to literature data are given in Tab. A.9.

5.5 Damage resistance of toughened thermosets

Researching and pushing the limits of composite materials' performance to new limits aims, besides the quest for knowledge and a deeper understanding of materials science relationships, at improving and developing new material solutions and applications. To do so and analyse the behaviour of BCP and CSR modified CFREs in a broader context, this chapter focusses on the impact behaviour of these materials within *thin* laminates. A total laminate thickness of $t=1.65$ mm and a CPT of 126.9 μm were anticipated. A cross-sectional micrograph of the

multidirectional layup used for the impact specimens (hand layup), in this case obtained from the CFRE/DGEBA system, can be found in Figure A.103. Supplementary numerical data are given in Table A.14. The laminate thickness for all systems was in a range of 1.55 to 1.8 mm.

For impact behaviour investigations the unmodified CFRE/DGEBA system was selected as a reference. Also, two BCP modified CFREs, i.e. 2 and 7-wt%, were chosen. Especially the latter one showed a much better fracture mechanical performance in the laminates than e.g. CFRE/DGEBA-BCP-10%, due to a prevailing nano-sized BCP-rich structure within the fibre composites. Furthermore, the CSR and CSR/BCP toughened hybrid system are in focus within this chapter. Five different energy levels were chosen to impact the specimens with. The data are summarized in Table 5.8 along with the corresponding impact velocities and strain rates. Impacting a material is accompanied by a spectrum of frequencies that might strongly change the materials response compared to the quasi-static load case, i.e. a ductile polymer matrix can embrittle and fail, since certain degrees of molecular movements are hindered. Such molecular effects need to be kept in mind during impact tests, even though the practically investigated length scale is totally different.

Table 5.8: Impact energies, corresponding velocities at impact, and strain rates. The strain rates were modelled using a simple finite element approach while considering the layup, the thickness of the CFREs and refer to the opposite side of the impact.

Impact energy [J]	Velocity at impact [m/s]	Strain rate [1/s]
1	1.0	6
3	1.7	12.5
7	2.6	20.6
9	3.0	23.8
13	3.6	31.3

Based on the unmodified reference system, Fig. 5.84 provides an overview of the force-time history over the 5 impact levels. Once the indenter hits the specimen the force measured by the load cell linearly increases (linear-elastic regime). If the linear elastic response regime is not exceeded the impact does not cause any failure within the composite and the indenter moves back, as seen for the 1 J case. The fluctuations of the data originate from sample vibrations under the indenter. Once the load reaches a critical threshold load the indentation deforms the material plastically, i.e. damage occurs as matrix fracture or delamination. This load level is denominated as delamination threshold load (DTL). However, such damage events do not necessarily appear in the force-time history if the load cell is insensitive to capture these, or if the damage events get lost in load fluctuations, as will be shown below. However, if the indenter causes fibre fracture, which is a highly energy dissipative mechanism, the load

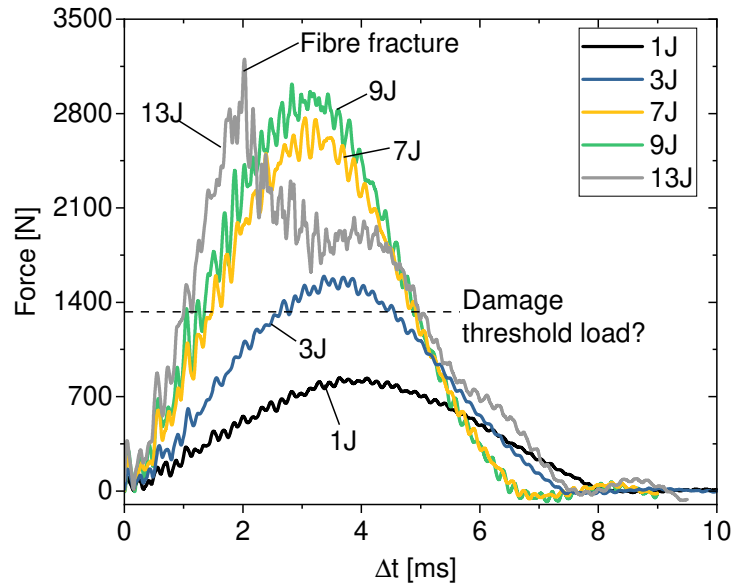


Figure 5.84: Force-time curve of the neat CFRE/DGEBA system for different energy levels. At an impact energy of 13 J the force-time curve shows a distinct force drop, indicative for severe fibre fracture within the specimen.

abruptly drops, as can be seen for the 13 J-case.

Davies et al. [35] developed a fracture mechanical model that relates Mode II delamination failure to the above mentioned *DTL*:

$$DTL = \sqrt{\frac{8\pi^2 E_f t^3}{9(1 - \nu^2)} G_{IIc}} \quad (5.36)$$

where E_f is the flexural modulus of the composite, t the thickness of the specimen, ν is the specimens Poisson ratio, assuming a homogenous, isotropic material as well as a single delamination in the middle of the specimen.

Based on this Equation and considering a delamination initiation value for the CFRE/DGEBA system of $G_{IIc}=1989 \text{ J/m}^2$, Eq. 5.36 yields a *DTL* of about 1329 N (under the assumption of a flexural modulus of 21 GPa and a thickness of $t=1.65 \text{ mm}$ and a Poisson ratio of 0.26). Indeed, some indicative load drops appear in that load region, yet are within a broad range of fluctuations. Nevertheless, if delamination should occur within the examined load range, no damage events should have taken place during the 1 J impact event.

Analysing the impact behaviour of the different CFREs at 9 J and 13 J, Fig. 5.85, one can see distinct differences between the material systems and their load response to the impacts, i.e. the maximum force the load cell measures varies. The differences originate from the resistance of the samples against the indent. Hence, if the samples are impacted and react elastically, as in the low impact energy case, the different materials all show more or less the same peak forces, defined by the carbon fibres and their layup, eventually damping the load due to a reduced stiffness of the matrix (not shown). However, if the material fails under

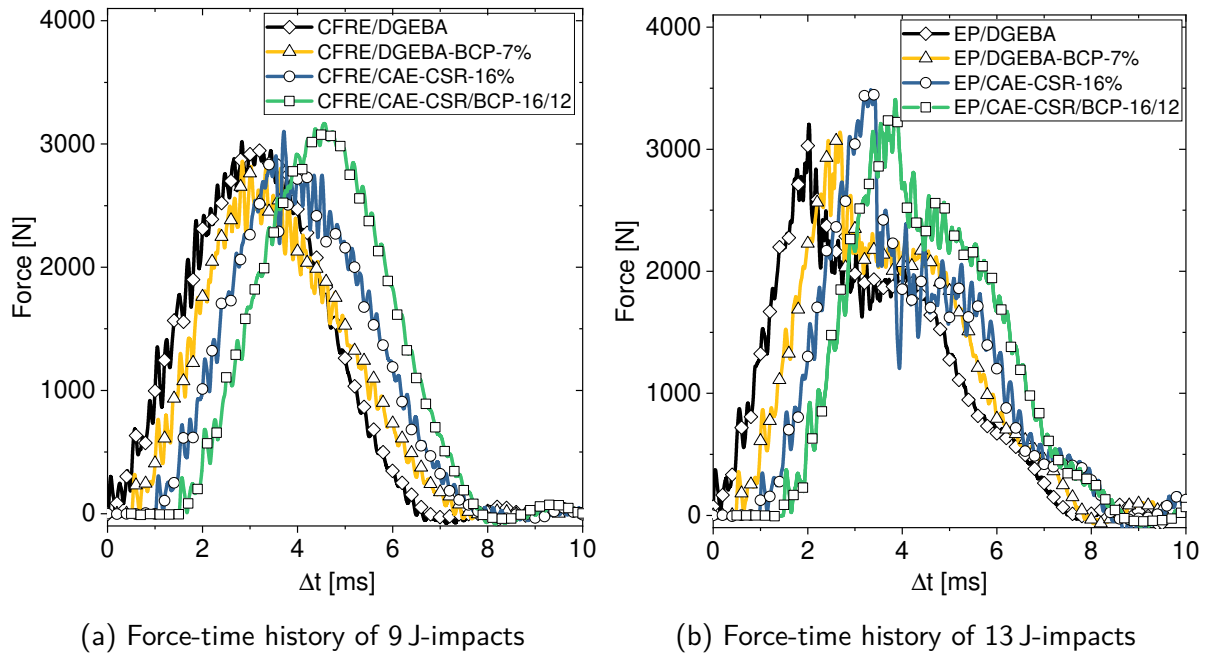


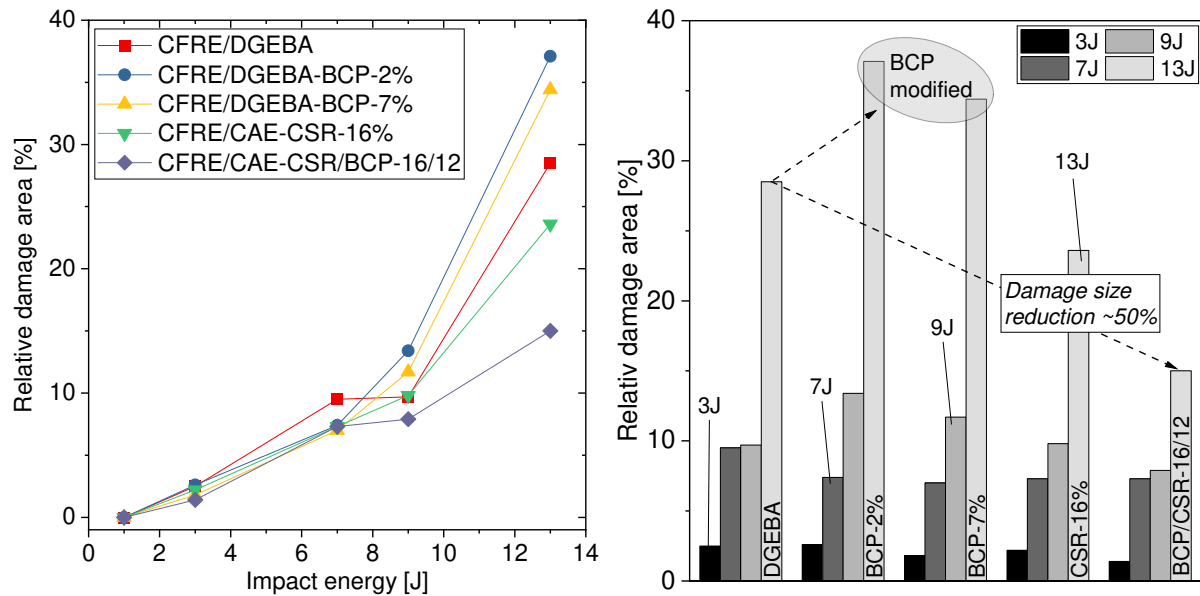
Figure 5.85: Force-time curves of the different CFREs during 9 J and 13 J impacts. At an impact energy of 13 J the force-time curve shows a distinct force drop, indicative for severe fibre fracture within the specimen.

the impact, i.e. highly non-linear inelastic deformation occurs, the load drops. In the case of the 9 J-impact the peak force of CFRE/CAE-CSR/BCP-16/12 was 215 N above the peak value of CFRE/DGEBA-BCP-7%, indicating early damage and failure of the latter system. In the case of the 13 J impacts, the sudden load drops all indicate severe fibre fracture. Hence, based on the force-time curve, the damage behaviour of the CFREs can be anticipated.

After impacting, the extent of the created damage within the different materials was investigated, using ultra-sound analyses and a confocal sensor to measure the permanent indentation depth. The obtained C-scans from the ultra-sound analyses are collected in the appendix, Fig. A.104. No damage was initiated in all 1 J impacted specimens, cf. Fig. A.105, confirming the assumption that 1 J impacts do not damage such thin panels, at least on the measuring length scale. Therefore, 1 J impacts represent a lower threshold level for impacts that can be endured, even without any matrix modifications. Furthermore, the C-scans show that the extent of damage increases with increasing impact energy. Also, the matrix modifications do not lead to a significant reduction of the damage size, at least in the 3 J and 7 J cases. However, after 9 J and 13 J impacts, the C-scan of the CSR/BCP hybrid toughened system (E) indicates a reduction of the damaged area. The BCP toughened systems CFRE/DGEBA-BCP-2% and -7%, on the other hand, rather show an increased damage size compared to CFRE/DGEBA.

Using *Matlab* data analyses software, the damage size of the various C-scans was evaluated

against a total scan size, yielding a relative damage area, allowing the comparison of the damages within the different CFREs, Fig. 5.86a. The damage threshold level A/\hat{A} during the C-scan was set to 30 %, i.e. every signal reduction below this value (*light blue*) was accounted as damaged-area. It becomes obvious that the extent of the impact damages was



(a) Relative damage area after impact over impact energy (b) Relative damage area and impact energy over the differently modified CFREs.

Figure 5.86: Areal (damage area) analyses of the differently modified CFREs as a function of the impact energy and the type of modifier. The relative damage area was determined via ultra-sound analyses and related to the total scan area.

not reduced at low impact energies for all investigated CFRE systems. However, after 9 J and 13 J impacts the detected damage areas varied largely, depending on the impacted CFRE. The plot illustrates that especially the CSR and CSR/BCP toughened system drastically reduced the damage size at higher impact energies.

To complement the analyses, Fig. 5.86b shows the relative damage area over the different types of matrix modification. First to note, the damage size of the BCP toughened systems increased over the damage size of CFRE/DGEBA, at 9 J and 13 J. Hence, the toughening of the DGEBA based matrix with BCPs did not yield any improvement, with regard to a damage size reduction. The damage within the hybrid toughened CSR/BCP system, on the other hand, was reduced by about 50% compared to the unmodified reference material, after 13 J impacts. For the toughened CFRE/CAE based systems, it seems as if the damage size was not reduced after having been impacted with 9 J. However, it should be kept in mind that the unmodified cycloaliphatic CFRE was not part of the impact study. It would be expected that the brittle CFRE/CAE system shows a highly brittle behaviour and even larger damage patterns.

A deeper analyses of the damage extent within CFRE/DGEBA and CFRE/CAE-CSR/BCP-

16/12 is provided in Fig. 5.87, which illustrates a collection of Computer Tomography (CT)-scans of both systems, after 3 J, 7 J and 9 J impacts. After 3 J impacts, the CT-scans

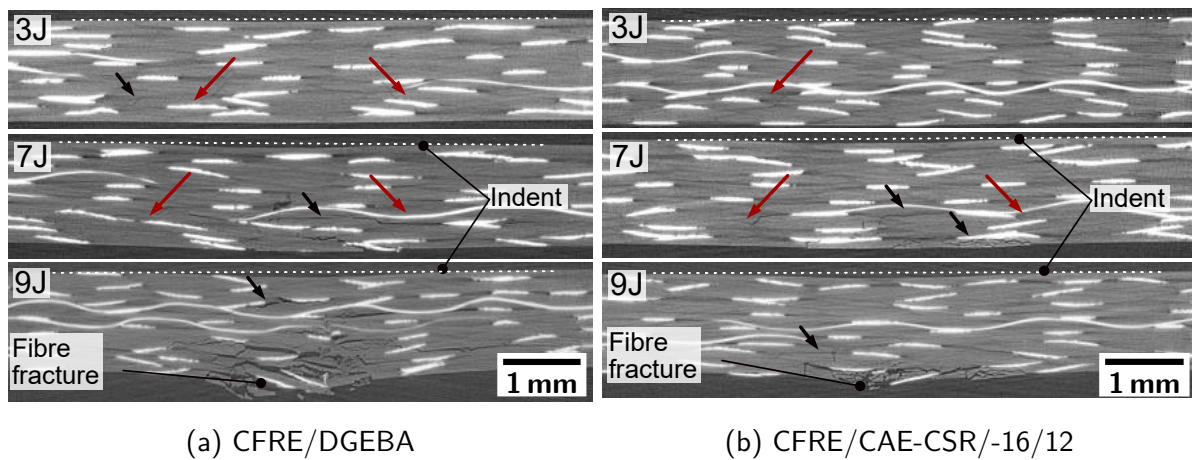


Figure 5.87: XRM CT-micrographs showing the inherent damage structure of an unmodified, thin CFRE panel (left) and the damage pattern of a highly toughened CFRE panel (right). The reduction of the extent of the damage is especially pronounced at an impact energy of 9 J, red arrows indicate the direction of cracks, black arrows selectively indicate cracks or delamination, the white dotted line shall support the visibility of the indents. The impact occurred from the top. Note, the selected images do not necessarily show the immediate centre of the impacted region.

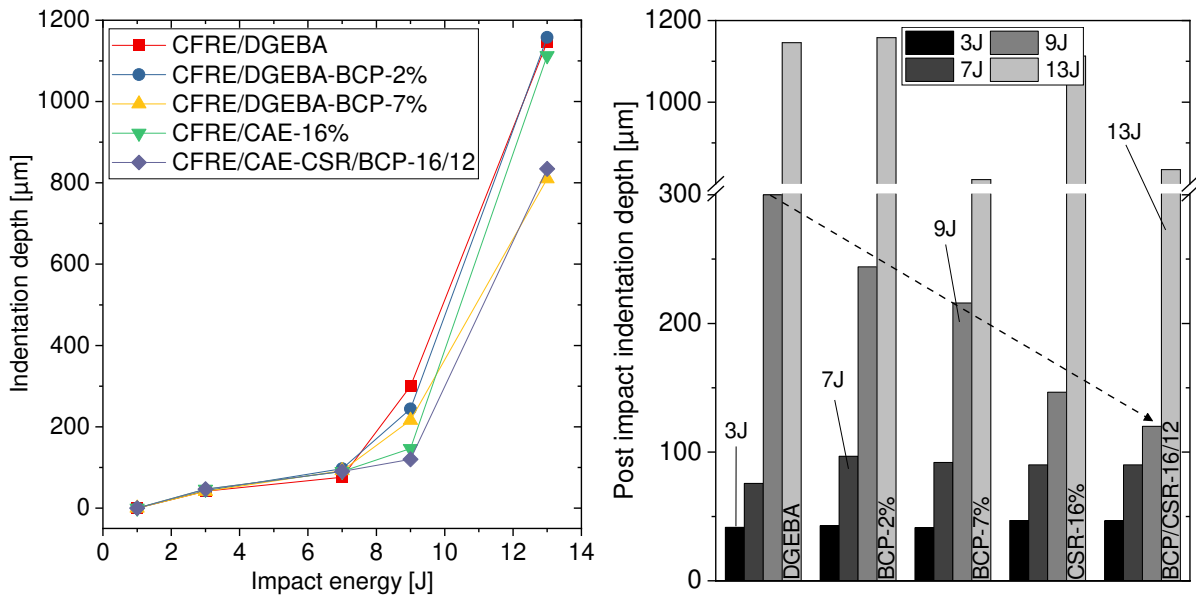
revealed barely any damages. However, both materials showed a characteristic pine-tree crack pattern, but no reverse-pine tree pattern was found, as suggested by Abrate [43] for *thin* laminates (Fig. 2.3). After 7 J impacts the damage pattern becomes more pronounced until at 9 J clearly fibre fracture on the bottom side of the panels occurred. Supplementary, Fig. A.106 shows the respective damage patterns after 13 J impacts.

Based on the findings so far, it seems the strong bonding between fibre and matrix in the CAE based systems, i.e. CFRE/CAE-CSR-16% and CFRE/CAE-CSR/BCP-16/12 enhanced the damage resistance of the composites. Whereas the DGEBA based epoxy systems showed a rather poor fibre-matrix interaction, i.e. were more prone to impact damages, cf. Fig. 5.76. However, based on the energy release rate to initiate delamination G_{IIC} , a relation solely to the interlaminar fracture toughness in shear mode cannot be the case.

Impact events always act in three dimensions. Ultrasound C-scans only provide proper insights into a material until the sound signal scatters, is refracted or changed in a way that it is not reflected to its source. Hence, if damage occurs in a composite layer close to the sound emitting source the C-scan gives the impression the part has experienced through-thickness damage. This downside of US scans becomes even more pronounced when an auxiliary reflector is used and the analysed signal is even more deteriorated, since it needs to travel through several interfaces (cf. Sec. 4.5). Thus, it is necessary to evaluate damages in

thickness direction.

Within this work a confocal sensor setup was used to examine the permanent dent depth that remained after the impacts in the specimens, Fig. 5.88. Similarly, as in the case of



(a) Permanent indentation depth after impact over the respective impact energy (b) Relationship between the indentation depth, the impact energy and the type of CFRE modification.

Figure 5.88: Analyses of the permanent indentation depth obtained via a confocal sensor.

the damage area, after low energy impacts below 9 J, no distinct difference between the indentation depths was found (Fig. 5.88a). However, the dent depths are in a critical range with regard to visual inspections of such impacted panels. Indentation depths of less than 100 μm can be characterized as BVIDs. Yet, after 9 J impacts and above, the indentation depths start to vary between the differently modified CFREs. A clearer picture provides Fig. 5.88b. At 9 J, the indentation depth decreases step-wise with the modifier concentration. After 13 J impacts the indentation depths have significantly increased. As shown by the force-time history and the US analyses, severe fibre fracture was initiated at such high load levels. But CFRE/CAE/CSR-BCP-16/12 shows one of the lowest indentation depths, at this load level.

Concluding so far, after low energy impacts of 1 J no damage was detected for all CFREs, i.e. the material is structurally damage resistant to such impacts. In the impact energy range from 3 to 7 J damages occur within the specimens, yet are hard to detect visually. The indentation depths were found to be in der critical BVID range of below 100 μm. At higher impact energies, a BCP and CSR modification of the epoxy matrix starts to pay out. With increasing modifier concentration, i.e. at 9 J, especially the indentation depth is drastically reduced from 300 μm (CFRE/DGEBA) to 120 μm (CFRE/CAE-CSR/BCP-16/12),

whereas the damage area stays in a range of 10 % over all tested CFREs. At very high impact energies (13 J), the damage patterns are determined by large scale fibre fracture. Based on US analyses and supported by XRM analyses, the size of the damage can be reduced in such cases by about 50 % within the CFRE/CAE-CSR/BCP-16/12 system over the CFRE/DGEBA reference system. Also the indentation depth was found to be far lower, specifically for this CFRE (cf. Fig. 5.88b).

To finally get a comprehensive idea of the actual damage volume, in an attempt to combine the above findings, a simplified *damage cone volume* was calculated based on the volume of a cone, i.e. $V = 1/3 \cdot G_{\text{base}} \cdot h$, where G_{base} is the area of the base and h the height of the cone. This geometry shall reflect the indented and plastically deformed volume of the sample. Respectively, the *relative damage area* (Fig. 5.86b) was accounted as G_{base} and the indentation depth (Fig. 5.88b) as h . Figure 5.89 summarizes the findings for 3 J, 7 J and 9 J impacts. 1 J and 13 J impacts have been omitted, since no damage was initiated or impacts were strongly biased by fibre fracture events and a penetration of the specimen.

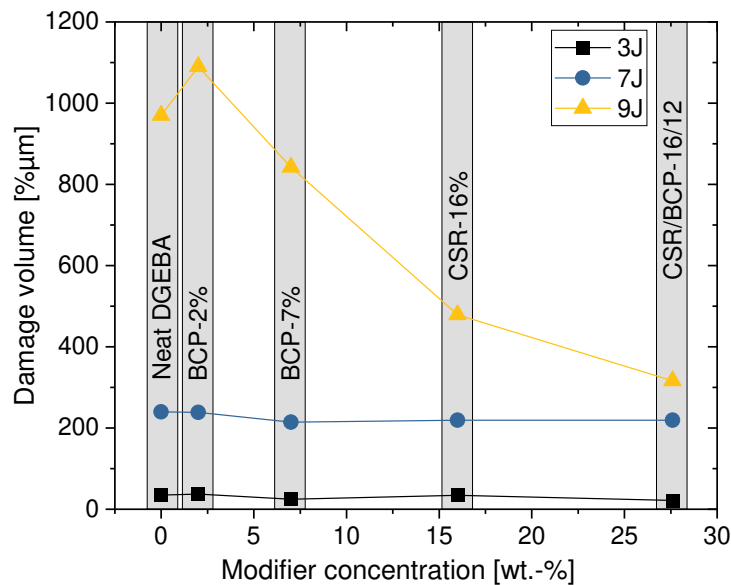


Figure 5.89: Damage volume of the differently modified CFREs, as a function of the total modifier concentration.

The graph illustrates and confirms that the applied matrix modifications do not reduce the damage caused by the indenter at 3 J and 7 J impacts. The damage volume stays constant over the whole range of modifier concentration. However, at 9 J impact energy, the matrix modifications become notably activated. The higher the modifier concentration is, the lower is the damaged volume. Especially the CSR/BCP-16/12 toughened system stands out and reduces the damage volume by about 67 % over the neat DGEBA based CFRE, which is a drastic reduction. The easy-to-process CFRE/CAE-CSR-16% system shows already a damage volume reduction of about 50 %. It seems that the damage volume reduction is independent of the type of matrix modification.

5.6 Core-shell rubber nanoparticles as highly efficient toughening agents for passenger car wheels

So far, it has been shown that the fracture mechanical properties of CFREs, such as the interlaminar fracture toughness and the impact resistance can be strongly enhanced if the underlying epoxy matrix is modified by BCP and/or CSR nanoparticles. It was also shown that fracture mechanical properties can be transferred from the matrix to the CFRE when certain boundary conditions, such as the presence of fibres are considered. The question that remains is, if the improvements and potential performance benefits of such resin modifications can also be transferred to real applications that are exposed to very complex mechanical stress situations.

Therefore, the transferability of toughening mechanisms and the fracture mechanical performance of a highly CSR nanoparticle modified epoxy matrix to a real application was investigated, using the example of a full-scale CFRE based passenger car wheel.

Lightweight CFRP based wheels are high performance components, whose first developments started about 50 years ago [258]. Manufacturing challenges and material performance limitations restricted the availability of such components to the consumer market up to the late 2000's. Especially the fracture toughness of epoxy matrices was (and is) inferior to metals and did not justify the application of carbon fibre reinforced wheels e.g. to the automotive market. Since then, manufacturing restrictions have been overcome. However, reaching a sufficient fracture toughness and fatigue resistance of such parts is still challenging. Today, CFRP based wheels are available for high performance passenger cars. The light weight structure contributes to a reduction of the rotating inertia of the wheel and allows for faster acceleration. In combination with the extraordinary high mechanical strength in fibre direction of CFRPs, the cornering stiffness is strongly improved and enables additionally safer driving conditions for vehicles [259, 260]. The light weight structure benefits the energy consumption or compensates for additional weight caused e.g. by battery systems in electrified cars [258].

The CFRP wheel market is fastly growing and CFRP based wheels are in focus of applied research and industry in a variety of sectors. One-piece CFRP wheels are e.g. offered by *Carbon revolution Ltd., Australia* to the consumer market [261], the aircraft industry tries to make use of the light weight potential of CFRP based wheels and to further reduce the weight of civil aircrafts [262], suppliers develop resin systems especially suited for CFRP wheel applications [263, 264] or work on strategies to ease up respective manufacturing processes [265]. Yet, most importantly, new test standards are developed e.g. by TÜV [266] that will most-likely allow access of CFRP based wheels to the passenger car wheel replacement market in the near future.

The interested reader can find some more information on the current state of composite wheel developments elsewhere [258].

To satisfy all those demands CFRP wheels, especially the matrix systems need to fulfil special processing and thermo-mechanical requirements, i.e. (i) low viscosities to process the materials via infiltration, filament winding or braiding processes, (ii) high thermal resistance (T_g), since wheels are closely located to the braking system of a car, where temperatures up to 160-170 °C can occur, (iii) high mechanical strength for high load carrying abilities (e.g. car chassis and passengers), (iv) as well as a high (fracture) toughness of the matrix system to withstand impacts, such as stone chipping, and subsequently hinder crack propagation by enhanced fatigue resistance [258].

Within a joint research project, two CFRP based car wheels were manufactured. The first one, a *reference* wheel based on a neat epoxy resin, the second one based on a highly CSR nanoparticle modified epoxy resin ($v_p \geq 30\%$). *Note: the type of carbon fibres and the matrix systems were the same for the matrix, the coupons as well as the demonstrator throughout this study.*

The impact resistance of wheels, as mentioned above, is a crucial parameter to be homologated by authorities and often restricts the application of wheels. Therefore, the impact resistance and the performance benefit of an unmodified and a CSR nanoparticle modified CFRE on the coupon level was compared to the damage resistance of the respectively manufactured wheel. The coupon level tests were conducted using a drop-tower device, similar to the setup shown in Sec. 4.5.1. Thereby, the *AITM1-0010 standard* was followed and samples were impacted with a hemi-spherical indenter, applying an impact energy of 30 J. The tests took place at $T = -30^\circ\text{C}$ to simulate cold weather conditions. Fig. 5.90 shows representative post-impact images of impact damages of the unmodified and the modified material systems obtained with ultrasound analyses (Sec. 4.6).

Damage is indicated by a loss of the initial sound wave amplitude (damping) by about -20 dB, i.e. the purple regions indicate delamination in between plies and other defects. Blue and green regions, on the other hand, show apparently undamaged areas of the samples, i.e. in these regions the sound signal is mostly reflected to the detector. The damage region in the unmodified coupon sample is sharply edged and about 3.7 times larger than in the modified rim, based on measurements using *ImageJ* image analysis software. Assuming a cone type of impact fracture caused by the hemispherical indenter, the damage volume is reduced drastically from about 3800 mm³ to 1046 mm³. However, the modified system shows a higher degree of sound wave damping than the unmodified system (green instead of light blue) in the presumably undamaged outer regions. Based on ultrasound measurements on not impacted samples, it was found that the CSR nanoparticles additionally damp the reflected sound signal by refraction, scattering or absorption. Hence, the extent of visible damage of the modified system is rather overestimated and might be even smaller than shown in Fig. 5.90b. This

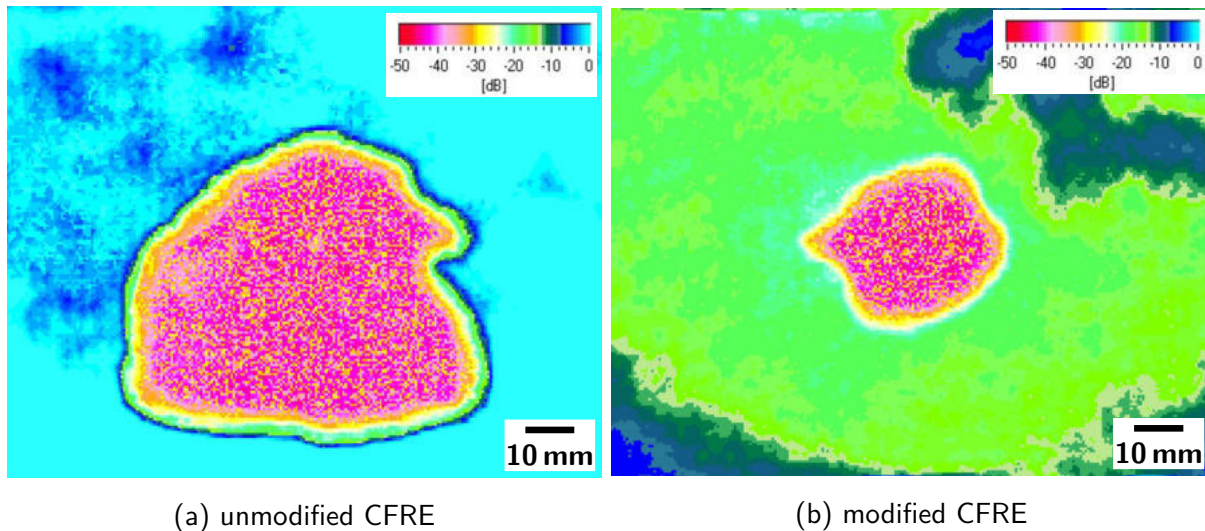


Figure 5.90: Post-impact ultra-sound analyses of unmodified and highly CSR nano particle toughened CFRE coupons; delamination and defects are indicated in red. The colour differences in the vicinity to the impact (light blue vs. light green) originate from sound wave distortions (scattering, refraction etc.) caused by the CSR nanoparticles, as discussed below

impressive damage volume reduction illustrates the benefits of CSR nanoparticles in CFREs.

Following the TÜV *guidelines for the testing and inspection of plastic wheels* [266], the CFRE wheels were impacted under an angle of 13° (impact energy $E_{imp}=1056$ J). This test simulates the damage resistance of a wheel when it is exposed to critical every day load situations, as driving over an obstacle with the outer rim flange. The most critical region for impact damages is thereby the spoke region. The failure criteria are according the TÜV standard either a *complete pressure loss within one minute* or *fracture outside the direct influence zone of the impact plate*. Figure 5.91 shows the indentation of the respective CFRE wheels (unmodified: left and modified: right) by an impacting bar at maximum deformation, captured with a high speed camera during the test. When comparing the location of the indenter in the left and in the right image (green), it becomes obvious that the indenter impacted the reference wheel much more than the highly CSR nanoparticle toughened one. In the untoughened case (left) the indenter causes severe damage of the rim, such as kinking of the spoke region. Furthermore, post damage analyses revealed fatal delamination failure throughout the whole rim (not shown). This was not the case in the CSR nanoparticle toughened version that nearly elastically deflected the impact and barely showed a damage outside the immediate indentation zone.

In summary, using the example of a CFRE based wheel, it is shown that a tailored CSR nanoparticle modification of a brittle epoxy matrix system is able to drastically improve the damage resistance of a complex CFRE structure. Fracture mechanical matrix properties that

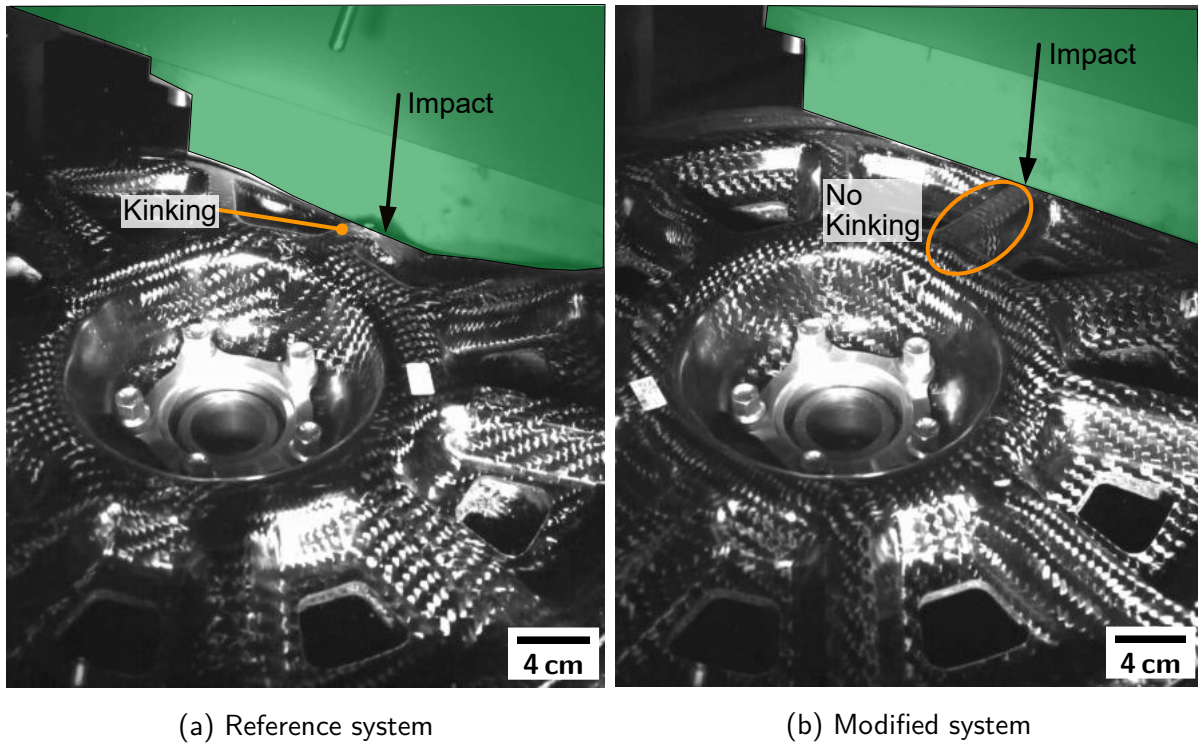


Figure 5.91: Comparison of the impact resistance of a neat and a highly toughened CFRP rim, shown is the maximum deformation at an impact energy of $E_{imp}=1056$ J, the indenter is highlighted in green

are initially created on a molecular level by nanoscale tougheners and their interaction with resin and hardener moieties, have huge effects on full scale applications by altering the underlying micro-structure. Also, the coupon test level is a useful tool to pre-assess the damage performance of a full-scale demonstrator, as seen from the impact tests.

6 Conclusions and Outlook

6.1 Conclusions

Within this work, the fracture mechanical performance and the impact behaviour of carbon fibre reinforced epoxies, toughened with block copolymers, core-shell rubber nanoparticles and blends thereof, was investigated. Thereby, the block copolymer modifier was in the focus of attention, with regard to (i) the BCP phase-separation behaviour on the matrix and the composite level, as single modifier and in combination with CSR nanoparticles, (ii) the influence on the thermo-mechanical properties, i.e. the underlying molecular network of the epoxy matrix, (iii) the effects of the created morphology on fracture mechanical properties, and (iv) the damage resistance of thin CFREs.

The BCP phase separation behaviour in the matrix was found to be a complex thermodynamically driven process. The underlying epoxy network structure was not affected and the

cross-linking reaction seems not to be influenced by the presence of the macromolecular BCPs. The glass transition temperature was essentially the same for all BCP toughened epoxy matrices. It was shown that the phase separation process, with regard to the processes and materials used within this work, is only driven by the degree of cure of the epoxy matrix. Hence, adjusting the curing cycle offers the possibility to gain control over the morphological variety of BCP/epoxy systems. With regard to mechanical properties, the introduction of BCPs reduce Young's modulus, strength and strain to failure. On the other hand, fracture mechanical properties, such as the critical stress intensity factor, was increased by about 240 % over the neat DGEBA based reference matrix ($K_{Ic,EP/BCP-10\%}=1.38 \text{ MPa}\sqrt{\text{m}}$). Both results can be related to the precipitated morphologies at different BCP concentrations within the epoxy matrices. Up to 5 wt.-%, the BCPs form BCP-rich, particle-like structures in the micron size range. Above 5 wt.-%, the BCPs form isle-like and epoxy-rich domain structures. Based on SEM imaging, a poor interface between the BCP-rich and epoxy-rich domains prevails, being detrimental to strength and strain. Blending the BCPs with CSR nanoparticles to increase the modifier concentration leads to a totally different (fracture) morphology, comprised of presumably BCP-rich and CSR-rich domains, which did not further improve fracture mechanical properties. The stress intensity factor was found to be even lower than the one of EP/BCP-10%, i.e. $K_{Ic,CSR/BCP-16/12}=1.28 \text{ MPa}\sqrt{\text{m}}$.

Introducing carbon fibres into the BCP modified epoxy matrices changed the underlying morphology. Up to 7 wt.-% the BCPs precipitated in nano-domains and strongly enhanced the Mode I interlaminar fracture toughness from $G_{Ic}=310 \text{ J/m}^2$ (CFRE/DGEBA) to $G_{Ic}=795 \text{ J/m}^2$ (CFRE/BCP-7%). Above 7 %, the BCPs formed again BCP-rich domains being self-similar to the morphologies found on the matrix level, yet on a totally different length scale. When this morphology formed in the CFRE, the interlaminar fracture toughness dropped to $G_{Ic}=610 \text{ J/m}^2$ (CFRE/BCP-10%). From a phase-separation point of view, the BCP phase-dimensions can be influenced by the CF concentration in the matrix. Reduced fibre volume concentrations (33 vol.-%) lead to BCP-richer domain structures, higher concentrations formed nano-sized precipitates (55 vol.-%). This behaviour might also be related to the sizing of the CF, which could affect the phase separation process of the BCPs by other physio-chemical interactions. The highest interlaminar energy release rate in Mode I within this work was obtained with the CSR toughened CAE-based system, $G_{Ic,CFRE/CSR-16\%}=956.7 \text{ J/m}^2$. The result is related to the high CSR nanoparticle concentration and the ideally suited particle size for cavitation events to initiate subsequent void growth of the epoxy matrix. The hybridized CFRE being modified with 16 wt.-% of CSR nanoparticles and 10 wt.-% of BCPs (CAE based matrix) did not show another enhancement of G_{Ic} , yet stayed on a energy release rate level similar to CFRE/BCP-7%, $G_{Ic,CFRE/CSR/BCP-16/12}=811.9 \text{ J/m}^2$. The result illustrates the restriction of the plastic zone size by the presence of the carbon fibres.

The interlaminar shear fracture toughness (Mode II, propagation) G_{IIc} was nearly constant for the DGEBA based CFREs, $G_{IIc} \approx 1800 \text{ J/m}^2$. However, the respective initiation values, based

on F_{\max} decreased with increasing BCP concentration from 1988 J/m² to about 1300 J/m², as long as a nano-sized morphology prevailed. When the phase-separation process leads to the formation of an epoxy-isle structure at 10 wt.-%, it was found that the matrix region in the vicinity to the carbon fibres was BCP depleted. This was accompanied with a sudden increase of the Mode II initiation values for the CFRE/DGEBA-BCP-10% system, back to the level of the reference system (CFRE/DGEBA). It seems that crack initiation is rather related to matrix properties (strain to failure and fracture toughness), whereas crack propagation is a fibre-matrix dominated property. The resistance to interlaminarly introduced shear cracks within the CAE based system ($G_{IIc}=1330$ J/m²) was far below the value of CFRE/DGEBA. However, G_{IIc} for the CAE based systems increased, when the matrix was modified with CSR nanoparticles and a blend of CSR and BCPs (hybrid). SEM analyses shows that the fibre-matrix interaction *improved* by CSR and CSR/BCP modification. CFRE/CAE-CSR/BCP-16/12 reached the highest resistance to shear introduced crack initiation and propagation within this work, $G_{IIc,init}=2191$ J/m² and $G_{IIc,init}=2136$ J/m², respectively.

The low velocity impact behaviour of toughened, multidirectional CFREs, having a thickness of only 1.65 mm was investigated. The impact tests and subsequent ultra-sound analyses, as well as confocal indentation depth analyses, revealed that the purely BCP toughened matrices, did not significantly reduce impact damages. Also, none of the modified systems shows any damage below 3 J impacts, i.e. they are inherently damage resistant. However, damages in the impact energy range from 3 to 7 J lead to BVIDs (indentation depth < 100 μm). The highly toughened systems CFRE/CAE-CSR-16% and CFRE/CAE-CSR/BCP-16/12 were able to drastically reduce the damage volume by about 50 % and 67 %, respectively, in the impact energy range from 9 to 13 J.

Finally, a real rim was successfully used to demonstrate the transferability of lab-scaled experiments to real applications. The strongly improving energy absorbing capabilities of CFREs, due to a CSR modification of the underlying matrix system, was shown.

6.2 Outlook

In summary, the phase separation of BCPs offers the possibility to tailor fracture mechanical properties on the matrix and CFRE level. Transferring them from the matrix to the CFRE is possible, yet not a simple process of *morphology transfer*, since the presence of CF provides another variable to the phase-separation process of BCPs.

Increasing the understanding of BCP/epoxy systems with regard to the underlying phase-separation mechanisms for the successful implementation within carbon fibre reinforced applications is key. Therefore, a variety of pathways should be followed to access these mechanisms. TMOR measurements have proven to be highly useful in determining the phase-separation behaviour of such versatile modifiers. Further investigations could focus on different block-copolymer concentrations in the epoxy matrix. Based on the idealized phase-separation process sketched in Fig. 5.52, it would be of interest how lower BCP concentrations precipitate under

isothermal conditions. Lower concentrations of BCPs yielded smaller precipitates, as shown in Fig. 5.47. Hence, if such a low amount of BCPs is blended with the epoxy resin, can the phase separation process be controlled in a way that nano-sized structures form, even on the matrix level? Can the phase-separation be adapted to highly concentrated systems omitting the formation of BCP-rich domain structures? Also, the BCPs have not been applied to the cycloaliphatic epoxy resin solely. The far lower molecular weight, and resulting higher cross-link density than DGEBA based resins might affect the BCP phase separation process totally different. This work only peaked at respective implications in a rather complex mixture of CAE, core-shell-rubber particles and block copolymers, which does not allow to derive implications about the phase-separation process of BCPs in CAE systems.

With regard to the fracture toughness and damage resistance of CFREs, it is believed that an upper threshold level is reached for classical epoxy matrix toughening in the range of 1.4 to 1.5 MPa $\sqrt{\text{m}}$. Further improvements cannot be achieved without modifying the underlying network architecture. Also, as shown, the fibre-matrix interphase plays a crucial role in manufacturing damage resistant and tolerant CFREs. In both cases BCPs might offer solutions, solely based on the possibility to tailor the block-structure of BCPs and eventually provide toughness and strength to a matrix system, as well as allowing a good bonding between fibre and matrix. Therefore, it will be of great benefit to fully understand the influence of carbon fibres (volume concentration and especially fibre sizing) on the phase separation process, i.e. respective investigations using DSC, infrared spectroscopy and TMOR are suggested.

References

- [1] United Nations Organizations, *The Paris Agreement*, Nov. 4, 2016. [Online]. Available: <https://unfccc.int/process-and-meetings/the-paris-agreement/the-paris-agreement>.
- [2] Bundesministerium für Bildung und Forschung (BMBF), *Hightech Strategie 2025*, Apr. 9, 2020. [Online]. Available: <https://www.hightech-strategie.de/de/hightech-strategie-2025-1726.html>.
- [3] European Commission, Ed., *Flightpath 2050: Europe's vision for aviation*, Policy/European Commission, Luxembourg: Publ. Off. of the Europ. Union, 2011, 25 pp., ISBN: 978-92-79-19724-6.
- [4] Premium Aerotec, *Umweltziele 2019-2022*, 2019. [Online]. Available: https://www.premium-aerotec.com/fileadmin/user_upload/data/Lieferanten/PAE_Umweltziele_de.pdf.
- [5] S. Pantelakis and K. Tserpes, Eds., *Revolutionizing Aircraft Materials and Processes*, Cham, Switzerland: Springer International Publishing, 2020, ISBN: 978-3-030-35346-9. DOI: 10.1007/978-3-030-35346-9.
- [6] H. Schürmann, *Konstruieren mit Faser-Kunststoff-Verbunden: mit 39 Tabellen*, 2., bearb. und erw. Aufl, ser. VDI-[Buch]. Berlin: Springer, 2007, 672 pp., ISBN: 978-3-540-72189-5.
- [7] A. Fernández, C. S. Lopes, C. González, and F. A. López, "Characterization of carbon fibers recovered by pyrolysis of cured prepregs and their reuse in new composites", in *Recent Developments in the Field of Carbon Fibers*, R. Khanna and R. Cayumil, Eds., InTech, Jul. 25, 2018, ISBN: 978-1-78923-519-7. DOI: 10.5772/intechopen.74281.
- [8] G. Schinner, J. Brandt, and H. Richter, "Recycling carbon-fiber-reinforced thermoplastic composites", *Journal of Thermoplastic Composite Materials*, vol. 9, no. 3, pp. 239–245, Jul. 1996, ISSN: 0892-7057, 1530-7980. DOI: 10.1177/089270579600900302.
- [9] B. Hannemann, S. Backe, S. Schmeer, F. Balle, U. P. Breuer, and J. Schuster, "Hybridisation of CFRP by the use of continuous metal fibres (MCFRP) for damage tolerant and electrically conductive lightweight structures", *Composite Structures*, vol. 172, pp. 374–382, Jul. 15, 2017, ISSN: 0263-8223. DOI: 10.1016/j.compstruct.2017.03.064.
- [10] K. Friedrich and U. P. Breuer, Eds., *Multifunctionality of polymer composites: challenges and new solutions*, Plastics design library, Amsterdam Boston Heidelberg London New York Oxford Paris: Elsevier, 2015, 964 pp., ISBN: 978-0-323-26434-1.
- [11] U. P. Breuer, *Commercial aircraft composite technology*. Cham, Switzerland: Springer International Publishing, 2016, ISBN: 978-3-319-31918-6.
- [12] U. P. Breuer and M. Latrille, "Einsatzmöglichkeiten und Restriktionen adaptiver CFK-Strukturen bei Verkehrsflugzeugen", Adaptronic Congress 2000, Potsdam, May 4, 2000.

-
- [13] G. W. Ehrenstein, *Faserverbund-Kunststoffe: Werkstoffe, Verarbeitung, Eigenschaften*, 2. völlig überarb. Aufl. München [u.a.]: Hanser, 2006, ISBN: 978-3-446-22716-3.
- [14] Thyssenkrupp Carbon Components GmbH, *Thyssenkrupp carbon components launches braided carbon wheels for the new BMW s 1000 RR (press release)*, Apr. 4, 2020. [Online]. Available: <https://www.thyssenkrupp-carbon-components.com/en/2020/04/04/thyssenkrupp-carbon-components-launches-braided-carbon-wheels-for-the-new-bmw-s-1000-rr/>.
- [15] J. Krummenacker, A. Klingler, J. Hausmann, and B. Wetzel, "Improvement of the cyclic loading resistance of highly loaded CFRP components by resin modifications", *Review of Aeronautical Fatigue Investigations in Germany during the Period April 2015 to March 2017 (TX1RP201720694)*, 2017.
- [16] A. J. Kinloch and R. J. Young, *Fracture behaviour of polymers*. London: Applied Science Publ, 1983, ISBN: 0-85334-186-9.
- [17] A. C. Garg and Y.-W. Mai, "Failure mechanisms in toughened epoxy resins - A review", *Composites Science and Technology*, vol. 31, no. 3, pp. 179–223, 1988, ISSN: 0266-3538. DOI: 10.1016/0266-3538(88)90009-7.
- [18] I. Srivastava and N. Koratkar, "Fatigue and fracture toughness of epoxy nanocomposites", *JOM*, vol. 62, no. 2, pp. 50–57, 2010, ISSN: 1047-4838. DOI: 10.1007/s11837-010-0032-8.
- [19] R. A. Pearson, H.-J. Sue, and A. F. Yee, Eds., *Toughening of Plastics*, ACS Symposium Series, Washington DC: American Chemical Society, 2000, ISBN: 0-8412-3657-7.
- [20] R. W. Hertzberg, R. P. Vinci, and J. L. Hertzberg, *Deformation and fracture mechanics of engineering materials*, 5. ed. Hoboken, NJ: Wiley, 2013, ISBN: 978-0-470-52780-1.
- [21] T. Noebel, "CFRP fuselage sizing/design", Guest lecture at Institute for Composite Materials, 2013.
- [22] R. Bagheri, B. T. Marouf, and R. A. Pearson, "Rubber-toughened epoxies: A critical review", *Polymer Reviews*, vol. 49, no. 3, pp. 201–225, 2009, ISSN: 1558-3724. DOI: 10.1080/15583720903048227.
- [23] A. F. Yee and R. A. Pearson, "Toughening mechanisms in elastomer-modified epoxies: Part 1 - mechanical studies", *Journal of Materials Science*, vol. 21, no. 7, pp. 2462–2474, 1986. DOI: 10.1007/BF01114293.
- [24] D. Quan and A. Ivankovic, "Effect of core-shell rubber (CSR) nano-particles on mechanical properties and fracture toughness of an epoxy polymer", *Polymer*, vol. 66, pp. 16–28, 2015, ISSN: 0032-3861. DOI: 10.1016/j.polymer.2015.04.002.

- [25] A. Klingler, A. Bajpai, and B. Wetzel, "The effect of block copolymer and core-shell rubber hybrid toughening on morphology and fracture of epoxy-based fibre reinforced composites", *Engineering Fracture Mechanics*, vol. 203, pp. 81–101, 2018, ISSN: 0013-7944. DOI: 10.1016/j.engfracmech.2018.06.044.
- [26] C. M. Bates and F. S. Bates, "50th anniversary perspective: Block polymers - Pure potential", *Macromolecules*, vol. 50, no. 1, pp. 3–22, 2016, ISSN: 0024-9297. DOI: 10.1021/acs.macromol.6b02355.
- [27] S. Maiez-Tribut, J. P. Pascault, E. R. Soulé, J. Borrajo, and R. J. J. Williams, "Nanostructured epoxies based on the self-assembly of block copolymers: A new miscible block that can be tailored to different epoxy formulations", *Macromolecules*, vol. 40, no. 4, pp. 1268–1273, 2007, ISSN: 0024-9297. DOI: 10.1021/ma062185l.
- [28] K. Yamanaka, Y. Takagi, and T. Inoue, "Reaction-induced phase separation in rubber-modified epoxy resins", *Polymer*, vol. 30, no. 10, pp. 1839–1844, 1989, ISSN: 0032-3861. DOI: 10.1016/0032-3861(89)90355-8.
- [29] A. Gilliot, "Matrix influence on the impact tolerance of carbon composites made of non-crimp fabric", Dissertation, Deutsches Zentrum für Luft- und Raumfahrt, Braunschweig, 2009.
- [30] B. Hannemann, "Multifunctional metal-carbon-fibre composites for damage tolerant and electrically conductive lightweight structures", Dissertation, Institut für Verbundwerkstoffe, Kaiserslautern, 2018.
- [31] W. Han, Y. Tang, and L. Ye, "Carbon fibre-reinforced polymer laminates with nanofiller-enhanced multifunctionality", in *The Structural Integrity of Carbon Fiber Composites*, P. W. R. Beaumont and C. Soutis, Eds., Cham: Springer International Publishing and Imprint Springer, 2017, pp. 171–197, ISBN: 978-3-319-46120-5. [Online]. Available: https://link.springer.com/chapter/10.1007/978-3-319-46120-5_8.
- [32] R. Kothari, "Full-scale static and fatigue testing of composite fuselage section", in *ICAF 2011 structural integrity: Influence of efficiency and green imperatives*, J. Komorowski, Ed., Dordrecht: Springer Netherlands, 2011, pp. 551–560, ISBN: 978-94-007-1664-3.
- [33] B. G. Falzon and R. S. Pierce, "Thermosetting composite materials in aerostructures", in *Revolutionizing Aircraft Materials and Processes*, S. Pantelakis and K. Tserpes, Eds., Cham: Springer International Publishing, 2020, pp. 57–86, ISBN: 978-3-030-35345-2. [Online]. Available: http://link.springer.com/10.1007/978-3-030-35346-9_3.
- [34] G. Schoeppner and S. Abrate, "Delamination threshold loads for low velocity impact on composite laminates", *Composites Part A: Applied Science and Manufacturing*, vol. 31, no. 9, pp. 903–915, Sep. 2000, ISSN: 1359835X. DOI: 10.1016/S1359-835X(00)00061-0.

-
- [35] G. Davies, X. Zhang, G. Zhou, and S. Watson, "Numerical modelling of impact damage", *Composites*, vol. 25, no. 5, pp. 342–350, 1994, tex.ids: davies_1994, ISSN: 00104361. DOI: 10.1016/S0010-4361(94)80004-9.
- [36] W. Cantwell and J. Morton, "Comparison of the low and high velocity impact response of CFRP", *Composites*, vol. 20, no. 6, pp. 545–551, Nov. 1989, ISSN: 00104361. DOI: 10.1016/0010-4361(89)90913-0.
- [37] G. Minak, M. Fotouhi, and M. Ahmadi, "Low-velocity impact on laminates", in *Dynamic Deformation, Damage and Fracture in Composite Materials and Structures*, Elsevier, 2016, pp. 147–165, ISBN: 978-0-08-100870-6. DOI: 10.1016/B978-0-08-100080-9.00006-3.
- [38] B. Aryal, E. Morozov, H. Wang, K. Shankar, P. Hazell, and J. Escobedo-Diaz, "Effects of impact energy, velocity, and impactor mass on the damage induced in composite laminates and sandwich panels", *Composite Structures*, vol. 226, p. 111 284, Oct. 2019, ISSN: 02638223. DOI: 10.1016/j.compstruct.2019.111284.
- [39] P. Robinson and G. Davies, "Impactor mass and specimen geometry effects in low velocity impact of laminated composites", *International Journal of Impact Engineering*, vol. 12, no. 2, pp. 189–207, Jan. 1992, ISSN: 0734743X. DOI: 10.1016/0734-743X(92)90408-L.
- [40] C. Breen, F. Guild, and M. Pavier, "Impact of thick CFRP laminates: The effect of impact velocity", *Composites Part A: Applied Science and Manufacturing*, vol. 36, no. 2, pp. 205–211, Feb. 2005, ISSN: 1359835X. DOI: 10.1016/S1359-835X(04)00153-8.
- [41] D. Cartié and P. E. Irving, "Effect of resin and fibre properties on impact and compression after impact performance of CFRP", *Composites Part A: Applied Science and Manufacturing*, vol. 33, no. 4, pp. 483–493, 2002, ISSN: 1359835X. DOI: 10.1016/S1359-835X(01)00141-5.
- [42] H. Liu, J. Liu, C. Kaboglu, H. Chai, X. Kong, B. R. Blackman, A. J. Kinloch, and J. P. Dear, "Experimental investigations on the effects of projectile hardness on the impact response of fibre-reinforced composite laminates", *International Journal of Lightweight Materials and Manufacture*, vol. 3, no. 2, pp. 77–87, Jun. 2020, ISSN: 25888404. DOI: 10.1016/j.ijlmm.2019.10.001.
- [43] S. Abrate, *Impact on Composite Structures*. Cambridge, GBR: Cambridge University Press, 2009, ISBN: 978-0-511-57450-4.
- [44] M. Caminero, I. García-Moreno, and G. Rodríguez, "Damage resistance of carbon fibre reinforced epoxy laminates subjected to low velocity impact: Effects of laminate thickness and ply-stacking sequence", *Polymer Testing*, vol. 63, pp. 530–541, Oct. 2017, ISSN: 01429418. DOI: 10.1016/j.polymertesting.2017.09.016.

- [45] R. C. Alderliesten, C. D. Rans, T. Beumler, and R. Benedictus, "Recent advancements in thin-walled hybrid structural technologies for damage tolerant aircraft fuselage applications", in *ICAF 2011 Structural Integrity: Influence of Efficiency and Green Imperatives*, J. Komorowski, Ed., Dordrecht: Springer Netherlands, 2011, pp. 105–117, ISBN: 978-94-007-1664-3. DOI: 10.1007/978-94-007-1664-3_8.
- [46] E. Fuoss, P. V. Straznicky, and C. Poon, "Effects of stacking sequence on the impact resistance in composite laminates - part 1: Parametric study", *Composite Structures*, vol. 41, no. 1, pp. 67–77, Jan. 1998, ISSN: 02638223. DOI: 10.1016/S0263-8223(98)00036-1.
- [47] D. Ghelli and G. Minak, "Low velocity impact and compression after impact tests on thin carbon/epoxy laminates", *Composites Part B: Engineering*, vol. 42, no. 7, pp. 2067–2079, Oct. 2011, ISSN: 13598368. DOI: 10.1016/j.compositesb.2011.04.017.
- [48] T. O'Brien, "Interlaminar fracture toughness: The long and winding road to standardization", *Composites Part B: Engineering*, vol. 29, no. 1, pp. 57–62, 1998, ISSN: 13598368. DOI: 10.1016/S1359-8368(97)00013-9.
- [49] J. Moosburger-Will, J. Jäger, J. Strauch, M. Bauer, S. Strobl, F. F. Linscheid, and S. Horn, "Interphase formation and fiber matrix adhesion in carbon fiber reinforced epoxy resin: Influence of carbon fiber surface chemistry", *Composite Interfaces*, vol. 24, no. 7, pp. 691–710, Sep. 2, 2017, ISSN: 0927-6440, 1568-5543. DOI: 10.1080/09276440.2017.1267513.
- [50] J. Hughes, "The carbon fibre/epoxy interface - A review", *Composites Science and Technology*, vol. 41, no. 1, pp. 13–45, Jan. 1991, ISSN: 02663538. DOI: 10.1016/0266-3538(91)90050-Y.
- [51] A. G. Atkins, "Intermittent bonding for high toughness/high strength composites", *Journal of Materials Science*, vol. 10, no. 5, pp. 819–832, 1975, ISSN: 0022-2461. DOI: 10.1007/BF01163077.
- [52] G. Bogoeva-Gaceva, E. Mäder, L. Häussler, and K. Sahre, "Parameters affecting the interface properties in carbon fibre/epoxy systems", *Composites*, vol. 26, no. 2, pp. 103–107, Feb. 1995, ISSN: 00104361. DOI: 10.1016/0010-4361(95)90409-S.
- [53] F. R. Jones, "Serendipity in carbon fibres: Interfaces and interphases in composites", in *The Structural Integrity of Carbon Fiber Composites*, P. W. R. Beaumont, C. Soutis, and A. Hodzic, Eds., vol. 20, tex.ids: jones_2017a, Cham: Springer International Publishing, 2017, pp. 71–97, ISBN: 978-3-319-46118-2. DOI: 10.1007/978-3-319-46120-5_5.

-
- [54] H. Kishi, N. Nakao, S. Kuwashiro, and S. Matsuda, "Carbon fiber reinforced thermoplastic composites from acrylic polymer matrices: Interfacial adhesion and physical properties", *Express Polymer Letters*, vol. 11, no. 4, pp. 334–342, 2017, ISSN: 1788618X. DOI: 10.3144/expresspolymlett.2017.32.
- [55] Y. Ou, C. González, and J. J. Vilatela, "Interlaminar toughening in structural carbon fiber/epoxy composites interleaved with carbon nanotube veils", *Composites Part A: Applied Science and Manufacturing*, vol. 124, p. 105477, Sep. 2019, ISSN: 1359835X. DOI: 10.1016/j.compositesa.2019.105477.
- [56] D. Quan, F. Bologna, G. Scarselli, A. Ivankovic, and N. Murphy, "Interlaminar fracture toughness of aerospace-grade carbon fibre reinforced plastics interleaved with thermoplastic veils", *Composites Part A: Applied Science and Manufacturing*, vol. 128, p. 105642, Jan. 2020, ISSN: 1359835X. DOI: 10.1016/j.compositesa.2019.105642.
- [57] D. Quan, F. Bologna, G. Scarselli, A. Ivanković, and N. Murphy, "Mode II fracture behaviour of aerospace-grade carbon fibre/epoxy composites interleaved with thermoplastic veils", *Composites Science and Technology*, vol. 191, p. 108065, May 2020, ISSN: 02663538. DOI: 10.1016/j.compscitech.2020.108065.
- [58] D. Quan, J. L. Urdániz, and A. Ivanković, "Enhancing mode I and mode II fracture toughness of epoxy and carbon fibre reinforced epoxy composites using multi-walled carbon nanotubes", *Materials & Design*, vol. 143, pp. 81–92, Apr. 2018, ISSN: 02641275. DOI: 10.1016/j.matdes.2018.01.051.
- [59] A. R. Ravindran, R. B. Ladani, C. H. Wang, and A. P. Mouritz, "Synergistic mode II delamination toughening of composites using multi-scale carbon-based reinforcements", *Composites Part A: Applied Science and Manufacturing*, vol. 117, pp. 103–115, Feb. 2019, ISSN: 1359835X. DOI: 10.1016/j.compositesa.2018.11.011.
- [60] A. R. Ravindran, R. B. Ladani, C. H. Wang, and A. P. Mouritz, "Synergistic delamination toughening of composites using multi-scale carbon reinforcements", *Composites Part B: Engineering*, vol. 161, pp. 18–28, Mar. 2019, ISSN: 13598368. DOI: 10.1016/j.compositesb.2018.10.031.
- [61] Y. Zeng, H.-Y. Liu, Y.-W. Mai, and X.-S. Du, "Effect of nanoparticle modification on composite mode II delamination", presented at the 13th International Conference on Fracture, Beijing, China, 2013.
- [62] H.-Y. Liu, G.-T. Wang, Y.-W. Mai, and Y. Zeng, "On fracture toughness of nanoparticle modified epoxy", *Composites Part B: Engineering*, vol. 42, no. 8, pp. 2170–2175, Dec. 2011, ISSN: 13598368. DOI: 10.1016/j.compositesb.2011.05.014.

- [63] D. Carolan, A. Ivankovic, A. J. Kinloch, S. Sprenger, and A. C. Taylor, "Toughened carbon fibre-reinforced polymer composites with nanoparticle-modified epoxy matrices", *Journal of Materials Science*, vol. 52, no. 3, pp. 1767–1788, 2017, ISSN: 0022-2461. DOI: 10.1007/s10853-016-0468-5.
- [64] M. T. Tatuebu, "Charakterisierung der mechanischen Eigenschaften von partikelmodifizierten Faserverbundwerkstoffen für den Flugzeugbau", Bachelor Thesis, TU Kaiserslautern, Kaiserslautern, Germany, Apr. 29, 2020.
- [65] S. Q. Deng, P. Rosso, L. Ye, and K. Friedrich, "Interlaminar fracture of CF/EP composites modified with nano-silica", *Solid State Phenomena*, vol. 121-123, pp. 1403–1406, Mar. 2007, ISSN: 1662-9779. DOI: 10.4028/www.scientific.net/SSP.121-123.1403.
- [66] S. Deng, L. Ye, and K. Friedrich, "Fracture behaviours of epoxy nanocomposites with nano-silica at low and elevated temperatures", *Journal of Materials Science*, vol. 42, no. 8, pp. 2766–2774, Apr. 2007, ISSN: 0022-2461, 1573-4803. DOI: 10.1007/s10853-006-1420-x.
- [67] Y. Tang, L. Ye, D. Zhang, and S. Deng, "Characterization of transverse tensile, interlaminar shear and interlaminar fracture in CF/EP laminates with 10wt% and 20wt% silica nanoparticles in matrix resins", *Composites Part A: Applied Science and Manufacturing*, vol. 42, no. 12, pp. 1943–1950, Dec. 2011, ISSN: 1359835X. DOI: 10.1016/j.compositesa.2011.08.019.
- [68] J. Masters and J. Au, Eds., *Fractography of Modern Engineering Materials: Composites and Metals*, ASTM International, Jan. 1, 1987, ISBN: 978-0-8031-0950-6. DOI: 10.1520/STP948-EB.
- [69] W. Cantwell and J. Morton, "The impact resistance of composite materials - A review", *Composites*, vol. 22, no. 5, pp. 347–362, Sep. 1991, ISSN: 00104361. DOI: 10.1016/0010-4361(91)90549-V.
- [70] F. H. Gojny, M. Wichmann, U. Köpke, B. Fiedler, and K. Schulte, "Carbon nanotube-reinforced epoxy-composites: Enhanced stiffness and fracture toughness at low nanotube content", *Composites Science and Technology*, vol. 64, no. 15, pp. 2363–2371, 2004, ISSN: 0266-3538. DOI: 10.1016/j.compscitech.2004.04.002.
- [71] V. Mirjalili and P. Hubert, "Modelling of the carbon nanotube bridging effect on the toughening of polymers and experimental verification", *Composites Science and Technology*, vol. 70, no. 10, pp. 1537–1543, Sep. 30, 2010, ISSN: 02663538. DOI: 10.1016/j.compscitech.2010.05.016.
- [72] D. L. Hunston, "Composite interlaminar fracture: Effect of matrix fracture energy", *Journal of Composites Technology and Research*, vol. 6, no. 4, p. 176, 1984, ISSN: 08846804. DOI: 10.1520/CTR10842J.

-
- [73] D. Hull and T. W. Clyne, *An introduction to composite materials*, 2. ed., reprinted., ser. Cambridge solid state science series. Cambridge: Cambridge University Press, 2001, ISBN: 0-521-38855-4.
- [74] P. van Velthem, W. Ballout, J. Horion, Y.-A. Janssens, V. Destoop, T. Pardoën, and C. Bailly, "Morphology and fracture properties of toughened highly crosslinked epoxy composites: A comparative study between high and low T_g tougheners", *Composites Part B: Engineering*, vol. 101, pp. 14–20, 2016, ISSN: 13598368. DOI: 10.1016/j.compositesb.2016.06.076.
- [75] N. T. Kamar, L. T. Drzal, A. Lee, and P. Askeland, "Nanoscale toughening of carbon fiber reinforced/epoxy polymer composites (CFRPs) using a triblock copolymer", *Polymer*, vol. 111, pp. 36–47, Feb. 2017, ISSN: 00323861. DOI: 10.1016/j.polymer.2017.01.009.
- [76] A. Charles and A. Rider, "Triblock copolymer toughening of a carbon fibre-reinforced epoxy composite for bonded repair", *Polymers*, vol. 10, no. 8, p. 888, Aug. 8, 2018, ISSN: 2073-4360. DOI: 10.3390/polym10080888.
- [77] Y. Zeng, H.-Y. Liu, Y.-W. Mai, and X.-S. Du, "Improving interlaminar fracture toughness of carbon fibre/epoxy laminates by incorporation of nano-particles", *Composites Part B: Engineering*, vol. 43, no. 1, pp. 90–94, Jan. 2012, ISSN: 13598368. DOI: 10.1016/j.compositesb.2011.04.036.
- [78] P. Karapappas, A. Vavouliotis, P. Tsotra, V. Kostopoulos, and A. Paipetis, "Enhanced fracture properties of carbon reinforced composites by the addition of multi-wall carbon nanotubes", *Journal of Composite Materials*, vol. 43, no. 9, pp. 977–985, May 2009, ISSN: 0021-9983, 1530-793X. DOI: 10.1177/0021998308097735.
- [79] H. J. Sue, R. E. Jones, and E. I. Garcia-Meitin, "Fracture behaviour of model toughened composites under mode I and mode II delaminations", *Journal of Materials Science*, vol. 28, no. 23, pp. 6381–6391, Dec. 1993, ISSN: 0022-2461, 1573-4803. DOI: 10.1007/BF01352201.
- [80] N. G. Ozdemir, "Toughening of carbon fibre reinforced polymer composites with rubber nanoparticles for advanced industrial applications", *Express Polymer Letters*, vol. 10, no. 5, pp. 394–407, 2016, ISSN: 1788618X. DOI: 10.3144/expresspolymlett.2016.37.
- [81] C. E. Rogers, "Investigating the micromechanisms of mode II delamination in composite laminates", Dissertation, Imperial College London, London, UK, 2009.
- [82] D. Zhang, L. Ye, S. Deng, J. Zhang, Y. Tang, and Y. Chen, "CF/EP composite laminates with carbon black and copper chloride for improved electrical conductivity and interlaminar fracture toughness", *Composites Science and Technology*, vol. 72, no. 3, pp. 412–420, Feb. 2012, ISSN: 02663538. DOI: 10.1016/j.compscitech.2011.12.002.

- [83] Y. Ye, H. Chen, J. Wu, and C. M. Chan, "Interlaminar properties of carbon fiber composites with halloysite nanotube-toughened epoxy matrix", *Composites Science and Technology*, vol. 71, no. 5, pp. 717–723, Mar. 2011, ISSN: 02663538. DOI: 10.1016/j.compscitech.2011.01.018.
- [84] T. Yokozeki, Y. Iwahori, S. Ishiwata, and K. Enomoto, "Mechanical properties of CFRP laminates manufactured from unidirectional prepregs using CSCNT-dispersed epoxy", *Composites Part A: Applied Science and Manufacturing*, vol. 38, no. 10, pp. 2121–2130, Oct. 2007, ISSN: 1359835X. DOI: 10.1016/j.compositesa.2007.07.002.
- [85] A. Tugrul Seyhan, M. Tanoglu, and K. Schulte, "Mode I and mode II fracture toughness of E-glass non-crimp fabric/carbon nanotube (CNT) modified polymer based composites", *Engineering Fracture Mechanics*, vol. 75, no. 18, pp. 5151–5162, Dec. 2008, ISSN: 00137944. DOI: 10.1016/j.engfracmech.2008.08.003.
- [86] M. Quaresimin and R. J. Varley, "Understanding the effect of nano-modifier addition upon the properties of fibre reinforced laminates", *Composites Science and Technology*, vol. 68, no. 3, pp. 718–726, Mar. 2008, ISSN: 02663538. DOI: 10.1016/j.compscitech.2007.09.005.
- [87] L. Amaral, R. Alderliesten, and R. Benedictus, "Towards a physics-based relationship for crack growth under different loading modes", *Engineering Fracture Mechanics*, vol. 195, pp. 222–241, 2018, ISSN: 0013-7944. DOI: 10.1016/j.engfracmech.2018.04.017.
- [88] A. Kaddour, M. Hinton, P. Smith, and S Li, "Mechanical properties and details of composite laminates for the test cases used in the third world-wide failure exercise", *Journal of Composite Materials*, vol. 47, no. 20, pp. 2427–2442, Sep. 2013, ISSN: 0021-9983, 1530-793X. DOI: 10.1177/0021998313499477.
- [89] G. W. Beckermann and K. L. Pickering, "Mode I and mode II interlaminar fracture toughness of composite laminates interleaved with electrospun nanofibre veils", *Composites Part A: Applied Science and Manufacturing*, vol. 72, pp. 11–21, May 2015, ISSN: 1359835X. DOI: 10.1016/j.compositesa.2015.01.028.
- [90] Z. Wang, X. Huang, L. Bai, R. Du, Y. Liu, Y. Zhang, and G. Zhao, "Effect of micro-Al₂O₃ contents on mechanical property of carbon fiber reinforced epoxy matrix composites", *Composites Part B: Engineering*, vol. 91, pp. 392–398, Apr. 2016, ISSN: 13598368. DOI: 10.1016/j.compositesb.2016.01.052.
- [91] E. M. Woo and K. L. Mao, "Evaluation of interlaminar-toughened poly(etherImide)-modified epoxy/carbon fiber composites", *Polymer Composites*, vol. 17, no. 6, pp. 799–805, Dec. 1996, ISSN: 0272-8397, 1548-0569. DOI: 10.1002/pc.10672.

-
- [92] P. Bruckbauer, "Struktur-Eigenschafts-Beziehungen von Interphasen zwischen-Epoxidharz und thermoplastischen Funktionsschichten für Faserverbundwerkstoffe", ISBN: 9783843938945, Dissertation, TU München, München, 2018. [Online]. Available: <https://mediatum.ub.tum.de/1427427>.
- [93] Y. Tang, L. Ye, Z. Zhang, and K. Friedrich, "Interlaminar fracture toughness and CAI strength of fibre-reinforced composites with nanoparticles - A review", *Composites Science and Technology*, vol. 86, pp. 26–37, 2013, ISSN: 0266-3538. DOI: 10.1016/j.compscitech.2013.06.021.
- [94] Z. Daneshjoo, M. M. Shokrieh, M. Fakoor, R. Alderliesten, and D. Zarouchas, "Physics of delamination onset in unidirectional composite laminates under mixed-mode I/II loading", *Engineering Fracture Mechanics*, vol. 211, pp. 82–98, Apr. 2019, ISSN: 00137944. DOI: 10.1016/j.engfracmech.2019.02.013.
- [95] S. H. Goodman, Ed., *Handbook of thermoset plastics*, 2nd ed, Westwood, N.J: Noyes Publications, 1998, 582 pp., ISBN: 978-0-8155-1421-3.
- [96] B. Bilyeu, W. Brostow, and K. P. Menard, "Epoxy thermosets and their applications I: Chemical structures and applications", *Journal of Materials Education*, vol. 21, no. 5, pp. 281–286, 1999.
- [97] G. Couture, L. Granado, F. Fanget, B. Boutevin, and S. Caillol, "Limonene-based epoxy: Anhydride thermoset reaction study", *Molecules*, vol. 23, no. 11, p. 2739, 2018, ISSN: 1420-3049. DOI: 10.3390/molecules23112739.
- [98] H. Lee and K. Neville, *Handbook of epoxy resins*. London: McGraw-Hill, 1982, ISBN: 978-0-07-036997-9.
- [99] M.-P. Pham, "Theoretical studies of mechanisms of epoxy curing systems", Dissertation, The University of Utah, Salt Lake City, Utah, USA, 2011.
- [100] F. Kolár and J. Svítlová, "Kinetics and mechanisms of curing epoxy/anhydride systems", *Acta Geodyn. Geomater.* Vol. 3, no. 147, p. 8, 2007.
- [101] E. M. Petrie, *Epoxy adhesive formulations*. New York: McGraw-Hill, 2006, 535 pp., ISBN: 978-0-07-145544-2.
- [102] I. M. Ward and J. Sweeney, *An introduction to the mechanical properties of solid polymers*, 2nd ed. Chichester, West Sussex, England: Wiley, 2004, Backup Publisher: ebrary, Inc, ISBN: 978-0-471-49626-7.
- [103] M. Neitzel, P. Mitschang, and U. Breuer, Eds., *Handbuch Verbundwerkstoffe: Werkstoffe, Verarbeitung, Anwendung*, 2nd ed., München: Carl Hanser Verlag GmbH & Co. KG, Jul. 2014, ISBN: 978-3-446-43696-1.
- [104] M. A. Boyle, C. J. Martin, and J. D. Neuner, "Epoxy resins", *ASM Handbook Volume 21 Composites*, pp. 78–89, 2001.

- [105] M. Philipp, "Nichtgleichgewichtsphänomene, Strukturbildung und Grenzflächeneinflüsse in netzwerkbildenden Systemen aus optischer und akustischer Sicht", Dissertation, Universität Luxemburg, Luxemburg, 2009.
- [106] A. I. Barabanova, B. V. Lokshin, E. P. Kharitonova, E. S. Afanasyev, A. A. Askadskii, and O. E. Philippova, "Curing cycloaliphatic epoxy resin with 4-methylhexahydrophthalic anhydride: Catalyzed vs. uncatalyzed reaction", *Polymer*, vol. 178, p. 121 590, Sep. 2019, ISSN: 00323861. DOI: 10.1016/j.polymer.2019.121590.
- [107] B. Elvers and F. Ullmann, Eds., *Ullmann's polymers and plastics: products and processes. Volume 4*, Weinheim: Wiley-VCH Verlag GmbH & Co. KGaA, 2016, 1407 pp., ISBN: 978-3-527-33823-8.
- [108] G.-H. Kwak, S.-J. Park, and J.-R. Lee, "Thermal stability and mechanical behavior of cycloaliphatic-DGEBA epoxy blend system initiated by cationic latent catalyst", *Journal of Applied Polymer Science*, vol. 78, no. 2, pp. 290–297, 2000, ISSN: 1097-4628. DOI: 10.1002/1097-4628(20001010)78:2<290::AID-APP80>3.0.CO;2-9.
- [109] A. J. Kinloch, "Mechanics and mechanisms of fracture of thermosetting epoxy polymers", in *Epoxy Resins and Composites I*, ser. Advances in Polymer Science, vol. 72, Springer Berlin Heidelberg, 1985, pp. 45–67, ISBN: 978-3-540-15546-1.
- [110] J. Karger-Kocsis and K. Friedrich, "Fatigue crack propagation and related failure in modified, anhydride-cured epoxy resins", *Colloid & Polymer Science*, vol. 270, no. 6, pp. 549–562, 1992, ISSN: 0303-402X. DOI: 10.1007/BF00658286.
- [111] M. Harsch, "Methoden und Ansätze zur spannungsarmen Vernetzung von-Epoxidharzen", ISBN: 978-3-934930-72-8, Dissertation, Institut für Verbundwerkstoffe, Kaiserslautern, 2008, 150 pp.
- [112] A. I. Barabanova, B. V. Lokshin, E. P. Kharitonova, I. V. Karandi, E. S. Afanasyev, A. A. Askadskii, and O. E. Philippova, "Cycloaliphatic epoxy resin cured with anhydride in the absence of catalyst", *Colloid and Polymer Science*, vol. 297, no. 3, pp. 409–416, Mar. 1, 2019, ISSN: 1435-1536. DOI: 10.1007/s00396-018-4430-8.
- [113] E. M. Woo and J. C. Seferis, "Cure kinetics of epoxy/anhydride thermosetting matrix systems", *Journal of Applied Polymer Science*, vol. 40, no. 7, pp. 1237–1256, 1990, ISSN: 1097-4628. DOI: 10.1002/app.1990.070400713.
- [114] L. Matějka, J. Lövy, S. Pokorný, K. Bouchal, and K. Dušek, "Curing epoxy resins with anhydrides. Model reactions and reaction mechanism", *Journal of Polymer Science: Polymer Chemistry Edition*, vol. 21, no. 10, pp. 2873–2885, 1983, ISSN: 1542-9369. DOI: 10.1002/pol.1983.170211003.
- [115] G. Levita, S. de Petris, A. Marchetti, and A. Lazzeri, "Crosslink density and fracture toughness of epoxy resins", *Journal of Materials Science*, vol. 26, no. 9, pp. 2348–2352, 1991, ISSN: 0022-2461. DOI: 10.1007/BF01130180.

-
- [116] M. K. Umboh, T. Adachi, T. Nemoto, M. Higuchi, and Z. Major, "Non-stoichiometric curing effect on fracture toughness of nanosilica particulate-reinforced epoxy composites", *Journal of Materials Science*, vol. 49, no. 21, pp. 7454–7461, Nov. 2014, ISSN: 0022-2461, 1573-4803. DOI: 10.1007/s10853-014-8450-6.
- [117] A. Zotti, S. Zuppolini, M. Zarrelli, and A. Borriello, "Fracture toughening mechanisms in epoxy adhesives", in *Adhesives - Applications and Properties*, A. Rudawska, Ed., InTech, Nov. 23, 2016, ISBN: 978-953-51-2783-3. DOI: 10.5772/65250.
- [118] B. T. Marouf, Y.-W. Mai, R. Bagheri, and R. A. Pearson, "Toughening of epoxy nanocomposites: Nano and hybrid effects", *Polymer Reviews*, vol. 56, no. 1, pp. 70–112, 2016, ISSN: 1558-3724. DOI: 10.1080/15583724.2015.1086368.
- [119] K. Utaloff, M. H. Kothmann, M. Ciesielski, M. Döring, T. Neumeyer, V. Altstädt, I. Gorman, and M. Henningsen, "Improvement of fracture toughness and glass transition temperature of DGEBA-based epoxy systems using toughening and crosslinking modifiers", *Polymer Engineering & Science*, vol. 59, no. 1, pp. 86–95, Jan. 2019, ISSN: 00323888. DOI: 10.1002/pen.24870.
- [120] B. Wetzels, "Mechanische Eigenschaften von Nanoverbundwerkstoffen aus Epoxidharz und keramischen Nanopartikeln", ISBN: 3-934930-65-4, Ph.D. dissertation, Institut für Verbundwerkstoffe, Kaiserslautern, 2006.
- [121] T. H. Hsieh, A. J. Kinloch, K. Masania, A. C. Taylor, and S. Sprenger, "The mechanisms and mechanics of the toughening of epoxy polymers modified with silica nanoparticles", *Polymer*, vol. 51, no. 26, pp. 6284–6294, 2010, ISSN: 0032-3861. DOI: 10.1016/j.polymer.2010.10.048.
- [122] H. Zhang, Z. Zhang, K. Friedrich, and C. Eger, "Property improvements of in situ epoxy nanocomposites with reduced interparticle distance at high nanosilica content", *Acta Materialia*, vol. 54, no. 7, pp. 1833–1842, 2006, ISSN: 13596454. DOI: 10.1016/j.actamat.2005.12.009.
- [123] E. Zohar, S. Baruch, M. Shneider, H. Dodiuk, S. Kenig, R. Tenne, and H. D. Wagner, "The effect of WS₂ nanotubes on the properties of epoxy-based nanocomposites", *Journal of Adhesion Science and Technology*, vol. 25, no. 13, pp. 1603–1617, 2012, ISSN: 0169-4243. DOI: 10.1163/016942410X524138.
- [124] A. J. Kinloch, M. L. Yuen, and S. D. Jenkins, "Thermoplastic-toughened epoxy polymers", *Journal of Materials Science*, vol. 29, no. 14, pp. 3781–3790, 1994, ISSN: 0022-2461. DOI: 10.1007/BF00357349.
- [125] S. P. Priya and S. K. Rai, "Studies on the mechanical performance of PMMA toughened epoxy–silk and PC toughened epoxy–silk fabric composites", *Journal of Reinforced Plastics and Composites*, vol. 25, no. 1, pp. 33–41, 2016, ISSN: 0731-6844. DOI: 10.1177/0731684406055453.

- [126] L. Becu-Longuet, A. Bonnet, C. Pichot, H. Sautereau, and A. Maazouz, "Epoxy networks toughened by core-shell particles: Influence of the particle structure and size on the rheological and mechanical properties", *Journal of Applied Polymer Science*, vol. 72, no. 6, pp. 849–858, 1999, ISSN: 0021-8995. DOI: 10.1002/(SICI)1097-4628(19990509)72:6<849::AID-APP10>3.0.CO;2-R.
- [127] M. Imanaka, I. Narita, Y. Nakamura, S. Hisaka, K. Fujiwara, S. Yoshida, and K. Hara, "Fracture properties of epoxy polymers modified with cross-linked and core-shell rubber particles", *Journal of Materials Science*, Sep. 23, 2020, ISSN: 0022-2461, 1573-4803. DOI: 10.1007/s10853-020-05339-2.
- [128] O. Gryshchuk and J. Karger-Kocsis, "Influence of the type of epoxy hardener on the structure and properties of interpenetrated vinyl ester/epoxy resins", *Journal of Polymer Science Part A: Polymer Chemistry*, vol. 42, no. 21, pp. 5471–5481, 2004. DOI: 10.1002/pola.20371.
- [129] M. Sharifi, C. Jang, C. F. Abrams, and G. R. Palmese, "Epoxy polymer networks with improved thermal and mechanical properties via controlled dispersion of reactive toughening agents", *Macromolecules*, vol. 48, no. 20, pp. 7495–7502, 2015, ISSN: 0024-9297. DOI: 10.1021/acs.macromol.5b00677.
- [130] I. Ryl, "Einfluss verschiedener Parameter auf die Domänengröße von partiell reagierten Substrukturen in Epoxidharzen", Bachelor Thesis, TU Hamburg-Harburg, Jul. 4, 2017.
- [131] A. Klingler and B. Wetzel, "Fatigue crack propagation in triblock copolymer toughened epoxy nanocomposites", *Polymer Engineering & Science*, vol. 57, no. 6, pp. 579–587, 2017. DOI: 10.1002/pen.24558.
- [132] J. Chen and A. C. Taylor, "Epoxy modified with triblock copolymers: Morphology, mechanical properties and fracture mechanisms", *Journal of Materials Science*, vol. 47, no. 11, pp. 4546–4560, 2012, ISSN: 0022-2461. DOI: 10.1007/s10853-012-6313-6.
- [133] R. M. Hydro and R. A. Pearson, "Epoxy toughened with triblock copolymers", *Journal of Polymer Science Part B: Polymer Physics*, vol. 45, no. 12, pp. 1470–1481, 2007, ISSN: 0887-6266. DOI: 10.1002/polb.21166.
- [134] L. M. Sáiz, A. B. Orofino, E. S. Rodríguez, I. A. Zucchi, and R. J. J. Williams, "Epoxy formulation including an acrylic triblock copolymer adapted for use in filament winding", *Polymer Engineering & Science*, vol. 56, no. 10, pp. 1153–1159, 2016, ISSN: 00323888. DOI: 10.1002/pen.24348.
- [135] T. H. Hsieh, A. J. Kinloch, A. C. Taylor, and I. A. Kinloch, "The effect of carbon nanotubes on the fracture toughness and fatigue performance of a thermosetting epoxy polymer", *Journal of Materials Science*, vol. 46, no. 23, pp. 7525–7535, 2011, ISSN: 0022-2461. DOI: 10.1007/s10853-011-5724-0.

-
- [136] S. Chandrasekaran, N. Sato, F. Tölle, R. Mülhaupt, B. Fiedler, and K. Schulte, "Fracture toughness and failure mechanism of graphene based epoxy composites", *Composites Science and Technology*, vol. 97, pp. 90–99, 2014, ISSN: 0266-3538. DOI: 10.1016/j.compscitech.2014.03.014.
- [137] J. N. Sultan, R. C. Liable, and F. J. McGarry, "Microstructure of two-phase polymers", *Polym. Symp.*, no. 16, pp. 127–136, 1971.
- [138] R. A. Pearson and A. F. Yee, "Toughening mechanisms in elastomer-modified epoxies: Part 3: The effect of cross-link density", *Journal of Materials Science*, vol. 24, no. 7, pp. 2571–2580, 1989, ISSN: 0022-2461. DOI: 10.1007/BF01174528.
- [139] J.-F. Hwang, J. A. Manson, R. W. Hertzberg, G. A. Miller, and L. H. Sperling, "Structure-property relationships in rubber-toughened epoxies", *Polymer Engineering and Science*, vol. 29, no. 20, pp. 1466–1476, Oct. 1989, ISSN: 0032-3888, 1548-2634. DOI: 10.1002/pen.760292008.
- [140] P. Peyser and Y. Steg, "The fracture behavior of CTBN modified epoxy", *The Journal of Adhesion*, vol. 25, no. 2, pp. 133–144, Apr. 1988, ISSN: 0021-8464, 1545-5823. DOI: 10.1080/00218468808071255.
- [141] N Chikhi, S Fellahi, and M Bakar, "Modification of epoxy resin using reactive liquid (ATBN) rubber", *European Polymer Journal*, vol. 38, no. 2, pp. 251–264, Feb. 2002, ISSN: 00143057. DOI: 10.1016/S0014-3057(01)00194-X.
- [142] B. Jansen, K. Tamminga, H. Meijer, and P. Lemstra, "Preparation of thermoset rubbery epoxy particles as novel toughening modifiers for glassy epoxy resins", *Polymer*, vol. 40, no. 20, pp. 5601–5607, Sep. 1999, ISSN: 00323861. DOI: 10.1016/S0032-3861(98)00774-5.
- [143] R. M. Medina Barrón, "Rubber toughened and nanoparticle reinforced epoxy composites", ISBN: 978-3-934930-80-3, Dissertation, Institut für Verbundwerkstoffe, Kaiserslautern, 2009.
- [144] D. Quan, R. A. Pearson, and A. Ivankovic, "Interaction of toughening mechanisms in ternary nanocomposites", *Polymer Composites*, vol. 33, p. 1516, 2017, ISSN: 0272-8397. DOI: 10.1002/pc.24368.
- [145] D. Carolan, A. J. Kinloch, A. Ivankovic, S. Sprenger, and A. C. Taylor, "Mechanical and fracture performance of carbon fibre reinforced composites with nanoparticle modified matrices", *Procedia Structural Integrity*, vol. 2, pp. 96–103, 2016, ISSN: 24523216. DOI: 10.1016/j.prostr.2016.06.013.
- [146] B. Wetzels, P. Rosso, F. Hauptert, and K. Friedrich, "Epoxy nanocomposites – fracture and toughening mechanisms", *Engineering Fracture Mechanics*, vol. 73, no. 16, pp. 2375–2398, 2006, ISSN: 0013-7944. DOI: 10.1016/j.engfracmech.2006.05.018.

- [147] S. Sprenger, "Epoxy resins modified with elastomers and surface-modified silica nanoparticles", *Polymer*, vol. 54, no. 18, pp. 4790–4797, 2013, ISSN: 0032-3861. DOI: 10.1016/j.polymer.2013.06.011.
- [148] D. Carolan, A. Ivankovic, A. J. Kinloch, S. Sprenger, and A. C. Taylor, "Toughening of epoxy-based hybrid nanocomposites", *Polymer*, vol. 97, pp. 179–190, 2016, ISSN: 0032-3861. DOI: 10.1016/j.polymer.2016.05.007.
- [149] Y. T. Wang, C. S. Wang, H. Y. Yin, L. L. Wang, H. F. Xie, and R. S. Cheng, "Carboxyl-terminated butadiene-acrylonitrile-toughened epoxy/carboxyl-modified carbon nanotube nanocomposites: Thermal and mechanical properties", *Express Polymer Letters*, vol. 6, no. 9, pp. 719–728, 2012, ISSN: 1788618X. DOI: 10.3144/expresspolymlett.2012.77.
- [150] C. Ocando, A. Tercjak, and I. Mondragon, "Nanostructured systems based on SBS epoxidized triblock copolymers and well-dispersed alumina/epoxy matrix composites", *Composites Science and Technology*, vol. 70, no. 7, pp. 1106–1112, 2010, ISSN: 0266-3538. DOI: 10.1016/j.compscitech.2010.02.020.
- [151] A. Bajpai, A. K. Alapati, and B. Wetzel, "Toughening and mechanical properties of epoxy modified with block co-polymers and MWCNTs", *Procedia Structural Integrity*, vol. 2, pp. 104–111, 2016, ISSN: 24523216. DOI: 10.1016/j.prostr.2016.06.014.
- [152] T. Gómez-del Río, A. Salazar, R. A. Pearson, and J. Rodríguez, "Fracture behaviour of epoxy nanocomposites modified with triblock copolymers and carbon nanotubes", *Composites Part B: Engineering*, vol. 87, pp. 343–349, 2016, ISSN: 13598368. DOI: 10.1016/j.compositesb.2015.08.085.
- [153] G. Gao, C. Zhou, H. Yang, and H. Zhang, "Influence of core-shell rubber particles synthesized with different initiation systems on the impact toughness of modified polystyrene", *Journal of Applied Polymer Science*, vol. 103, no. 2, pp. 738–744, 2007, ISSN: 1097-4628. DOI: 10.1002/app.25030.
- [154] Z. Li, S. Song, X. Zhao, X. Lv, and S. Sun, "Grafting modification of the reactive core-shell particles to enhance the toughening ability of polylactide", *Materials*, vol. 10, no. 8, p. 957, Aug. 16, 2017, ISSN: 1996-1944. DOI: 10.3390/ma10080957.
- [155] R. A. Ramli, W. A. Laftah, and S. Hashim, "Core-shell polymers: A review", *RSC Advances*, vol. 3, no. 36, p. 15 543, 2013, ISSN: 2046-2069. DOI: 10.1039/c3ra41296b.
- [156] K.-F. Lin and Y.-D. Shieh, "Core-shell particles designed for toughening the epoxy resins. II. core-shell-particle-toughened epoxy resins", *Journal of Applied Polymer Science*, vol. 70, no. 12, pp. 2313–2322, 1998, ISSN: 0021-8995.

-
- [157] D. S. Kim, K. Cho, J. K. Kim, and C. E. Park, "Effects of particle size and rubber content on fracture toughness in rubber-modified epoxies", *Polymer Engineering & Science*, vol. 36, no. 6, pp. 755–768, Mar. 1996, ISSN: 0032-3888, 1548-2634. DOI: 10.1002/pen.10463.
- [158] M. Jux, B. Finke, T. Mahrholz, M. Sinapius, A. Kwade, and C. Schilde, "Effects of Al(OH)O nanoparticle agglomerate size in epoxy resin on tension, bending, and fracture properties", *Journal of Nanoparticle Research*, vol. 19, no. 4, p. 139, Apr. 2017, ISSN: 1388-0764, 1572-896X. DOI: 10.1007/s11051-017-3831-9.
- [159] B. Lauke, "Fracture toughness modelling of polymers filled with inhomogeneously distributed rigid spherical particles", *Express Polymer Letters*, vol. 11, no. 7, pp. 545–554, 2017, ISSN: 1788618X. DOI: 10.3144/expresspolymlett.2017.52.
- [160] J. Chen, A. J. Kinloch, S. Sprenger, and A. C. Taylor, "The mechanical properties and toughening mechanisms of an epoxy polymer modified with polysiloxane-based core-shell particles", *Polymer*, vol. 54, no. 16, pp. 4276–4289, 2013, ISSN: 0032-3861. DOI: 10.1016/j.polymer.2013.06.009.
- [161] G. Giannakopoulos, K. Masania, and A. C. Taylor, "Toughening of epoxy using core-shell particles", *Journal of Materials Science*, vol. 46, no. 2, pp. 327–338, 2011, ISSN: 0022-2461. DOI: 10.1007/s10853-010-4816-6.
- [162] F. S. Bates, "Polymer-polymer phase behavior", *Science*, vol. 251, no. 4996, pp. 898–905, 1991, ISSN: 0036-8075. DOI: 10.1126/science.251.4996.898.
- [163] Y. Mai and A. Eisenberg, "Self-assembly of block copolymers", *Chemical Society Reviews*, vol. 41, no. 18, p. 5969, 2012, ISSN: 0306-0012. DOI: 10.1039/c2cs35115c.
- [164] M. Szwarc, M. Levy, and R. Milkovich, "Polymerization initiated by electron transfer to monomer. a new method of formation of block copolymers", *Journal of the American Chemical Society*, vol. 78, no. 11, pp. 2656–2657, Jun. 1956, ISSN: 0002-7863, 1520-5126. DOI: 10.1021/ja01592a101.
- [165] D. Leibig, J. Morsbach, E. Grune, J. Herzberger, A. H. Müller, and H. Frey, "Die lebende anionische Polymerisation: Quicklebendig seit 60 Jahren", *Chemie in unserer Zeit*, vol. 51, no. 4, pp. 254–263, Aug. 2017, ISSN: 00092851. DOI: 10.1002/ciuz.201700774.
- [166] M. T. Bashar, U. Sundararaj, and P. Mertiny, "Morphology and mechanical properties of nanostructured acrylic tri-block-copolymer modified epoxy", *Polymer Engineering & Science*, vol. 54, no. 5, pp. 1047–1055, 2014, ISSN: 00323888. DOI: 10.1002/pen.23648.
- [167] H. Kishi, Y. Kunimitsu, J. Imade, S. Oshita, Y. Morishita, and M. Asada, "Nanophase structures and mechanical properties of epoxy/acryl triblock copolymer alloys", *Polymer*, vol. 52, no. 3, pp. 760–768, 2011, ISSN: 0032-3861. DOI: 10.1016/j.polymer.2010.12.025.

- [168] J. M. Dean, R. B. Grubbs, W. Saad, R. F. Cook, and F. S. Bates, "Mechanical properties of block copolymer vesicle and micelle modified epoxies", *Journal of Polymer Science Part B: Polymer Physics*, vol. 41, no. 20, pp. 2444–2456, 2003, ISSN: 0887-6266. DOI: 10.1002/polb.10595.
- [169] P. M. Lipic, F. S. Bates, and M. A. Hillmyer, "Nanostructured thermosets from self-assembled amphiphilic block copolymer/epoxy resin mixtures", *Journal of the American Chemical Society*, vol. 120, no. 35, pp. 8963–8970, 1998, ISSN: 0002-7863. DOI: 10.1021/ja981544s.
- [170] J. M. Dean, P. M. Lipic, R. B. Grubbs, R. F. Cook, and F. S. Bates, "Micellar structure and mechanical properties of block copolymer-modified epoxies", *Journal of Polymer Science Part B: Polymer Physics*, vol. 39, no. 23, pp. 2996–3010, 2001, ISSN: 0887-6266. DOI: 10.1002/polb.10062.
- [171] M. Bonnet, *Kunststoffe in der Ingenieur Anwendung*. Wiesbaden: Vieweg+Teubner, 2009, ISBN: 978-3-8348-0349-8. DOI: 10.1007/978-3-8348-9303-1.
- [172] H. Kishi, Y. Kunimitsu, Y. Nakashima, T. Abe, J. Imade, S. Oshita, Y. Morishita, and M. Asada, "Control of nanostructures generated in epoxy matrices blended with PMMA-*b*-PnBA-*b*-PMMA triblock copolymers", *Express Polymer Letters*, vol. 9, no. 1, pp. 23–35, 2015, ISSN: 1788618X. DOI: 10.3144/expresspolymlett.2015.4.
- [173] E. M. Redline, C. Declet-Perez, F. S. Bates, and L. F. Francis, "Effect of block copolymer concentration and core composition on toughening epoxies", *Polymer*, vol. 55, no. 16, pp. 4172–4181, 2014, ISSN: 0032-3861. DOI: 10.1016/j.polymer.2014.06.016.
- [174] A. Bajpai, B. Wetzel, A. Klingler, and K. Friedrich, "Mechanical properties and fracture behavior of high-performance epoxy nanocomposites modified with block polymer and core-shell rubber particles", *Journal of Applied Polymer Science*, vol. 137, no. 11, p. 48471, 2020, ISSN: 1097-4628. DOI: 10.1002/app.48471.
- [175] S. Ritzenthaler, F. Court, E. Girard-Reydet, L. Leibler, and J. P. Pascault, "ABC triblock copolymers-epoxy-diamine blends. 2. parameters controlling the morphologies and properties", *Macromolecules*, vol. 36, no. 1, pp. 118–126, Jan. 2003, ISSN: 0024-9297, 1520-5835. DOI: 10.1021/ma0211075.
- [176] A. Bajpai, B. Wetzel, and K. Friedrich, "High strength epoxy system modified with soft block copolymer and stiff core-shell rubber nanoparticles: Morphology, mechanical properties, and fracture mechanisms", *Express Polymer Letters*, vol. 14, no. 4, pp. 384–399, 2020, ISSN: 1788618X. DOI: 10.3144/expresspolymlett.2020.32.
- [177] R. Barsotti, "Nanostrength - Block copolymers for epoxy toughening", Thermoset Resin Formulators Association at the Hilton Suites Chicago Magnificent Mile in Chicago, Illinois, 2008. [Online]. Available: <http://www.trfa.org/erc/docretrieval/uploadedfiles/>

- Technical%20Papers/2008%20Meeting/Barsotti-Arkema_paper-Block_copolymers.pdf.
- [178] C. Fodor, G. Kali, R. Thomann, Y. Thomann, B. Iván, and R. Mülhaupt, "Nanophasic morphologies as a function of the composition and molecular weight of the macromolecular cross-linker in poly(n-vinylimidazole)-l-poly(tetrahydrofuran) amphiphilic conetworks: Bicontinuous domain structure in broad composition ranges", *RSC Advances*, vol. 7, no. 12, pp. 6827–6834, 2017, ISSN: 2046-2069. DOI: 10.1039/c6ra25356c.
- [179] S. Ritzenthaler, E. Girard-Reydet, and J. P. Pascault, "Influence of epoxy hardener on miscibility of blends of poly(methyl methacrylate) and epoxy networks", *Polymer*, vol. 41, no. 16, pp. 6375–6386, 2000, ISSN: 0032-3861. DOI: 10.1016/S0032-3861(99)00817-4.
- [180] H. E. Romeo, I. A. Zucchi, M. Rico, C. E. Hoppe, and R. J. J. Williams, "From spherical micelles to hexagonally packed cylinders: The cure cycle determines nanostructures generated in block copolymer/epoxy blends", *Macromolecules*, vol. 46, no. 12, pp. 4854–4861, 2013, ISSN: 0024-9297. DOI: 10.1021/ma400778s.
- [181] F. Meng, S. Zheng, H. Li, Q. Liang, and T. Liu, "Formation of ordered nanostructures in epoxy thermosets: A mechanism of reaction-induced microphase separation", *Macromolecules*, vol. 39, no. 15, pp. 5072–5080, 2006, ISSN: 0024-9297. DOI: 10.1021/ma060004%2B.
- [182] R. J. J. Williams, B. A. Rozenberg, and J.-P. Pascault, "Reaction-induced phase separation in modified thermosetting polymers", in *Polymer Analysis Polymer Physics*, ser. Advances in Polymer Science, vol. 128, Berlin, Heidelberg: Springer Berlin Heidelberg, 1997, pp. 95–156, ISBN: 978-3-540-61218-6.
- [183] C. Ocando, A. Tercjak, M. D. Martín, J. A. Ramos, M. Campo, and I. Mondragon, "Morphology development in thermosetting mixtures through the variation on chemical functionalization degree of poly(styrene- b -butadiene) diblock copolymer modifiers. thermomechanical properties", *Macromolecules*, vol. 42, no. 16, pp. 6215–6224, 2009, ISSN: 0024-9297. DOI: 10.1021/ma900885b.
- [184] W. Fan, L. Wang, and S. Zheng, "Nanostructures in thermosetting blends of epoxy resin with polydimethylsiloxane-block-polycaprolactone-block-polystyrene ABC triblock copolymer", *Macromolecules*, vol. 42, no. 1, pp. 327–336, 2009, ISSN: 0024-9297. DOI: 10.1021/ma8018014.
- [185] M. Asada, S. Oshita, Y. Morishita, Y. Nakashima, Y. Kunimitsu, and H. Kishi, "Effect of miscible PMMA chain length on disordered morphologies in epoxy/PMMA-b-PnBA-b-PMMA blends by in situ simultaneous SAXS/DSC", *Polymer*, vol. 105, pp. 172–179, 2016, ISSN: 0032-3861. DOI: 10.1016/j.polymer.2016.10.025.

- [186] G. Sadowski, *Thermodynamik der Polymerlösungen*, ser. Berichte aus der Thermodynamik. Aachen: Shaker, 2003, 257 pp., ISBN: 978-3-8322-1252-0.
- [187] S. Z. D. Cheng, *Phase transitions in polymers: the role of metastable states*, 1st ed. Amsterdam ; Boston: Elsevier, 2008, 307 pp., ISBN: 978-0-444-51911-5.
- [188] H. Kishi, Y. Kunimitsu, Y. Nakashima, J. Imade, S. Oshita, Y. Morishita, and M. Asada, "Relationship between the mechanical properties of epoxy/PMMA-b-PnBA-b-PMMA block copolymer blends and their three-dimensional nanostructures", *Express Polymer Letters*, vol. 11, no. 10, pp. 765–777, 2017, ISSN: 1788618X. DOI: 10.3144/expresspolymlett.2017.74.
- [189] H. M. Chong and A. C. Taylor, "The microstructure and fracture performance of styrene–butadiene–methylmethacrylate block copolymer-modified epoxy polymers", *Journal of Materials Science*, vol. 48, no. 19, pp. 6762–6777, 2013, ISSN: 0022-2461. DOI: 10.1007/s10853-013-7481-8.
- [190] K. Faber and A. Evans, "Crack deflection processes - I. Theory", *Acta Metallurgica*, vol. 31, no. 4, pp. 565–576, Apr. 1983, ISSN: 00016160. DOI: 10.1016/0001-6160(83)90046-9.
- [191] K. Faber and A. Evans, "Crack deflection processes - II. Experiment", *Acta Metallurgica*, vol. 31, no. 4, pp. 577–584, Apr. 1983, ISSN: 00016160. DOI: 10.1016/0001-6160(83)90047-0.
- [192] S. Zhao, L. S. Schadler, R. Duncan, H. Hillborg, and T. Auletta, "Mechanisms leading to improved mechanical performance in nanoscale alumina filled epoxy", *Nanocomposites - Processing, Characterization, Properties, Applications and Modelling, selected papers from Nanocomposite Special Symposium of ACCM-5, with regular papers*, vol. 68, no. 14, pp. 2965–2975, 2008, ISSN: 0266-3538. DOI: 10.1016/j.compscitech.2008.01.009.
- [193] D. Quan, N. Murphy, P. Cardiff, and A. Ivankovic, "The intrinsic fracture property of a rubber-modified epoxy adhesive: Geometrical transferability", *Engineering Fracture Mechanics*, vol. 203, pp. 240–249, Nov. 2018, ISSN: 00137944. DOI: 10.1016/j.engfracmech.2018.04.035.
- [194] K. B. Broberg, *Cracks and Fracture*. Burlington: Elsevier, 1999, ISBN: 978-0-08-050327-1.
- [195] B. Lauke, "On the effect of particle size on fracture toughness of polymer composites", *Composites Science and Technology*, vol. 68, no. 15, pp. 3365–3372, Dec. 2008, ISSN: 02663538. DOI: 10.1016/j.compscitech.2008.09.011.
- [196] M. F. Kanninen and C. H. Popelar, *Advanced fracture mechanics*, ser. Oxford engineering science series 15. New York: Oxford University Press, 1985, 563 pp., ISBN: 978-0-19-503532-2.

-
- [197] Y. Huang and A. J. Kinloch, "Modelling of the toughening mechanisms in rubber-modified epoxy polymers", *Journal of Materials Science*, vol. 27, no. 10, pp. 2763–2769, 1992, ISSN: 0022-2461. DOI: 10.1007/BF00540703.
- [198] G. H. Michler, *Kunststoff-Mikromechanik: Morphologie, Deformations- und Bruchmechanismen*. München: C. Hanser, 1992, 384 pp., ISBN: 978-3-446-17068-1.
- [199] A. J. Kinloch, "Relationships between the microstructure and fracture behavior of rubber-toughened thermosetting polymers", in *Rubber-Toughened Plastics*, C. K. Riew, Ed., vol. 222, Series Title: Advances in Chemistry, Washington, DC: American Chemical Society, May 5, 1989, pp. 67–91, ISBN: 978-0-8412-2404-9. DOI: 10.1021/ba-1989-0222.ch003.
- [200] R. Bagheri and R. A. Pearson, "Role of particle cavitation in rubber-toughened epoxies: II. Inter-particle distance", *Polymer*, vol. 41, no. 1, pp. 269–276, 2000, ISSN: 0032-3861. DOI: 10.1016/S0032-3861(99)00126-3.
- [201] R. A. Pearson and A. F. Yee, "Influence of particle size and particle size distribution on toughening mechanisms in rubber-modified epoxies", *Journal of Materials Science*, vol. 26, no. 14, pp. 3828–3844, 1991, ISSN: 0022-2461. DOI: 10.1007/BF01184979.
- [202] K.-Y. Kim, L. Ye, and K.-M. Phoa, "Interlaminar fracture toughness of CF/PEI and GF/PEI composites at elevated temperatures", *Applied Composite Materials*, vol. 11, no. 3, pp. 173–190, 2004, ISSN: 0929-189X. DOI: 10.1023/B:ACMA.0000026586.12629.7e.
- [203] R. Bagheri and R. A. Pearson, "Role of particle cavitation in rubber-toughened epoxies: I. Microvoid toughening", *Polymer*, vol. 37, no. 20, pp. 4529–4538, 1996, ISSN: 0032-3861. DOI: 10.1016/0032-3861(96)00295-9.
- [204] Y. Huang and A. J. Kinloch, "The role of plastic void growth in the fracture of rubber-toughened epoxy polymers", *Journal of Materials Science Letters*, vol. 11, no. 8, pp. 484–487, 1992, ISSN: 0261-8028. DOI: 10.1007/BF00731112. [Online]. Available: <http://dx.doi.org/10.1007/BF00731112>.
- [205] S.-Y. Fu, X.-Q. Feng, B. Lauke, and Y.-W. Mai, "Effects of particle size, particle/matrix interface adhesion and particle loading on mechanical properties of particulate-polymer composites", *Composites Part B: Engineering*, vol. 39, no. 6, pp. 933–961, Sep. 2008, ISSN: 13598368. DOI: 10.1016/j.compositesb.2008.01.002.
- [206] B. Lauke, "Effect of particle size distribution on debonding energy and crack resistance of polymer composites", *Computational Materials Science*, vol. 77, pp. 53–60, Sep. 2013, ISSN: 09270256. DOI: 10.1016/j.commatsci.2013.04.017.

- [207] A. J. Kinloch and D. L. Hunston, "Effect of volume fraction of dispersed rubbery phase on the toughness of rubber-toughened epoxy polymers", *Journal of Materials Science Letters*, vol. 6, no. 2, pp. 137–139, Feb. 1987, ISSN: 0261-8028, 1573-4811. DOI: 10.1007/BF01728963.
- [208] S. Wu, "A generalized criterion for rubber toughening: The critical matrix ligament thickness", *Journal of Applied Polymer Science*, vol. 35, no. 2, pp. 549–561, 1988, ISSN: 0021-8995. DOI: 10.1002/app.1988.070350220.
- [209] C. B. Bucknall, A. Karpodinis, and X. C. Zhang, "A model for particle cavitation in rubber-toughened plastics", *Journal of Materials Science*, vol. 29, no. 13, pp. 3377–3383, Jul. 1994, ISSN: 0022-2461, 1573-4803. DOI: 10.1007/BF00352036.
- [210] J. D. Menczel and R. B. Prime, Eds., *Thermal analysis of polymers: fundamentals and applications*, Hoboken, N.J: John Wiley, 2009, 688 pp., ISBN: 978-0-471-76917-0.
- [211] D. Raghavan, J. He, D. Hunston, and D. Hoffman, "Strain rate dependence of fracture in a rubber-toughened epoxy system", *The Journal of Adhesion*, vol. 78, no. 8, pp. 723–739, Aug. 2002. DOI: 10.1080/00218460213493.
- [212] Huntsman International LLC, *Selector guide for formulators*, 2012.
- [213] Huntsman International LLC, *Data sheet Huntsman Aradur HY917*, 2017.
- [214] Daicel Corp., *Data sheet Daicel Celloxide 2021p*, 2019.
- [215] S. L. Kirshenbaum, S. Gazit, and J. P. Bell, "An alternative liquid rubber for epoxy resin toughening: Improving poly(*n*-butyl acrylate) rubber-epoxy compatibility by use of acrylonitrile and acrylic acid copolymers and terpolymers", in *Rubber-Modified Thermoset Resins*, C. K. Riew and J. K. Gillham, Eds., vol. 208, Series Title: Advances in Chemistry, Washington, D.C.: American Chemical Society, Dec. 5, 1984, pp. 163–177, ISBN: 978-0-8412-2390-5. DOI: 10.1021/ba-1984-0208.ch011.
- [216] J.-M. Boutillier, "Nanostrength: Copolymères acryliques nanostructurés, technologie et applications", *Innov'days / Dijon*, Nov. 22, 2012.
- [217] J. C. Salamone, *Polymeric materials encyclopedia*. Boca Raton: CRC Press, 1996, ISBN: 0-8493-2470-X.
- [218] S. Hongo and K. Yoshida, "Rubbery Polymer containing resin, cured product thereof and production method thereof", European pat. 2275489B1, Nov. 13, 2019. [Online]. Available: <https://patents.google.com/patent/EP2275489B1/de>.
- [219] Toho Tenax Europe GmbH, *Produktprogramm und Eigenschaften für Tenax® HTA Filamentgarn*, Apr. 2011.
- [220] J. Karger-Kocsis, H. Mahmood, and A. Pegoretti, "Recent advances in fiber/matrix interphase engineering for polymer composites", *Progress in Materials Science*, vol. 73, pp. 1–43, 2015, ISSN: 00796425. DOI: 10.1016/j.pmatsci.2015.02.003.

-
- [221] Hexcel Corporation, *Data sheet HexForce® G1157 D 1300 HS06K Carbon Fabric*, Apr. 2017.
- [222] U. Müller, M. Philipp, M. Thomassey, R. Sanctuary, and J. Krüger, "Temperature modulated optical refractometry: A quasi-isothermal method to determine the dynamic volume expansion coefficient", *Thermochimica Acta*, vol. 555, pp. 17–22, Mar. 2013, ISSN: 00406031. DOI: 10.1016/j.tca.2012.12.011.
- [223] D. Jackson dos Santos, J. R. Gouveia, M. Philipp, A. C. Augusto, N. M. Ito, and J. K. Krüger, "Temperature modulated optical refractometry: A novel and practical approach on curing and thermal transitions characterizations of epoxy resins", *Polymer Testing*, vol. 77, p. 105915, Aug. 2019, ISSN: 01429418. DOI: 10.1016/j.polymertesting.2019.105915.
- [224] M. Philipp, B. Zimmer, M. Ostermeyer, and J. K. Krüger, "Polymerization-induced shrinkage and dynamic thermal expansion behavior during network formation of polyurethanes", *Thermochimica Acta*, vol. 677, pp. 144–150, Jul. 2019, ISSN: 00406031. DOI: 10.1016/j.tca.2019.01.012.
- [225] H. J. Paus, *Physik in Experimenten und Beispielen*, 3., aktualisierte Aufl. München: Hanser, 2007, 1043 pp., ISBN: 978-3-446-41142-5.
- [226] Y. Liu and P. H. Daum, "Relationship of refractive index to mass density and self-consistency of mixing rules for multicomponent mixtures like ambient aerosols", *Journal of Aerosol Science*, vol. 39, no. 11, pp. 974–986, Nov. 2008, ISSN: 00218502. DOI: 10.1016/j.jaerosci.2008.06.006.
- [227] L. Bergmann and C. Schaefer, *Optik*, 9. Aufl, H. Niedrig, Ed., ser. Lehrbuch der Experimentalphysik 3. Berlin: de Gruyter, 1993, 1277 pp., ISBN: 978-3-11-012973-1.
- [228] D. W. v. Krevelen and K. t. Nijenhuis, *Properties of polymers: their correlation with chemical structure: their numerical estimation and prediction from additive group contributions*, 4th, completely rev. ed. Amsterdam: Elsevier, 2009, 1004 pp., ISBN: 978-0-08-054819-7.
- [229] K. P. Menard, *Dynamic mechanical analysis: a practical introduction*. Boca Raton, Fla: CRC Press, 1999, 208 pp., ISBN: 978-0-8493-8688-6.
- [230] C. A. May, Ed., *Epoxy resins: Chemistry and technology*, 2. ed., rev. and expanded., New York: Dekker, 1988, ISBN: 0-8247-7690-9.
- [231] J. Karger-Kocsis and K. Friedrich, "Microstructure-related fracture toughness and-fatigue crack growth behaviour in toughened, anhydride-cured epoxy resins", *Composites Science and Technology*, vol. 48, no. 1, pp. 263–272, 1993, ISSN: 0266-3538. DOI: 10.1016/0266-3538(93)90143-5.

- [232] B. Erman and J. E. Mark, "4 - The molecular basis of rubberlike elasticity", in *Science and Technology of Rubber (Third Edition)*, J. E. Mark, B. Erman, and F. R. Eirich, Eds., Burlington: Academic Press, Jan. 1, 2005, pp. 157–182, ISBN: 978-0-12-464786-2. DOI: 10.1016/B978-012464786-2/50007-9.
- [233] J. Karger-Kocsis and S. Fakirov, Eds., *Nano- and micromechanics of polymer blends and composites*, Munich: Hanser, 2009, 604 pp., ISBN: 978-1-56990-435-0.
- [234] J. M. Charlesworth, "Effect of crosslink density on molecular relaxations in diepoxide-diamine network polymers. part 2. the rubbery plateau region", *Polymer Engineering & Science*, vol. 28, no. 4, pp. 230–236, 1988, ISSN: 00323888. DOI: 10.1002/pen.760280406.
- [235] T. L. Anderson, *Fracture mechanics: Fundamentals and applications*, 2nd ed. Boca Raton and Fla. [u.a.]: CRC Press, 1995, ISBN: 0-8493-4260-0.
- [236] K. Friedrich, Ed., *Application of fracture mechanics to composite materials*, Composite materials series vol. 6, Amsterdam; New York: New York, NY USA: Elsevier; Distributors for the U.S. and Canada, Elsevier Science Pub. Co, 1989, 671 pp., ISBN: 978-0-444-87286-9.
- [237] A. Saxena and Hudak, S.J., Jr., "Review and extension of compliance information for common crack growth specimens", *International Journal of Fracture*, vol. 14, no. 5, pp. 453–468, 1978, ISSN: 0376-9429. DOI: 10.1007/BF01390468.
- [238] K. Xiao, L. Ye, and Y. Kwok, "Effects of pre-cracking methods on fracture behaviour of an araldite-f epoxy and its rubber-modified systems", *Journal of Materials Science*, vol. 33, no. 11, pp. 2831–2836, 1998, ISSN: 0022-2461. DOI: 10.1023/A:1017533819817.
- [239] J. G. Williams, *Fracture mechanics of polymers*, ser. Ellis Horwood series in engineering science. Chichester : New York: E. Horwood ; Halsted Press, 1984, 302 pp., ISBN: 978-0-470-20013-1.
- [240] R. Reber, J. de Haan, J. Mayer, M. Petitmermet, and E. Wintermatnel, "Intralaminar fracture of weft-knitted carbon fiber reinforced peek", in *Fracture of Polymers, Composites and Adhesives, Second ESIS TC4 Conference on Fracture of Polymers, Composites and Adhesives*, ser. European Structural Integrity Society, vol. 27, Elsevier, 2000, pp. 123–133, ISBN: 978-0-08-043710-1. DOI: 10.1016/S1566-1369(00)80013-8.
- [241] J. G. Williams, "Introduction to linear elastic fracture mechanics", in *Fracture Mechanics Testing Methods for Polymers, Adhesives and Composites*, ser. European Structural Integrity Society, vol. 28, Elsevier, 2001, pp. 3–10, ISBN: 978-0-08-043689-0. DOI: 10.1016/S1566-1369(01)80024-8.
- [242] G. R. Irwin, "Analysis of stresses and strains near the end of a crack traversing a plate", *Journal of Applied Mechanics*, no. 24, pp. 361–364, 1957.

-
- [243] B. Blackman, A. J. Brunner, and J. G. Williams, "Mode II fracture testing of composites: A new look at an old problem", *Engineering Fracture Mechanics*, vol. 73, no. 16, pp. 2443–2455, 2006, ISSN: 0013-7944. DOI: 10.1016/j.engfracmech.2006.05.022.
- [244] F. Blateyron, "Chromatic confocal microscopy", in *Optical Measurement of Surface Topography*, R. Leach, Ed., Berlin, Heidelberg: Springer, 2011, pp. 71–106, ISBN: 978-3-642-12012-1. DOI: 10.1007/978-3-642-12012-1_5.
- [245] W. Hillger and F. K. von Wachter, "Ultraschallprüfung an Faserverbundkunststoffen Grundlagen, Methoden der bildhaften Darstellung und Ergebnisse", *Materialwissenschaft und Werkstofftechnik*, vol. 22, no. 6, pp. 217–224, Jun. 1991, ISSN: 0933-5137, 1521-4052. DOI: 10.1002/mawe.19910220607.
- [246] ASNT and R-D Tech Corp, Eds., *Introduction to phased array ultrasonic technology applications: R/D Tech guidelines*, 2. print, Advanced practical NDT series, Waltham, Mass: R/D Tech Corp, 2005, 356 pp., ISBN: 978-0-9735933-0-3.
- [247] J. Goldstein, Ed., *Scanning electron microscopy and x-ray microanalysis*, 3rd ed, New York: Kluwer Academic/Plenum Publishers, 2003, 689 pp., ISBN: 978-0-306-47292-3.
- [248] S. C. Mayo, A. W. Stevenson, and S. W. Wilkins, "In-line phase-contrast X-ray imaging and tomography for materials science", *Materials*, vol. 5, no. 12, pp. 937–965, May 24, 2012, ISSN: 1996-1944. DOI: 10.3390/ma5050937.
- [249] R. Hanke, T. Fuchs, M. Salamon, and S. Zabler, "X-ray microtomography for materials characterization", in *Materials Characterization Using Nondestructive Evaluation (NDE) Methods*, Elsevier, 2016, pp. 45–79, ISBN: 978-0-08-100040-3. DOI: 10.1016/B978-0-08-100040-3.00003-1.
- [250] S. Garcea, Y. Wang, and P. Withers, "X-ray computed tomography of polymer composites", *Composites Science and Technology*, vol. 156, pp. 305–319, Mar. 2018, ISSN: 02663538. DOI: 10.1016/j.compscitech.2017.10.023.
- [251] Carl Zeiss Microscopy GmbH, *Technical note - Contrast with a 3D X-ray microscope*, 2020. (visited on 07/14/2020).
- [252] J. Vogtmann, A. Klingler, T. Rief, and M. Gurka, "Post mortem analyses of interfacial interaction between a single carbon fibre and epoxy resin using 3D X-ray microscopy", 2021, (to be published).
- [253] J. I. Kroschwitz, Ed., *Concise encyclopedia of polymer science and engineering*, New York: Wiley, 1990, 1341 pp., ISBN: 978-0-471-51253-0.
- [254] R. A. Pearson and A. F. Yee, "Toughening mechanisms in thermoplastic-modified epoxies: 1. Modification using poly(phenylene oxide)", *Polymer*, vol. 34, no. 17, pp. 3658–3670, 1993, ISSN: 0032-3861. DOI: 10.1016/0032-3861(93)90051-B.

- [255] J. A. Choren, S. M. Heinrich, and M. B. Silver-Thorn, "Young's modulus and volume porosity relationships for additive manufacturing applications", *Journal of Materials Science*, vol. 48, no. 15, pp. 5103–5112, Aug. 2013, ISSN: 0022-2461, 1573-4803. DOI: 10.1007/s10853-013-7237-5.
- [256] R. Selzer, *Fraktographische Analyse des Versagensverhaltens von kohlenstoffaserverstärkten Polymer-Verbundwerkstoffen unter Feuchteinfluß*, ser. Berichte aus der Werkstofftechnik. Aachen: Shaker, 1996, 189 pp., ISBN: 978-3-8265-1205-6.
- [257] K. Liu and E. Kiran, "Pressure-induced phase separation in polymer solutions: Kinetics of phase separation and crossover from nucleation and growth to spinodal decomposition in solutions of polyethylene in *n*-pentane", *Macromolecules*, vol. 34, no. 9, pp. 3060–3068, Apr. 2001, ISSN: 0024-9297, 1520-5835. DOI: 10.1021/ma000816k.
- [258] M. Tomasini, "Use of fiber-reinforced plastics in wheels for passenger cars", in *5th International Munich Chassis Symposium 2014*, P. E. Pfeffer, Ed., Series Title: Proceedings, Wiesbaden: Springer Fachmedien Wiesbaden, 2014, pp. 717–739, ISBN: 978-3-658-05978-1. DOI: 10.1007/978-3-658-05978-1_51.
- [259] Porsche AG, *Braided carbon wheels for the porsche 911 turbo s exclusive series (press release)*, Aug. 18, 2017. [Online]. Available: https://presse.porsche.de/prod/presse_pag/PressResources.nsf/Content?ReadForm&languageversionid=767979.
- [260] S. Czypionka and F. Kienhöfer, "Weight reduction of a carbon fibre composite wheel", *Science and Engineering of Composite Materials*, vol. 26, no. 1, pp. 338–346, Jan. 28, 2019, ISSN: 2191-0359. DOI: 10.1515/secm-2019-0018.
- [261] J. Dingle, "Lightweight carbon fibre composite automotive wheels - from concept to industrialisation", Plenary lecture, 22nd International Conference on Composite Materials, Melbourne, Australia, Aug. 12, 2019.
- [262] Fraunhofer LBF, *Concept development for an aircraft wheel made of fiber-plastic composite (Annual report 2017)*, 2017. [Online]. Available: <https://2017.lbf-jahresbericht.de/en/>.
- [263] Henkel AG & Co. KGaA, *Henkel to showcase growing loctite MAX resin portfolio at JEC world 2019 (press release)*, Feb. 27, 2019. [Online]. Available: <https://www.henkel.com/press-and-media/press-releases-and-kits/2019-02-27-henkel-to-showcase-growing-loctite-max-resin-portfolio-at-jec-world-2019-915760>.
- [264] Henkel AG & Co. KGaA, *Henkel and Carbon Revolution join forces (press release)*, Oct. 7, 2019. [Online]. Available: <https://www.henkel.com/press-and-media/press-releases-and-kits/2019-10-07-henkel-and-carbon-revolution-join-forces-987318>.
- [265] Evolime GmbH. "Evolime - radial composites". (Aug. 8, 2020), [Online]. Available: <http://evolime.de/>.

-
- [266] K. Baltruschat, S. Dittmar, and T. Tallafuß, "Guidelines for the testing and inspection of plastic wheels for passenger cars and motorcycles", in *9th International Munich Chassis Symposium 2018*, P. Pfeffer, Ed., Wiesbaden: Springer Fachmedien Wiesbaden, 2019, pp. 769–783, ISBN: 978-3-658-22050-1.
- [267] R. F. Fischer, "Polyesters from epoxides and anhydrides", *Journal of Polymer Science*, vol. 44, no. 143, pp. 155–172, 1960, ISSN: 1542-6238. DOI: 10.1002/pol.1960.1204414314.
- [268] Y. R. Ham, S. H. Kim, Y. J. Shin, D. H. Lee, M. Yang, J. H. Min, and J. S. Shin, "A comparison of some imidazoles in the curing of epoxy resin", *Journal of Industrial and Engineering Chemistry*, vol. 16, no. 4, pp. 556–559, Jul. 2010, ISSN: 1226086X. DOI: 10.1016/j.jiec.2010.03.022.

A Appendices

A.1 Curing reactions of epoxies with anhydrides

To initiate a cross-linking reaction between an epoxide group and an anhydride curing agent (cf. Fig. A.92a) an initiation step (ring opening) by an accelerator or catalyst is required, since the reactivity between both species alone is quite low [99, 111]. The ring opening can either start at the epoxide group [114] or the anhydride ring [113]. Common accelerators are e.g. tertiary amines, as shown in Fig. A.92b [98, 112].

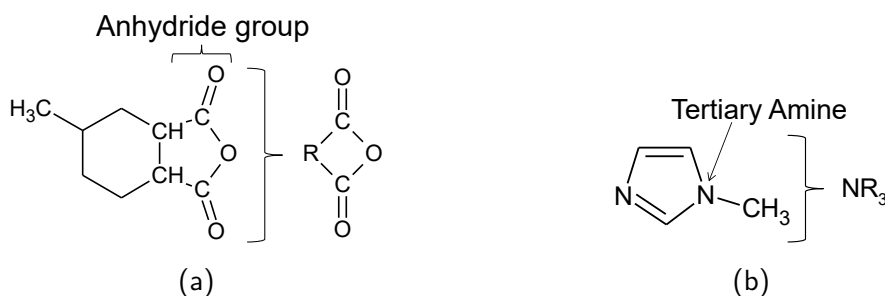
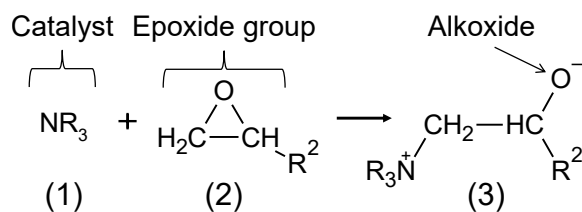


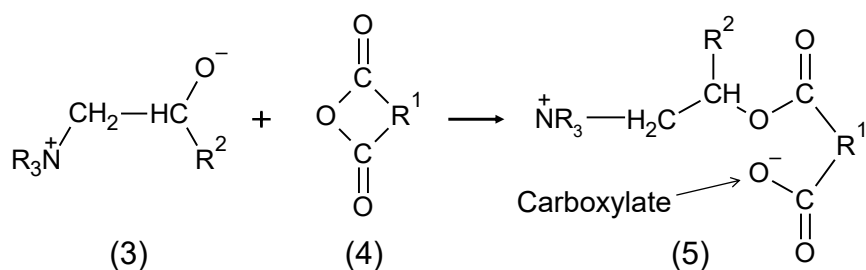
Figure A.92: a) Molecular structure of a cycloaliphatic anhydride (Methyltetrahydrophthalic anhydride - MTHPA) and a b) tertiary amine accelerator (1-methylimidazole)

In the following a well accepted catalysed reaction mechanism between an epoxy resin and an anhydride curing agent is presented (Fig. A.93) [114]. Note, other species, such as hydroxyl groups (-OH), which are usually present in technical resins [112], or even H₂O from air humidity can unintentionally initiate, accelerate and influence the process of the curing reaction [97, 99, 100, 106, 112–114]. In a first initiation step, the catalyst (1) attacks the epoxide group of the epoxy molecules (2) and creates a highly reactive alkoxide group (O⁻, 3). In a second step (Fig. A.93b), the opened epoxy reacts with an anhydride molecule (4), i.e. opens the anhydride ring, and forms a new carboxylate (COO⁻) group at the same time (5). The third step then (Fig. A.93c), enables the network formation between the epoxy and the anhydride. The formed molecule (5) uses its carboxylate group to attack another epoxide group (2) and react with it (6). It becomes obvious that three reactive sites are now available for further reaction (two epoxide groups and one alkoxide), hence a continuation of the process leads to a three dimensional, cross-linked network.

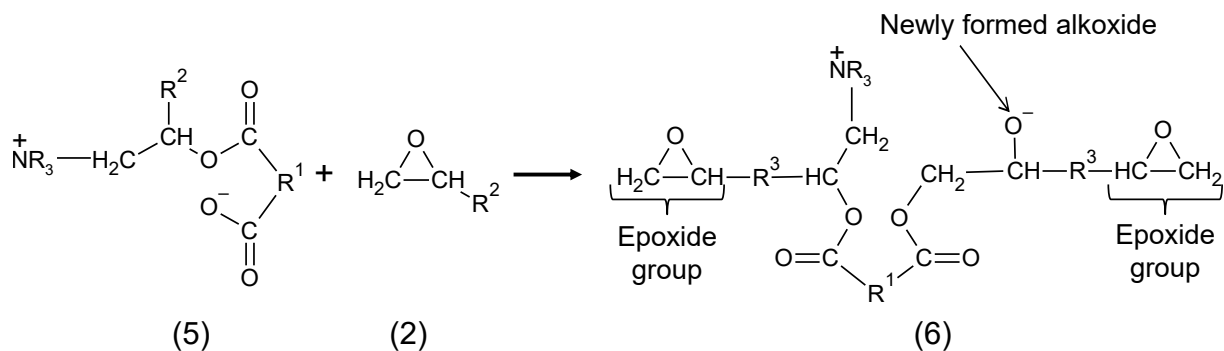
At the same time, the reaction could also be initiated at the anhydride ring structure, rather than at the epoxide group (cf. Fig. A.94). This would provide an alkoxide group for further reactions [98, 101, 267]. This latter reaction mechanism is more likely to occur in cycloaliphatic epoxies, since the epoxide groups are part of the cyclic structure (cf. Fig. 2.8b) and tend to be less active in the presence of tertiary amines. As it becomes obvious, tertiary amines do not only initiate or catalyse a reaction, they rather change the whole reaction mechanism. For now it is still unclear if the tertiary amine is irreversibly participating in the esterification (as an initiator) [268] or remains unbound at the end of the reaction (as a catalyst) [112].



(a) Step 1: Initiation reaction between tertiary amine catalyst and epoxide group yields highly reactive alkoxide group



(b) Step 2: Alkoxyde group opens anhydride ring and reacts with it



(c) Step 3: Network formation, two epoxide groups and one alkoxide (O^-) are available for further reaction

Figure A.93: Accelerated reaction mechanism between an epoxide group and an anhydride

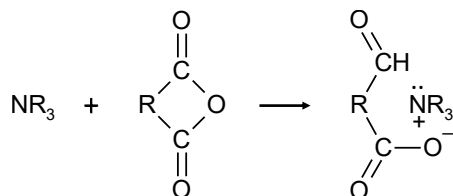


Figure A.94: Catalyzed ring opening of anhydride

A.2 Post-curing investigations

Unreacted resin, hardener and accelerator moieties within epoxy based polymers can have different effects on their final properties. They can e.g. cause a chemical post-cross-linking over time (aging) and change the glass transition temperature or their mechanical properties. On the other hand, such species can also be beneficial for a materials' performance, such as for fracture toughness, since they provide a certain flexibility to the system. However, post-curing phenomena should be avoided since the properties are altered by time and/or temperature.

To examine the post-curing behaviour of the different matrix systems, with regard to the reference curing-cycle (cf. Fig. 4.21), the residual reactivity of the systems was investigated via non-isothermal DSC scans.

Fig. A.95a shows a comparison between EP/DGEBA and the EP/BCP-10% system. Both systems exhibit a similar degree of post-curing η of 5.1% and 4.8%, respectively (cf. Eq. 4.7). The approximate start of the post-curing reaction starts around 80°C in both cases. Knowing

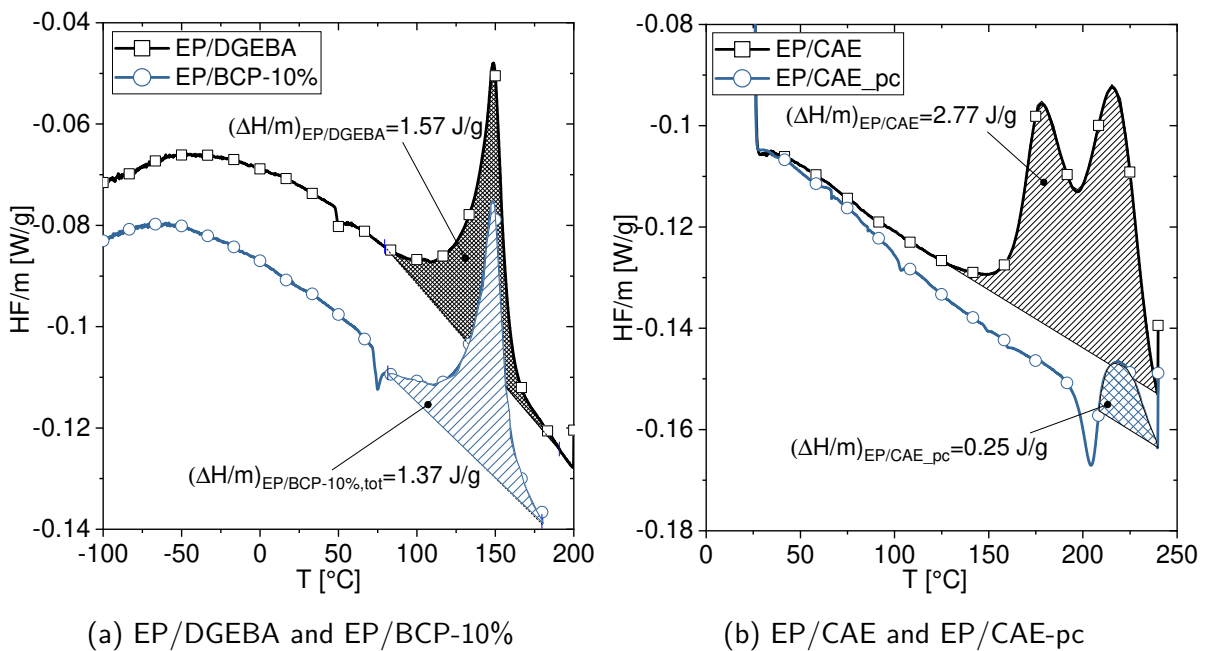


Figure A.95: Left: post-curing phenomena of EP/DGEBA and EP/BCP-10%: the degree of post curing seems not to be affected by the presence of BCPs, right: the degree of post-curing is larger in the EP/CAE matrix than in the EP/DGEBA system, but is strongly reduced after a post-curing treatment of 10h at 190°C. The data are normalized to the sample weight, the dashed areas indicate the excess enthalpy.

the applied curing cycle has a peak temperature of 140°C, which is kept for 4 hours, it seems that the matrices were not fully cured by this process. A longer curing cycle or a higher peak temperature would have been beneficial in this case.

Fig. A.95b depicts a similar representation of the EP/CAE system. The post-curing effect is split in two peaks and is in total larger ($\Delta H/m_{EP/CAE,tot}=2.77$ J/g) than in EP/DGEBA. The first peak most-likely represents a post-curing effect similar to the EP/DGEBA system, i.e. previously unreacted moieties react with each other. The second peak is rather related to the already discussed slightly insufficient concentration of accelerator (cf. Sec. 5.3.1), i.e. the second peak indicates an uncatalyzed chemical reaction between cycloaliphatic epoxy and anhydride. With respect to the total reaction enthalpy (cf. Fig. 5.59), the degree of post-curing in the system is about 8.1%. To supplement the investigation of the post-curing behaviour, a EP/CAE sample was post-cured for 10 h at 190°C (EP/CAE-pc). The post-curing effect nearly vanished ($\Delta H/m_{EP/CAE-pc,tot}=0.25$ J/g, $\eta \sim 0.6\%$).

Similar observations were made via dynamic mechanical analyses. Fig. A.96 shows a comparison between a specimen that was cured following the reference curing cycle (EP/CAE) and a post-cured specimen (EP/CAE-pc, 10 h at 190°C). A pronounced shoulder in the course of $\tan \delta$ is present, similarly as in the data set of the loss modulus, which indicates the post-curing phenomenon. E' drops at around 150°C when relaxations of uncured moieties take place.

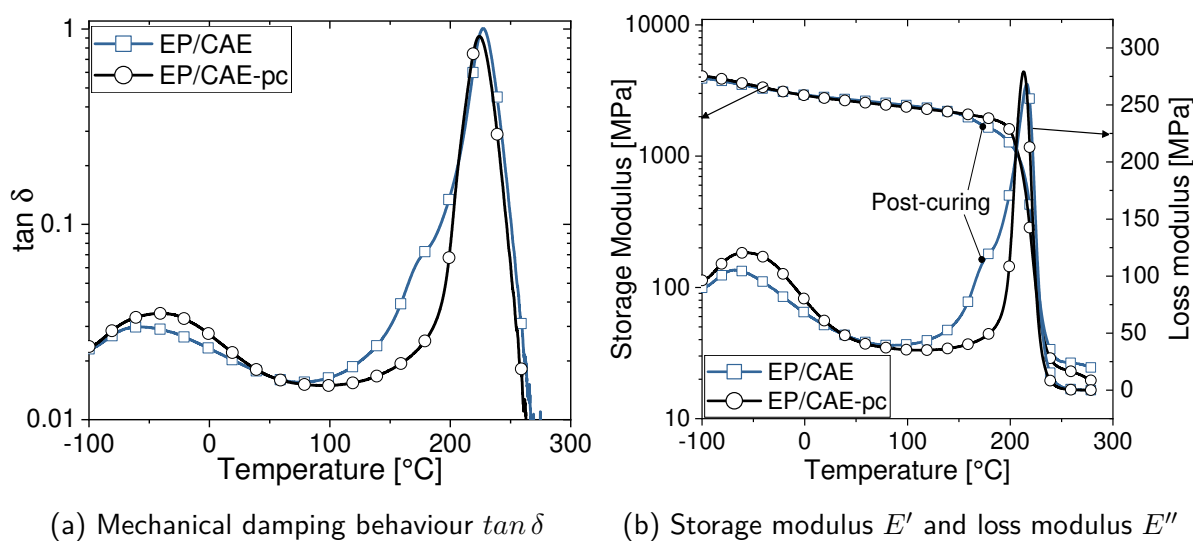
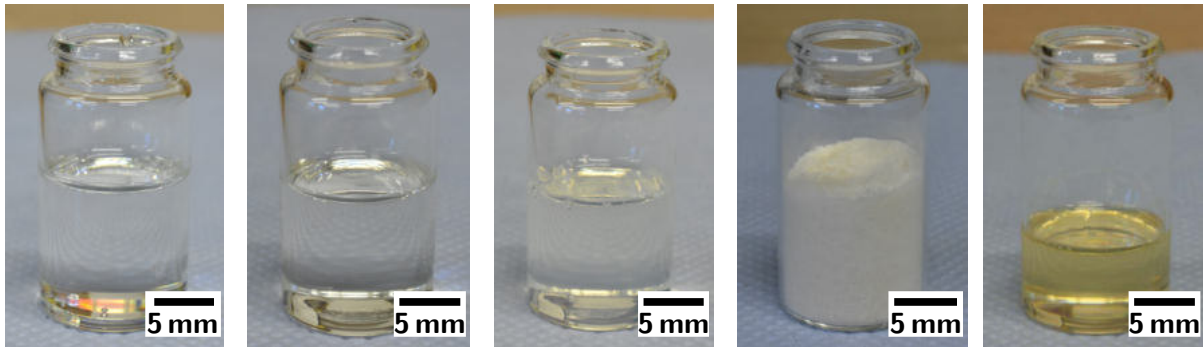


Figure A.96: Thermo-mechanical analyses of EP/CAE having been cured according the reference curing cycle and having been post-cured for 10 h at 190°C, EP/CAE-pc

A.3 Collection of supplemental tables, figures and other data



(a) DGEBA epoxy resin - Sika Biresin CR144
 (b) CAE resin - Daicel Celloxide P2021
 (c) Nanoparticle modified CAE resin - Kaneka MX553
 (d) BCP powder - Arkema Nanostrength M52N
 (e) BCP powder (d) dissolved in DGEBA resin (a), 25 wt.-%

Figure A.97: Optical appearance of the neat resin systems (a and b), the CSR nanoparticle modified CAE epoxy resin system (c, 30 wt.-%), the BCP powder in the pristine state (d) and a mixture of 25 wt.-% BCP and DGEBA based epoxy resin (e). A representation of the CSR/BCP hybrid epoxy resin is not shown.

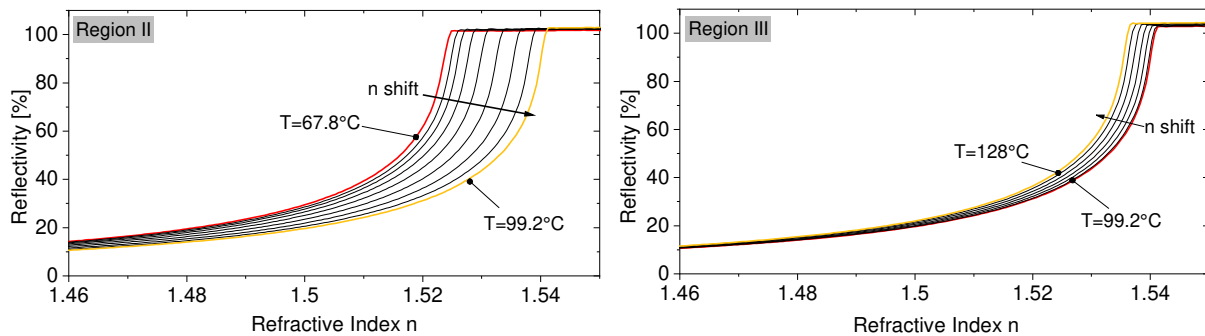


Figure A.98: Supplementary Fresnel curves to Fig. 5.38 from region II and III, showing the development of refractivity within the EP/DGEBA sample due to polymerization induced mass density changes (region II) and temperature (region III), red: starting temperature, yellow: end temperature

Table A.9: List of references to Fig. 2.6. *Neat*, *Rigid*, *Carbon based*, *Compliant*, *Interleaved* and *Others* refer to the type of modification used. The data was collected irrespective a ENF or ELS test was used to determine $G_{IIc,c}$. If available fracture initiation values (NL or Vis) were selected.

$G_{Ic,c}$ [J/m ²]	$G_{IIc,c}$ [J/m ²]						$G_{IIc,c}/G_{Ic,c}$	Reference
	<i>Neat</i>	<i>Rigid</i>	<i>Carbon based</i>	<i>Compliant</i>	<i>Interleaved</i>	<i>Others</i>		
417	969						2.3	[67]
511		929					1.8	[67]
729		750					1.0	[67]
300			1000				3.3	[78]
270			750				2.8	[78]
420			1750				4.2	[78]
480			1450				3.0	[78]
343	768						2.2	[79]
492				942			1.9	[79]
825				664			0.8	[79]
137	1292						9.4	[68]
165	1806						10.9	[68]
340				1325			3.9	[68]
372	1090						2.9	[80]
517				1156			2.2	[80]
840				1489			1.8	[80]
950				1823			1.9	[80]
1305				1976			1.5	[80]
803				1739			2.2	[80]
1127				2000			1.8	[80]
208	1293						6.2	[81]
250	1217						4.9	[81]
446	717						1.6	[82]
607			808				1.3	[82]
420	1300						3.1	[83]
580			1625				2.8	[83]
605			1800				3.0	[83]
620			1700				2.7	[83]
650			1650				2.5	[83]
86	605						7.0	[84]
170			786				4.6	[84]
620	680						1.1	[85]
480			765				1.6	[85]
427	750						1.8	[86]
133						850	6.4	[86]
290				300			1.0	[86]
125			1550				12.4	[86]
219.5						883.1	4.0	[87]

Continued

$G_{Ic,c}$ [J/m ²]	$G_{IIc,c}$ [J/m ²]						$G_{IIc,c}/G_{Ic,c}$	Reference
	<i>Neat</i>	<i>Rigid</i>	<i>Carbon based</i>	<i>Compliant</i>	<i>Interleaved</i>	<i>Others</i>		
200						800	4.0	[88]
240						900	3.8	[88]
220	650						3.0	[88]
317						1284	4.1	[89]
352					1983		5.6	[89]
152					1541		10.1	[89]
133					2006		15.1	[89]
348	350						1.0	[90]
399		400					1.0	[90]
467		475					1.0	[90]
522		525					1.0	[90]
477		480					1.0	[90]
900	1140						1.3	[65]
1100		1280					1.2	[65]
1390		1730					1.2	[65]
520	1100						2.1	[61, 62]
620		1150					1.9	[61, 62]
600		1150					1.9	[61, 62]
580		1180					2.0	[61, 62]
560		1100					2.0	[61, 62]
1100				1150			1.0	[61, 62]
1150				1550			1.3	[61, 62]
1250				1400			1.1	[61, 62]
1100				1100			1.0	[61, 62]
165	290						1.8	[91]
220				580			2.6	[91]
390				920			2.4	[91]
490				1300			2.7	[91]
530				1250			2.4	[91]
375	1000						2.7	[92]
1125				1050			0.9	[92]
500	1000						2.0	[92]
750				950			1.3	[92]

Table A.10: Influence of BCP, CSR and BCP/CSR concentration on relaxation phenomena and *global* network formation of epoxy matrices

System	Modifier [wt.-%]	* α -relax phenomena [°C]				E'_{T_g+50K} MPa	** M_c [g/mol]	n_c [10 ²¹ 1/cm ³]
		PBud	PBuA	PMMA	EP			
EP/DGEBA	0	/	/	/	154.54	27.7	129	3.73
EP/CAE	0	/	/	/	227.51	25.17	164	2.94
BCP	0	/	-24.45	95.39	/	/	/	/
EP/BCP-0.5%	0.5	/	/	/	154.03	26.8	133	3.62
EP/BCP-1%	1	/	/	/	154.64	27.0	132	3.64
EP/BCP-2%	2	/	/	/	154.54	25.6	140	3.45
EP/BCP-5%	5	/	-32.98	92.70	154.99	24.2	147	3.26
EP/BCP-7%	7	/	-27.11	107.22	154.92	22.1	161	2.98
EP/BCP-10%	10	/	-23.69	110.12	154.51	19.5	183	2.62
EP/CAE/CSR-16%	16	-81.95	/	/	224.37	19.02	215	2.24
EP/CAE/CSR/BCP-16/12	27.6	-78.83	-22.38	106.12	223.62	14.75	277	1.74

*based on $\tan \delta_{\max}$

** M_c : Average molecular weight between cross-links

Table A.11: Overview of the tensile properties of the neat, the BCP, CSR and BCP/CSR modified EP systems

System	E [MPa]	σ_{\max} [MPa]	$\varepsilon_{\sigma, \max}$ [%]	σ_{ys} [MPa]	ε_{ys} [%]	σ_f [MPa]	ε_f [%]
EP/DGEBA	3020±47	82.7±1.9	5.0±0.3	47.3±4.3	1.6±0.1	78.2±1.8	6.7±0.5
EP/CAE	3409±106.3	58.9±4.0	2.0±0.2	43.8±2.0	1.6±0.2	58.9±4.0	2.0±0.2
EP/BCP-2%	2960±16	77.1±4.7	4.6±0.8	40.0±1.3	1.6±0.1	75.5±3.9	6.2±0.3
EP/BCP-5%	2692±138	74.5±0.6	5.1±0.1	38.7±6.6	1.6±0.3	73.1±2.2	5.5±0.5
EP/BCP-7%	2490±12	53.3±0.6	3.3±0.1	38.2±0.7	0.9±0.1	53.3±0.6	3.3±0.1
EP/BCP-10%	2430±17	43.8±2.0	2.6±0.3	36.7±0.2	0.7±0.0	43.8±2.0	2.6±0.3
EP/CSR-16%	2330±22	63.9±1.4	3.9±0.2	38.2±1.0	1.8±0.1	63.9±1.4	3.9±0.2
EP/CSR/BCP-16/12	2080±13	49.2±4.0	3.5±0.7	37.5±0.4	2.1±0.0	49.2±4.0	3.5±0.7

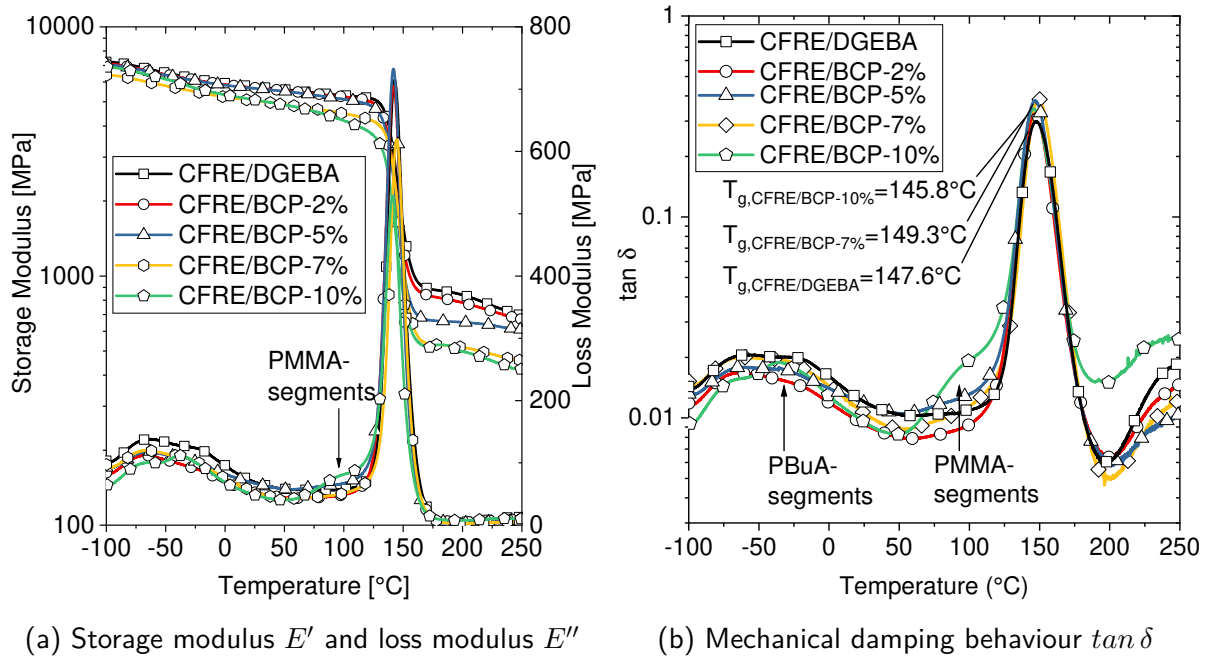


Figure A.99: Thermo-mechanical behaviour of BCP modified carbon fibre reinforced epoxy (DGEBA). The data were measured using the same test parameters as described in Sec. 4.3.3, the unidirectional samples were tested 90° off the fibre orientation; The influence of the BCP modification shows nearly no effect on the dynamic glass transition temperature of the epoxy matrix system ($\tan \delta$, right Figure), i.e. the cross-linked epoxy governs the properties throughout all BCP modified CFREs. Due to the presence of the stiff carbon fibres, E' has shifted to higher values compared to the matrix systems without CF (cf. Fig. 5.53a). Once the phase-separation process has changed from a BCP-nano domain morphology to an epoxy-isle morphology pronounced PBuA- and PMMA-related relaxations of respective segments appear in the course of the loss modulus and $\tan \delta$ (cf. Sec. 5.4.1).

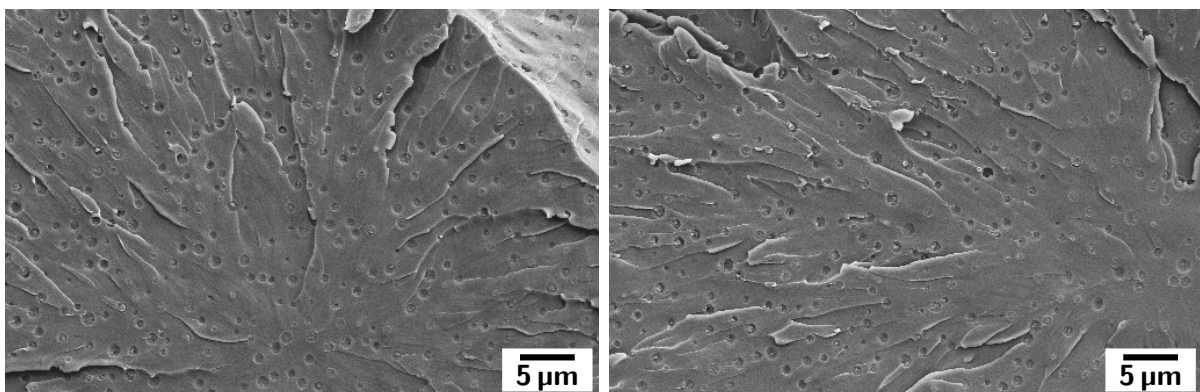


Figure A.100: Fracture surfaces of EP/BCP-5% cured under ambient pressure (left) and under $p=24$ bar (right). The fracture surfaces were both generated via cryo-fracture in liquid nitrogen. The BCP-rich precipitates have very similar dimensions. No influence of the BCP-precipitation size was found

Table A.12: Critical stress intensity factor K_{Ic} and energy release rate G_{Ic} of the neat, the BCP, CSR and BCP/CSR modified EP systems as well as the plastic zone size, calculated according Eq. 4.22

System	K_{Ic} [MPa \sqrt{m}]	G_{Ic} [J/m ²]	r_p [μ m]
EP/DGEBA	0.58 \pm 0.06	98.5 \pm 19.4	9.3
EP/CAE	0.51 \pm 0.03	71.7 \pm 10.3	6.3
EP/BCP-0.5%	0.70 \pm 0.05	*152.5 \pm 22.9	13.6
EP/BCP-1%	0.73 \pm 0.02	*172.7 \pm 13.1	14.9
EP/BCP-2%	0.85 \pm 0.03	214.0 \pm 16.2	23.7
EP/BCP-5%	1.02 \pm 0.02	342.0 \pm 32.3	36.9
EP/BCP-7%	1.25 \pm 0.09	557.6 \pm 86.9	57.2
EP/BCP-10%	1.38 \pm 0.04	696.1 \pm 45.9	75.16
EP/CSR-16%	1.40 \pm 0.07	748.3 \pm 65.1	71.71
EP/CSR/BCP-16/12	1.28 \pm 0.01	692.7 \pm 5.8	61.47

*determined based on the flexural modulus of the EP/DGEBA system

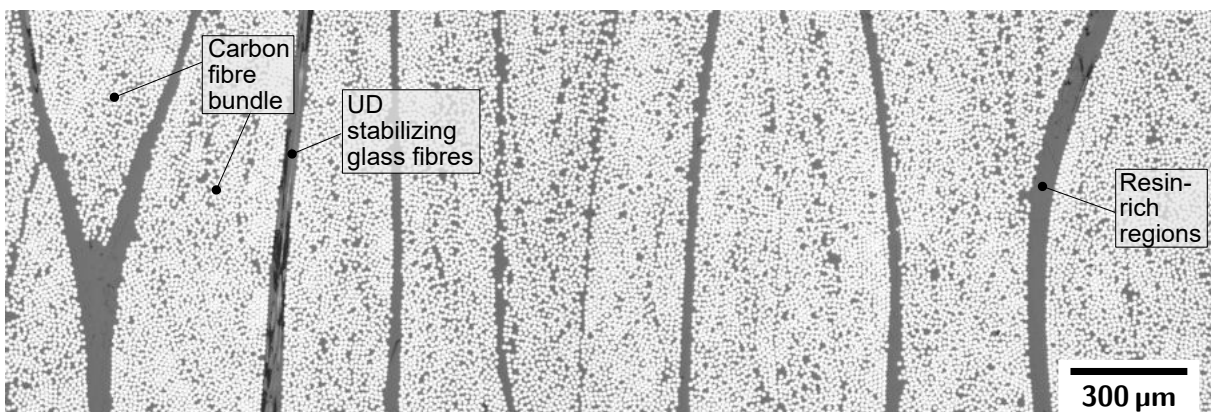


Figure A.101: Cross-sectional image (light-microscopy) of the unidirectional CFRE/DGEBA system, being comprised a 12-layer stack of Toho Tenax HTA40 E13 carbon fibres. Partially, glass fibres are visible that allow handling of the fabric. The fabric is well impregnated by the matrix, i.e. no pores were detected, even though, resin-rich regions are present.

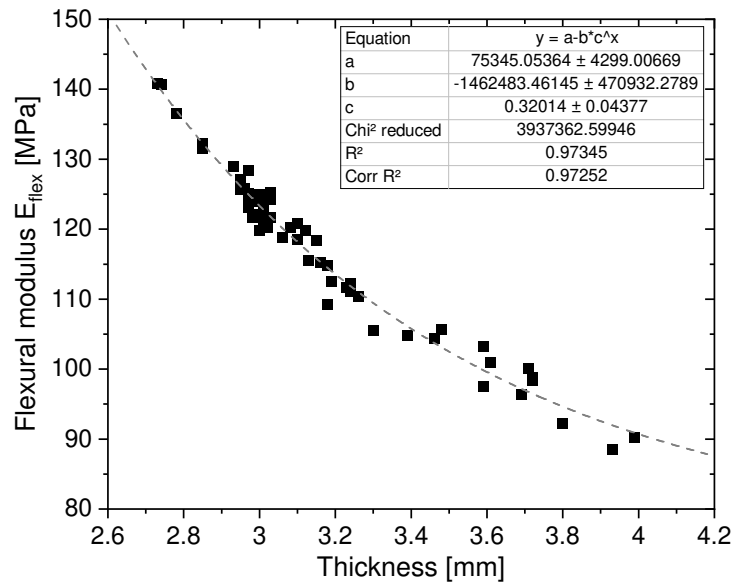


Figure A.102: Flexural modulus E_f of unidirectional laminates as a function of thickness t and respectively carbon fibre volume fraction v_f . The data were fit via an exponential function given in the graph, in order to access the flexural modulus for measuring Mode II interlaminar fracture toughness (cf. Sec. 5.4.3). The data were measured according DIN EN ISO 14125.

Table A.13: Overview of the interlaminar energy release rate (initiation and propagation) in Mode I and Mode II of the neat, the BCP, CSR and BCP/CSR modified CFRE systems

System	$G_{Ic,c,init,NL}$ [J/m ²]	$G_{Ic,c,prop}$ [J/m ²]	$G_{IIc,c,init,vis}$ [J/m ²]	$G_{IIc,c,init,Fmax}$ [J/m ²]	$G_{IIc,c,prop}$ [J/m ²]
EP/DGEBA	103.8±9.0	310.5±31.3	911.2±168.8	1988.9±366.4	1847±233.9
EP/CAE	104.3±21.6	435.0±27.3	/	1330.8±134.7	1331.2±73.9
EP/BCP-2%	166.1±5.8	451.0±18.8	/	1643.4±496.8	1725.0±229.9
EP/BCP-5%	135.6±15.5	577.2±20.7	/	/	/
EP/BCP-7%	241.3±24.6	795.3±29.7	630.2±244.8	1298.9±227.3	1802.1±127.4
EP/BCP-10%	234.6±32.2	610.0±68.5	766.3±134.7	1982.3±338.9	1878.3±303.3
EP/CSR-16%	255.4±31.2	956.7±9.6	574.9±36.5	1550.6±80.5	1491.7±45.7
EP/CSR/BCP-16/12	288.7±38.5	811.9±68.8	1105.4±346.6	2191.2±48.7	2136.0±38.0

Table A.14: Peak force and post-impact properties of BCP and CSR modified CFRE after impact (1-13 J)

System	Impact energy [J]	Peak force [F]	Damage area [mm ²]	Rel. damage area [%]	Indentation depth [μm]	Sample thickness [mm]
CFRE/DGEBA	1	839.7	0	0	0	1.64
	3	1593.5	22.5	2.5	41.6	1.57
	7	2767.6	85.5	9.5	75.7	1.60
	9	3109.8	87.3	9.7	300.0	1.63
	9 (2.)	3030.0	205.2	22.8	787.5	1.69
	13	3203.6	256.5	28.5	1145.9	1.70
CFRE/BCP-2%	1	850.0	0	0	0	1.64
	3	1578.0	23.4	2.6	42.9	1.55
	7	2691.8	66.6	7.4	96.8	1.57
	9	3105.0	120.6	13.4	243.9	1.63
	9 (2.)	3069.6	212.4	23.6	547.7	1.71
	13	2958.9	333.9	37.1	1157.9	1.65
CFRE/BCP-7%	1	865.9	0	0	0	1.70
	3	1629.0	16.2	1.8	41.2	1.58
	7	2671.3	63.0	7.0	92.0	1.56
	9	2950.8	105.3	11.7	215.9	1.68
	9 (2.)	2239.7	320.4	35.6	1021.1	1.73
	13	3140.0	309.6	34.4	809.9	1.67
CFRE/CSR-16%	1	856.3	0	0	0	1.70
	3	1610.0	19.8	2.2	46.8	1.63
	7	2686.3	65.7	7.3	90.2	1.60
	9	3106.3	88.2	9.8	146.6	1.64
	9 (2.)	2615.2	162	18.0	871.7	1.72
	13	3486.4	212.4	23.6	1113.0	1.66
CFRE/CSR-BCP-16/12	1	818.4	0	0	0	1.58
	3	1577.4	12.6	1.4	46.7	1.57
	7	2751.0	65.7	7.3	90.1	1.75
	9	3166.0	71.1	7.9	120.0	1.80
	9 (2.)	3086.1	135	15.0	171.7	1.70
	13	3406.9	135	15.0	834.6	1.76

9(2.) denominates the second impact at 9 J impact energy

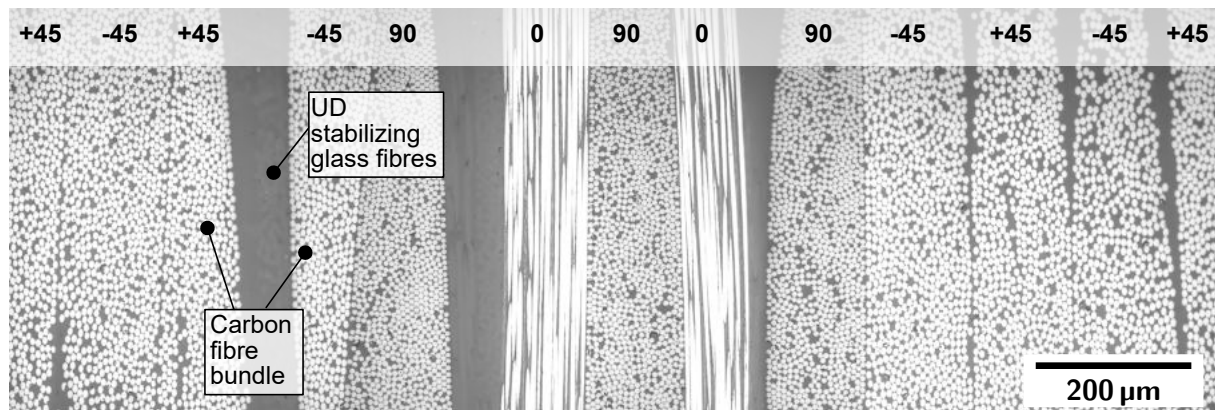


Figure A.103: Cross-sectional image (light-microscopy) of the multidirectional CFRE/DGEBA system, being comprised a 13-layer stack of Toho Tenax HTA40 E13 carbon fibres. The lay-up represents the structure of a state-of the art airplane fuselage. Partially, glass fibres are visible that allow handling of the fabric. The fabric is well impregnated, i.e. no pores were detected. The numbers at the top give the fibre orientation.

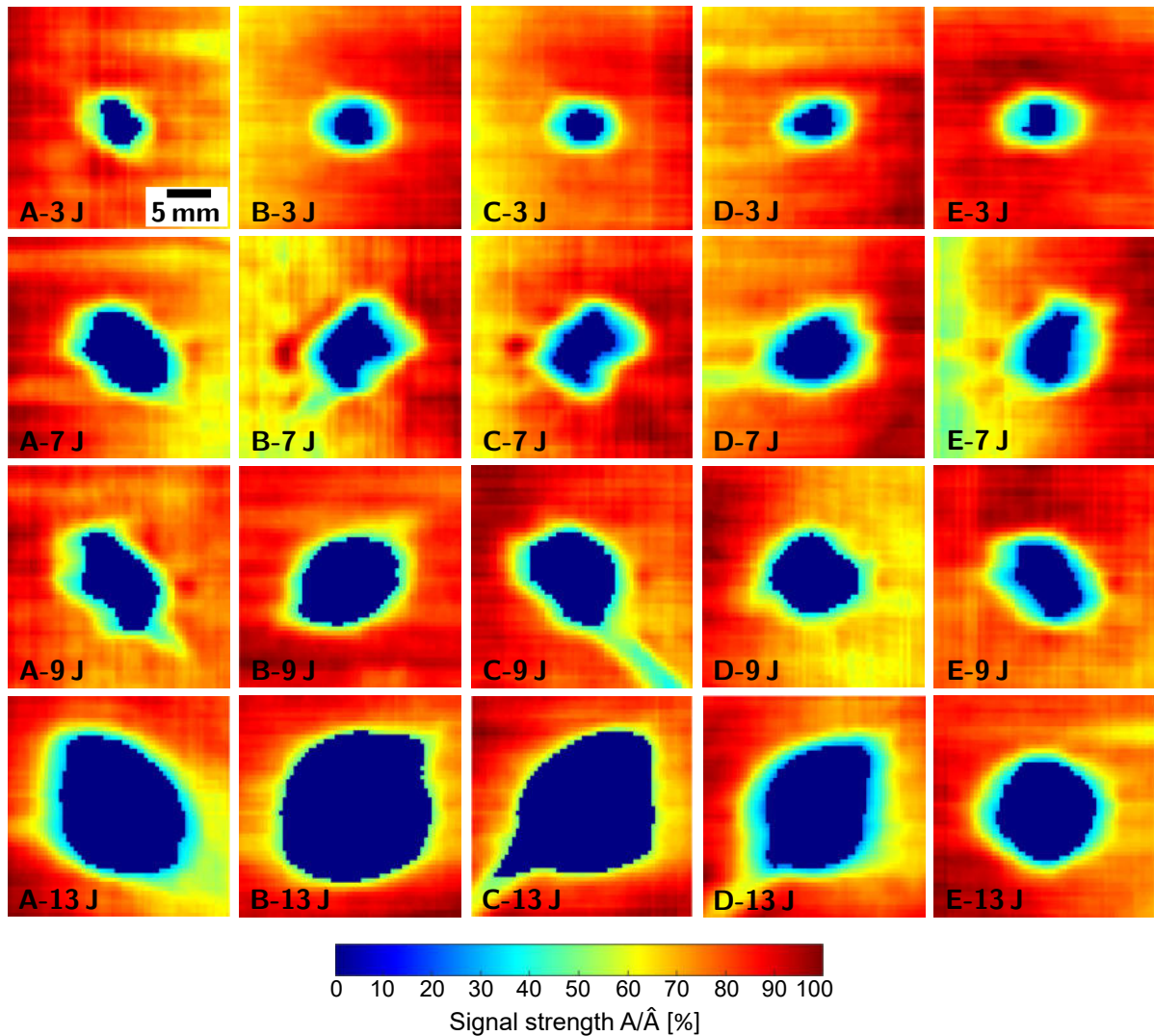


Figure A.104: C-scans obtained via ultra-sound analyses of BCP and/or CSR modified CFREs after impact with different impact energies, ranging from 3 to 13 J. A:CFRE/DGEBA, B:CFRE/DGEBA-BCP-2%, C:CFRE/DGEBA-BCP-7%, D:CFRE/CAE-CSR-16%, E:CFRE/CAE-CSR/BCP-16/12; the scale bar given in A-3 J is valid for all images. The colour coding represents the degree of amplitude loss, when the signal is detected by the pulse-echo US-setup A versus the initially emitted signal \hat{A} . Damage is indicated by blue areas, red or orange indicates that no damage occurred within those regions.

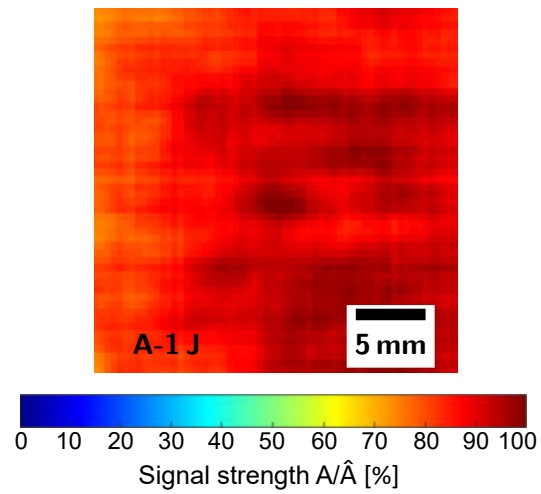


Figure A.105: C-scan image after 1 J impact of the CFRE/DGEBA system: no visible damage

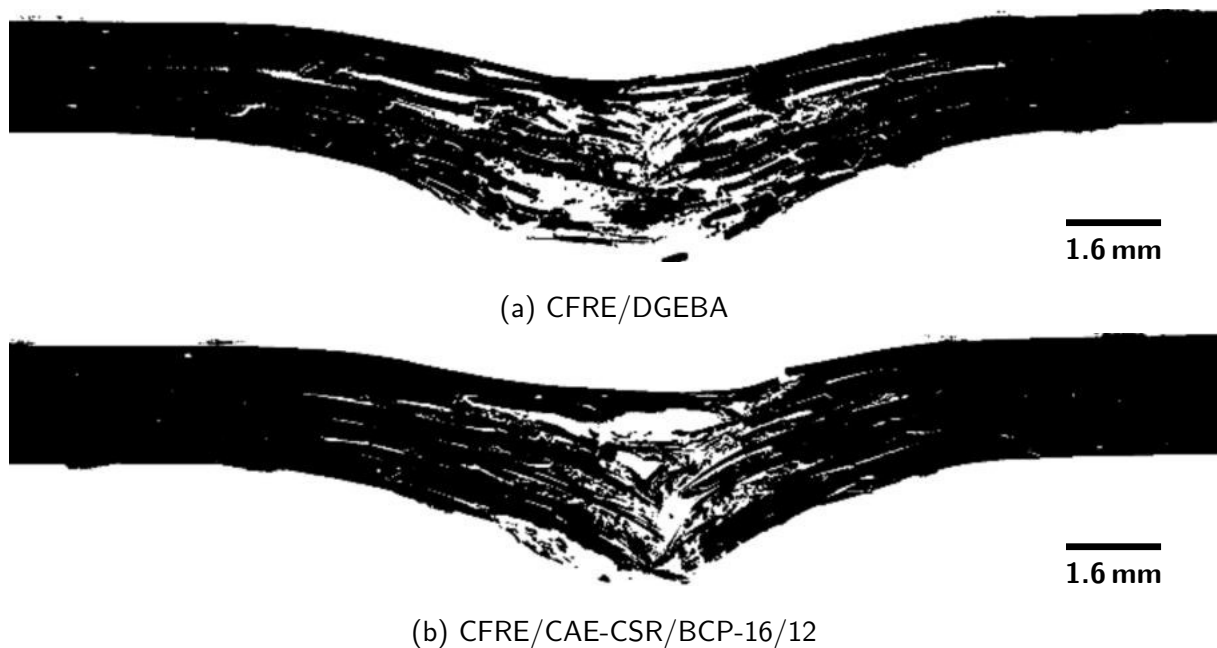


Figure A.106: XRM micrographs showing the inherent damage structure after a 13 J impact on a thin CFRE panel. The figure illustrates the different damage patterns obtained for a untoughened epoxy based fibre reinforced composite (CFRE/DGEBA, top) and a highly toughened one (CFRE/CAE-CSR/BCP-16/12, bottom).

Publications and Conference Contributions

Publications

1. A. Bajpai, B. Wetzel, **A. Klingler**, K. Friedrich, Mechanical properties and fracture behavior of high-performance epoxy nanocomposites modified with block polymer and core-shell rubber particles, *Journal of Applied Polymer Science* 136, 48471 (2019).
DOI: 10.1002/APP.48471
2. C. Goergen, **A. Klingler**, S. Grishchuk, D. May, B. Wetzel, P. Mitschang, Novel Approach in B-Staging of an Epoxy Resin for Development of rCF Non-Woven Prepregs for RTP Processing, *Key Engineering Materials* 809, 521-526 (2019).
DOI: 10.4028/www.scientific.net/KEM.809.521
3. **A. Klingler**, A. Bajpai, B. Wetzel, The effect of block copolymer and core-shell rubber hybrid toughening on morphology and fracture of epoxy-based fibre reinforced composites, *Engineering Fracture Mechanics*, 203, 81–101 (2018).
DOI: 10.1016/j.engfracmech.2018.06.044
4. A. Bajpai, A.K. Alapati, **A. Klingler**, B. Wetzel, Tensile properties, fracture mechanics properties and toughening mechanisms of epoxy systems modified with soft block copolymers, rigid TiO₂ nanoparticles and their hybrids, *Journal of Composites Science*, *Journal of Composites Science*, 2, 72-89 (2018).
DOI: 10.3390/jcs2040072
5. **A. Klingler**, B. Wetzel, Fatigue crack propagation in triblock copolymer toughened epoxy nanocomposites, *Polymer Engineering & Science*, 57, 579–587 (2017).
DOI: 10.1002/pen.24558
6. **A. Klingler**, L. Sorochynska, B. Wetzel, Toughening of Glass Fiber Reinforced Unsaturated Polyester Composites by Core-Shell Particles, *Key Engineering Materials* 742, 74–81 (2017).
DOI: 10.4028/www.scientific.net/KEM.742.74
7. J. Krummenacker, **A. Klingler**, J. Hausmann, B. Wetzel, Improvement of the cyclic loading resistance of highly loaded CFRP components by resin modifications, *Review of Aeronautical Fatigue Investigations in Germany during the period April 2015 to March 2017*, Technical Report, International Committee on Aeronautical Fatigue (ICAF), 2017.
DOI: none

Conference Contributions

1. **A. Klingler**, B. Wetzel, U. Breuer, K. Friedrich, Interlaminar Shear Properties of Toughened Carbon Fibre Reinforced Composites, 22nd International Conference on Composite Materials, Melbourne, Australia, 2019

2. **A. Klingler**, B. Kelkel, T. Rief, M. Gurka, B. Wetzel, Charakterisierung der Faser-Matrix Haftung mittels Einzelfaser-Broutman-Test und Schademissionsanalyse, 22. Symposium „Verbundwerkstoffe und Werkstoffverbunde“, Kaiserslautern, Germany, 2019
3. **A. Klingler**, B. Wetzel, Block copolymer and core shell rubber hybrid toughening of epoxy based carbon fibre reinforced composites, 22nd European Conference on Fracture, Belgrade, Serbia, 2018
4. **A. Klingler**, B. Wetzel, Fracture mechanical properties of triblock copolymer and core-shell rubber toughened carbon fibre reinforced nanocomposites, 8th International Conference on Fracture of Polymers, Composites and Adhesives, Les Diablerets, Switzerland, 2017
5. **A. Klingler**, L. Sorochynska, B. Wetzel, Toughening of Glass Fiber Reinforced Unsaturated Polyester Composites by Core-Shell Particles, Verbundwerkstoffe – 21. Symposium Verbundwerkstoffe und Werkstoffverbunde, Bremen, Germany, 2017
6. **A. Klingler**, B. Wetzel, Fatigue crack propagation in self-assembling nanocomposites, 8th International Conference on “Times of Polymers and Composites”, Ischia, Italy, 2016

Supervised Theses

1. Leschiera, Irene: "From matrix to laminate toughness in CFRP parts", Diploma thesis, Department of Chemical, Materials and Production Engineering, University of Naples Federico II (Naples, Italy), 2016
2. Tschemerow, Viktor: "Einfluss der Funktionalisierung von CNTs auf die Endeneigenschaften eines CNT-modifizierten lastwechselfesten Harzsystems", Studienarbeit, IVW-Bericht 16-092, 01/2017
3. Walter, Evgenij: "Einfluss von Zinkoxidtetrapoden auf die mechanischen Eigenschaften von Faserverbundwerkstoffen", Studienarbeit, IVW-Bericht 17-022, 07/2017
4. Talo Tatuebu, Marius: "Charakterisierung der mechanischen Eigenschaften von partikelmodifizierten Faserverbundwerkstoffen für den Flugzeugbau", Bachelorarbeit, IVW-Bericht 20-009, 04/2020
5. Altenhofen, Stephanie: "Einfluss von Nanopartikeln und Block-Copolymeren auf die Druckeigenschaften und Bruchzähigkeit von Epoxidharzen bei niedrigen Temperaturen", Studienarbeit, IVW-Bericht 20-025, 10/2020

Curriculum Vitae

Personal Data

Name Andreas Peter Klingler
Place of birth Worms, Germany
Nationality German

Work Experience

Since 09/2015 Research Associate
 Leibniz-Institute for Composite Materials (IVW GmbH),
 Kaiserslautern, Germany
01/2015 – 09/2015 Engineer, Goodyear Dunlop Tires Operation SA,
 Colmar-Berg, Luxembourg

Education

09/2019 – 12/2019 Visiting Researcher at the Centre for Advanced Materials Technology
 University of Sydney, Sydney, Australia
 University of Auckland, Auckland, New Zealand
09/2015 – 02/2021 PhD, TU Kaiserslautern, Kaiserslautern, Germany
11/2014 – 06/2014 Diploma Thesis, Nanomaterials Research Group
 University of Toronto, Toronto, Canada
01/2012 – 06/2012 Erasmus Exchange Program,
 Luleå University of Technology, Luleå, Sweden,
10/2007 – 09/2014 Diploma Program Mechanical Engineering,
 TU Kaiserslautern, Kaiserslautern, Germany